SAPIENZA
UNIVERSITÀ DI ROMA

ISTITUTO ITALIANO
DI TECNOLOGIA
CENTER FOR LIFE NANO- & NEURO-SCIENCE

REGIONE
LAZIO

Infrared laser spectroscopy of proteins at the nanoscale

Dipartimento di Scienze di Base e Applicate per l'Ingegneria
PhD course: Mathematical Models for Engineering, Electromagnetics and Nanosciences
Curriculum: Materials Science

Istituto Italiano di Tecnologia, Center for Life Nano- & Neuro-Science
Regione Lazio Financed Project: Studio di spettroscopia laser alla scala nanometrica di proteine

Maria Eleonora Temperini
ID number 1651569

Advisor
Prof. Michele Ortolani

Co-Advisor
Dr. Valeria Giliberti

Academic Year 2023/2024, XXXVI cycle

Infrared laser spectroscopy of proteins at the nanoscale
PhD thesis. Sapienza University of Rome

This thesis has been typeset by LaTeX and the Sapthesis class.

Author's email: mariaeleonora.temperini@uniroma1.it

Abstract

The intricate mechanisms governing protein activity, crucial in life processes and diverse applications like bioelectronics and biomedicine, necessitate experimental advancements for a comprehensive understanding. Nanosciences present innovative pathways to investigate certain unexplored aspects influencing protein functionality. One example of this is the effect of externally applied electric fields, especially on proteins naturally exposed to such fields, like membrane proteins within cell membranes. Among these, proton/ion transporters such as photosensitive microbial rhodopsins appear as relevant examples. However, experimental techniques capable of correlating the investigations of protein conformational changes with the controlled voltage potentials to which the proteins are subjected are currently lacking. To bridge this gap, here it is proposed a novel technique based on the state-of-the-art AFM-IR nanospectroscopy platform. It integrates the sensitivity of infrared (IR) spectroscopy to protein conformation with electric field control, exploiting a metallic atomic force microscope (AFM) tip as both a mechanical IR detector and a nanoelectrode. Initial experiments on the prototype photosensitive protein Bacteriorhodopsin demonstrate its potential, with future perspectives aimed at exploring the effects of transmembrane electric potential on protein dynamics. In a broader sense, this innovative work stands as a significant advancement toward unraveling the intricate interplay between molecular structure and electric fields at the nanoscale.

Introduction

Experimental advancements are crucial for delving into the intricate mechanisms involved in the protein activity, given their crucial functions in various life processes and their wide-ranging applications across fields such as bioelectronics and biomedicine [1, 2, 3]. Despite significant knowledge gained through complementary biophysical techniques, certain aspects and parameters potentially relevant for protein functionality remain unexplored. Indeed, proteins are not static entities but rather dynamic *molecular machines* capable of performing a wide range of functions within living organisms, producing mechanical movements in response to specific stimuli. The integration of nanosciences and nanotechnologies into this framework is therefore outstanding as they can offer novel solutions to biological questions and applications beyond conventional bulk systems, allowing for precise control over protein dynamics and interactions.

One of the interesting aspect to further investigate involves examining the effects of externally applied electric fields on protein properties. Specifically, the interaction between proteins and an external field can induce changes in their conformation or impact their dynamic behavior, potentially influencing their biological functions and charge transport processes [4, 5]. Proteins situated within the lipid cell membrane, particularly those acting as proton/ion transporters, represent the perfect prototype of molecules natively subjected to an electric field. This characteristic is exemplified by photosensitive microbial rhodopsins central to this PhD thesis [6]. The biophysical aspect inherently linked to the cell membrane is indeed the difference in electrical potential between the inside and the outside of the cell (order of tens of mV), which makes membrane proteins subjected to relatively strong electric fields of the order of $\frac{10mV}{10nm} - \frac{100mV}{10nm} \sim 10^6 \frac{V}{m} - 10^7 \frac{V}{m}$ capable to exert forces on the molecular structure. Despite this, the description of the electric fields on membrane protein dynamics at the molecular level is speculative at the moment, due to the lack of nanoscale probes able to monitor the sequence of the protein conformational changes while exposed to a controlled external electric field at the level of an individual cell membrane. The application of static electric fields at the two sides of a single molecule has long posed an experimental challenge since the discovery of the Stark effect in the early days of quantum mechanics [7], i.e. the shifting and splitting of spectral lines in atoms and molecules due to the presence of an electric field. Thus, while the influence of electric fields on membrane proteins is evident, comprehensive understanding at the molecular level necessitates innovative experimental techniques to unlock this aspect of biophysics.

Among the techniques available for the functional characterization of proteins, electrophysiology methods stand out as the gold standard for investigating ion permeation

through transmembrane proteins while maintaining control over the voltage potential across the lipid membrane. These approaches facilitate the direct recording of ionic currents through a small (few-micron diameter) portion of the membrane, even within intact cells, by employing a micropipette filled with an electrolyte solution and a recording electrode (patch-clamp method). By allowing user-defined membrane potentials, these methods enable the measurement of ion currents, providing valuable insights into the voltage-dependent permeability of transmembrane proteins. More in general, in recent decades, the development of nanotechnologies has led to numerous advancements in protein-based bioelectronics, leveraging various electrical devices and techniques at the single-molecular level, which are not achievable with conventional ensemble approaches [8]. These include scanning probe microscopy (SPM)-based protein junctions and solid-state nanogap-based (1-10 nm) bioelectronic devices, where electrodes are fabricated through micro/nano processing or electrochemical methods [9, 10, 11]. Such devices can be employed to monitor electron transport processes and can also be applied to transmembrane proteins on lipid membrane patches or reconstructed lipid monolayers embedding the protein of interest [12, 13].

Understanding the correlation between transport properties and the conformational state of molecules requires the integration of fluorescence or vibrational spectroscopy sensitive to protein structure and its variations with controlled applied voltage [14]. Nonetheless, the classical optics approaches have inherent limitations, particularly concerning the low sensitivity and spatial resolution, which typically involve working with large numbers of nominally identical molecules in thick films or suspensions, inhibiting the investigation of conformational changes as a function of controlled membrane potential and/or ion concentration gradient through a single nanometer-thick membrane ($\sim$ 5-10 nm). More recently, near-field optical approaches have facilitated the translation of spectroscopy measurements to the nanoscale, achieving the sensitivity necessary to probe objects with nanometer dimensions or thicknesses. Methods based on near-field optical energy enhancement have already been applied to Raman spectroscopy, allowing insights into the relationship between electron transport and molecular conformation and/or inter-molecular organization as a function of applied voltage bias [15, 16, 17, 18]. However, comparable nanoscale voltage-dependent vibrational studies using infrared (IR) absorption spectroscopy, the most prevalent technique for studying protein conformational states, have not yet been reported.

During my PhD work, I developed a novel technique that merges the sensitivity of IR spectroscopy to the conformational changes of proteins with the possibility to precisely control an applied external electric field with nanometric resolution. This breakthrough is made possible through the utilization of SPM methods, specifically an atomic force microscope (AFM), in conjunction with the state-of-the-art IR nanospectroscopy techniques. The employed approach, known as AFM-IR, relies on detecting sample photothermal expansion through the AFM probe operating in contact mode [19]. In 2019, my research group successfully demonstrated the capability of the AFM-IR technique to discern subtle conformational changes in photosensitive proteins upon light activation at the level of single cell membranes. These experiments were conducted for the first time on the prototype photosensitive protein Bacteriorhodopsin [20]. In the first part of my PhD thesis, I also conducted

AFM-IR experiments to investigate the conformational dynamics of the light-gated Channelrhodopsin protein [21], driven by its significance in the field of neuroscience. Furthermore, the nanospectroscopy setup has then been customized by integrating an external electric circuit and creating electrical contacts with the metallic AFM tip and sample support. Beyond the preliminary electric-field-induced effects observed on Bacteriorhodopsin and here reported, the real aim, in perspective, is to explore the effects of a controlled electric membrane potential on the subtle conformational changes associated with the photoactivity of transmembrane proteins.
This experimental effort marks the first instance of combining vibrational spectroscopy and the electrical mode of AFM, paving the way for unprecedented insights into the intricate interplay between molecular structure and electric fields at the nanoscale.
The structure of this PhD thesis is outlined as follow:

- In Chapter 1, the structural and functional characteristics of the transmembrane proteins central to my research are introduced, specifically focusing on microbial rhodopsins such as Bacteriorhodopsin and Channelrhodopsin. Additionally, an overview of conventional biophysical techniques used in protein analysis is provided, emphasizing their complementary nature and limitations.

- In Chapter 2, the capability of IR spectroscopy in examining the structural components and dynamic behaviors of proteins is explored. Near-field strategies aimed at enhancing IR radiation sensitivity to reduce the number of probed molecules are also discussed.

- In Chapter 3, the possible effects observed in proteins when subjected to static electric fields are presented, particularly focusing on observable variations in IR spectra. Typical nanoscale experiments for conducting transport measurements or voltage-dependent studies on molecules are also outlined. Furthermore, I propose the development of the voltage-controlled AFM-IR platform as an innovative technique for electric-field-dependent nanospectroscopy in the mid-IR range.

- In Chapter 4, the working principles of various IR techniques used in my research is presented, including the voltage-controlled AFM-IR setup. The advancements in IR experimental techniques over time are highlighted, particularly underlining the improvements in spatial resolution from diffraction-limited micrometer volumes to a few nanometer scales.

- In Chapter 5, a detailed account is provided regarding the experiments that I conducted using the AFM-IR approach to observe the photoactive response of the Channelrhodopsin sample at the nanoscale.

- In Chapter 6, the results obtained from the customized AFM-IR technique are examined, with a focus on electric-field-induced effects on the IR response of polymeric samples (PMMA and PVDF) used as template systems. Importantly, preliminary results from experiments conducted with the voltage-controlled platform on Bacteriorhodopsin samples are presented.

- In Chapter 7, results from a side part of my PhD project are reported. It involves time-resolved experiments on the Bacteriorhodopsin protein. These studies are conducted using a home-built IR-microscope employing a quantum cascade laser source, the optical design of which is detailed at the end of Chapter 4. The results of a such experiment serve as benchmarks for potential future AFM-IR time-resolved studies.

Contents

Chapter 1

Photosensitive transmembrane protein

Transmembrane protein molecules embedded in the lipid cell membrane are the gates for ions and molecules linking the extracellular and intracellular environments, and are the keys in several biological processes including metabolism, respiration, and signalling [22, 23]. Almost all of these cellular mechanisms rely on a sequence of transient large-scale **protein conformational changes**, i.e. collective rearrangements involving subdomains of hundreds of atoms that can involve time scales around μs-ms, which are triggered by specific stimuli (ligand-binding, pH change, absorption of light) [24, 25]. Unraveling the way the proteins sense and respond to such stimuli is central to understand living organism at the molecular level [26]. One biophysical aspect inherently common to all transmembrane proteins is the electric potential difference between the two sides of the lipid membrane, i.e. the **membrane potential** [22, 23]. However there is still a gap in the elucidation on how this parameter can affect and alter the protein functionality due to the lack of proper experimental approaches.
In this chapter, I introduce the definition of the membrane potential, the structure and the function of **photosensitive microbial rhodopsins**, with a specific focus on the two proteins investigated during my PhD work (Bacteriorhodopsin and Channelrhodopsin). I then delve into the experimental techniques typically employed for protein investigation, offering diverse and complementary insights. Finally, I present the idea of the **innovative technique** based on **nanospectroscopy in the infrared** approach, that I developed and used during my PhD project to address, in perspective, the significant knowledge gap in the photosensitive protein investigation, elucidating the intricate relationship between **membrane potential** and **protein activity**.

1.1 Membrane potential

Almost all of the biological cells are made of a plasma membrane composed by a lipid bilayer that forms the barrier between the internal part of the cell and the extracellular environment. The presence of transmembrane proteins across the lipid bilayer, which act as channels or pumps, makes the membrane permeable

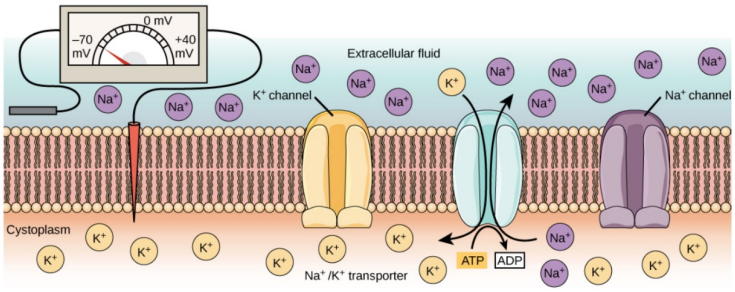

Figure 1.1. Illustration of transmembrane proteins embedded in the lipid cell membrane. At the resting potential (-70 mV), the voltage-gated K^+ and Na^+ channels (yellow and purple protein respectively) are closed, while Na^+/K^+ pump (light blue protein) contribute to maintain constant the membrane potential [28].

to the flow of ions (e.g. H^+,K^+, Na^+, Ca^+, Cl^-...), otherwise unable to pass through the hydrophobic lipid region. The concentrations of the ions in the inter- and extra-cellular side determine the potential difference across the cell membrane, which can be defined in first approximation as $V = \phi_{IN} - \phi_{OUT}$, where ϕ_{IN} and ϕ_{OUT} are the electric potentials inside and outside the cell, respectively [27]. For a non-excitable cell the typical values of V range from -80 mV to -40 mV, due to the fact that the internal side of the cell is usually more negative with respect to the outside (Fig.1.1). The precise value of the membrane potential depends on several factors: concentration of ions (both diffusible and non-diffusible), activity of the sodium-potassium (Na^+/K^+) pump and variable permeability of the cell membrane for ions. The protein ion channels directly involved in the control of the membrane potential can be divided in two categories: (i) passive channels, which are pores through which the molecules pass depending on their concentration gradient and they contribute to establish the resting membrane potential; (ii) active channels, which open and close allowing the ion transport either depending on the change of the membrane potential (voltage-gated channels), or after binding to some other protein molecules (ligand-gated channels), or even after other external stimuli (e.g. light, mechanical stimulus, variation of the temperature...).
Among living cells, only the category of excitable ones, including some plant cells and neurons and muscle cells in animals, can change the value of the resting membrane potential by generating an action potential [29, 30]. This is a transitory and propagating variation of the membrane potential generated by a stimulus and through which the excitable cells transmit signals to target tissues. The process consists of different steps, as shown in Fig.1.2. The hypopolarization is the initial increase of the membrane potential to the value of the threshold potential. The latter is the value at which proteins that act as voltage-gated sodium channels open causing a large influx of sodium ions. This step is called the depolarization phase during which the inside of the cell becomes positive. The step of extreme positive value is the overshoot phase. After the overshoot, the sodium permeability suddenly decreases due to the closing of its channels. The overshoot value of the cell potential opens voltage-gated potassium channels, which causes a large potassium efflux, decreasing the cell electropositivity. This step is the repolarization phase, whose purpose is to restore the resting membrane potential. The repolarization

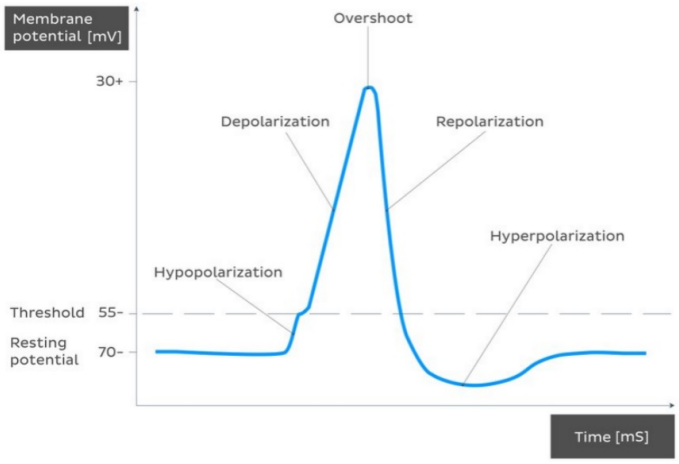

Figure 1.2. Graph of the trend of the membrane potential during the action potential [31].

always leads first to the hyperpolarization, a state in which the membrane potential is more negative than the default membrane potential. But soon after that, the membrane establishes again the values of membrane potential.

1.2 Photosensitive rhodopsins

Among transmembrane proteins that regulate the ion flux and thus the membrane potential, there is a special category of photosensitive proteins, also called rhodopsins, whose channel or pump activity is regulated by the absorption of visible radiation in the 400-700 nm range [32, 33]. Their sensitivity to light arises from the presence of the retinal, a polyene chromophore, covalently bound to the protein structure that changes conformation thanks to a photoisomerization process. Free in solution, the retinal has an absorbance maximum at 380 nm but the surrounding protein forms a specific pocket for binding the retinal cofactor, typically resulting in a large redshift of the retinal absorbance. The precise wavelength value depends on the specific protein mutant that can be affected by several factors, such as the protonation state and the electrostatic interactions of the chromophore with charged and polar amino acids [34]. As a consequence of the retinal photochemical reaction, the protein follows a vibrational relaxation, assuming different conformational states that allow it to fulfill its activity. The sequence of these rhodopsin states is called photocycle, as proteins recover their initial state (also called dark-adapted state) within few milliseconds or seconds after the initial excitation.

Rhodopsins can be classified as microbial or animal rhodopsins, also termed type-I and type-II rhodopsins, respectively. It has been indeed observed that in Eukaryotes, Bacteria, and Archaea the rhodopsins are employed for energy conversion or the initiation of intra- or inter-cellular signaling, while in animals they are a specialized subset of G-protein coupled receptors (GPCRs) employed, for example, in visual and non-visual phototransduction [36]. G proteins act indeed as molecular switches inside cells and are involved in the transmission of signals within cells from external stimuli.

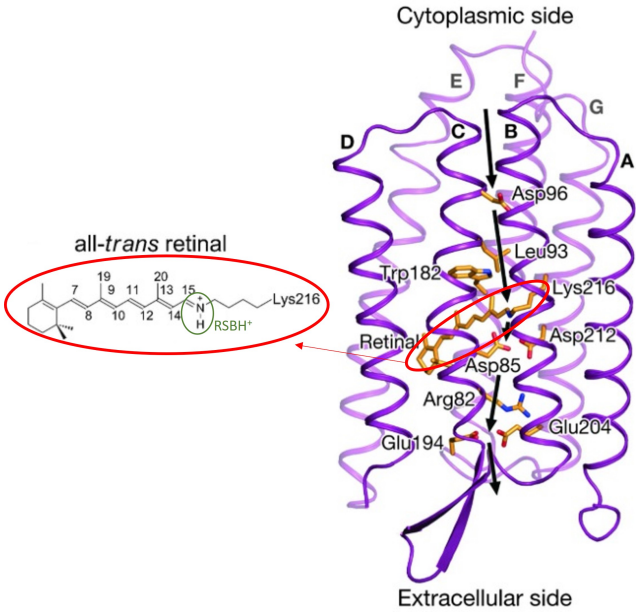

Figure 1.3. Example of the structure of a microbial rhodopsin protein. The α-helices are labeled from A to G proceeding from the N-terminus to the C-terminus and are connected by loops and β-sheet links. The covalently bound retinal chromophore is represented with sticks in the center of the protein. Adapted from [35].

When located inside the cell, G proteins are activated by GPCRs that span the cell membrane: signaling molecules bind to a domain of the GPCR located outside the cell causing in turn an intracellular GPCR domain to activate a particular G protein through a collision coupling mechanism. The final change in the cell function results then from a cascade of additional signaling events triggered by the G protein.
Anyhow, both microbial and animal rhodopsins possess a similar secondary structure made of seven transmembrane (TM) α-helices with the N- and C-terminus facing outside and inside of the cell, respectively, and the retinal linked through a Schiff base ($C = N$) to a lysine residue in the middle of the seventh transmembrane helix (Fig.1.3). The retinal Schiff base (RSB) is protonated (RSBH+) in most cases, and changes in protonation state are part of the signaling or transport activity of rhodopsins. After the light stimulus, the retinal undergoes the all-*trans*/13-*cis* isomerization in microbial rhodopsins and the 11-*cis*/all-*trans* isomerization in animal rhodopsins (Fig.1.4 a), where the n-*cis* notation indicates the isomeric conformation of the $C_n = C_{n+1}$ bond in the polyene chain. The retinal photochemical reaction occurs in hundreds of femtoseconds and its dynamic has been widely investigated both theoretically and experimentally thanks to ultrafast spectroscopy techniques, leading to a two-state Franck-Condon model. As the energy barrier for the rotation around the double C=C bond is high, isomerization becomes possible only in the first excited electronic state, where the chromophore becomes twisted with a torsional motion toward a minimum in the excited-state before relaxing into the ground state. In microbial rhodopsins, all-*trans*-retinal is typically isomerized into the 13-*cis* form (Fig.1.4 b, right panel), even though the reversion to the all-*trans* can occur [38]. As an example, the selectivity of isomerization for Bacteriorhodopsin proteins

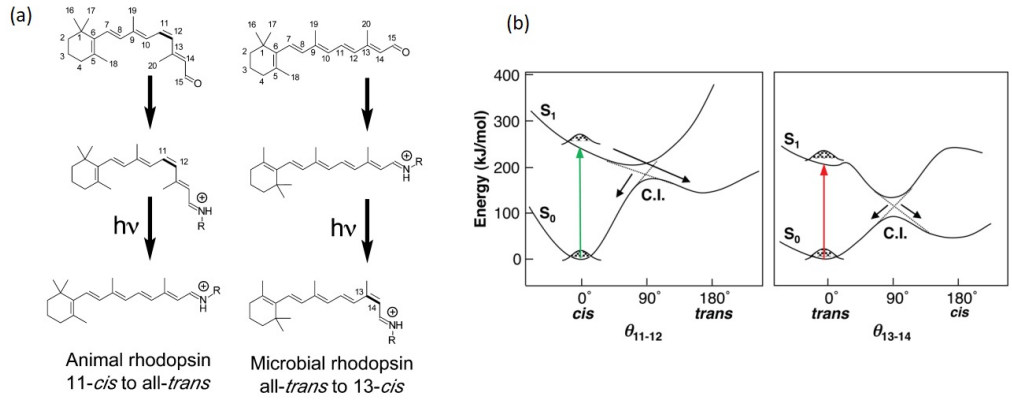

Figure 1.4. a)Ground-state and excited state conformation of the retinal chromophore of animal (left) and microbial (right) rhodopsins. b) Potential energy profiles along the reaction coordinate (the dihedral angle of $C_{11} = C_{12}$ and $C_{13} = C_{14}$ bonds) of animal(left) and microbial (right) rhodopsins [37].

(introduced below) is 100%, and the quantum yield of the all-*trans*/13-*cis* isomerization was found to be 0.64 [37]. The case of the 11-*cis*-retinal to all-*trans*-retinal isomerization for animal rhodopsins is also reported in the left panel of Fig.1.4 b. More complex three-states models have also been proposed to describe the retinal photoisormerization process [39].
After the general presentation of rhodopsins, here on I will focus on microbial rhodopsins that are the unique proteins studied in this PhD thesis. In particular, I now introduce the Bacteriorhodopsin and Channelrhodopsin proteins that are the two samples on which I conducted experimental IR measurements. The detailed description of these two proteins also gives the opportunity to deepen the aspects related to the microbial rhodopsin photocycle and activity.

1.2.1 Bacteriorhodopsin

Bacteriorhodopsin (BR) is a photosensitive transmembrane protein naturally found in the *Halobacterium salinarium*, a bacterium belonging to the class of eukaryotes, which lives in aqueous environments with a high salt concentration. The function of the BR is to act as a proton pump, following the absorption of visible light [40]. That is, the conformational changes that the protein may undergo as result of a photochemical reaction allow the transfer of protons from the intracellular environment to the extracellular one, generating a proton gradient which is then converted into chemical energy through the synthesis of adenosine triphosphate (ATP) by another membrane protein, the ATP-synthase. BR makes up 75% of the mass of the entire purple membrane in which it is located (so called due to its characteristic color) and it is organized in a grid made of two-dimensional hexagons. Each unit of the hexagon contains a trimer of protein molecules, while the rest of the membrane is made of lipids. BR consists of a single polypeptide chain of 248 amino acids, 70% of which are hydrophobic. The polypeptide chain crosses the membrane with a seven α-helix structure and the retinal is linked to a lysine 216 residue in the

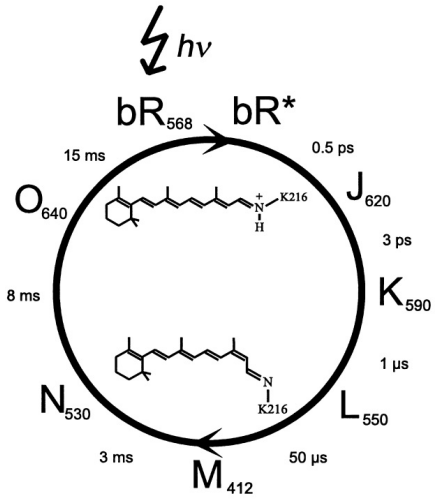

Figure 1.5. BR photocycle. The bR* state is the dark-adapted state, while the other intermediates are indicated with the letters J, K, L, M, N and O. The subscripts of each intermediate indicate the wavelengths in nanometers at which the maximum absorption occurs and the times between subsequent intermediates are the characteristic life-times of each intermediate [41].

seventh helix by means of a RSB, while the connections of the helices are constituted by loops and β-sheets. The retinal separates the channel that forms between the helices for the passage of the proton into the cytoplasmic channel (CC) and the extracellular channel (EC). Both channels contain amino acids that have a key role in proton transport: the aspartic acid 85 (Asp-85) residue of the EC accepts the proton from the protonated $RSBH^+$ after the retinal photoisomerixation and the Asp-96 residue is subsequently the responsible for RSB reprotonation.
As already told in general for rhodopsins, BR absorbs visible light and encounters a reversible photocycle with several intermediates, spectrally distinct, conventionally indicated with the letters J, K, L, M, N and O. The subscripts in Fig.1.5 indicate the wavelengths in nanometers of the maximum absorption in the spectral range of the visible radiation for the respective intermediate, while the times represent the intermediate life-time.

BR is the most studied photosensitive protein and the mechanisms involved in all its conformational changes leading to the transition of the protons in the various intermediates are already well-known in detail. The investigation of these mechanism has been possible also thanks to infrared difference spectroscopy studies, as will be explained in Chapter 2 sec.2.3.1. Despite this, a deep understanding of the dependence of functional conformational changes of BR on the membrane potential is still an open issue due to the lack of experimental approaches.
Upon the retinal photoisomerization from all-*trans* to 13-*cis*, the BR passes through the conformational states named as J and K in few picoseconds, reaching the L state in a timescale of the microsecond order. In the transition between L and M intermediates, the Asp-85 residue accepts a proton from the Schiff base and at the same time a proton is released into the extracellular environment. Reaching the N intermediate, the seventh α-helix undergoes a movement to allow the orientation of

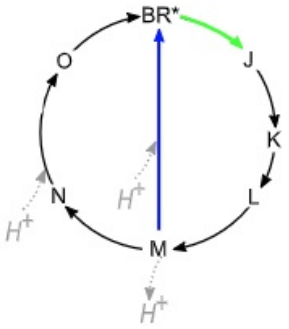

Figure 1.6. BRD96N photocycle [20].

the Schiff base to the purchase a proton and to reprotonate. The last intermediate O corresponds to the reprotonation of the Asp-96 residue that is involved in the proton transport process and the simultaneous reisomerization of the retinal from 13-*cis* to all-*trans*. While recovering the BR dark-adapted state the Asp-85 residue transfer a proton to the release site on the extracellular side. It is important to emphasize that the photocycle kinetics strongly depends on environment conditions, as hydration state and pH value which is not surprising for a proton pump.
The detailed knowledge on BR structure and activity came from the applicability of different biophysical techniques which have often been further developed with research on BR itself and have delivered important contributions also to the investigation of more complex systems. Some examples, further detailed in sec.1.3, are X-ray and electron crystallography and solid-state nuclear magnetic resonance (NMR) spectroscopy employed for the investigation of the protein structure, and time-resolved visible and vibrational spectroscopy applied to the photo-induced BR dynamics. The interest in understanding the activity of this protein was initially driven by the wish to uncover the biological mechanism of the proton-pump, taking BR as a prototype and model in the field of rhodopsins. Nowadays, further studies are also conducted in the perspective of applications of BR molecules in the biotechnology field. These include the development of light batteries for harvesting energy from sunlight, utilization in artificial retinas and optical information recording [42]. This versatility arises from the BR capability in charge transportation upon visible light activation [43, 44]. For this purpose, it has been essential the development and synthesis of BR mutants, in which one or more amino acid residues are substituted with different one altering the photocycle features. The mutants therefore support the investigation studies on the residue role in the protein activity [45, 46] and, at the same time, they can be engineered to optimize the dynamic characteristics needed for the specific protein employment [47].

I now briefly introduce the protein mutant used in the experiments of this thesis. This is the "slow mutant" BRD96N in which the aspartic acid Asp-96 has been replaced by asparagine-96 (Asn-96). Aspartic acid and asparagine are also indicated with the letters D and N respectively, from which the name of the D96N mutant derives to indicate the amino acid substitution at position 96. This mutant is obtained with genetic mutations of BR expressed by the *Escherichia coli* bacterium. The residue 96 thus loses its function of proton donor for the Schiff base whose

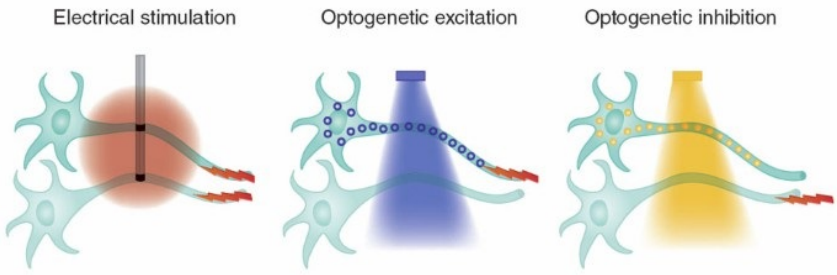

Figure 1.7. Schematic representation of the optogenetics approach in which the excitation and inhibition of neuronal cells is selectively conducted on the target cells expressing light-sensitive proteins [50].

reprotonation must take place directly from the aqueous solution (see *Appendix I*). The D96N mutant is therefore characterized by a longer lifetime for the intermediate M, in which the Schiff base is deprotonated, so that the whole photocycle is slowed down from about 30 ms to more than 2 s [48]. As will be further discussed below, the use of this slow mutant allows the intermediate M to be characterized in a more reproducible way by IR spectroscopy since a second visible wavelength can be employed to short the photocycle from the M intermediate directly to the dark-adapted state. Specifically, the M intermediate of the BRD96N mutant absorbs at 405 nm, so that after the photoexcitation with the green light (565 nm) a blue illumination can be employed to control the recover of the BR dark-adapted state, as schematically depicted in Fig.1.6.

1.2.2 Channelrhodopsin

Channelrhodopsin (ChR) is a naturally occurring light-gated ion channel that is present in unicellular green algae (*Chlamydomonas reinhardtii*) and it is important for allowing these cells to find suitable light levels. The relevance of ChR grew starting from 2002, when Georg Nagel, Ernst Bamberg and Peter Hegemann have demonstrated that it is possible to express this type of microbial rhodopsins also in mammalian cells [49]. This discovery set the grounds for the research field named optogenetics, in which the control of the activity of neurons or other cell types with light is developed and investigated. The photosensitive proteins, once genetically expressed in excitable mammalian cells such as neurons and muscle cells, have indeed proved to be a powerful tool allowing the optical control for the cell stimulation. In these cells, controlled transport of specific ions across the cell membrane allows the cell to receive, process, and propagate information to and from neighboring cells, based on continuous fluctuations of the electrostatic potential between the internal and the external side of the membrane. This approach therefore opened the way to a deeper understanding of the neural activity with high temporal and spatial resolution thanks to the employment of light to selectively activate or inhibit genetically labeled cells in place of more invasive electrical contacts (Fig.1.7).
Two types of Channelrhodopsin exist: ChR1, which is an ion selective channel, and ChR2 which, on the contrary, is a non-specific ion channel. The second species is the most studied in the field of optogenetics due to its capability of being expressed

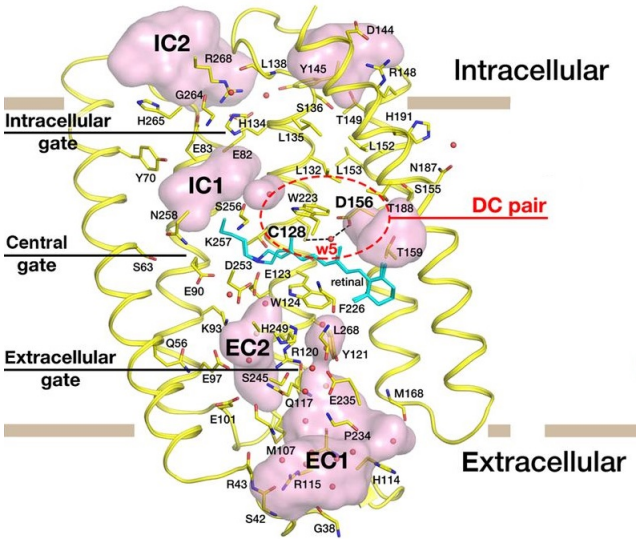

Figure 1.8. Structure of the Channelrhodopsin-2 [51].

in neural cells and therefore being used in photostimulation processes. Channelrhodopsin is a chain of 315 amino acids consisting of seven α-helix units that cross the cell membrane, linked by short loops and β-sheet fragments. Thanks to X-ray crystallographic measurements, it was observed that the ChR molecules tend to form dimers with disulfide bonds between N-terminal amino acids. The retinal is placed in the center of the helical structure, covalently bonded to lysine-257 through a protonated Schiff base, and divides the protein between the intracellular and extracellular side. When the retinal absorbs a photon, it switches from all-*trans* to 13-*cis* form, changing its structure and opening the protein pore, through which the ions begin to flow due to the effect of the concentration gradient and the electric potential. In the absence of light, ChR does not present a transmission channel between the intracellular and extracellular environments, but it is possible to identify four cavities (Fig.1.8), separated by three polypeptide chain sections named gates: the central gate (CG), near the retinal, that separates the intracellular cavity 1 (IC1) from the extracellular cavity 2 (EC2); the intracellular gate (ICG), which is placed instead between intracellular cavities 1 (IC1) and 2 (IC2), and the extracellular gate (ECG) between the extracellular ones (EC1 and EC2). Another gate, which has relevant effects on the lifetime of the channel opening, is the one formed by the amino acid residues aspartic acid Asp-156 and cystein Cys-128. The mutation of one of the two residuals causes a deceleration in the closing and opening process of the channel that slows down the photocycle of the protein. The four gates, as a consequence of the retinal isomerization, undergo conformational changes, which determine the opening of the pore putting the successive cavities in communication, thus forming a channel between the cytoplasmic and the external environment.

Like other rhodopsins, the ChR photocycle is made of several intermediates. The retinal in the dark-adapted state has an absorption maximum at wavelengths around 470 nm. The electronic properties of the retinal are then modulated by the electrostatic structure of the surrounding environment that varies over time during which

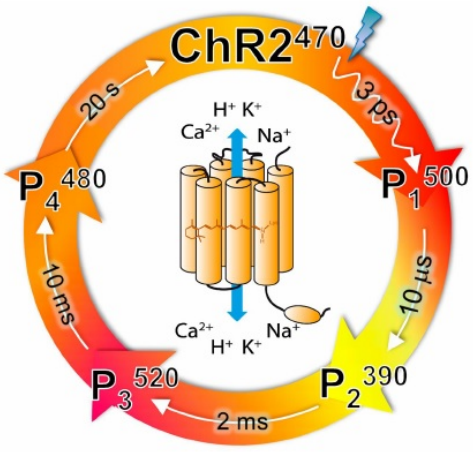

Figure 1.9. ChR photocycle. The ChR2 state is the dark-adapted state, while the other intermediates are P_{1-4}. The superscripts of each intermediate indicate the wavelengths in nanometers at which the maximum absorption occurs and the times between subsequent intermediates are the characteristic life-times [52].

the ChR passes through the different intermediates. With the isomerization of the retinal from all-*trans* to 13-*cis*,the intermediate P_1^{500} is formed. In the intermediate notation the superscript indicates the wavelength in nanometers at which maximum absorption occurs and the subscript is a number that allows to identify the temporal ordering of the intermediates. Subsequently, the Schiff base deprotonates and the protein changes conformation to the P_2^{390} state. With the reprotonation of the Schiff base, the intermediate P_3^{520} is formed, which is the open conductive state of the protein, also named *O*. During the decay of this intermediate to P_4^{480}, state the channel closing takes place. The final step of relaxation to the ground state occurs in an very long time interval compared to that of the BR, of about 20 seconds. In the photocycle scheme of Fig.1.9 the life times of the various intermediates are also reported. The first proton acceptor from the Schiff base has been identified with the residue Asp-253, while the internal donor is Asp-156. In the transition from the closed to the open state, a movement of the second α-helix also takes place allowing the passage of water inside the protein [52].
The mutant employed in my thesis experiments is the C128S protein mutant in which the substitution of cysteine in position 128 (Cys-128) with the non-polar serine amino acid removes a disulfide bridge from the molecule. This mutation is demonstrated to block the protein in the open intermediate state, and the energy barrier between the open and closed states, however, can be overcome with green light illumination [53] enabling an on-off switching of the ChR2 channel gate by alternating the use of the two wavelengths. This concept is better explicated by photocurrent measurements reported in Fig.1.10. The experiments have been conducted on the wild-type ChR2 (Fig.1.10a) and on the C128S slow mutant (Fig.1.10c-d) in response to pulses of 470 nm blue light (blue bars). The observed photocurrents reveal that the conducting state P_3^{520} accumulates in the case of the mutant and the closing of the channel after light-off is observed to slow down by four orders of

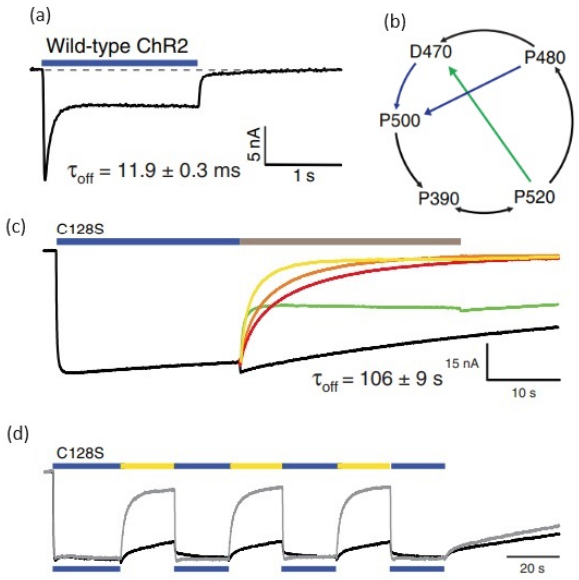

Figure 1.10. a)Photocurrent measurements conducted on the wild-type ChR2. b) Schematic of the ChR2 photocylcle. c) Photocurrent measurements conducted on the C128S mutant, employing a second pulse of longer wavelength to accelerate the off kinetics (green=530 nm, yellow=546 nm, orange=570 nm, red=600 nm). d) Bi-stable switching of the C128S mutant alternating pulses of two different wavelengths. Adapted from [53].

magnitude. The off kinetics to restore the dark-state (Fig.1.10b), however, can be accelerated with a second light pulse (grey bar) of longer wavelength following the excitation pulse. The highest acceleration of the off-kinetics is seen with 530-nm light, which is close to the absorption maximum of the P_3^{520} conducting state, even if the current inactivation is only partial, as a result of substantial absorption of this wavelength by the dark state. In contrast, light of longer wavelengths showed a slower, but more complete, inactivation. Thus, alternating the excitation and inhibition with different wavelengths of light allows for reversible on-off switching of the protein conductivity.

1.3 Analytical methods for photosensitive proteins

As can be inferred by the intermediate sequences during the rhodopsin photocycle, the functional activity of photosensitive proteins is based on structural changes that can be as subtle as protonation changes of a single amino acid, few H-bond changes over thousands of H-bonds existing inside a protein or reorientation of single amino acid side chain. Various biophysical techniques are commonly employed to investigate both the structure and activity of proteins, comprising applications to transmembrane proteins within intact cells, individual membrane patches excised from cells or reconstructed lipid bilayers. In order to explore the potential and limitations of these experimental approaches, I provide here an overview supported by a summary table (Fig.1.11) of the methods frequently employed in protein

		Structural information	Dynamic information	Kinetic of conductive state	Experiments as a function of membrane potential	Limitations for functional study
Structural techniques	X-ray crystallography	√				*"Frozen" state of the protein*
	Nuclear magnetic resonance	√				*"Frozen" state of the protein*
	Cryogenic electron microscopy	√				*"Frozen" state of the protein*
	Time-resolved serial crystallography	√	√			*Only small conformational changes*
Functional techniques	High-speed AFM		√			*Lack of sensitivity to specific conformational changes*
	Fluorescence resonance energy transfer microscopy	√ (FRET)	√	√	√	• *Sensitivity to dynamic of specific labelled residues* • *Possible interference between excitation laser and retinal absorption*
	Infrared spectroscopy	√	√	√		*Limited to bulk systems*
	Raman spectroscopy	√	√	√		*More sensitive to the retinal conformational changes*
	UV-visible spectroscopy	√	√	√		*Sensitivity only to the retinal dynamic*
	Electrophysiology			√	√	*Lack of sensitivity to conformational changes*

Figure 1.11. Potential and limitations of biophysical techniques applied to the protein investigation.

investigation. They can be broadly classified as structural and functional techniques, with the latter including scanning probe methods, spectroscopy and microscopy techniques and electrophysiology, which is the standard technique where one can gain insights into the dependence on protein activity on the membrane potential and to which I dedicate a particular focus here.
X-ray crystallography, nuclear magnetic resonance (NMR) spectroscopy and the more sophisticated cryogenic electron microscopy (cryo-EM) are widely used to reveal protein structures with atomic resolution [54, 55, 56]. Such structural techniques have been applied also to photosensitive transmembrane proteins [57, 58, 59], although the requirement of purification of proteins is still a big challenge and hence a limitation for these approaches [60]. Moreover, these techniques can not track the modifications on the structures connected with the protein activity, unless one is able to freeze the protein in a specific intermediate conformation. This is partially true for X-ray crystallography because time-resolved serial femtosecond crystallography (SFX) methods exist for ten years now [61]. SFX has limitations though, since large conformational changes and slower intermediates are not detectable because they disrupt the microcrystal order necessary for diffraction and each crystal is destroyed by the X-ray pulse, so continuously refreshed microcrystals are required [62].
In addition to structural investigation methods, other biophysical techniques offer information on the functional activity of proteins. This is the case for atomic force microscopy (AFM), fluorescence resonance energy transfer (FRET) microscopy, vibrational and visible spectroscopy and electrophysiology.
The scanning probe techniques based on AFM operating in high-speed mode have been used to study the kinetics of single molecules of photosensitive proteins at

the individual cell membrane level [63, 64]. Thanks to the nanometer resolution of the AFM probe is indeed possible to monitor structural variations, such as channel opening and helix tilting, through high-speed topographic measurements. However, AFM technique can not solve the specific molecular mechanisms involved in the protein dynamics.
In the context of microscopy investigation, the mechanism of FRET involves a donor fluorophore in an excited electronic state, which may transfer its excitation energy to a nearby acceptor molecule in a non-radiative way through long-range dipole-dipole interactions [65, 66]. Energy transfer efficiency is extremely sensitive to the distance between the acceptor and the donor, making FRET able to observe specific protein conformation changes involving small changes in distance between the two fluorophores. However, in a protein the information is limited to the molecular mechanism involving the labeled residues so that this method can not provide information on the overall protein dynamics. In addition, in the specific case of photosensitive transmembrane proteins, the light in the visible range used for the fluorescence microscopy can interfere with the photoactivation of the proteins.
Vibrational spectroscopy techniques, which are sensitive to the intrinsic vibrations of chemical bonds inside the molecules, provide an additional possibility to study molecular mechanisms with high chemical specificity and temporal resolution [67]. Among these, IR absorption spectroscopy is the fundamental tool employed in my PhD thesis. As explained further in Chapter 2, the technique exploits the absorption of IR radiation by chemical bonds, enabling the identification of specific vibrations of amino acid side chains, functional groups, and hydrogen bonds within proteins. It not only provides molecular sensitivity to the chemical composition of a sample but also to the protein structure components, allowing the isolation and tracking of subtle molecular variations in dynamic processes. Similarly, Raman spectroscopy represents another important vibrational methodology based on the inelastic scattering of photons interacting with molecules. The difference in energy between the incident and scattered photons is known as the Raman shift and corresponds to the energy of the vibrational mode. Concerning the study of photosensitive proteins, ultraviolet-visible (UV-VIS) resonance Raman spectroscopy enhances sensitivity to vibrational modes of retinal and its environment by using incident wavelengths in resonance with electronic transitions [68, 69]. However, this technique loses information on conformational changes of the protein structure, as the signal remains very weak. Regarding the retinal photoexcitation, the electronic transitions can also be probed by means of absorption UV-VIS spectroscopy [70].
Clearly, functional methods aimed at tracking conformational changes rely on the support of structural information provided by the complementary techniques and molecular dynamic simulations. This complementarity is essential for gaining insights into the interpretation of recorded observations. However, it remains a challenge to investigate a direct correlation between structural changes in photosensitive proteins and their functionalities along with the influence of membrane potential on these processes. None of the mentioned techniques can precisely correlate these information due to the inability to apply and precisely control a uniform external electric field on the sample, because of experimental constrains. On the contrary, electrophysiology methods, which are discussed in the following section, offer the experimental configuration that permits both the examination and application of

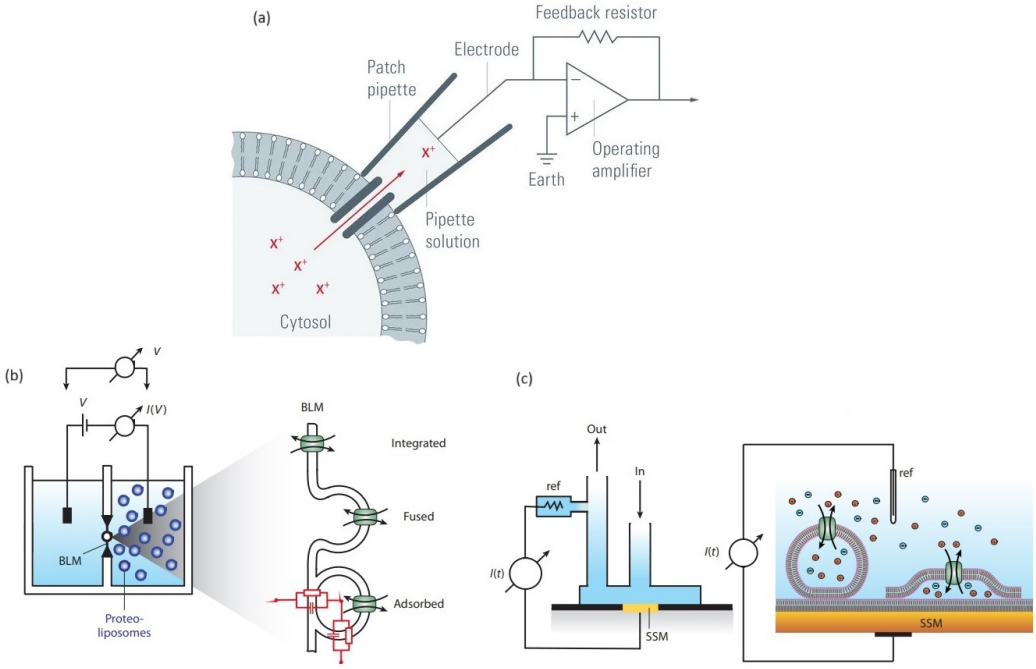

Figure 1.12. Schematic depiction of a) a patch-clamp experiment on a cell, b) a free-standing planar bilayer configuration separating the two compartments of a cuvette and c) a solid-supported membranes (SSMs) configuration for electrophysiology measurements [71].

transmembrane potential on individual cell membranes, although without direct insight into protein structure.

1.3.1 Electrophysiology methods for transmembrane proteins

The electrophysiology refers to the investigation of the electrical properties of cells and tissues [71]. Among the techniques discussed in the previous section, electrophysiology stands out as perhaps the most versatile method for functionally characterizing transport processes of membrane proteins. The proteins of interest are typically either in the natural biological lipid membrane or an artificial one, influencing the recorded signals. The system can be therefore approximated as a parallel arrangement of a resistor and a capacitor with capacitance C to account for the membrane influence. Electrophysiological measurements involve detecting currents *I(t)* generated through the membrane or transmembrane potentials *V(t)* resulting from the activity of transport proteins. Recording these physical quantities provides equivalent information, as they are connected by the relation $C \cdot V(t) = \int I(t)dt$. For the study of ion channels, the patch-clamp method is a common approach in electrophysiology [72]. This method involves a micropipette filled with an electrolyte solution and a recording electrode in contact with the membrane of an isolated cell, while a second electrode serves as a reference ground electrode in the surrounding liquid environment (Fig.1.12a). As a specific form of a voltage-clamp experiment, it iteratively measures and maintains the membrane potential at a desired value by

applying the necessary current. Because the currents applied to the cell must be equal and opposite in charge to the current going across the cell membrane at the set voltage, the recorded currents indicate how the cell reacts to changes in membrane potential. However, these methods are limited to large cells, such as mammalian neurons, cardiomyocytes, and muscle cells, and are not suitable for the detection of bacterial proteins due to the small size of the host organism.
Alternative approaches have been developed for investigating the transport properties of bacterial proteins in natural membrane patches or artificial reconstituted vesicles. These approaches include experiments conducted in liquid cuvettes with free-standing lipid membranes separating two compartments, where electrodes connected to the circuit are inserted (Fig.1.12b). In this configuration, used also on BR samples [73], proteins can be directly integrated into the lipid membrane, or vesicles containing the proteins can be fused or adsorbed onto the free-standing membrane. In the latter case, capacitive coupling effects must be considered for transport current measurements. Another possible configuration involves solid-supported membranes (SSMs) formed on a glass chip in a flow-through cuvette (Fig. 1.12c). Vesicles or membrane fragments containing the protein of interest are adsorbed on the SSM, and the current is measured with a circuit connected to the SSM and the reference electrode (Fig.1.12c). The distinctive benefit of SSM-based electrophysiology becomes evident when examining membrane proteins derived from bacteria and intracellular compartments within eukaryotic cells [74]. By isolating and reintegrating bacterial transporters into lipid vesicles, it is possible to study them without encountering complications arising from interactions with other membrane components or the intracellular environment.
While electrophysiology stands as a powerful tool for investigating the functional properties of proteins, it has limitations when studying protein conformational changes. One significant challenge lies in the inability to directly visualize the structural alterations of proteins during dynamic processes. This limitation becomes particularly pronounced when attempting to discern subtle and rapid alterations in protein structure. Furthermore, electrophysiology may face challenges in capturing variations occurring in regions not directly involved in ion channel gating or transport processes. Proteins often undergo intricate conformational rearrangements that extend beyond the immediate vicinity of ion-conducting pores, and electrophysiological methods may not be sufficient to capture them. To simultaneously observe changes in transport and channel activity and conformational alterations within the protein structure, electrophysiology methods have been combined with fluorescence measurements in living cells as well as in artificial lipid membranes [75, 76, 77]. In particular, incorporating FRET donor and acceptor pairs into the protein of interest while performing electrophysiological recordings provides sensitivity for monitoring molecular interactions and conformational changes. However, also this kind of approach is limited to the specific labeled residues and may interfere with the natural behavior of the proteins under investigation.

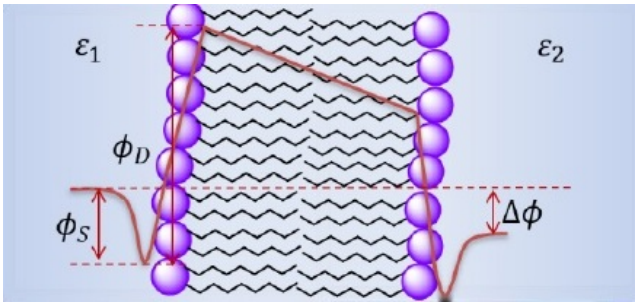

Figure 1.13. Potential curve (red line) across a bilayer lipid membrane, defined by the surface potential ϕ_S, dipole potential ϕ_D and transmembrane potential $\Delta\phi$ [78].

1.4 General objective of the present thesis work

The lack of appropriate experimental techniques does not make feasible the evaluation of the dependence of photosensitive protein activity (and of membrane protein in general) on the membrane potential value at the sub-molecular level to uncover changes in the position, protonation or oxidation of specific amino acids. Since the values of the membrane potential are typically of tens of mV, it results in electric field strengths of about $10^7 \frac{V}{m}$, assuming the thickness of cell membranes to be only 5-7 nm. The local electric fields at specific locations inside the protein can also be one order of magnitude greater respect to the global electric field estimated from the transmembrane potential, due to the dipole potentials of charged or polar amino acid residues. A protein molecule under such an intense electric field will behave quite differently than in an homogeneous aqueous solution, being affected by forces that can modify the molecular structure and therefore the functional conformational changes. This can be easily inferred from Fig.1.13 where the trasmembrane potential $\Delta\phi$ is indicated as the difference between the lipid dipole potential ϕ_D and the surface potential ϕ_S at the lipid/solution interface.
The suitable experimental approach would rely on the capability to control and change the value of the transmembrane potential (as in a patch-clamp electrophysiology experiment) while monitoring the functional changes of the transmembrane proteins, which can be done by vibrational spectroscopy.
Considering this framework, the main objective of my PhD work was precisely the development of an alternative IR spectroscopy technique capable of controlling the voltage potential applied on a sample with nanometric resolution while monitoring at the same time the vibrational modes. The approach requires to overcome the limits imposed by the diffraction of light to reach the needed sensitivity of IR radiation at the nanoscale. The suitable method, whose working principle and experimental details will be discussed in Chapter 2 sec.2.5 and in Chapter 4 sec.4.2.3, is based on the near-field technique AFM-IR operating in AFM contact mode (as opposed to AFM tapping mode or non-contact mode). Therein, the IR enhancement is obtained thanks to a nanoplasmonic gap configuration. The sample is in fact placed between a metallic surface and a metallic AFM tip probe, which for the first time are also envisioned as electrodes always in direct contact with the sample (Fig.1.14). This guarantees a precise and local control of the applied voltage on nanometer areas, avoiding any different effects that can arise from the inhomogeneity of the sample.

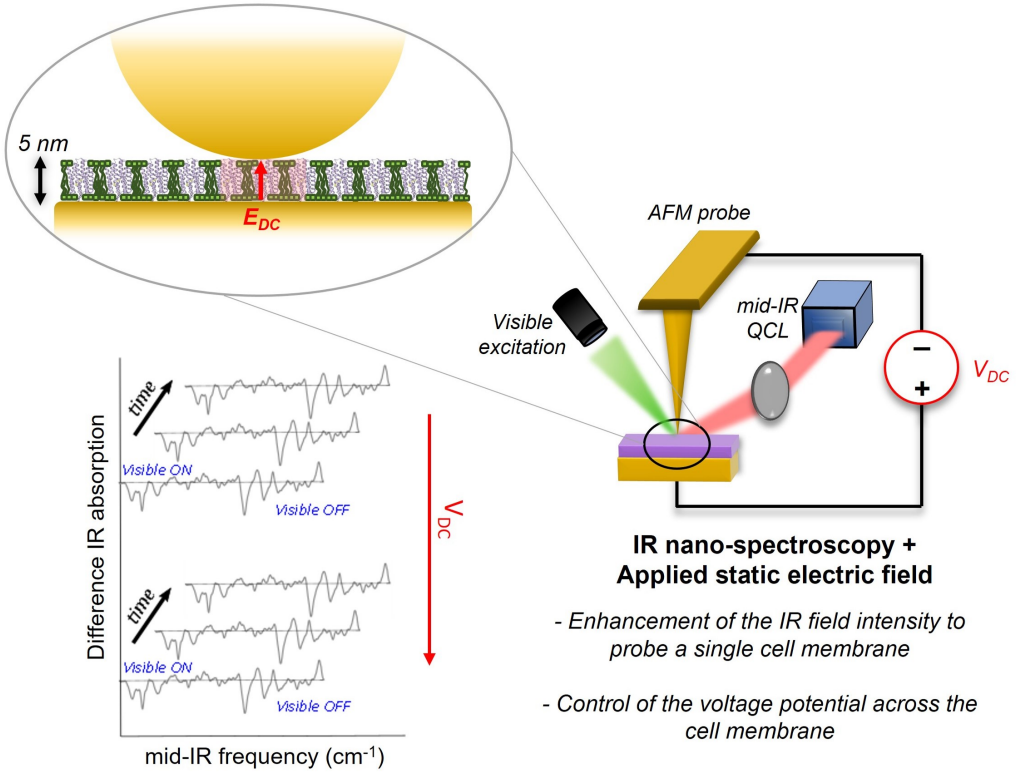

Figure 1.14. Schematic representation of the general objective of the present PhD work. The IR nanospectroscopy platform AFM-IR is implemented with an external electric circuit to apply a controlled potential through the metallic AFM tip. The setup permits to envision experiments to access the spectral IR response of light-activated photosensitive proteins at the level of a single cell membrane while having control on the transmemebrane potential.

This new technique, after been tested and validated on polymeric samples where effects of the local electric field on the IR spectra could be clearly observed and explained, appears as a relevant experimental advance in the study of transmembrane protein activity taking into account the membrane potential that is present in living cells.

Chapter 2

IR spectroscopy of proteins: principles and state-of-the-art

The understanding of the mechanisms governing the activity of photosensitive transmembrane proteins has been significantly advanced through the application of **IR spectroscopy**. Among various biophysical techniques, IR spectroscopy stands out due to its label-free approach, time-resolution capabilities, and sensitivity to reversible structural changes. Overcoming the limitations due to the diffraction of light and the low sensitivity of IR spectroscopy has allowed the extension of this spectroscopic tool to the nanoscale in recent decades, further enhancing its potential and enabling the investigation of these proteins at the level of **individual cell membranes** [20, 21]. In this chapter, I delve into the principles of IR investigation and the specific case of protein studies, elucidating the various strategies employed to enhance spatial and temporal resolutions in experiments. I then discuss **nanospectroscopy** methods based on atomic force microscopy (AFM), particularly focusing on **AFM-IR**, that is the one used in my PhD project.

2.1 Infrared spectroscopy principles

IR spectroscopy is an absorption spectroscopic technique, which allows one to obtain information on chemical composition of the sample under examination through the interaction of electromagnetic radiation with the quantized vibrational levels of matter. First of all, I recall that IR absorption is a single-molecule phenomenon, therefore there is no lower fundamental limit to the number of molecules required to observe it, but only practical limits, which I will try to overcome in this PhD work through near-field nanospectroscopy.
The mid-IR region (4000-400 cm^{-1}, 2.5-25 μm) is the one of interest for the study of biomolecules since they are made of C, O, N and H atoms and therefore they have fundamental vibrations in the range of 1000-2000 cm^{-1}, while molecules with heavier atoms have vibrations in the far-IR (400-10 cm^{-1}, 25-1000 μm), as we shall see below with a simplified Morse oscillator model. The vibrational modes of a molecule with many atoms are also referred as normal modes because the excitation of any given mode does not affect the others, thus identifying the vibrations of all atoms in a molecule with the same frequency. All molecules have 3N total

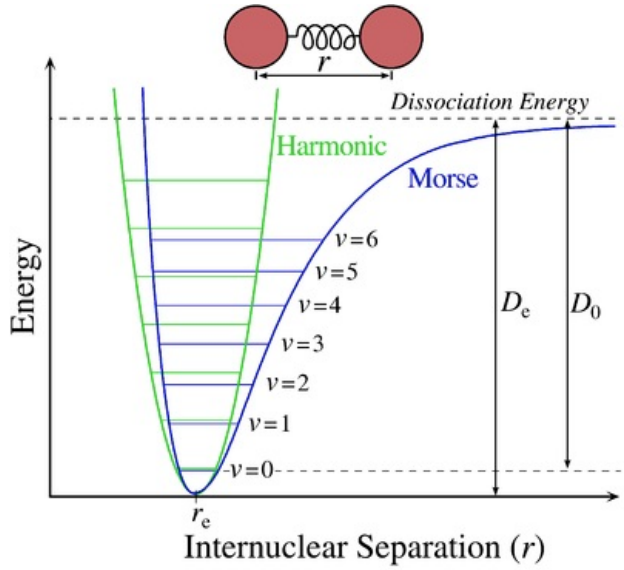

Figure 2.1. Comparison of the potential energy as a function of interatomic distance for an harmonic oscillator and a Morse oscillator [79].

degrees of freedom (where N is the number of atoms in the molecule), reduced by 3 translational and 3 rotational degrees of freedom. The remaining motions of the atoms (3N-6) are displacements of the atoms from their mean positions, which are precisely the normal modes corresponding to the number of vibrational degrees of freedom, therefore a molecule have 3N-6 normal modes. The vibrational modes are generally divided in *stretching* modes and *bending* modes. In *stretching* modes there is a periodic variation of the bond length between two atoms that can be symmetrical or asymmetrical. In *bending* modes, it is the angle between two bonds or between a group of atoms and the rest of the molecule that varies. These modes are further classified assuming specific names such as *scissoring* and *rocking*, *twisting* and *wagging*. To describe the phenomenon of IR absorption, one can start from the case of a diatomic molecule. The Morse oscillator is the most widely used model to describe the vibrational interaction between atoms in diatomic molecules, since, respect to a quantum harmonic oscillator, it takes into account the anharmonicity of real bonds. The Morse potential energy as a function of interatomic distance (Fig.2.1) is of the form:

$$V(r) = D_e(1 - e^{a(r-r_e)})^2 \tag{2.1}$$

where r is the interatomic distance, r_e the equilibrium distance, D_e is the dissociation energy of the molecule and $a = \sqrt{\frac{k_e}{2D_e}}$ with k_e the force constant. Whereas in a quantum mechanic description the energy spacing between vibrational levels in the quantum harmonic oscillator is constant, in the Morse potential the energy between adjacent levels decreases with increasing the vibrational level so that the spacing energy of the Morse levels results to be

$$E_{n+1} - E_n = h\nu - (n+1)\frac{(h\nu)^2}{2D_e} \tag{2.2}$$

where h is the Planck's constant and n the vibrational quantum number (n=0,1,2,...). ν is the frequency

$$\nu = \frac{a}{2\pi}\sqrt{\frac{2D_e}{m_r}} \tag{2.3}$$

with $m_r = \frac{m_1 m_2}{m_1+m_2}$ the reduced mass of the system.
In order to be IR active a vibrational transition must have a transition probability that is different from zero. The transition for an electric dipole between the states n and m of the same electronic state is given by

$$\epsilon_{n,m} = \langle \phi_e \psi_m | \vec{\mu} | \phi_e \psi_n \rangle \tag{2.4}$$

according to Born-Oppenheimer approximation where ψ is the nuclear wavefunction and ϕ_e the electronic wavefunction. Since only the vibrational function changes in the transition, the integral over the electronic coordinates gives the permanent dipole moment in the specific electronic state $\vec{\mu_0} = \langle \phi_e | \vec{\mu} | \phi_e \rangle$ and the matrix element of eq.2.4 can be written as

$$\epsilon_{n,m} = \langle \psi_m | \vec{\mu_0} | \psi_n \rangle = \int \psi_m^* \vec{\mu_0} \psi_n d\vec{R} \tag{2.5}$$

where $\vec{R}$ are the nuclear coordinates.
The electric dipole transition occurs if the element matrix of eq.2.5 is non-zero. The electric dipole moment $\vec{\mu_0}(\vec{R})$ can be expanded in a Taylor series around the nuclear coordinates at the equilibrium $\vec{R_0}$ obtaining

$$\vec{\mu_0}(\vec{R}) = \vec{\mu_0}(\vec{R_0}) + \left.\frac{\delta \vec{\mu}(\vec{R})}{\delta R}\right|_{\vec{R_0}} (\vec{R} - \vec{R_0}) + ... \tag{2.6}$$

Substituting the dipole moment expansion in eq.2.5 we obtain that the first term is equal to zero because $\vec{\mu_0}(\vec{R_0})$ has not dependence on $\vec{R}$ and the nuclear wavefunctions of a harmonic oscillator are orthogonal $\langle \psi_m | \psi_n \rangle = 0$. Thus, to get a results that is nonzero at the first order, the dipole moment must change during the vibration transition $\frac{d\mu}{dR} \neq 0$ and $m = n \pm 1$. We have therefore shown that the IR absorption selection rule for a diatomic molecule is that a vibrational transition is allowed only if the dipole moment changes within the internuclear distance and only vibrational transitions between neighboring energy levels are possible.
In the more complex case of a polyatomic molecule with N atoms, each of the 3N-6 normal modes can involve displacements of atoms in terms of variations in distances or angles and it is IR active only if it produces a net change in the dipole moment of the molecule.
The IR spectrum of a molecule therefore presents a sequence of absorption bands as a function of the radiation frequency characterized by the central position at the frequency ν determined by the strength of the chemical bonds and the atom masses, the stiffer the chemical bond (e.g. triple respect to single) the higher the energy required to excite the vibrations. In a macromolecule, the absorption frequency is also affected by the environment of the specific chemical bond and normal mode frequency variations can be usually connected with conformational changes such as the ones takig place in the photocycles of rhodopsins. The intensity

of the absorption expresses instead the transition probability from the ground to the excited energy state of the functional group involved in the absorption phenomenon, which is proportional to the dipole moment variation. The last characteristic of an IR absorption band is the width that may be due to the lifetime of the vibration (intrinsic) and to the heterogeneity of the given mode in the system, however this is usually difficult to observe in condensed matter at room temperature.
In addition to qualitative information on the type of chemical bonds present in a sample, IR spectroscopy also allows for a quantitative analysis of the present species. If we consider a beam of monochromatic radiation of I_0 intensity incident on the sample and we measure the radiation of intensity I, for the Lambert-Beer law the ratio between the two intensities, defined as transmission T, is equal to

$$T = \frac{I}{I_0} = e^{-k_\lambda l} \tag{2.7}$$

where k_λ is the attenuation coefficient, which depends on the medium and on the radiation wavelength λ, and l is the radiation path within the sample. The absorbance A is then defined as

$$A = -logT = k_\lambda l \tag{2.8}$$

and in solution as

$$A = \epsilon_\lambda C l \tag{2.9}$$

where ϵ_λ ($\frac{1}{mol\,cm}$) is the molar absorption coefficient and C ($\frac{mol}{l}$) is the sample molar concentration. From the Lambert-Beer law one gets the relationship between the attenuation of light and the properties of the material it passes through

$$I = I_0 e^{-\epsilon_\lambda C l} \tag{2.10}$$

At the same concentration C of the absorbent species, the absorption will be greater if the sample is thicker. In an infrared spectroscopy experiment it is therefore necessary to prepare the sample in the optimal condition to have a sufficiently high absorbance signal (typically equal to 10-20% of the intensity of the incident radiation). If the path taken by the radiation through the medium is too long, there will be no transmitted light and, on the other hand, if the sample is too thin the absorption signal will be too low to be detected. These experimental requests are clearly in contrast with the achievement of the limit of performing infrared spectroscopy of a single molecule, or of a few molecules, which instead is a goal reached in this thesis thanks to IR nanospectroscopy in near-field approach.

2.2 IR spectroscopy of proteins

IR spectroscopy, as a non-invasive technique, is widely employed in the study of proteins due to its sensitivity to chemical bonds. Since the vibrational energy of these bonds depends on intra- and inter-molecular interactions, it enables the distinction also of their secondary structure components in a label-free way. The IR spectrum of polymer chains, such as proteins, is the result of the vibrations of different amino acid residues, but also, and above all, of the vibrations of the peptide bonds that

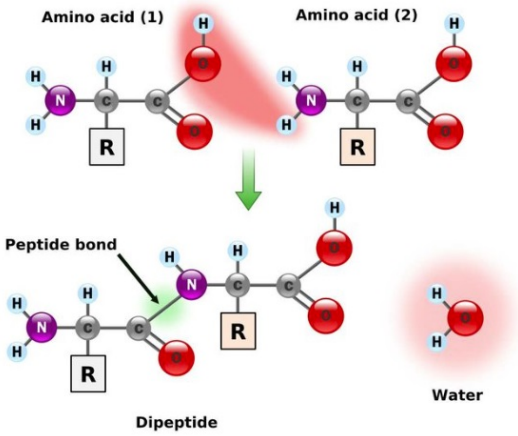

Figure 2.2. Structure of an amino acids and the formation of the peptide bond to connect consecutive amino acids in the protein chain [80].

Band	Frequency (cm^{-1})	Vibational mode
Amide A	3300	NH stretching
Amide B	3100	NH stretching
Amide I	1600-1700	C=O stretching
Amide II	1480-1575	NH bending, CN stretching
Amide III	1229-1301	NH bending, CN stretching
Amide IV	625-767	OCN bending
Amide V	640-800	out-of-plane NH bending
Amide VI	537-606	out-of-plane C=O bending
Amide VII	200	backbone twist

Table 2.1. Assignments of the characteristic IR bands of proteins

bind consecutive amino acids (Fig.2.2). These last vibrational modes give rise to nine spectral bands mostly in the mid-IR range, which are called amides A,B and I-VII (tab.2.1). The main absorption bands are the amide I and amide II bands. The amide I band is centered around 1650 cm^{-1} and is almost entirely associated with the stretching vibration of the C=O group of the peptide bond. This vibration is strongly dependent on the nature of the side chains and is important for the analysis of the protein secondary structure. The amide II band, on the other hand, is found at a frequency of about 1550 cm^{-1} and is mainly related to the in-plane bending vibration of the NH group and from stretching of the CN group, presenting a lower but still significant dependence on the secondary structure. One of the interests in the IR study of proteins is to precisely relate the spectral information to the secondary structure. The amide I band can indeed be centered between 1700 and 1600 cm^{-1} and the exact frequency of this vibration depends on the nature of the hydrogen bonds involving the peptide bonds, i.e. the secondary structure of the polypeptide chain. In fact, the lengths and angles of the peptide bonds change according to the structure (α-helix, β-sheet or turn and disorder conformation), thus modifying the position of the absorption bands. As an example of the differences

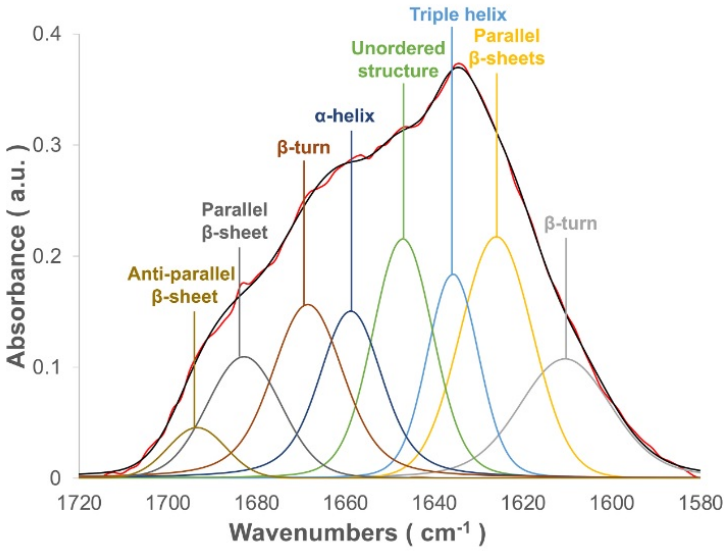

Figure 2.3. Representative spectral deconvolution of eight resolved components of the Amide I absorption band. The red line is the original amide I absorption band and the black line is the calculated spectrum after the curve fitting process. Each spectral component is identified with a different color and assigned to a protein secondary structure element [81].

between the two main secondary structure components, the α-helix structure has an helical shape that is due to the presence of hydrogen bonds between amino groups and carboxyl groups of non-adjacent amino acids with the side chains always arranged orthogonal to the helix axis, while the β-sheet looks like two neighboring peptide filaments always held together by hydrogen bonds to form a very planar and compact structure. The spectral weight distribution of the amide I band is therefore sensitive to changes in the secondary structure, since this band is the convolution of absorptions associated with different contributions of the secondary structure (Fig. 2.3). Furthermore, the intricate sensitivity of the amide I vibration to secondary protein structures is attributed to a phenomenon known as transition dipole coupling. This mechanism involves a resonance interaction between the oscillating dipoles of adjacent amide groups. The strength of this coupling is intricately tied to both the relative orientations and the distances separating these dipoles within the protein structure. When these dipoles synchronize at the same frequency, the coupling effect is significantly amplified. Consequently, instead of observing a single frequency, the absorption frequency splits due to the dependency on the relative phase of the oscillator movement. Another significant consequence of strong coupling is that the oscillation is no longer confined to a single oscillator, resulting in the delocalization of the excited state [82].

Thanks to its sensitivity to the protein structure, IR spectroscopy is a tool not only employed in static condition of the protein but also in the more interesting detection of secondary structure variations, both transient and permanent, in a very wide time interval, from fs to days. In a protein the changes that can be observed in hours or days, are for example related to the degradation of the secondary structure in favor

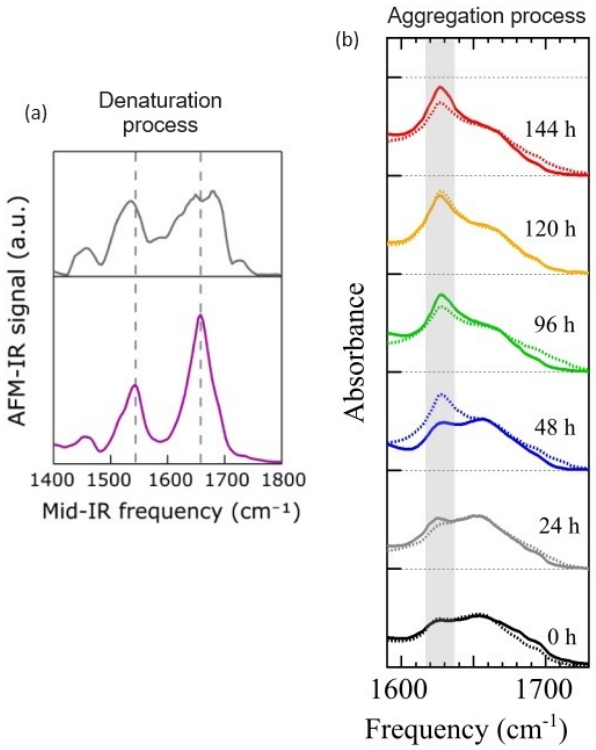

Figure 2.4. a)Example of comparison of IR spectra acquired on thick lipid-membrane stacks loaded with the protein Bacteriorhodopsin: the grey curve is from a sample degraded by exposure to the atmosphere, the pink curve is from a freshly deposited sample. The physical-chemical degradation of proteins can be detected in the IR absorption spectra by looking at changes in the two amide bands. In general, broader amide bands indicate disordered peptide bond lengths and strengths due to unfolding of the protein secondary structure [83]. b) Example of IR spectra acquired during the aggregation process of the α-synuclein protein (continuous lines) and of the α-synuclein protein co-incubated with RNA molecules (dashed lines). An increase in the β-sheet component centered around 1630 cm^{-1} is observed as the sampling time increases.

of a disordered and amorphous form that is possible to observe as a variation of the spectral weight of the amide I components (Fig.2.4a). In some other cases, some specific intrinsically disordered protein, associated with neurodegenerative diseases, are subjected to modification of their structure leading to the formation of aggregates in a fibril-like form, where the β-sheet structure is the characteristic component (Fig.2.4b). The last two examples refer to processes that are not reversible and whose effect is evident looking at the amide I band of the IR spectra a two different times, because of the implication of a substantial number of amino acid in the secondary structure variation. On the contrary, some fast and reversible processes take place inside the proteins, which are related to their functional operation, as the ion pump/channel activity already introduced for photosensitive rhodopsins.

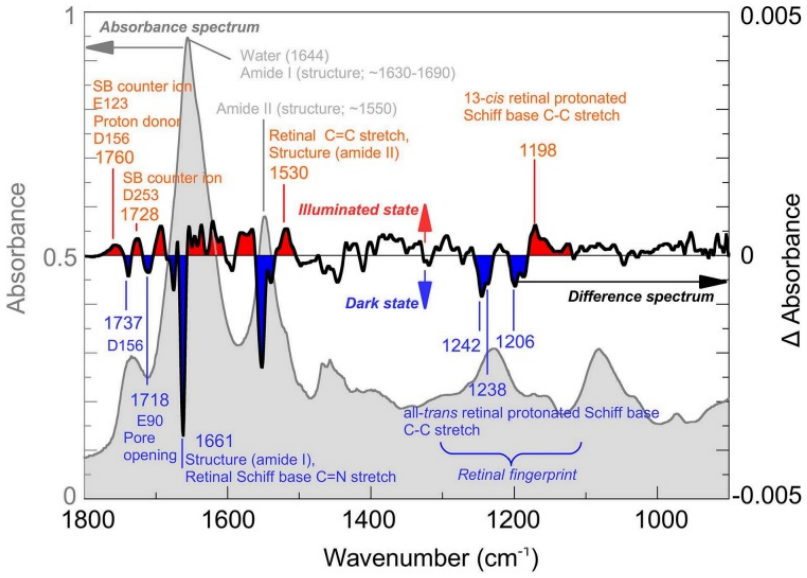

Figure 2.5. Example of an IR difference-spectrum (black line) of ChR2 superimposed to the IR absorption spectrum (grey line)[84].

2.3 Study of protein activities

2.3.1 Difference IR spectroscopy method

The variations of the protein structure involved in the functional activity are usually very small and only some parts of the protein or even single amino acids undergo modifications of the molecular bonds. This means that their spectral signatures are mostly masked in the rich IR absorption spectra of the macromolecule. To have detailed structural information it is therefore necessary to reduce the number of groups which contribute to the IR spectrum, applying a filter that enables the selection of relevant signals, which may be as low as 10^{-5}. This is obtained with difference spectroscopy method where absorption changes associated with the reaction of a protein are selectively extracted from the constant absorption background. It consists in the acquisition of an IR spectrum in the rest-state and in the perturbed state of the protein and the subsequent subtraction of them. More precisely, the variation in absorbance between the two state is calculated as

$$\Delta A = -log \frac{I_{perturbed}}{I_{rest-state}} \tag{2.11}$$

where $I_{perturbed}$ and $I_{rest-state}$ are the intensity of the transmitted IR radiation that interacted with the protein in the perturbed and rest-state, respectively. In these experiments, it is needed to have care to maintain constant the sampled volume, the concentration, the temperature, the pH, and other parameters that can affect the modification of the IR absorption response, apart from the specific reaction which is instead induced by a specific stimulus (e.g. light for photosensitive proteins). Conventional IR difference-spectroscopy is usually performed with Fourier-tranform infrared spectroscopy (FTIR) that will be presented in detail in Chapter 4

sec.4.1 and *Appendix II*. This experimental technique is based on the employment of a broadband source (blackbody radiator) and an interferometer, resulting in a simultaneous detection of all the spectral component. The great stability of the technique over time, ensures the high signal-to-noise ratio needed to probe subtle absorbance differences. The ΔA is directly measured by triggering an IR spectrometer with an external electronic signal synchronized with the physical stimuli that produce the protein conformational changes (in our case, illumination with LEDs). This acquisition way guarantees that the absorption changes at all wavenumbers are measured simultaneously, thus corresponding to the same state of the protein sample, and it improves the signal-to-noise because the two spectra of the rest and perturbed state are taken one immediately after the other, removing the need for a reference measurement. The price to be paid is that the absolute absorbance is not measured, and must be determined separately with a conventional Lambert-Beer-based measurement.
The difference-absorption spectrum ΔA results in positive and negative peaks that represent changes in absorption band position, intensity, and/or width as a response to modifications in the molecular conformation, orientation, interactions, or polarity. Some bands may also appear or disappear as chemical modification of groups in the sample can change the nature of some vibrations, as in the case of protonation changes of amino acid residues. Furthermore, another advantage of IR difference spectroscopy is that it does not require the use of a homogeneous and pure sample, since other molecules, contaminants or degraded proteins do not respond to the external perturbation, thus not contributing to the final IR difference spectrum. As an example, in Fig. 2.5 an IR difference spectrum for the ChR-2 protein is displayed. The difference curve (black) is superimposed to the absorption spectrum (grey) and presents negative bands (blue) that occur due to the dark state and positive bands (red) related to the illuminated state. Due to the fact that the variations are subtle and involve few amino acids or H-bonding, it is interesting and possible to assign the ΔA bands to specific residues, which is not feasible in the measurements obtained with a static absorbance approach. In general, the assignment of bands in the IR difference spectra is based on experiments conducted on sample mutants or labeled isotopes in combination with computational chemistry methods [85], and then of course on the literature results. The computational methods mainly rely on QM/MM simulations where the protein system is treated in distinct levels. Quantum mechanical (QM) calculations are applied to the study of chemical properties of the site of interest, whereas the surrounding protein environment is included and calculated using less computationally expensive molecular mechanics (MM) methods. Since isotope labeling and site directed mutagenesis can alter the protein functionality or dynamic, sometimes other strategies are preferred to facilitate band assignments. With double-difference spectroscopy, for example, is possible to further simplify the IR-difference signal, since IR difference spectra from two samples, differing only in one aspect (e.g., one is isotopically labeled and the other not, one is a full length protein and the other is a construct lacking a structural domain, etc.), are subtracted from each other to reveal specific feature.
So far the only membrane proteins that can be studied with IR difference spectroscopy using an external stimulus are photosensitive proteins. For example, proteins whose activity is triggered by changing transmembrane voltage cannot be studied with

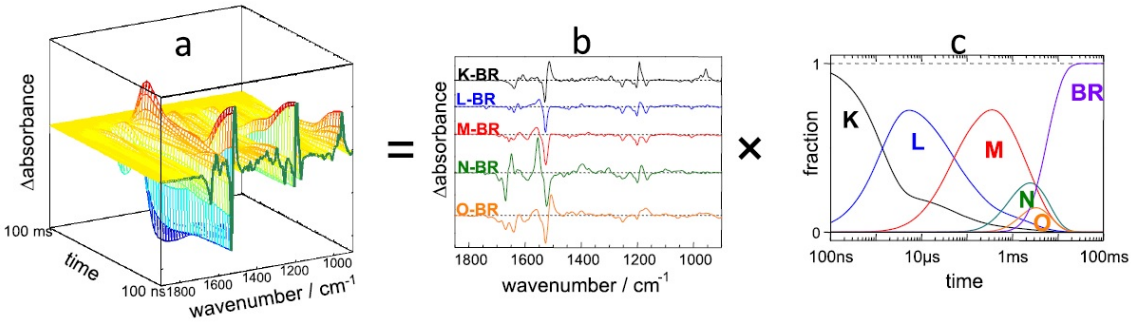

Figure 2.6. (a) Synthetic time-resolved IR spectra of the BR photocycle. The time-resolved data is the result of (b) the IR difference spectra to respect the initial state for all the intermediates and (c) the time evolution of each intermediate [86].

FTIR due to the impossibility of applying a controlled and constant electric field on a large number of proteins, which is a requirement imposed by the IR sensitivity in order to detect the sample response.

2.3.2 Time-resolved IR spectroscopy

Conventional FTIR requires an integration time, since several interferograms has to be averaged to obtain a spectrum, so that in a difference-spectroscopy experiment the protein states have to be stable for at least few seconds. For this reason, alternative time-resolved IR methods with better time resolution are particularly useful to detect the many relevant steps in protein functionality taking place in the time scale of microseconds or milliseconds and to follow, at the same time, the evolution of vibrations in a long temporal range after the perturbation.

The time resolution of the FTIR interferometer itself can be improved operating in rapid-scan mode, achieving a time resolution of around 10 ms and in the step-scan mode suitable to cover the time region from tens of nanoseconds to hundreds of milliseconds (see Chapter 4, sec.4.1). A complementary approach is the one employing monochromatic radiation sources as external cavity quantum cascade lasers (QCLs, see Chapter 4, sec.4.2.2) emitting in the mid-IR range. They can be employed to obtain time-trace following the evolution of specific vibration with time resolution from 10 ns to 100 ms, where the limitations are only due to the detector and electronics response and the stability of the source itself. They typically have a tunability of 100-200 cm^{-1} so that it is possible to reconstruct time-resolved IR spectra measuring kinetic traces at many nearby wavenumbers [87]. However, it has to be noted that the collected time-resolved data represents the averaged spectral properties of all the intermediates weighted by their time-variable fraction and the decomposition of the recorded data into spectra and time evolution for each intermediate is not trivial (Fig.2.6).

Photosensitive proteins are a suitable system to be investigated with time-resolved measurements, since fast and selective visible light pulses can be delivered (from fs to ns long). Moreover, the counterpart of this type of experiments is that the reaction has to be repeated for a minimum number of times so that reversible processes with

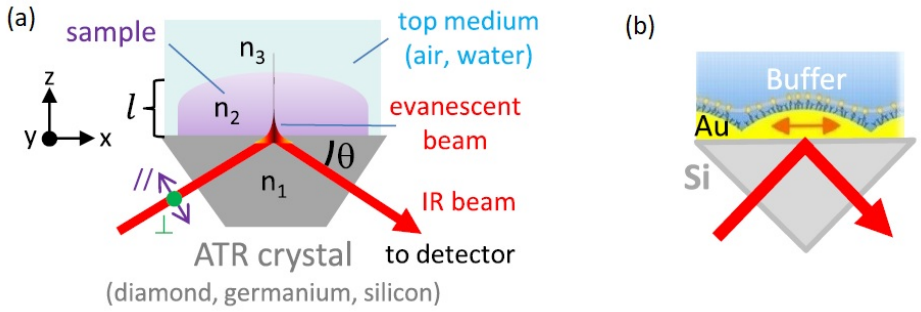

Figure 2.7. Experimental configuration of a)ATR and b) SEIRA [91].

fast recovery are preferable. In step-scan FTIR, for example, a minimum of 500 measurement are repeated to complete an acquisition but repetitions of the order of 10^5 may be needed [88]. Experiments conducted with ultrafast IR laser probes can also require 10^6 photoexcitation of the system to cover a spectral interval of 500 cm^{-1} [89]. However, recent experimental developments are leading to the acquisition of time-resolved data in a single shot experiment using sophisticated frequency-comb generation from QCLs [90].

2.4 Approaches to increase the IR sensitivity

Despite its wide application in the study of biological systems, IR spectroscopy suffers from a low sensitivity and thus a huge number of molecules is required to get a detectable IR response. The typical molar extinction coefficient for IR-active vibrations is of the order of 10^2 M^{-1} cm^{-1}, over 100 times lower than that of the corresponding electron transitions in the UV-VIS, mostly due to the ion mass being much larger than the electron mass, which is clearly a fundamental physical limit. This results in typical protein concentrations of 0.1 to 1 mM to obtain absorption in the range 0.1-0.5 absorbance units (transmittance T $\sim 8-3\%$), which is the minimum requirement for IR difference spectroscopy for the functional study of photosensitive rhodopsins. Signal-to-noise ratio in the range of 10^4-10^5 is indeed necessary to probe all light-induced IR absorption variations. Moreover, for measurements in liquid solution the IR absorption of water molecules must also be taken into account since it may mask the signal of other molecules. For both reasons the sample preparation and the experimental method chosen to conduct the experiment are critical. The problem of the intense water absorption can be addressed by working with highly concentrated solutions of protein or with hydrated protein films in a transmission configurations with very short optical path length inside the sample or different reflection configurations sensing only a thin surface layer. Otherwise an IR source, as an external cavity QCL, with spectral power density much higher than blackbody source, has to be used [92].
To reduce the number of proteins probed and to reach the sensitivity of few layers or even monolayer of proteins, different strategies and approaches can be used. One of them, is the Attenuated Total Reflection (ATR) configuration in FTIR. It is based on the use of a crystal with a prism-shape made of a material with high

refractive index and transparent in the IR range (Ge, Si, ZnS, diamond...). The sample is deposited on the larger horizontal surface of the trapezoidal or triangular prism and the IR radiation is totally reflected at the interface between the crystal and the sample in contact with it (Fig.2.7 a). The sample is thus probed by a non-radiative and evanescent electromagnetic field that penetrates into the sample with an exponentially decaying intensity and a penetration depth d_p of about 0.1λ, where λ is the wavelength of light. The specific value of d_p depends on the refractive index of the two material $n_{1,2}$ and on the angle of incidence θ of the IR radiation on the prism surface as

$$d_p = \frac{\lambda}{2\pi n_1 \sqrt{sin^2\theta - (\frac{n_2}{n_1})^2}} \tag{2.12}$$

This configuration differs from the transmittance mode, where the IR beam completely goes through the sample and then ATR permits to detect only tens of protein layers. ATR is thus commonly employed for the study of transmembrane proteins stacks where the proteins are investigated in their natural or artificially reconstructed lipid bilayer. This is achieved by drying the lipid membranes to form multilayers and subsequently the membranes are rehydrated with a buffer solution. The exponential decay of the electromagnetic field on the ATR prism surface also allows to avoid the IR absorption signal of the solution, since the first portion of the surface is filled with the protein sample only [93].
The achievement of the extreme sensitivity required to detect single molecules or monolayers with dimensions much smaller than the wavelength of light λ has been made possible also through near-field optics approaches by employing subwavelength apertures or particles directly coupled to light. Placing the sample at very short distances z«λ from the near-field source enables the collection of the local enhanced intensity of the electromagnetic field and facilitates probing the sample response. One effective approach involves using engineered metallic nanostructures designed to provide a highly confined enhancement of the local field intensity by several orders of magnitude. This is made possible by the resonant excitation of plasmons, which are collective electron oscillations arising when an external electromagnetic wave interacts with the free-electrons of a metallic material. They can be sustained either at metallic-dielectric interface, assuming a propagating wave character, such as the Surface Plasmon Polaritons (SPPs), or localized into metallic nanostructures and then called Localized Surface Plasmons (LSPs) [94]. Because of the use of metallic matter, plasmonics is often referred to as "optics with metals" and it enables the translation of optical spectroscopies into the nanoscale, particularly in nanometric regions with sub-wavelength dimensions referred to as *hot spots*, where high fields are experienced with an enhanced intensity of the order of 10-100. The density of charge carriers $\rho(t)$ and the current density $J(t)$ become increasingly sensitive to nanostructure dimensions. Consequently, a strong enhancement of the electric field occurs in metallic nanoparticles with sharp corners or protrusions, typically in volumes with minimum dimensions of 10–100 nm (Fig.2.8a). This region size can be further reduced in a plasmonic nanocavity (or nanogap) configuration, achieved by coupling two nanostructures with a nanometer or even sub-nanometer gap (Fig.2.8b). An alternative configuration for nanocavities involves a single nanoparticle separated from a metal film by a thin dielectric layer of a few nm. This arrangement, known

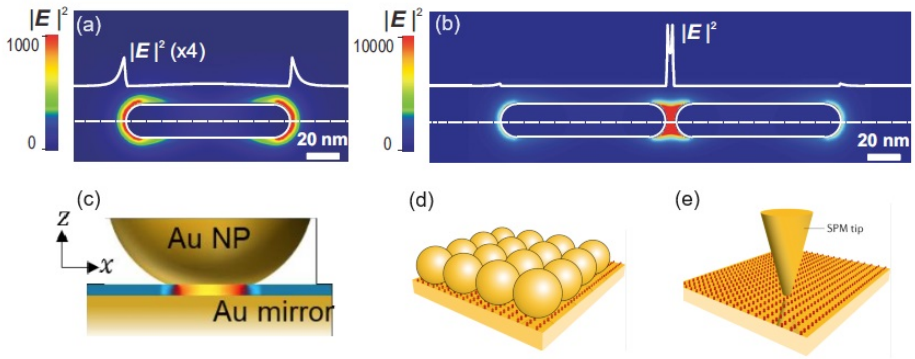

Figure 2.8. a) Simulated maps of near-field intensity enhancement for a gold 100-nm-long nanorod and b) two-rod with 4-nm gap [95]. c) Nanoparticle-on-mirror cavity with strong optical field confinement in the gap [96]. d) Example of an array of nanoparicles-on-mirror configuration for SERS applications on a target molecule and e) Tip-enhanced configuration where the nanoparticles are replaced by a single scanning probe microscope (SPM) tip [97].

as nanoparticle-on-mirror or metal-insulator-metal cavity, allows the metallic nanostructure to interact with its image induced on the other side of the metallic layer, generating a plasmonic *hot spot* centered in the nanocavity between the nanoparticle and the metallic substrate (Fig.2.8c). Clusters and arrays of nanostructures, as well as configurations involving nanoparticles-on-mirror, are therefore the tools employed in Surface-Enhanced Raman Spectroscopy (SERS), from the IR to the UV region, and Surface-Enhanced IR Absorption Spectroscopy (SEIRA) to realize far-field measurements exploiting the field enhancement in the near-field regime (Fig.2.7 b). One aspect that has to be taken into account in SEIRA is the selectivity for vibrations with a transition dipole moment perpendicular to the metal surface, arising from the Gauss theorem and therefore the surface selection rules. This can change the relative intensity of the absorption bands, making direct comparisons with conventional transmission or ATR measurements not immediate, but it can be exploited to determine the surface orientation of adsorbed molecules by comparing bands with orthogonal dipole moment vectors. In contrast to early SEIRA studies employing metal island films [100, 101], more innovative approaches involve the use of explicitly engineered plasmonic nanoatennas with mid-IR resonance [102, 103, 104]. Metallic nanoparticles made of materials like gold, silver, copper, or aluminum exhibit plasmon resonances at wavelengths determined by material properties, as well as the shape and size of the structure, so that the nanoantenna and the periodicity of the array can be precisely designed and optimized to achieve resonance matching with various chemical groups, depending on the specific target. Beyond single-resonance plasmonic antennas, more intricate approaches such as arrays of antennas with diverse resonances can be explored to cover at the same time multiple frequency bands in the IR. This approach provides the opportunity to span a broad range of molecular vibrations and gather detailed insights into various functional groups within a molecule [98] (Fig.2.9). In ref.[99], I conducted a study within this framework, where a double-resonance array is designed and used for mid-IR detection of human extracellular vesicles, as briefly summarized in panel b of Fig.

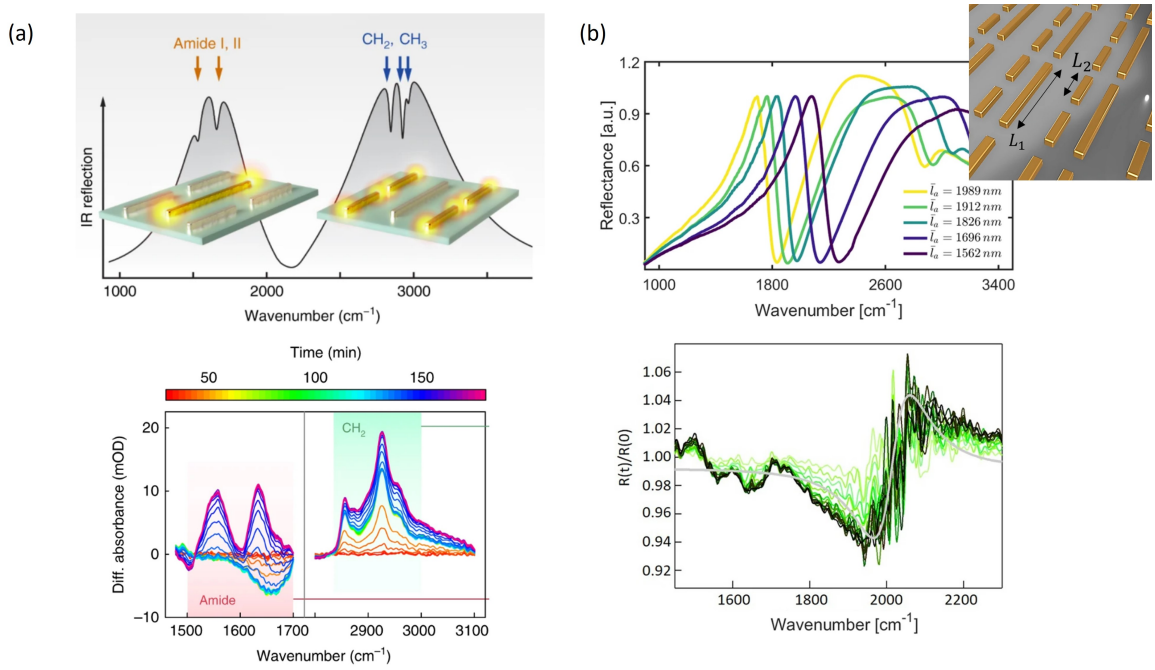

Figure 2.9. a) Top panel: Design of gold a nanoantenna array with double resonance, engineered to simultaneously overlap with the vibrational signatures of both the amide I and II, and the CH_2, CH_3 absorption bands, allowing for the simultaneous enhancement and detection of lipid and protein induced absorption changes. Bottom panel: Time-dependent differential absorption spectra acquired during the lipid membrane formation and protein-binding experiments on the nanoantenna surface. Adapted from [98]. b) Top panel: Reflectance spectra of a double resonant gold nanoantenna array for different values of the lattice constant. The mid-IR device has been designed to detect human exosomes through the vibrational absorption of their protein content. Indeed, for instance the nanoantenna array with $l_0 = 1912$ nm displays a first resonance around 1700 cm^{-1} that is suitable for SEIRA spectroscopy of the amide bands of proteins. At the same time, a sharp reflectivity drop around 1900 cm^{-1} produced by the interaction of the second resonance with the first is strongly sensitive to changes in the refractive index at the interface between the metal antenna and the sample and thus it is employed as a surface plasmon resonance (SPR) for mass-sensing. Bottom panel: Time-dependent reflectance spectra acquired during the functionalization process of the nanoantenna surface with antibodies. The spectra are normalized to the one at t=0 and they show the increase of the amide bands and the SPR sensing signal as the redshift of the zero-crossing point of the S-shaped curve fitting to the 1800–2100 cm^{-1} feature. Adapted from [99], a work conducted during my PhD course.

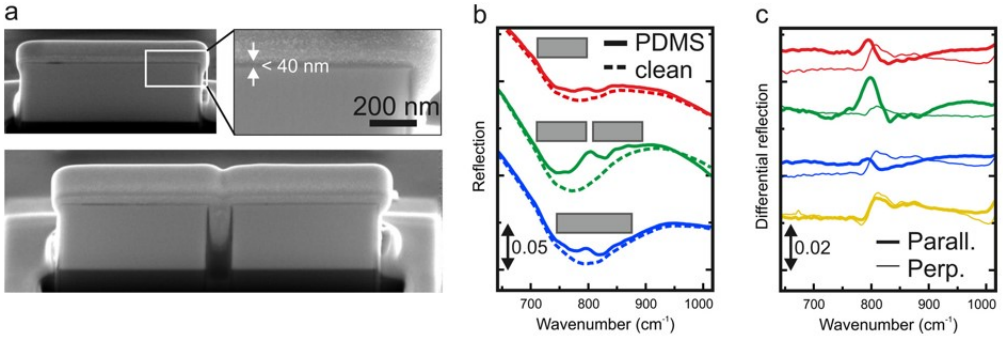

Figure 2.10. a) Cross-sectional SEM images of PDMS-covered antennas. The length of the single-arm antenna is 3 μm, while individual arms of the gap antenna are 2 μm long. b) The experimental reflection spectra acquired after PDMS spin coating on three different antenna samples (solid lines) and reference spectra from the clean samples (dashed lines): single-arm antennas with length L= 2.0 μm (red), gap antennas with L= 2.0 μm arm length (green), and single-arm antennas with L= 3.0 μm (blue). c) The difference spectra obtained after subtraction of the spectra from antennas coated with AZ-5214 polymer. Thicker lines correspond to polarization parallel to the antenna axis, thinner lines to perpendicular polarization. The color coding is the same as in panel b, and the yellow lines refer to an undoped antenna sample [105]. This work has been performed by the group where I worked for my PhD.

2.9. While gold is the most used material for these applications, also semiconductors, such as heavily doped germanium [105], have been employed to realize nanoantenna platform enhancing the mid-IR response of molecules placed on them (see Fig.2.10).

As discussed further in Chapter 4 sec.4.1.2, it is essential to note that even in these approaches based on a near-field phenomenon, the dimension of the sensing area (prism surface, metallic rough or nanostructured arrays) is however limited to the size of the IR focus spot. One has to consider that the diffraction of the long IR wavelengths (2.5 μm to 25 μm in the mid-IR range) limits the lateral resolution Δx of IR spectroscopic imaging to several micrometers according to the Abbe's formula:

$$\Delta x = \frac{\lambda}{2nsin\theta} \tag{2.13}$$

so that a microscope image cannot contain information of a detail or of an object greater than Δx, where λ is the wavelength of light and $nsin\theta$ the numerical aperture of the collecting optics. So that ATR, SEIRA and SERS are suitable for the sensing of samples with thicknesses of the order of few nanometers or single molecules placed in the *hot spot* regions but they cannot provide better spatial resolution than the usual microscopy. This means that the prism surface or the nanostructured platform have to be densely filled with the sample covering an area comparable to the IR focus. Note that is not easy at all to obtain uniform reconstructed membrane films embedding the proteins of interest over such large areas. Hence, there follows the need to obtain IR sensitivity at the nanoscale to move over the investigation of individual membrane patches.

2.5 Tip-enhanced spectroscopy methods for IR spectroscopy

To overcome the issues arising from diffraction and to achieve nanometer spatial resolution, in the last decade near-field spectroscopy techniques based on scanning probe microscopy (SPM) methods have been invented and further developed exploiting the nanometer tip probes as optical antennas to access the spectral signals of samples in the near-field region below the tip. The tip-enhanced methods therefore rely on the enhancement and spatial confinement of light in the close vicinity of the apex of a metallic plasmonic nanotip, which tipically has a cone shape, enabling the spectral information of the sample to be probed (Fig.2.8e). The frequency of resonant excitation of plasmons ω_p of most metals is typically in the visible and UV range, although enhancement effects have been achieved by engineering the tip to exhibit a dipolar antenna resonance also in the IR range [106]. In vibrational spectroscopy, the tip-enhanced techniques represent the local or "single-point" declination of SERS and SEIRA. In these techniques, precise control of the size of the resonant nanogap is possible, and the nanoscale tip serves as the sole signal amplifier allowing for nanoscopy of vibrational signatures with nanometer spatial resolution, in contrast to the rough or nanostructured metallic surfaces employed in diffraction-limited approaches. In some configurations, the gain of the spectral signal can be further enhanced in a nanocavity-like arrangement, where the mirror of the metallic probe is a metallic surface on which the nanometer-thick sample is placed [20, 107].
In the IR range, the scattering scanning near-field optical microscopy (s-SNOM) technique [108], the photothermal-induced resonance (PTIR) technique, also known as AFM-IR [19] and the Photo-induced Force Microscopy (PiFM) appear as the last and most advanced development of the IR spectroscopy. Thanks to the fact that they are based on a near-field approach, these techniques permit to solve all the issues of the IR radiation on the resolution limit and dimension of detectable objects, moving in the direction of the single-molecule spectroscopy [109].
The s-SNOM method is based on a optical detection and it measures the scattered light from the sample modified by the tip-sample interaction allowing for probing the local dielectric properties with nanoscale resolution (Fig.2.11 a). The scattered field can be written as $E_{scat} \propto \alpha_{eff} E_{inc}$, where α_{eff} is the effective polarizability (Fig.2.11 b), which is a function of the dielectric properties of the tip ϵ_{tip} and of the sample ϵ_s. The detection is based on oscillation of the AFM tip at its mechanical resonance frequency Ω, as commonly done in AFM tapping mode. This allows to modulate the scattered field non-linearly generating higher harmonics in the frequency domain and suppress the background signals by lock-in detection at higher harmonics $n\Omega$ of the tip. This near-field method has been widely employed especially in the study of condensed matter [112, 113, 114, 115, 116]. Few examples of its application exists also in biological system [117], as for the case of s-SNOM experiments conducted on Bacteriorhodopsin for the identification of its distribution, density and orientation in dried purple membrane patches [111, 118] (Fig. 2.11 c) and also immersed in bulk aqueous solution [119]. In PiFM, the detected signal is due to the electromagnetic force between the dipolar charge oscillations in the illuminated tip and the induced polarization in the sample. The tip is positioned in close proximity to the sample

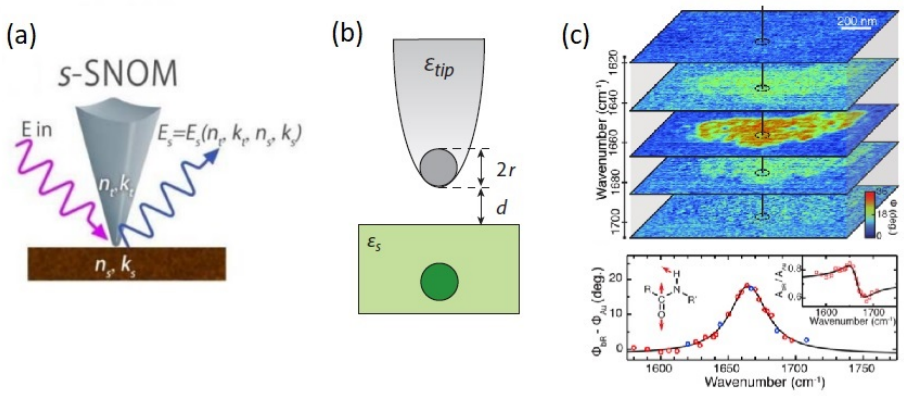

Figure 2.11. a) Schematic representation of s-SNOM. The light scattered by nanometer scale regions directly under the AFM probe tip is detected. The scattered field depends on the complex optical constants of both the tip and sample and contains rich information about nano-optical phenomena. b) Illustration of the dipole-mirror approximation of the tip-sample system in s-SNOM [110]. c) Example of a spatio-spectral s-SNOM sequence of near-field phase images (upper panel) acquired at incremental laser wavelengths on a purple membrane showing the emergence and disappearance of IR-vibrational amide I contrast. Local near-field phase spectrum (lower panel) derived from the full sequence of 26 images at different wavelengths (circles) with fit to the imaginary part of a Lorentzian. Blue circles denote the scans shown in the upper panel. Inset: Corresponding normalized amplitude spectrum (squares) with fit to the real part of a Lorentzian [111].

and externally driven by a piezoelectric element to force an oscillatory motion of the cantilever at the frequency coinciding with its mechanical resonance. The incident light is modulated at a given frequency f_m matching one mechanical resonance of the cantilever (homodyne detection) or the difference/sum of the cantilever resonance frequencies (heterodyne detection). In the presence of photo-induced forces, the cantilever develops motions that depend on f_m, and these motions can be detected by analyzing the signal of the cantilever position.

On the contrary, the AFM-IR is the tip-enhanced technique in the IR range whose detection is based on the contact between tip and sample. As further detailed in Chapter 4 sec.4.2.3, the sharp AFM tip, which can both operate in contact and tapping mode, indeed serves the function of mechanical detector to measure the local photothermal expansion of the sample induced by the absorption of IR light (Fig.2.12a). In details, the absorption of optical energy matching the vibrational modes of the sample causes a local heating due to their non-radiative decay and therefore a thermal expansion. After the IR excitation, the sample thermalizes with a characteristic time ranging from 0.1 ns to a few ms (see Fig.2.12b) depending on the sample thickness, thermal conductivity and other thermal properties. The small thermal expansion is then transduced by the AFM tip in contact with the sample into large cantilever oscillations whose amplitude is ultimately detected using the photodiode detector of the AFM system (see representative spectra in Fig.2.12c-d obtained on polymer samples). The overall AFM-IR signal intensity can therefore be factored in different contributions according to each step within this

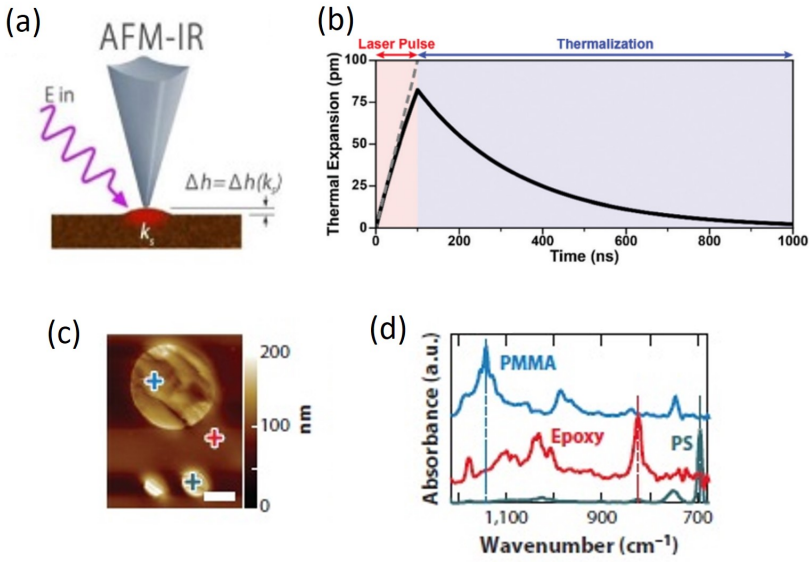

Figure 2.12. a) Schematic representation of AFM-IR. It directly detects light absorbed by the sample using the AFM probe tip to sense thermal expansion that primarily depends on the absorption coefficient. b) Simulated photothermal expansion of the sample (solid black line) accounting for heat diffusion during (red shade) and after (blue shade) the absorption of incident IR radiation. The dashed grey line represents a hypothetical linear expansion that neglects heat diffusion during. c) AFM topography image of a example of sample made of PMMA and PS particles in epoxy matrix. d) AFM-IR spectra of the three different materials obtained tuning the emitted wavelength of the laser source and recording the cantilever amplitude at each wavelength to retrieve the absorption spectrum [110, 121].

signal transduction chain [120]:

$$S_{AFM-IR} \propto H_{AFM} H_{exp} H_{therm} H_{opt}(\lambda) I(\lambda) \tag{2.14}$$

where H_{therm}, H_{exp}, and H_{AFM} refer to the contributions from the sample temperature, the sample expansion, and the AFM cantilever oscillation dynamics, respectively. $I(\lambda)$ is the incident laser intensity at wavelength λ, which is measured with a photodetector before the AFM-IR spectral acquisition, and $H_{opt}(\lambda)$ is the optical contribution to the signal, defined as the fraction of light absorbed by the sample, related to its complex refractive index $\hat{n}(\lambda) = n(\lambda) + ik(\lambda)$. Consequently, $H_{opt}(\lambda)$ is the only factor that depends on the wavelength and on the absorption coefficient, $\alpha = \frac{4\pi k(\lambda)}{\lambda}$, while the others only scale the overall spectral intensity but do not affect the relative peak intensities or peak shapes.

AFM-IR characterization is mostly used for the study of biological samples thanks to their thermal expansion coefficient [122, 123, 124, 125, 126], such as bacteria, cells, lipids, proteins, but it has also be applied to polymers [127], quantum dots [128] or plasmonic nanostructures [129]. Its way of operating leads to the idea of implementing the technique for the study of nanoscale phenomena that depend on the electric field. In the AFM-IR contact-mode one can indeed take advantage of the metallic tip to apply an external voltage to the sample while performing IR

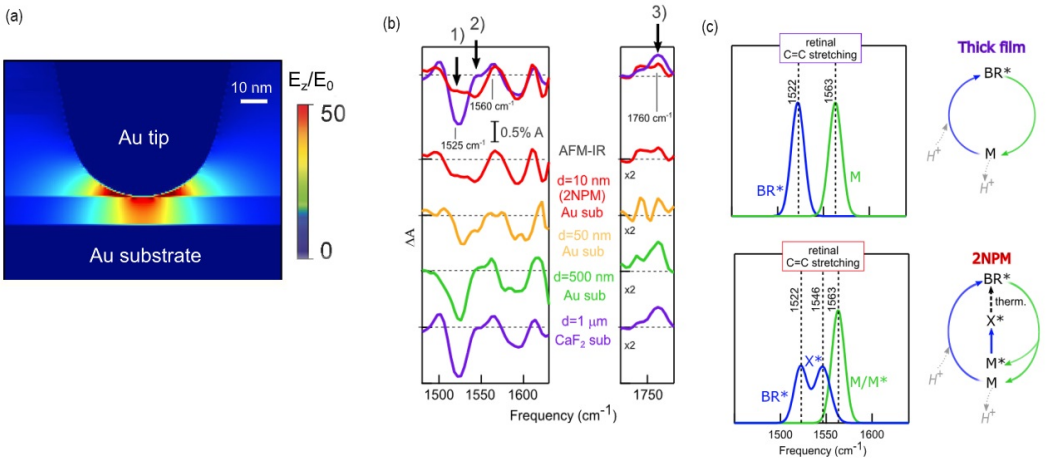

Figure 2.13. a)Simulated maps of IR E-field component normal to the membrane plane normalized to the incident E_0. b) AFM-IR difference-spectra on BR samples of different thickness. c) Model of the unbranched (thick film) and branched (two native purple-membrane, 2NPM) photocycles [20].

spectroscopy measurements.
In 2019, it has already been demonstrated by my research group that it is possible to use AFM-IR for the detection of conformational changes of BR proteins at the level of a double cell membrane system with a total thickness of 10 nm [20]. In this work, Giliberti et al. exploit the plasmonic field enhancement in the nanogap between a gold-coated AFM tip and a gold substrate (Fig.2.13a) to reach the sensitivity of 10^2 proteins probed in a area whose dimensions are well below the diffraction limit for conventional IR difference-spectroscopy. The results obtained on the two-membrane system clearly show the spectral features related to the protein photoactivity, in the spectral region expected from literature data obtained with conventional FTIR spectroscopy. However, comparing them also with the results of AFM-IR measurements conducted on thicker samples consisting of stack of overlapped membranes with a total thickness of 50 nm, 500nm and 1 μm (see Fig.2.13b), some variation arise. They are attributed to a branched photocycle, so that only a fraction of proteins follows the standard one contributing to the net proton transport through the membrane. While the remaining proteins undergo a different photocycle branch with zero net proton transport through the membrane, which is characterized by retinal C=C vibration frequency slightly shifted respect to the standard photocycle (Fig.2.13c). The alteration of the photocycle for proteins probed with AFM-IR on the double membrane system can be related to several reasons, such as the alteration of the standard protein conformational changes and reprotonation process due to less freedom in the arrangement of those proteins directly in contact to solid surfaces, or variation in the membrane surface potential due to the presence of the gold surface and the metallic AFM tip. This represents the state-of-the-art in IR investigation of photosensitive proteins, enabling studies with unprecedented sensitivity. It also serves as starting point paving the way for observing protein conformational changes at the level of individual cell membranes as a function of the transmembrane potential.

Chapter 3

Studies of electric field effects on proteins

The interest in performing optical spectroscopy of molecules under external electric fields is very broad: it ranges from the fundamental research to study internal electric fields in biomolecules to the interest on the relationships between molecular structure and electrical properties or other functionalities [130, 131]. Indeed, understanding the effects of electric fields on molecules, and in particular on proteins, is not only fundamental for advancing our knowledge of biological systems but also holds promise for innovative applications in medicine, biotechnology and materials science [3, 132, 133, 134]. In recent years, advances in simulations have enabled to study the effects of electric fields on proteins at a molecular level. Specifically, molecular dynamics simulations are based on the investigation of the dynamics of conformational variations of a molecule where atoms are allowed to move over time. Therefore, they can provide insights into how **electric fields influence the dynamic behavior of proteins**, helping to uncover mechanisms behind field-induced conformational changes [4, 5].
From the experimental side, **optical spectroscopies** are able to reveal **conformational changes of molecules or charging effects** [135, 136] when an external voltage is applied to single molecular layers. The conventional far-field spectroscopy methods, however, are often difficult to apply at the nanometric scales. Furthermore, the interest in moving towards the study and use of single-molecule scale systems is also driven by the desire to miniaturize microelectronic technologies based on molecular junctions or biocompatible materials. In optogenetics, where the photosensitive rhodopsins found application, the request is due to the will of approaching the study of biomolecular systems as close as possible to their natural conditions, taking into account the possible nanoscale heterogeneity in the composition of the membrane as well as the membrane potential. Hence the aim of my thesis to study photosensitive proteins at the level of the single cell membrane.
In this Chapter, I generally elucidate how **IR spectra can discern the presence and impact of an electric field on molecular systems**, by providing a broad overview of the possible effects that arise in a protein when subjected to an external electric field and by exploring phenomena such as the conformational changes and the Vibrational Stark Effect. I will present methods grounded in **scanning**

probe microscopy and **near-field optics**, which have facilitated the observation of material properties with nanometer resolution, with a particular focus on the study of transport properties and electric-field-dependent effects even without optical probes. Among various experimental strategies, I will also lay the foundation of the experiments of my PhD work, specifically of the AFM-IR technique.

3.1 IR spectroscopy for revealing electric-field-dependent effects

As explained in Chapter 2, sec.2.2, IR spectroscopy is a powerful and versatile label-free tool for elucidating the impact of electric fields on molecules, providing valuable insights into their structural and conformational changes. The vibrational modes are indeed intimately linked to the chemical structure, making IR spectroscopy sensitive to any change in the bond conformation, protonation or oxidation state. Moreover, vibrational frequencies, intensities and bandwidths are also affected by intra- and intermolecular interactions and in general to local electric fields, so that voltage-induced variations in the protein conformation can be observed with IR spectroscopy. When these effects are less pronounced, such as because of a reduced degree in orientational freedom, another effect may be dominant in causing variations in the IR spectra due to the presence of static electric fields on organic molecules. This phenomenon is known as Vibrational Stark Effect (VSE) and arises from the interaction between the vibrational levels of molecules and electric fields. Unlike other effects, the VSE does not rely on changes in molecular structure or orientation. Instead, it manifests as a variation in the vibrational transition energy due to the anharmonicity of the molecular potential. Consequently, this effect serves as a spectral probe for the presence and quantification of static electric fields, offering a non-invasive and direct method to study the impact of electric fields on molecular systems. Actually, the VSE has already been observed in immobilized proteins in frozen solutions and also exploited at room temperature to probe local electric field within the molecules by introducing VSE probes [137, 138].

3.1.1 Effects of static electric fields on proteins

When a molecule is subjected to an external electric field, it can respond in ways that result from its charge distribution and polarization characteristics. Starting from simple considerations, charged molecules experience forces within the electric field, leading to reorientations and movements while polar molecules, having a neutral net charge, develop partial charges along their structure due to differences in electronegativity, inducing dipoles align with the electric field and resulting in molecular distortion. In complex macromolecules, such as proteins, the peptide units represent electric dipoles that do not cancel each other in a common conformational structure of the protein backbone, inducing a macrodipole formation along the overall protein structure, so that any change in protein orientation or content will result in a substantial change of the macrodipole moment of the molecule [140]. Moreover, many amino acid residues, such as aspartate, glutamate, lysine, arginine and histidine are electrically charged. Therefore, electric fields applied to proteins,

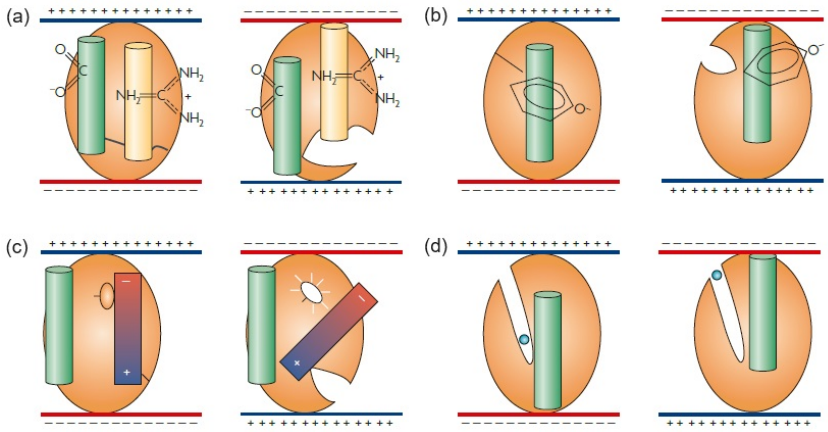

Figure 3.1. Possible voltage-induced conformational changes occurring in a membrane protein (orange oval) mediated by the defined regions of the protein (green and yellow cylinders). a) Charged amino acid residues may move within membranes in response to changes in voltage. The side groups of Asp and Arg are shown. b) Reorientation of an intrinsic residue dipole. c) An α-helix with a dipole moment reorientates when the field is changed. The oval that is attached to the α-helix corresponds to a fluorophore that is quenched on the left and unquenched on the right, indicating a conformational change. d) A channel within the protein can redistribute ions (light blue circle) according to the direction of the field and initiate a conformational change. Alternatively, a conformational change may form a channel that confers voltage dependence to the process as the ions move in the channel [139].

can cause conformational changes, altering the three-dimensional arrangement of atomic bonds within the molecule. These effects include movements of charged amino acid residues modifying their positions and leading to shifts in the protein overall shape and function, or variation of the balance between different forces that stabilize the protein structure, such as hydrogen bonding and hydrophobic/hydrophilic interactions [141, 142]. Other possible consequences are dissociation of ionizable groups, orientation of permanent dipoles and induction of dipoles due to the polarizability of the molecule [143, 144]. It is therefore evident that the electric field experienced by a molecule can impact its stability, activity and interactions with other molecules.
One has also to consider that in a homogeneous solution where molecules are free to rotate and the dimension of molecules is small, the electric field effects discussed above are generally negligible. This is because they primarily induce orientation rather than significant changes in the molecular conformational structure. However, these effects are amplified by a few orders of magnitude and become important if the molecules are embedded in a cell membrane or vesicle [145, 139, 146], as for the case of voltage-gated or light-gated ion channels (Fig.3.1). Additionally, in these membrane proteins, electric fields can alter the processes involving migration of ions and other charged species across the cell membrane, thereby affecting the cellular activity and the protein function in itself.
The vibrational characteristics of proteins, primarily associated with their secondary structure and bonding, may therefore undergo discernible alterations. The electric fields can originate externally, affecting the entire molecule, or internally, affecting

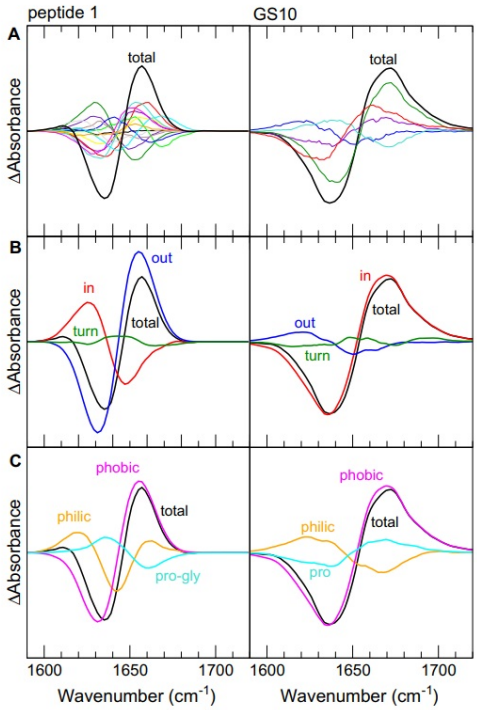

Figure 3.2. Computed unfolded–folded amide I difference spectrum of the single peptide groups and the total signal for peptide 1 (15 amino acid residues) and GS10 (10 amino acid residues) [147]. The labels indicate the peptide groups with the hydrogen-bonded C=O dipoles pointing inwards (in) or towards the solvent (out), and with hydrophobic (phobic) or hydrophilic (philic) residues.

specific sites within the structure. Detailed molecular-level understanding, together with valuable information about stability and flexibility of the protein structure, is indeed fundamental for revealing the intricate mechanisms governing the response of protein conformation to external electric stimuli and the dynamic interplay between proteins and electrical environments. With IR spectroscopy, one can effectively observe changes in the vibrational modes of protein molecules, such as variations in bond angles, stretching, and bending. The amide I band in the protein IR spectrum, which is indicative of structural components like α-helices and β-sheets, exhibits shifts and intensity variations in the presence of static electric fields. Such changes can be attributed to alterations in the hydrogen bonding network within the protein, influencing its overall conformation. Additionally, modifications in the protein side-chain vibrations can be observed, allowing to discern changes in the local environment of amino acid residues, contributing further to the understanding of conformational dynamics and eventual alteration of some processes under static electric fields.

As an example, in Fig.3.2 from ref. [147] the computed difference spectra of the unfolded-folded states of two β-based peptides are reported. The different colors identify the diverse single peptide groups, which can be classified as those with the hydrogen-bonded C=O dipoles pointing inwards or towards the solvent, and with hydrophobic or hydrophilic residues. The negative–positive signal in the case of

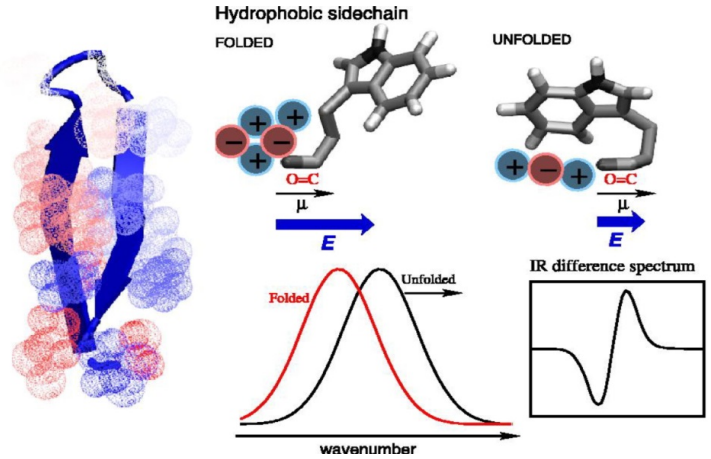

Figure 3.3. Representation of the effect of the hydrophobic residue on the amide I mode vibrational frequency of the peptide group in the folded and unfolded state of the protein [147].

hydrophobic groups is attributed to the effect of the electric field exerted by the environment on the C=O dipoles. As shown in Fig.3.3, it can be seen that for the hydrophobic side-chain the component of the electric field $\vec{E}$ along the C=O dipole direction is lower in the unfolded state, giving rise to the observed shift to higher frequencies of the amide I band with respect to the folded state. This is an example of how the interpretation of IR difference spectra signals can be linked to the effect of local electric fields within the protein structure. Importantly, this interpretation can be extended to understand the broader scenario of the effects induced by an external electric field on the overall protein structure.
When the effects on the IR spectra resulting from molecular flexibility or environmental factors are minimized or controlled, such as in frozen samples, the VSE can emerge as the predominant effect, even in proteins samples [138].

3.1.2 Vibrational Stark Effect

As anticipated, one of the consequence of the application of electric fields on molecules that can be observed on vibrational spectra is the so-called Vibrational Stark Effect (VSE). Electric fields affect any process or transition that involves the movement of charge and Stark spectroscopy is a general term describing the study of spectral changes in the presence of electric fields. The Stark effect was observed for the first time by the German physicist J. Stark in 1913 looking at the splitting in the absorption lines of molecular hydrogen caused by an external electric field and it has proven to be a widely useful approach for characterizing the change in dipole moment and polarizability for electronic and vibrational transitions.
In 1995, the chemists A. Chattopadhyay and S.G. Boxer reported that the IR absorbance of the CN stretching mode in the anisonitrile molecule changed proportionally with the strength of an electric field imposed on the molecule [148]. Thereafter, Vibrational Stark Spectroscopy (VSS) has been employed to correlate information inferred from the vibrational spectral properties of molecules with the electric fields they experience in a wide range of molecular systems and materials

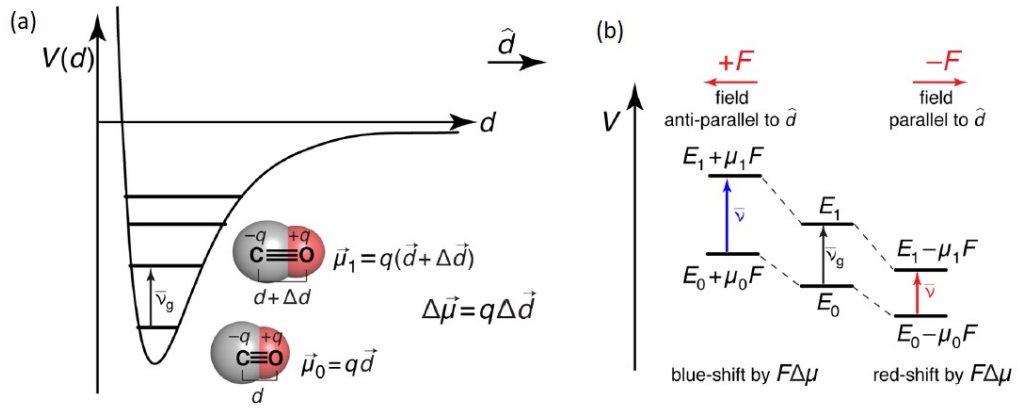

Figure 3.4. a) The anharmonic form of molecular potential energy surfaces implies that bonds will be slightly longer and so possess slightly larger dipole moments in their vibrational excited states. b) Ground and excited vibrational states are stabilized differently by an electric field, resulting in a shift in the transition energy [156].

[149, 150, 151, 152, 153, 154, 155].

Theory. The VSE derives from the anharmonicity of the molecular potential and relies on the shift of vibrational lines due to the presence of an external electric field. Indeed, if one consider the molecular potential energy curve for a diatomic molecule this potential is anharmonic, and one consequence of this is that when a molecule goes to higher vibrational energy levels, its bond becomes slightly larger $\Delta\vec{d}$. If this diatomic molecule possesses a permanent dipole moment $\vec{\mu}_0 = q\vec{d}$, then its dipole moment will be lager in the first vibrational excited state compared with the ground state $\vec{\mu}_1 = q(\vec{d} + \Delta\vec{d})$ (Fig.3.4 a). Since these states have different dipoles, they will be populated differently upon the application of an external field, $\vec{F}_{ext}$, depending on the orientation between the dipole and the field (Fig.3.4 b). Therefore, the applied electric field will produce a shift in the vibrational transition energy that can be probed by IR and Raman spectroscopy and results to be linear with the difference in the dipole moments of the two vibrational states

$$\Delta\nu = -\Delta\vec{\mu} \cdot \vec{F}_{ext} - \frac{1}{2}\vec{F}_{ext} \cdot \underline{\Delta\alpha} \cdot \vec{F}_{ext} \tag{3.1}$$

where $\underline{\Delta\alpha}$ is the difference-polarizability tensor. If the electric field strength is below 100 $\frac{MV}{cm}$, the quadratic term with regard to $\underline{\Delta\alpha}$ can be neglected, so that the change in the vibrational frequency $\Delta\nu$ directly correlates with the change in the strength of the electric field. The sensitivity of a vibrational frequency to an external electric field (and therefore the variation of a vibration dipole) is called Stark tuning rate and typical values are measured to be around 0.5-2 cm^{-1} per unit of electric field in $\frac{MV}{cm}$ applied along the vibrational dipole axis. These tuning rates imply vibrational difference dipoles of 0.03-0.12 D (1 D = 16.8 $\frac{cm^{-1}}{(MV/cm)}$, electric dipole moment unit called a "Debye"). A polyatomic molecule has obviously a more complex electrostatic and vibrational structure, but limiting the attention to high-frequency vibrations of specific functional groups, they can be considered to be largely decoupled from the rest of the molecule and behave similarly to the diatomic case so that for such

a vibrational transition the $\Delta\vec{\mu}$ is aligned with the axis of the vibrational mode bond. Another assumption is that the vibrational frequency shift $\Delta\nu$, arising from changes in the environment of the probed molecule, can be fully attributed to the external electric field, while the difference dipole moment $\Delta\vec{\mu}$ is unaffected so that the vibrational frequency shift responds linearly.
Experimentally, the Stark shift can be measured and difference dipole moment can be calculated consequently. This is realized by means of VSS, in which external fields are applied to molecules and the effect on the vibrational spectrum is recorded. The measurement consists of acquiring the IR spectrum of the sample in the presence and absence of the applied electric field. By analyzing the small differences between the spectra, the vibration difference dipole can be determined. For an isotropic, immobilized sample, and assuming $\Delta\nu$ smaller than the inhomogeneous line width, the change in absorbance under the influence of an external field can be written as the sum of the zeroth, first, and second derivatives of the absorption spectrum weighted by ν [148]:

$$\Delta A(\nu) = (f\vec{F}_{ext})^2\{A_\chi A(\nu) + \frac{B_\chi \nu}{15hc}\frac{d}{d\nu}(\frac{A(\nu)}{\nu}) + \frac{C_\chi \nu}{30h^2c^2}\frac{d^2}{d\nu^2}(\frac{A(\nu)}{\nu})\} \tag{3.2}$$

where A_χ depends on the transition polarizability and hyperpolarizability

$$B_\chi = \frac{1}{2}\{5Tr(\underline{\Delta\alpha}) + (3cos^2\chi - 1)[3(\vec{p}\cdot\underline{\Delta\alpha}\cdot\vec{p} - Tr(\underline{\Delta\alpha})]\} \tag{3.3}$$

and

$$C_\chi = |\Delta\mu|^2[5 + (3cos^2\zeta - 1)(3cos^2\chi - 1)] \tag{3.4}$$

In these equations, h is the Planck's constant and c is the speed of light. ζ is the molecular angle between $\vec{\mu}$ and the transition moment $\vec{M}$ (usually equal or close to 0°), while χ is the experimental angle between $\vec{F}_{ext}$ and the polarization of the probing light field. f is an experimental local field correction factor. It is a tensor in a general treatment but is typically approximated by a scalar for simplicity. Also, the inhomogeneity of f within the volume of a molecule and its variability between different molecules are typically ignored. The field experienced at any point in space within a molecule can in fact be approximated as the sum of two terms

$$\vec{F}_{int} = \vec{F}_{matrix} + f\vec{F}_{ext} \tag{3.5}$$

The matrix field $\vec{F}_{matrix}$ is the internal local field in the absence of an applied field. It accounts for the solvent reaction field and for the field due to other organized local structure, such as nearby molecule residues. $\vec{F}_{ext}$ is the average field external to the sample molecule in the nearby solvent and is the one that appears in eq.3.2. The external field is equal to the applied field, which in parallel-plate geometries is the applied voltage, known accurately, divided by the electrode spacing. To summarize the spectral information inferred by ΔA, an applied electric field broadens an isolated transition due to $\Delta\vec{\mu}$, giving rise to a Stark effect line shape which is approximately the second derivative of the absorption spectrum. The reason is that molecules whose $\Delta\vec{\mu}$ is oriented parallel or antiparallel to the electric field have their transition energy most shifted to lower or higher energy, respectively. However, the majority

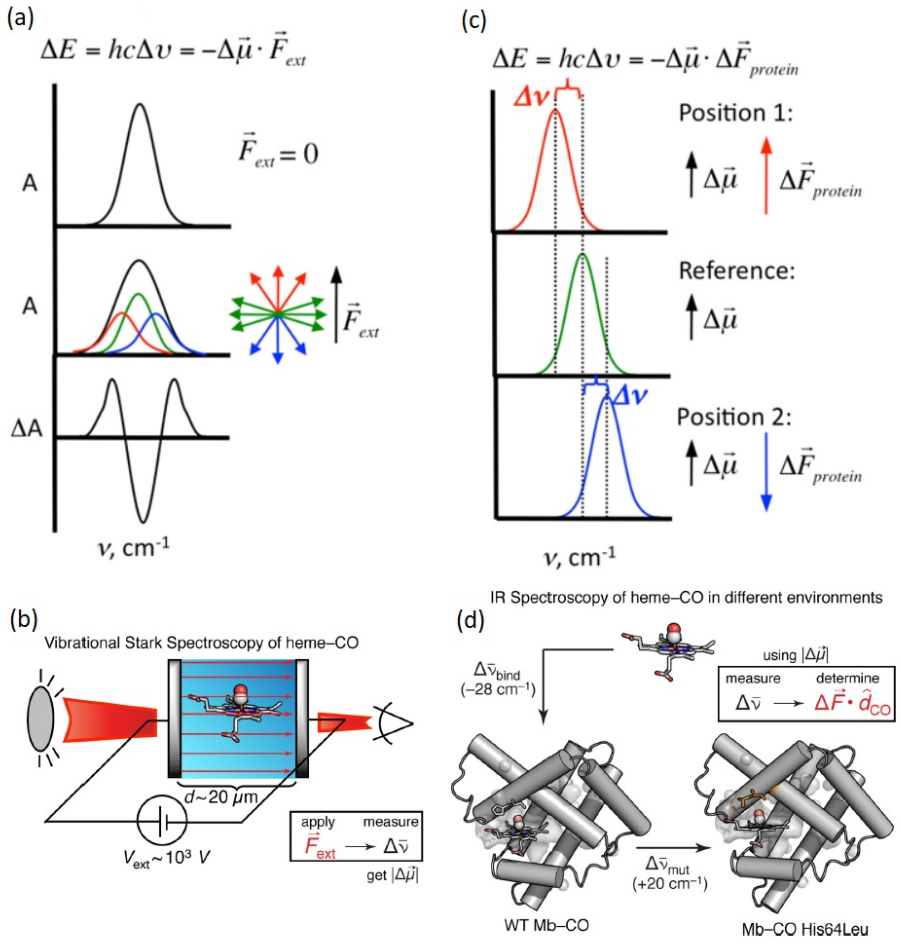

Figure 3.5. a) Schematic illustration of the origin of the second derivative line shape for a Stark spectrum of an isotropic, immobilized sample. Vectors corresponding to $\Delta\vec{\mu}$ parallel, antiparallel, and perpendicular to the applied field $\vec{F}_{ext}$ are shown in red, blue, and green, respectively. Respect to the energy in absence of the external field, some orientational subpopulations are shifted to lower energy (red), some to higher energy, and (blue) some remain about the same (green). The result is a broadened band, and the Stark spectrum is the field-on minus field-off difference spectrum with a second derivative line shape. Note that the spectral shifts are assumed to be much smaller than the inhomogeneous line width. b) Representation of a vibrational Stark spectroscopy experiment. External electric fields are applied to an isotropic sample and the perturbation caused to the IR spectrum is recorded, yielding the Stark tuning rate. c) Schematic illustration of the procedure for the Stark probe for electric fields in complex organized systems. If the Stark tuning rate is an intrinsic property of the probe oscillator, then placing the oscillator in different matrix electric fields should shift the observed spectrum according to the projection of the matrix (e.g., protein) field on the bond direction. d) Representation of an experiment in which the frequency shifts caused by changing the environment surrounding a molecule can be translated into electric field differences. Images adapted from Ref.[156, 157].

of molecules lie at or near the equator so their transition energies are shifted less or not at all, as shown in Fig.3.5a. Most absorption lines are not symmetrical and this

requires high quality absorption spectra, since a rigorous comparison of the shape of the lines of the second derivative of the absorbance with respect to the Stark data has to be conducted. To the extent that the transition is polarizable, the electric field induces a dipole and typically this occurs primarily in the direction of the applied field. Hence, this induced difference dipole mimics a difference dipole in an oriented sample, and the observed effect is a band shift resulting in first derivative line shape of the absorption change, whose sign depends on the sign of the change in polarizability, which is often, but not always, greater in the excited state than the ground state. Therefore, fitting with eq. 3.2 the difference-absorption spectra obtained as the difference between the sample in presence and absence of the applied electric field, one can estimate $\Delta\vec{\mu}$ from the coefficient of the second derivative term C_χ.
Up to now, the case in which the Stark shift is studied by applying an external electric field to the molecules has been presented, allowing for example to obtain the value of $\Delta\vec{\mu}$ in a molecule (Fig.3.5b) [149, 157]. A different case are the Internal Stark Effect (ISE) experiments aimed at observing vibrational shifts related to local electric fields within molecules. These experiments use molecules featuring specific functional groups or chemical bonds that respond to alterations in the local electric environment and are thus exploited as Stark reporter [158, 159]. Some studies are indeed carried out by knowing $\Delta\vec{\mu}$ (obtained by Stark spectroscopy) and recording IR spectra at different environmental conditions surrounding a molecule to estimate the differences in the electric fields $\vec{F}_{matrix}$ projected along the bond of interest from the frequency shift (Fig.3.5c), using the Stark tuning rate as the conversion factor (Fig.3.5d) [137, 160]. This method has been successfully applied, for instance, to determine the strength of electrostatic fields in proteins [161] or to measure the transmembrane potential in vesicles [162]. A significant example for our topics of interest is the time-resolved application of vibrational Stark probes to study functional changes of Sensory Rhodopsin II by means of thiocyanate protein variants, changing the site where the VSE probe was introduced [163]. Also vibrational scattering scanning near-field optical microscopy (s-SNOM) studies have been conducted to probe local variations and heterogeneities in electric fields and local chemical environment between nano-domains of polymer systems, relying on the observation of a different type of Internal Stark shift [164].

3.1.3 Limitations of far-field IR approaches

The application of far-field IR spectroscopy for studying the effects of electric fields on molecules has its inherent limitations. Firstly, as already mentioned in section 2.4 of Chapter 2, the spatial resolution and sensitivity of IR spectroscopy in standard approach requires millimeter-squared sample area for effective probing, posing a considerable challenge when attempting to conduct experiments involving external electric fields. One can design an experiment based either on an electrochemical cell where the molecules are in solution or on two plate electrodes enclosing the sample of interest. However, the possible technical issues and difficulties must be considered. These are related to the interference of the ions in solution or to the need to realize electrodes that allow the passage of optical signals to and from the matter under test, so that one or both electrodes must be made transparent to light,

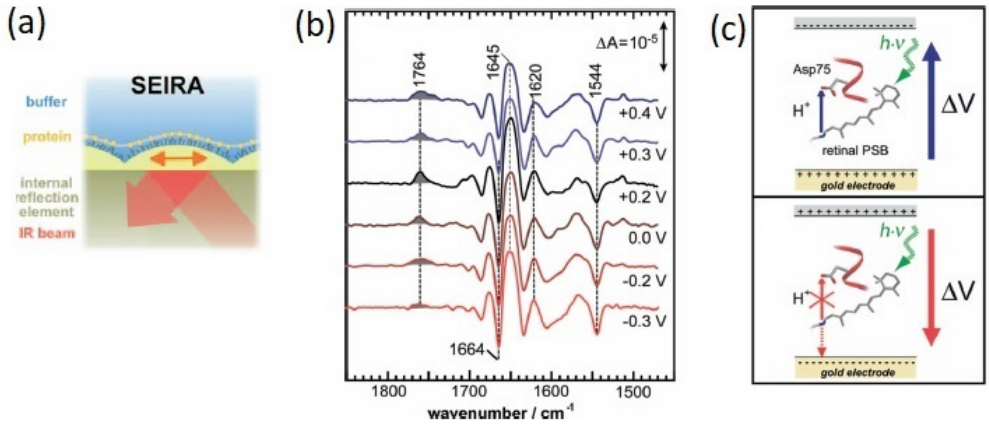

Figure 3.6. a) Experimental configuration of the SEIRA experiment on a monolayer of Sensory Rhodopsin II. b) IR difference spectra recorded at potentials from -0.4 V to -0.3 V. c) Sketch of the light-induced proton transfer reaction from the donating retinal Schiff base SRII to the accepting carboxylic side chain of D75 at two opposite polarization of the applied potential [168].

by using either ultra-thin metal layers that are conducting and semi-transparent or perforated electrodes (gratings or hole arrays). Moreover, a number of molecules of the order of 10^{15} is detected limiting the possibility of having a homogeneous sample of molecules in terms of composition and orientation, which may be important conditions for the study of conformational changes, electronic and transport properties. Hence, in contrast to electrophysiological methods conducted on proteins integrated into the cellular membrane, studies employing these spectroscopic techniques have so far been limited to homogeneous polymeric films or liquid samples [151, 165, 166, 167]. As far as I know, the only experimental exception to the limited studies on voltage-dependent IR spectra is presented in the work conducted by J. Heberle and colleagues in ref. [168]. In this work a monolayer of Sensory rhodopsin II is realized through particularly strong adhesion via the C-terminal His-tag of the protein to a functionalized rough gold surface on the top of an ATR silicon prism. The surface plasmon polariton generated in the SEIRA experiment at the metal surface penetrates into the medium with a decay length of 8 nm sampling only those molecules that are within this short distance from the solid surface. The peculiarity is that the gold surface is exploited as an electrode while the other side of the protein is exposed to a buffer solution, acting as liquid electrolyte (Fig.3.6 a), so that it is possible to control and vary the electric potential between the ends of the protein. In particular, in ref.[168], light-induced difference-spectra are acquired at different values of the applied voltage, revealing distinct structural changes of the retinal cofactor and variation on the proton transfer dependent on the applied potential (Fig.3.6 b-c). As already stated in section 2.4 of Chapter 2, the main limit of SEIRA is diffraction of light that constrains the size of the sampled area not to be smaller than the radiation wavelength. An homogeneous layer of proteins has thus to be reconstructed avoiding any thickness variation or holes in the film, which are crucial parameters that influence the effective value of electric fields when an external voltage

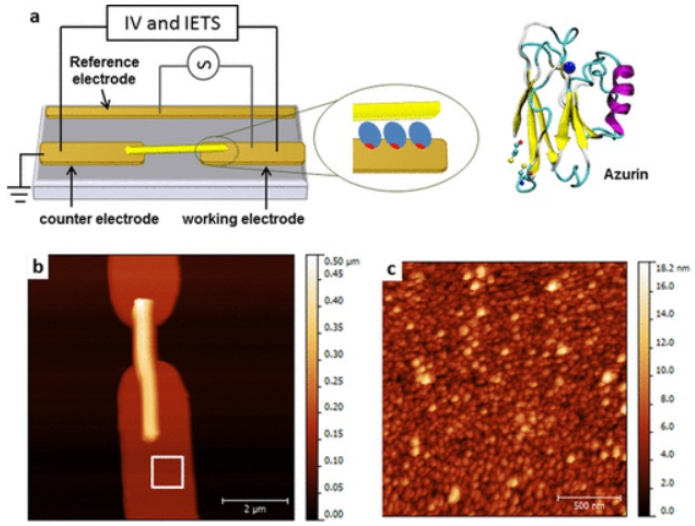

Figure 3.7. a) Scheme of the Azurin junction fabricated by trapping nanowires by an AC electric field for I–V and IETS measurement. b) Atomic force microscopic image of the nanowire, lying on the working and counter electrodes, after the electrostatic trapping. c) AFM image of the square that is indicated in image b, showing dense monolayer Az clusters on the gold electrode [169].

is applied. Moreover, the geometry of the gold surface is not precisely known and under control, because the layer that creates SEIRA must be rough and disordered by definition, so that the electric field assumes different values depending on the position.

3.2 Experimental strategies at the nanoscale

The exploration of physical and chemical phenomena, such as the impact of static electric fields, on samples characterized by nanometric dimensions or thickness and exhibiting nanoscale heterogeneity, has become feasible through the utilization of advanced techniques developed for the high-resolution characterization of material and molecule properties. In order to conduct these studies, structures must be miniaturized to nanometer dimensions to serve as mechanical, electrical, or optical probes either in direct contact or in proximity to the samples. Molecular junctions, where a single molecule is positioned between two metallic surfaces for electron transport measurements, exemplify this requirement. Typically, molecular monolayers are deposited on a flat metallic surface with single metallic nanoparticles serving as the top electrode. For instance, this configuration has been used to conduct transport measurements on proteins, as demonstrated by the inelastic electron tunneling spectroscopy (IETS) on the azurin protein mentioned in ref.[169] (Fig.3.7). The measurement of characteristic I-V curves and the subsequent calculation of the second derivative ($\frac{d^2I}{dV^2}$) provide valuable information about molecular vibrations. This insight into molecular electronics helps in understanding electron transport mechanisms, particularly those based on electron–phonon coupling.
More in general, methods based on scanning probe microscopy (SPM) play a pivotal

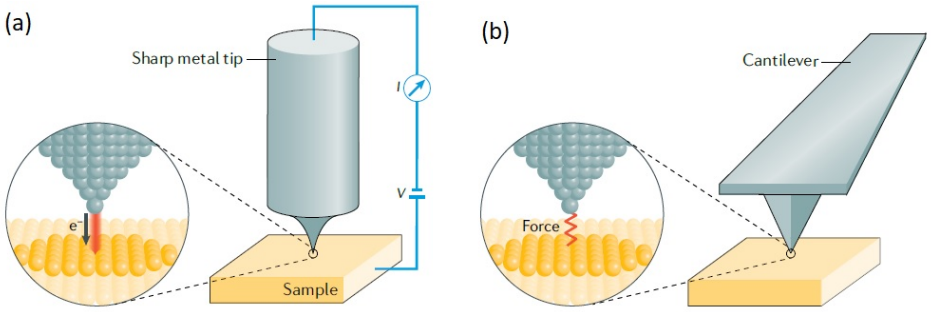

Figure 3.8. Basics of scanning probe microscopy setup. a) Scanning tunnelling microscopy (STM) collects the tunnelling current between the tip apex and the sample when a bias voltage is applied. b) Atomic force microscopy (AFM) detects local forces of interaction between the tip and the sample and the corresponding mechanical parameters through a spring-like cantilever [170].

role among nanoscale techniques due to their ability to perform nanoimaging by raster-scanning a nanometric tip or collecting local information when placed in a fixed position. These methods not only permit to measure transport properties but also to visualize morphological, mechanical, and electrical information at the nanoscale. Consequently, they allow researchers to delve into intricate details of nanomaterials and nanostructures, revealing their behavior even under the influence of external factors such as static electric fields.
In addition to nanoimaging, spectroscopy approaches leveraging the electromagnetic enhancement of light have been instrumental in advancing the understanding of nanoscale phenomena. As already discussed for IR spectroscopy in Chapter 2 sec.2.4, these techniques enhance the sensitivity of optical and vibrational spectroscopy methods, enabling the detection and characterization of properties, subtle changes and interactions at the nanoscale.

3.2.1 Methods based on Scanning Probe Microscopy

When the understanding of matter at its nanoscopic and molecular level is the target of research, a class of methods widely employed are SPMs. Their operation is based on a nanometric sharp tip that can physically raster-scan samples and locally collect information from the surface. The two main approaches are scanning tunnelling microscopy (STM) and atomic force microscopy (AFM), whose invention made possible for the first time the imaging of solid surfaces or molecules placed on them with nanometric and even atomic resolution. Besides the imaging application, SPM mechanisms have been implemented and modified opening up the possibility of measuring a large class of physical quantities with nanometric resolution, such as electric currents, forces, temperatures and even mechanical and optical properties. SPM techniques can therefore be employed also in the study of the effects of electric fields on molecules, exploiting the conducting scanning probe tip that is connected to the electrical bias circuit, which can be used to both apply the bias locally and to sense the response of matter by means of a mechanical or electrical readout.
STM employs a metallic tip sharpened to a single atom to measure currents from conductive samples (Fig.3.8 a). It operates at a working distance that allows the

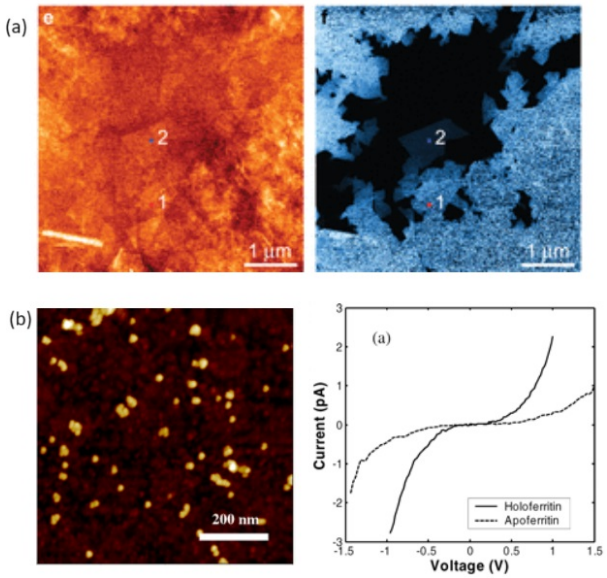

Figure 3.9. a) AFM image of a defect region of a reduced graphene oxide film (left, z-range=6 nm) and the corresponding current image (right, current range = 200 nA), showing the absence of current over electrically disconnected segments and the differences in the current over regions of different thickness [179]. b) AFM image of apoferritin molecules (left) and conductive-AFM I-V measurements of single holoferritin and apoferritin molecules (right) [180].

quantum mechanical effect based on electron tunnelling when the tip/sample junction is polarized with a low voltage bias (10 mV to a few V), resulting in the measurement of a current that is sensitive to the tip/sample distance with an exponential dependence on it. The fine and precise movement of the tip is achieved by means of piezoelectric transducers that are able to displace the tip with sub-Angstrom precision. Beyond its imaging capabilities, the STM permits a diverse array of experiments, including Scanning Tunneling Spectroscopy (STS) measurements [171]. STS is particularly instrumental in probing the electronic properties of materials, offering the capability to measure the density of electronic states and the band gap as a function of electron energy. In the context of STS, the voltage applied between the STM tip and the sample dictates the energy of the tunneling electrons, allowing for the acquisition of energy-dependent information. By systematically measuring the tunneling current in relation to varying voltages, characteristic current-voltage (I-V) curves are generated. The first derivative of these curves ($\frac{dI}{dV}$) provides valuable insights into the local density of states [172, 173, 174]. Among various electric-field-dependent effects studied by SPM probes, the Stark shift of the quantum levels of molecules and solids can be detected by electronic STS [175, 176]. Moreover, in specific instances involving molecules adsorbed on metallic surfaces, the second derivative of the I-V curves ($\frac{d^2I}{dV^2}$), becomes particularly informative, as in IETS experiments [177, 178].

In contrast to the STM method, AFM possesses the capability to image a wide range of surfaces, including non-conductive ones, while operating in ambient conditions. This is achieved through a mechanism relying on the measurement of interaction

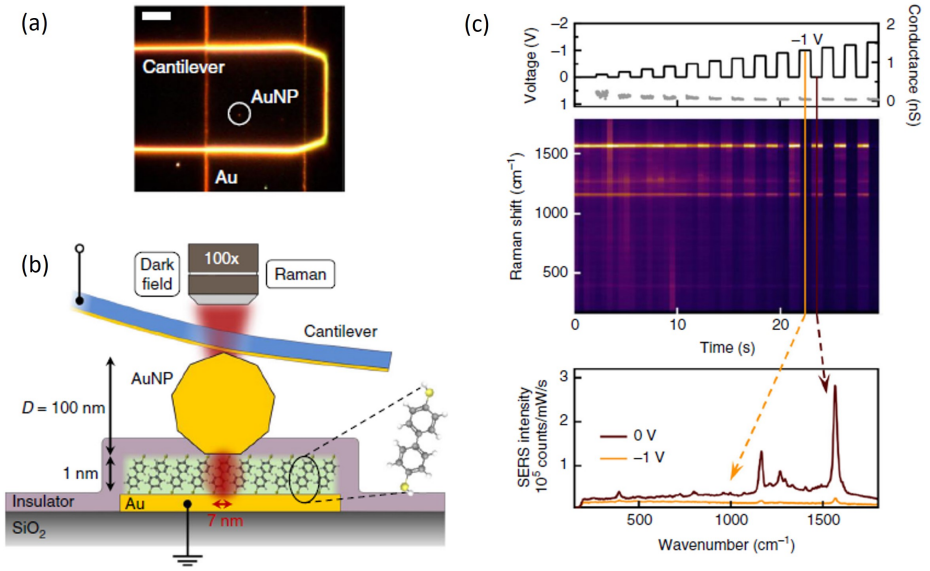

Figure 3.10. a)Top view of the semitransparent cantilever used to electrically contact the gold nanoparticle in the white circle. Scale bar is 10 μm. b) Detailed sketch of the experimental configuration for the Raman measurements on the biphenyl-dithiol molecular junction. c) Results of the real-time SERS experiment for increasingly negative bias voltage [18].

forces between the tip and the sample (Fig.3.8 b), as it will be further described in section 4.2.1. The sharp tip is indeed mounted at the extremity of a spring-like cantilever, which deflects in response to the force applied to it. In addition to providing surface topography details, AFM proves capable in discerning electric-field-dependent phenomena. This extends to detecting effects like the volume expansion observed in piezoelectric materials, alterations in morphology of objects under an electric field, and the thermal expansion of polar materials when subjected to AC fields [181, 182, 183]. Furthermore, in other applications, the AFM tip itself, made of conductive materials, can function as an electrode, enabling current measurements in what is known as the conductive-AFM (C-AFM) technique. The operation of the C-AFM is similar to STM, relying on the bias application between the tip and sample and the measurements of the current or tunneling current between the two. Therefore, a current-to-voltage amplifier enables the acquisition of the current distribution on the sample at a given DC bias, while simultaneously acquiring the surface topography (Fig.3.9a). Otherwise, in a fixed position, C-AFM can perform I-V spectroscopy measuring the current as a function of the DC bias that is swept forward and backward within a predefined bias range at a given rate (Fig.3.9b).

3.2.2 Near-field spectroscopy approaches

As can be easily deduced from the discussion in Chapter 2 sec.2.4, the plasmonic strategies based on nanocavities that are designed to obtain the optical sensitivity

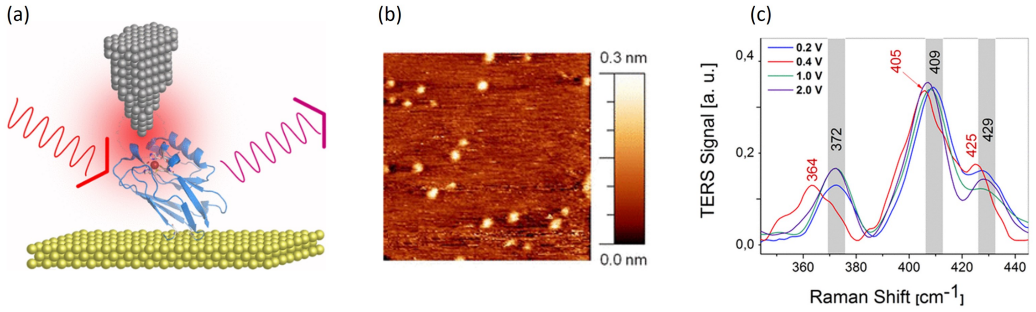

Figure 3.11. a) Experimental configuration of the ATM-TERS experiment on a single molecule of azurin. b) STM image of azurin proteins on a gold surface (60×60 nm). c) Normalized TERS spectra from an azurin monolayer on a gold surface collected under a tunneling current I= 0.1 nA, at various values of the applied bias [17].

for the study of monolayers or single molecules, involve leveraging metallic materials not just for enhancing optical properties but also as integral components that can be exploited as electrodes in nanoscale approaches [15, 18, 184, 185]. Several techniques exist which are capable of producing well-controlled nanoscale spacers to obtain arrays of nanoparticles-on-mirror structures over large areas, where the spacing region between the nanostructure array and the continuous metal surface is filled by the material of interest(Fig.2.8d). This can be easily obtained for small molecules both by top-down techniques, such atomic or molecular layer deposition, or by bottom-up coatings such as self-assembled monolayers (SAMs).

As an example, I report here a vibrational spectroscopy work that is not conducted on proteins and that is more related to the field of molecular electronics. It appears anyhow relevant as a near-field strategy to perform an experiment probing the conformation of a molecule as a function of the applied bias. Specifically, in ref.[18], conductive transparent cantilever electrically contacts individual gold nanoparticles used as one electrode of a molecular junction of biphenyl-dithiol (Fig.3.10a-b), while maintaining optical access to the monolayer deposited on a flat gold surface. The enhanced optical field within the nanoparticle-on-mirror plasmonic gap enables strong surface enhanced Raman spectroscopy of the molecules. A strong reduction in SERS signal is observed when $|V| > 0.5$ V, saturating above 1.0 V (Fig.3.10c). The reduced molecular Raman cross-sections is attributed to a twisting of π-orbitals across the C–C bond linking the two rings of the molecules that disrupts their delocalisation reducing the molecule polarizability. This work thus provides an example of experiments that can probe the conformation of a molecule normally invisible in electrical transport measurements but pivotal for the design and exploitation of molecules in electronic nano-devices.

In addition to surface-enhanced experiments, as already anticipated in Chapter 2 sec.2.5, the coupling of SPM methods with the fundamentals of near-field optics offer the possibility to achieve effective sensitivity in spectroscopic methods within a single *hot spot* to probe nanometer-sized objects or heterogeneous samples at the nanoscale. In parallel to the previously discussed near-field techniques for IR spectroscopy (see Chapter 2 sec. 2.5), a notable approach employed in Raman spectroscopy is known as Tip-Enhanced Raman Scattering (TERS). TERS exploits

the process of raster-scanning a metallic tip over a sample using both STM and AFM probes, operating in a non-contact mode. The optical enhancement of the plasmonic tip can significantly boost the Raman signal by a factor ranging from 10^4 to 10^6. While conventional experiments primarily used STM signals for localizing and characterizing molecules without applying a bias to them, recent advancements have led to the adoption of more sophisticated STM-TERS spectroscopy methods. The latter involve collecting the vibrational spectrum of molecules while varying the applied voltage bias through the scanning-probe tip [16, 17]. As an example, in ref. [17] an STM-TERS experiment is conducted on azurin molecule which is a redox metalloprotein. The vibrational spectra of the single molecule collected varying the bias applied by the tip evidence some differences in protein vibrational response that are connected with the charging and electrostatic field related effects occurring within the protein (see Fig.3.11). This nanoscale approach offers a unique opportunity to gain insights into the intricate relationships between electron transport and the conformation or inter-molecular organization of molecules.

3.3 Our strategy: AFM-IR with applied electric field

In the specific case of the objective of this PhD work of the study to be performed on transmembrane proteins, the need for the lipid environment to preserve the stability and functionality of the proteins has led us to prefer a tip-enhanced approach due to the difficulty to reconstruct homogeneous monolayers of the lipid-protein system over large areas. Moreover, in the exploration of protein conformational changes, mid-IR absorption spectroscopy is a more prevalent technique than IETS or Raman spectroscopy within the respective spectral range. The amide I band, which manifests in the IR absorption spectra between 1600 and 1700 cm^{-1}, serves as a standard spectroscopic fingerprint in biochemistry. This band is widely employed to precisely characterize even the most subtle protein conformational changes.
The IR nanospectroscopy techniques, as previously discussed in Chapter 2 sec.2.5, extend the field of IR investigations to the nanoscale, providing opportunities to study monolayers of molecules, proteins embedded in a single cell membrane, or even individual molecules. Building upon the experimental setup of these tip-enhanced methods, it becomes feasible to exercise precise and localized control over another crucial parameter: the electric field experienced by molecules within the probed area. The metallic AFM tip and sample support can indeed be harnessed as electrodes, allowing the application and control of a bias V_{DC}. This additional capability provides valuable insights into the effects that may influence and modify protein structures and functionalities. However, the tapping working mode, essential for detection in s-SNOM and PiFM, involves intermittent contact between the probe tip and the sample, hindering the ability to apply a constant static electric field through the AFM tip. In contrast, AFM-IR operates in a pure contact mode, making it a more suitable approach for investigating electric-field-dependent effects on proteins at the nanoscale. Hence, for my PhD project, we implemented our AFM-IR platform with an electric circuit analogous to a conductive-AFM setup. This unique capability positions the AFM-IR with the integrated DC circuit as a powerful tool for precisely exploring and understanding the intricate interplay

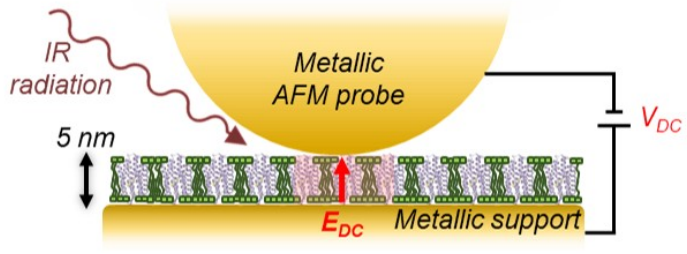

Figure 3.12. Sketch of the AFM-IR nanospectroscopy setup with the integrated electric circuit applied to an individual cell membrane system embedding photosensitive proteins.

between electric fields and protein behavior with nanoscale resolution.

Chapter 4

New experimental techniques to bring the IR spectroscopy of proteins to the nanoscale

In this chapter, I delve into the fundamentals of IR spectroscopy, from the **conventional far-field methodology** to the **state-of-the-art field of nanospectroscopy**, explaining the working principles behind the techniques and instruments employed throughout my PhD project.

4.1 Fourier Transform IR spectroscopy-FTIR

Fourier Transform IR spectroscopy (FTIR) is the main and widely used standard technique to perform IR spectroscopy. It basically consists of a black-body source, an interferometer and a detector for IR radiation. The great advantage of FTIR spectroscopy is that it employs a broadband source without using any prism, slit or grating for the detection, but all the emitted wavelengths hit the detector at the same time. This results in a excellent signal-to-noise ratio, as there is no intensity decrease along the beam path, apart from the interaction with the sample, and optimization of the acquisition time for an IR spectrum. The optical device that allows for the spectra detection is an interferometer that measures the interference pattern between two light beams. Hence, the detector reveals an interferogram in the time-domain that is then converted in a spectrum in the frequency domain by Fourier transform computations. Fig.4.1 shows the basic elements and the working principle of a Michelson interferometer. Other type of interferometer with different optical configurations exist, but the basics of operation are similar so that the following discussion and the operating principles of FTIR presented in *Appendix II* will be relevant anyhow.

The acquisition time of a FTIR measurement depends on two factor: i) the single scan time acquisition that is related also to the spectral resolution required, because the better the spectral resolution, i.e. the longer the scan length, the worse the time resolution will be at a given velocity of the movable mirror; ii) the number of repeated scans N to acquire a spectrum, which depends on the signal-to-noise ratio that increases as $\sqrt{N}$. In fact, whereas the signal adds coherently,

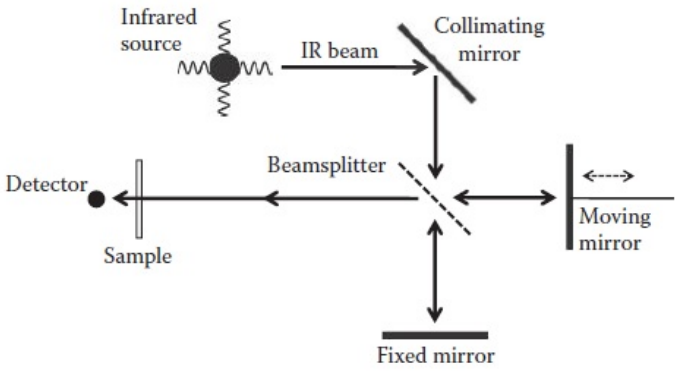

Figure 4.1. Optical scheme of a Michelson interferometer for FTIR spectroscopy [186].

the measurement noise does not, as it is random and hence increases only with $\sqrt{N}$. Therefore, to obtain a better SNR the acquisition is typically repeated by averaging of interferometers obtained over many scans, thus increasing the time needed to obtain a spectrum. However, to increase the time resolution of a single scan an detect time-dependent phenomena, FTIR interferometers can operate in *rapid-scan* or *step-scan* mode. In rapid-scan acquisition the moving mirror travels at a constant velocity usually greater than 0.1 $\frac{mm}{s}$. During the movement of the mirror relative to the beamsplitter (forward and backward) two symmetric interferograms are recorded and each double-sided interferogram can be split in two single-sided. In this manner, the time resolution is increased because the time to return the moving mirror is effectively used for data recording. Whereas, in *step scan* mode there are no mechanical restriction to achieve high time-resolution, which is limited only by the detection response. Indeed, the movable mirror is moved in step by step and kept fixed at each sampling position. At each position the kinetic process of the sample under investigation is initiated and recorded and once it is concluded the mirror is moved to the next position to restart the process. After the complete acquisition over all the mirror positions, the kinetics recorded at each sampling step are recombined to obtain the time-resolved interferograms, one for each time-point after the beginning of the kinetic. From them, the IR spectra are computed by Fourier transform as for the continuous-scan mode. In any case, it must be taken into account that the kinetic process that wants to be detected must be repeated at each sampling position of the mirror, therefore it must either be a reversible and repeatable phenomenon or a fresh sample re-circulation mechanism must be integrated. Moreover, signal averaging is usually applied to increase the SNR.
The sources typically employed are thermal light sources, named Globar (from *glow-bar*), whose spectral behavior corresponds approximately to that of a black body. The preferred material for making Globar is silicon carbide that is shaped as rods and when inserted into a circuit that supplies electric current, it is heated to temperatures of 1000 to 1650° C, thus emitting radiation from about 2 to 50 μm wavelength. A wheel with circular apertures of various sizes is placed in front of the source to let part of the emitted radiation pass towards the interferometer. The wheel can then be turned to select the size of the aperture which determines the size

of the beam and focus, choosing the one that is most suitable for that experiment. The minimum diameter of the aperture is $0.25mm$.
As for the detectors, the DTGS detector is one of the most employed. It is a pyroelectric detector belonging to the class of thermal detectors, which do not directly respond to radiation, but only to the generated heat. The DTGS is made of a crystal of deuterated triglycine sulfate with electrodes on two sides. One of those electrodes has a black coating , which is exposed to the incident radiation. The incident light is thus absorbed on the coating causing some heating of the crystal because the heat is conducted through the electrode into the crystal. As a result, the crystal produces a pyroelectric voltage that one can electronically detect. When equipped with a KBr window, DTGS detectors are sensitive from 400 cm^{-1} to beyond 4000 cm^{-1}. However, DTGS has a slow response to changes in IR intensity at different speeds and this is ultimately what determines the speed at which the moving mirror can be translated in an interferometer. A second disadvantage of DTGS is its noise level, which is relatively high if compared to other types IR detectors. DTGS detectors are fine for routine analysis, while for demanding applications other types of detector element materials have been developed such as mercury cadmium telluride (MCT). MCT is a photoconductor and when it absorbs light, electrons are knocked loose creating an electrical current proportional to the intensity of the radiation. They are 4 times faster and 10 times less noisy than DTGS detectors, but they also have some disadvantages. They are expensive, have a cutoff at 700 cm^{-1} and required to be cooled by means of thermoelectric cooling or with liquid nitrogen (T=77 K) to reduce electronic noise. Therefore, the choice of the detector depends on the request of the experiment and the sample.
In the experimental investigations conducted for my PhD thesis, I used the Bruker VERTEX 70v interferometer. Known for its superior performance and remarkable signal-to-noise ratio, this instrument incorporates advanced technology to ensure accurate and reliable results. Notably, the VERTEX 70v is designed to operate in a vacuum environment, enhancing the precision of measurements and it is equipped with a liquid-nitrogen-cooled MCT detector. The latter is a critical component for difference spectroscopy detection on photosensitive proteins, whose spectral variations are of the order of 10^{-2}-10^{-3}.

4.1.1 Bringing FTIR to the diffraction limit

A FTIR spectrometer coupled with a microscope permits to perform IR spectroscopy on sample of small size or with a heterogeneous composition on the micrometer scale. The microscope optics is typically based on reflective mirrors and Cassegrain condenser/objective elements. They are composed of two reflective mirrors, one parabolic and one hyperbolic, arranged to achieve focusing on the sample of all light wavelengths traveling through it and to collect back the light from the sample. In transmission mode two Cassegrain elements are used as focusing condenser and collecting objective, while in reflection mode only one is used for both focusing on the sample and collecting the reflected light (Fig.4.2 a-b). Moreover, knife-edge apertures are used to define the size and shape of the IR beam before it goes through the Cassegrain and reaches the motorized x-y stage where the sample is placed. IR microscope spectra may results to be noisy due to reflectance losses at

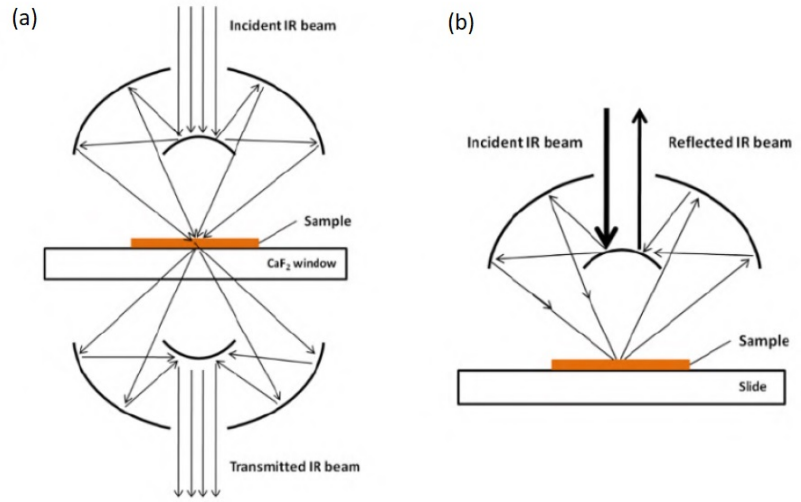

Figure 4.2. Optical scheme of Cassegrain objective and condenser systems used in transmission (left) and reflection (centre) mode.

the many mirrors in the microscope, the apertures blocking parts of the beam and the small size of the samples, so that the use of a high sensitivity, low-noise, and liquid-nitrogen-cooled MCT detector is essential. Employing a globar source, along with an optimal interferometer, microscope, and detector configuration, allows for the acquisition of high-quality IR spectroscopy results over a defined area of 20x20 μm^2. To push the boundaries of spatial resolution even further and extend the capability to analyze smaller objects, experiments often turn to the use of advanced light sources, such as synchrotron radiation. Synchrotron radiation offers several advantages, including a high degree of brilliance and broad spectral coverage. These characteristics make it an ideal light source for micro-FTIR applications that demand exceptional spatial resolution exploring IR response within samples at the microscale. Indeed, synchrotron radiation is a powerful source of electromagnetic radiation produced by charged particles accelerated to relativistic speeds with an acceleration perpendicular to their velocity. This is obtained within a circular path guided by magnetic fields and the emitted radiation is characterized by an high brilliance, defined as the photon flux per unit area and opening angle. The emitted radiation from synchrotron sources spans a vast spectrum of energies, from the hard X-ray to the far-IR. This remarkable breadth of energy wavelengths enables synchrotron facilities to supply to diverse scientific efforts, each with specific objectives and applications. Around the synchrotron storage ring, various specialized facilities are strategically positioned to capture and selectively utilize different segments of this broad radiation spectrum. In Fig.4.3 the map of the BESSY II synchrotron facility at the Helmholtz-Zentrum Berlin (HZB) is reported as an example. As part of my PhD research, I conducted difference spectroscopy experiments aimed at characterizing samples of photosensitive proteins at the IRIS beamline within BESSY II.
Moreover, as described in section 4.4 where I provide details of our home-built IR-microscope, the use of quantum cascade lasers as radiation source in microscopy experiments holds the potential to achieve resolutions approaching the diffraction

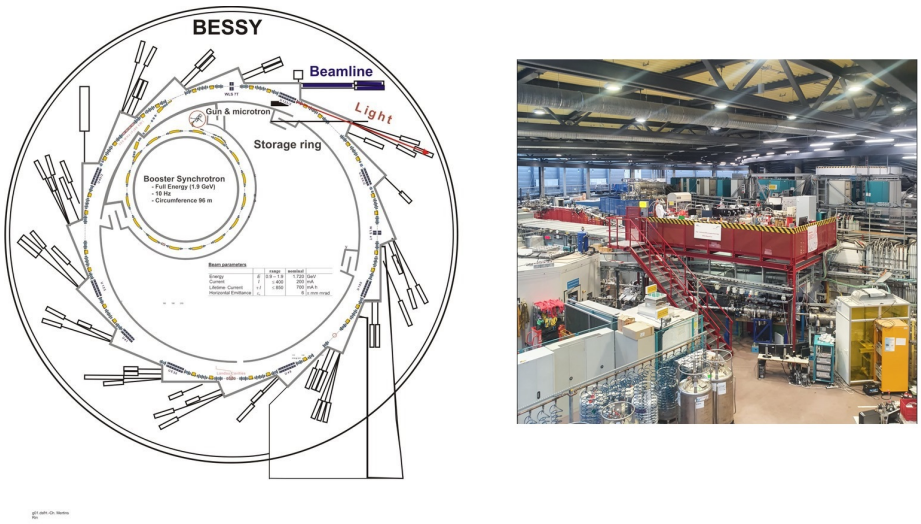

Figure 4.3. Representation of the components and facilities of the synchrotron BESSY II at HZB centrum in Berlin.

limit and compensates for the low SNR in some specific applications [187, 188].

4.1.2 The problem of resolution in microscopy

Despite the possibility of focusing light on smaller dimensions than in the case of standard FTIR spectroscopy, the spatial resolution of IR microscopy is however limited by diffraction. This arises from the Heisenberg's uncertainty principle, which is applicable on electromagnetic waves. According to this principle, the spatial resolution , which is defined as the minimum distance at which two sources could be distinguished in an optical observation, would depend on the uncertainty in the momentum of the light, in such a way that $\Delta x \cdot \Delta k_x \geq \frac{1}{2}$. This condition forces Δx to be a non-zero quantity for any finite value of Δk_x. The practical value of the spatial resolution therefore depends on both the wavelength of the light, which is related to $k = \frac{2\pi}{\lambda}$, and the measurement system used for the observation.
In a optical system, the lateral resolution at a fixed wavelength λ can be estimated by the Abbe's formula of eq.2.13 that is affected by the numerical aperture of the optical system, defined as $NA = nsin\theta_{max}$. It depends on the refractive index of the surrounding medium n and on the maximum collection angle of the optical system θ_{max}. Two significant drawbacks are immediately clear. First, for the best practical conditions, the experimental value of Δx is about half of the wavelength, enforcing a loss of information at the image plane, because an object much smaller than the wavelength would be not correctly detected by optical methods. This means that the mid-IR radiation wavelengths are too large to capture nanoscale details or objects. Second, the wavelength-dependent lateral resolution can limit the applicability of IR analysis for mapping of the chemical distribution of components with characteristic peaks in different spectral regions or for calculating intensity map ratios.
In recent years, significant advances have been made in optical microscopy within

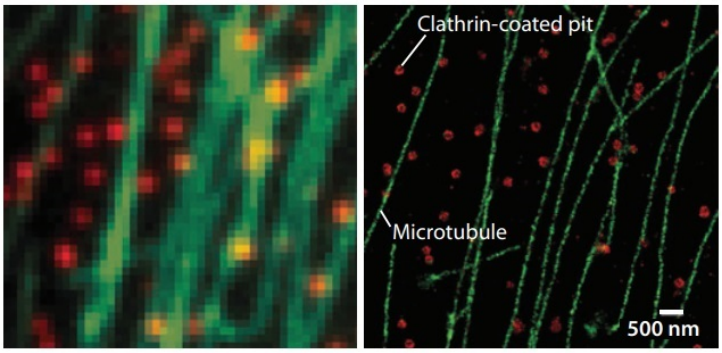

Figure 4.4. Comparison of a conventional fluorescence image (left panel) and a STORM image of the same sample area (right panel) [191].

the visible range, showcasing the emergence of super-resolution imaging techniques. These methods have demonstrated the ability to achieve spatial resolutions approximately ten times higher than the limitations imposed by the diffraction limit, typically around 200–300 nm. Notably, super-resolution fluorescence microscopy techniques have played a pivotal role in enhancing the resolution of biological ,structures through the exploitation of non-linear effects [189, 190]. These include Stimulated Emission Depletion (STED) microscopy, along with related methods utilizing other reversible saturable optically linear fluorescence transitions (RESOLFTs), and Saturated Structured-Illumination Microscopy (SSIM). Another category of techniques focuses on the precise localization of individual fluorescent molecules. Examples of such techniques include Stochastic Optical Reconstruction Microscopy (STORM), Photoactivated Localization Microscopy (PALM), and Fluorescence Photoactivation Localization Microscopy (FPALM).
These methods, although highly powerful for imaging objects with sub-wavelength dimensions, face limitations when extended into the IR range. This constraint arises from their reliance on fluorescence-based principles, which are inherently tied to the visible spectrum. So that in the case of IR spectroscopy and imaging, different strategies have to been employed to overcome the challenges imposed by diffraction.

4.2 IR spectroscopy at the nanoscale

As already been anticipated in Chapter 2 when attenuated total reflection methods (ATR), surface-enhanced vibrational spectroscopies (SERS,SEIRA) and tip-enhanced spectroscopy techniques (TERS,s-SNOM,AFM-IR) were presented, the limitations in optical sensitivity and spatial resolution due to diffraction can be overcome either by exploiting electromagnetic evanescent waves as opposed to free propagating waves or bringing optics on the nanometer scale, in the so-called near-field regime [192, 193]. To resume, experimental methods based on ATR, SERS and SEIRA can reach the sensitivity of samples probed at the nanoscale (such as monolayer sample, thin films, 2D materials...). However, since the surface area of the substrates/sample interface is often significantly larger than the wavelength, the resolution is still defined by the focal spot size. The further step to really approach the nanoscale resolution of

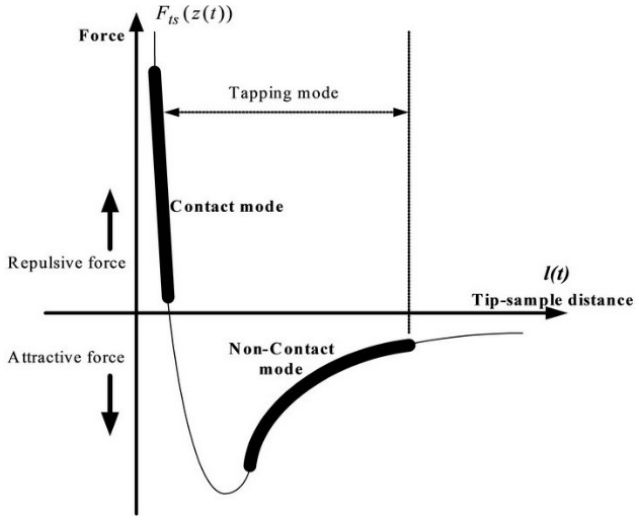

Figure 4.5. Force curve as a function of tip-sample distance in AFM.

optical measurement is the use of a nanoscale scanning probe coupled to a radiation source, as is done in tip-enhanced techniques.
I will now present in detail the tip-enhanced method in the mid-IR that has been employed in my PhD work, i.e. the AFM-IR technique. I will first of all describe separately the two main components of the instrument, which are the atomic force microscope and the mid-IR QCL source, and then conclude by describing the operating principles of the AFM-IR.

4.2.1 Atomic force microscopy

Atomic force miscroscope is an instrument that enables to get information on surface topographies and also mechanical properties with nanometer or even atomic spatial resolution. Its operating mode is based on the measure of interaction forces between a nanometer sharp probe tip and the surface of a sample. The tip is placed at the extremity of a micrometer cantilever which is free to bend in the z-direction and able to scan the sample in the xy plane. The tip-sample interaction forces can act in short ranges, such as chemical ones, or in long ranges, as the case for van der Waals or electrostatic forces. The interaction potential can then be described by the Lennard-Jones form that represents an intermolecular pair potential

$$V_{L-J} = 4\epsilon[(\frac{\sigma}{r})^{12} - (\frac{\sigma}{r})^{6}] \tag{4.1}$$

where ϵ is the depth of the potential well and a measure of how strongly the two particles attract each other, σ is the distance at which the intermolecular potential is zero and r is the distance between the two particles. The first term proportional to r^{-12} is the repulsive part originating from short-range forces, while the second one, proportional to r^{-6} denotes an attraction due to long-range forces (Fig.4.5). As a result of these interaction forces ($F = -\frac{\partial V}{\partial z}$) along the z-direction perpendicular to the sample, the cantilever, on which the tip is mounted, undergoes a deflection. The movement of the cantilever is detected by a laser which impinges and is reflected on

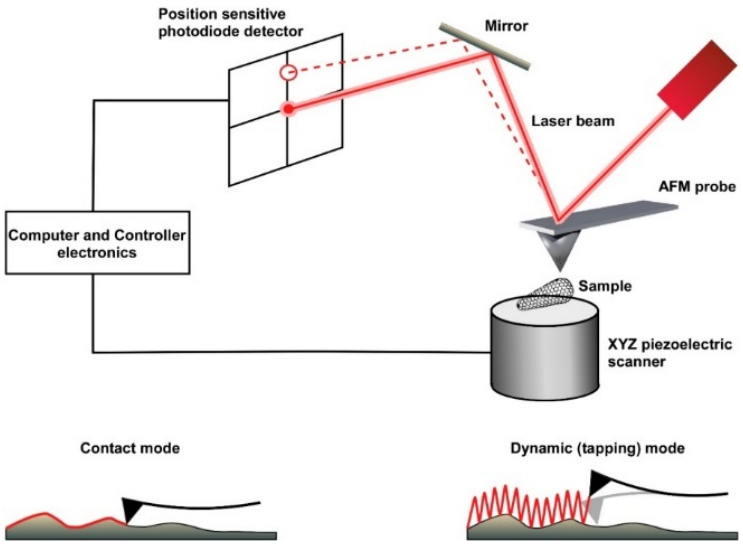

Figure 4.6. Schematic basic of AFM setup [194].

the upper surface of the cantilever itself. A four-quadrant photodiode detector reveals the position variation of the reflected laser and then determines the measurement of the cantilever height variation while the tip scans the surface of the sample (Fig.4.6). The fundamental parameters to describe the cantilever movement in z-direction are the Young's modulus Y and the density ρ, from which the force constant K and the resonance frequency f_0 are calculated. Considering a cantilever of length L, width w and thickness t, K results as

$$K = \frac{Ywt^3}{4L^3} \tag{4.2}$$

while the frequency resonance of the spring-like system is

$$f_0 = 0.162 \frac{t}{L^2} \sqrt{\frac{Y}{\rho}} \tag{4.3}$$

Typical values of f_0 are in the range of 20-200 kHz. AFM can operate in three diverse modalities depending on the different regimes of tip-sample interaction: contact, tapping and non-contact. In contact mode a force is exerted on the cantilever to maintain tip and sample in contact. The roughness of the surface generates a repulsive thrust on the tip of the AFM which can be detected in two ways: by directly measuring the vertical displacement of the cantilever on which a constant force is applied, or, through a feedback system, a constant height can be imposed on the cantilever and the topography is obtained from the variation of the force that is applied to maintain the position constant in z. The disadvantages of this mode are related to the possible damage to the sample, as for the case of biological materials, or to the tip itself which can break or get dirty in the scanning process. Additionally, drag forces can reduce the lateral resolution.
In non-contact mode the tip close to the sample surface, but not in contact, is forced to oscillate at a frequency close to the intrinsic mechanical resonance frequency of the cantilever by means of a piezolectric device. The van der Waals forces, which

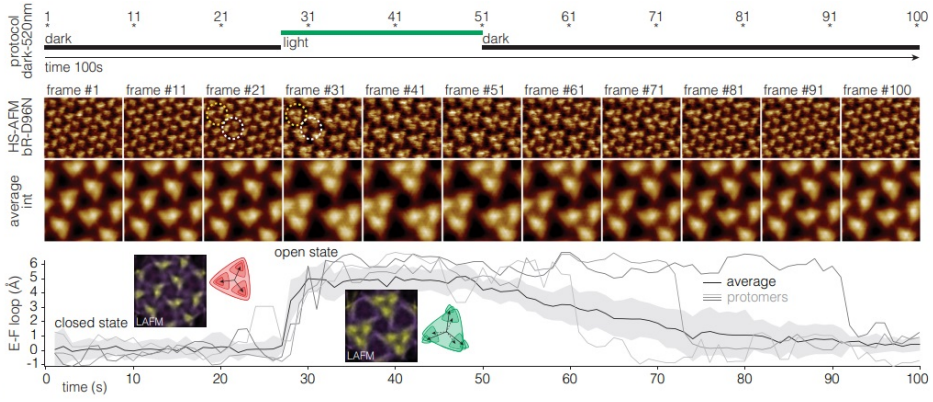

Figure 4.7. Top:Light protocol. Middle: High-resolution HS-AFM images and corresponding correlation averages of BR trimer (white dashed circle) and trefoil, defined as the three nearest-neighbor protomers that gather upon light-activated conformational changes (yellow dashed circle). The average of 12 loop displacement of the protomers (black line) and of three individual protomers (grey line). The insets are AFM maps of molecules in the closed (frames 1–26) and open (frames 28–49) state. [195].

are strongest from 1 nm to 10 nm above the surface, act to decrease the resonance frequency of the cantilever. This decrease in frequency combined with the feedback loop system maintains a constant oscillation amplitude or frequency by adjusting the average tip-sample distance.

In tapping mode the tip is positioned close the surface of the sample and it is driven to oscillate, with a constant amplitude (up to 100 nm). Therefore it passes from the non-contact regime to the contact regime, being affected by forces at long and short range. Due to the effect of the interaction with the sample surface, the oscillation amplitude of the tip tends to vary and a feedback system is therefore necessary to keep it constant, from which the topography is obtained. Although the force exerted by the tip on the sample is greater than in the contact mode, the probability of damage is reduced as the contact time is shorter and the forces in the x and y directions also decrease.

In order to scan the sample surface in the x-y plane, the sample is placed on a stage whose position can be controlled through the use of piezoelectric motors. Piezoelectric materials are electromechanical transducers that convert the electrical signal into a mechanical deformation. By applying small potential differences, fine movements of the sample can be made under the AFM tip. During raster scanning of the sample stage, it is also scanned in the z-direction via feedback control to maintain the tip-sample contact strength or distance constant.

The characteristics of the cantilever can be strategically optimized to enhance the temporal response of measurements, enabling the execution of high-speed Atomic Force Microscopy (HS-AFM) experiments. Besides the topography of a steady state of the sample, this modality allows for real-time observation and precise analysis of fast phenomena at the nanoscale. An illustrative example is found in the research conducted in ref. [195] within the context of photosensitive protein activity. Conformational changes in BR are observed with a temporal resolution down to the millisecond, delineating the kinetics of individual molecules exposed to

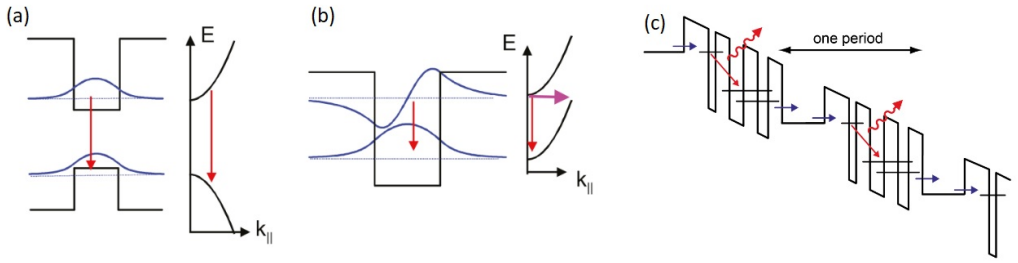

Figure 4.8. a) Inter-band transition of electrons in conventional semiconductor lasers. b) Inter-subband transition of electrons within the semiconductor conduction band in QCLs. c) Schematic of a conduction band diagram of a QCL alternating the relaxation/injection regions and the active regions [196].

both continuous and short light pulses. In Fig.4.7, the case of BR D96N illuminated with a 30-second-long pulse is reported, demonstrating the capability of HS-AFM imaging to monitor the molecular response of these proteins.

4.2.2 Quantum cascade laser

Quantum cascade lasers (QCLs) emit in the mid to the far-IR range and are made of semiconductor heterostructures that exhibit varying band gaps and a very precise composition. The thickness of the semiconductor layers, also called quantum wells, is in the nanometer range so that the electron are confined and their energy is quantized in the direction perpendicular to the plane of the layers. The photon emission is thus achieved by inter-subband transitions of electrons within the semiconductors conduction band (Fig.4.8 b), while in conventional semiconductor lasers it takes place by radiative recombination of electrons from the conduction band with holes from the valence band (inter-band transitions) (Fig.4.8 a). In QCLs therefore the emission wavelength does not depend on the band gap of the semiconductor material, but is tailored by adjusting the quantum well thickness and material properties in a wide region to the particular need. A QCL is composed by several periods of an elemental structure based on two region: the active region and the relaxation/injection region. The active region is a standard three level system where each level is a confined state, while in the relaxation/injection region the electrons are transported to the following active region. Under an applied bias, an electron is injected via resonant tunneling in the upper state of the active region and relax to the lower state emitting a photon. From here the electron is transported through the relaxation region and then injected into the upper state of the following period where it will again be able to emit a photon, giving rise to the emission cascade along the periodic structure (Fig.4.8c), typically consisting of up to 40 repetitions. The selection rule for optical transitions implies that only modes with electrical vector parallel to the growth direction (TM polarized modes) participate in the laser action, hence edge emitting QCLs emit polarized light. The width of the gain curve, a part from the central wavelength, is a also parameter that can be tailored in QCLs. Lasers based on a continuum of the states on the low-energy end, instead of only two discrete levels, have indeed been realized. QCLs can differ for the cavity design, which is typically of three types: Fabry Perot (FP), distributed feedback (DFB) and external cavity (EC) (Fig.4.9).

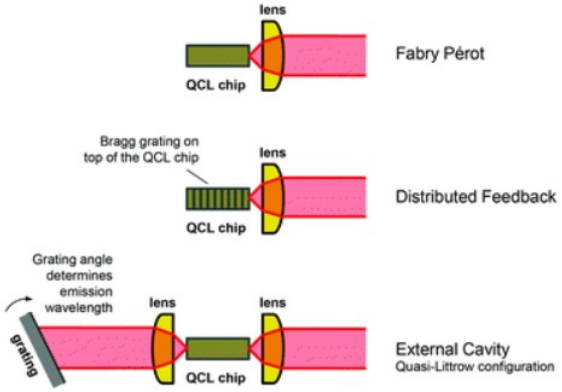

Figure 4.9. Different configurations of QCLs cavity [197].

Depending on the configuration, the overall gain provided by the active region is reduced by the sum of all losses related to the respective resonator design, which include waveguide losses due to light propagation in the laser chip, mirror losses stemming from the facets and losses arising from wavelength-selective grating. The FP configuration is simply based on high reflection coatings on the facets of the QCL chip, where the distance between the mirrors must allow constructive interference to meet the conditions for light amplification. However, the standing wave condition is fulfilled for a large number of longitudinal modes, resulting in multimode emission over a wide spectral range.
The DFB design consists of a Bragg grating integrated into the laser waveguide along the light propagation direction, thus selecting a single mode. The emission wavelength is tunable within a range of 5 cm^{-1} by changing the injection current and/or the operation temperature. Both methods of tuning lead to a change in the effective refractive index of the laser chip material and thus shift the resonance wavelengths of the Bragg grating.
The external cavity EC design, in addition to the FP chip, enables spectral tuning by an external diffraction grating, whose angle variation allows tuning ranges of up to several hundred wavenumbers. The EC-QCLs exist in pulsed and standard continuous wave (CW) (frequently used for condensed phase spectroscopy both in far-field and near-field regime) and mode-hop-free MHF–CW configuration, where a mode tracking system has been developed to precisely match the EC length and diffraction grating angle during the tuning process.
Compared to other mid-IR sources, QCLs therefore provide coherent and polarized light with high spectral power of the order of $mW - W$ (respect to μW of globar sources). Moreover, they can work at room temperature with versatile operation modes and a wide tunability. [197]
The high emission intensity of the tunable QCLs is a particularly advantageous characteristic in protein investigation, notably for determining the secondary structure in the amide I-amide II region. Indeed, it has been demonstrated that the QCL spectral power allows for an extension of liquid cell optical path up to 38 μm [92]. This increase of accessible optical path length unlocks experimental possibilities in a spectral region conventionally constrained by high water absorbance. However,

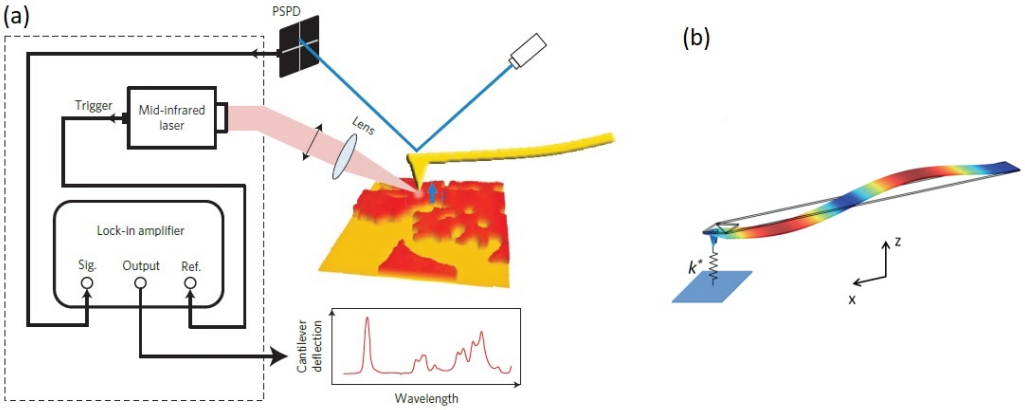

Figure 4.10. a) Schematic of the AFM-IR experimental setup. b) Tip-sample interaction approximated with a spring k* connecting them [107].

it is important to note that EC-QCLs come with certain drawbacks, such as noise associated with pulse-to-pulse intensity fluctuations of around 2% and wavelength reproducibility issues stemming from their tuning mechanism. To mitigate laser intensity noise, various setups and methods, including balanced detection, can be employed. This strategy has been successfully implemented in detecting proteins within a liquid cell of 26 μm, even at a low protein concentration of 0.0025 $\frac{mg}{mL}$ [198]. In balanced detection, the laser beam is divided into two equal-intensity beams: the signal beam (interacting with the sample) and the reference beam. The resulting signals detected on the MCT detector are subtracted from each other, yielding a balanced output that effectively suppresses any intensity changes affecting both beams.
Another direction for exploiting QCLs in protein investigation involves conducting kinetic experiments sub-μs temporal resolution. Commercial FTIR spectrometers operating in rapid scan mode typically offer a time resolution of around 5–10 ms, significantly constraining their applicability in addressing biological dynamics. On the other hand, the step-scan modality, although overcoming the limitation in time resolution, is constrained by sensitivity to experimental disturbances and prolonged experimental recordings. Within this context, time-resolved IR difference spectroscopy utilizing tunable CW QCLs has proven effective in tracking structural and protonation changes in photosensitive proteins [87, 199]. This approach provides both high temporal resolution and a broad spectral range, addressing the limitations posed by traditional FTIR spectrometers and offering valuable insights into dynamic biological processes.

4.2.3 AFM-IR

The nanospectroscopy AFM-IR technique consists basically on the local measurement of the IR absorption of a sample using an AFM system as a mechanical detector (Fig.4.10a). The IR radiation is emitted by a pulsed and tunable QCL source and typically focused on a sample area of tens of microns in diameter. When the IR photon energy is in resonance with one of the IR-active vibration modes of the

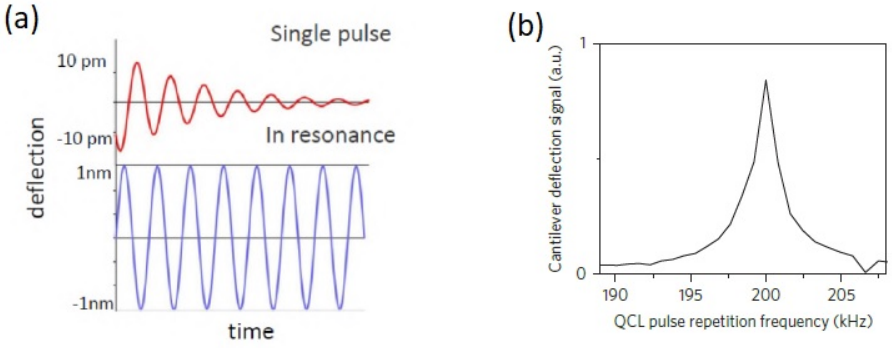

Figure 4.11. a) Comparison of the cantilever deflection after as single laser pulse and in mechanical resonance with the repetition frequency of the laser pulses. b) Dependence of the cantilever deflection on the repetition frequency of QCL pulses. The data show a resonant peak at the cantilever second bending mode frequency in contact with the sample. [107].

sample, molecules transit into an excited vibrational state, which non-radiatively dissipates into molecular vibrational modes of lower energies in a very short time scale of the order of 10 ps. Because of the anharmonicity of molecular potentials, the effective molecular volume increases leading to an overall photo-thermal expansion of the irradiated sample. Therefore, the AFM tip probe, which is placed in contact with the sample, experiences a force causing a variation in the cantilever defection and its subsequent oscillation [197]. Modelling the tip in contact with the sample as a spring-like system (Fig.4.10b), the force exerted on the tip by the sample upon the IR absorption results to be linearly proportional to the variation in the tip-sample distance $\Delta\delta$ following the Hook's law

$$F_{t-s} = k\Delta\delta \tag{4.4}$$

where k is the elastic constant which depends both on the geometry of the tip and the composition of the tip and the sample. The Derjaguin-Muller-Toporov model for the elastic contact with adhesion of two locally spherical bodies, permits to explicate the terms involved in this force as

$$F_{t-s} \approx 2E^*\sqrt{R}\sqrt{\delta}\Delta\delta \tag{4.5}$$

assuming the tip-sample distance change $\Delta\delta$ much smaller than the indentation depth of the tip δ. The other parameters that appear are the reduced Young's modulus E^* and the tip apex radius R. The variation $\Delta\delta$ can be estimated as a thermal expansion

$$\Delta\delta = \delta k_T \Delta T \tag{4.6}$$

where k_T is the thermal expansion coefficient and ΔT is the temperature increase induced in the sample volume under the AFM tip.

Just to give an idea of the order of magnitude of this physical quantities in an AFM-IR experiment similar to the ones conducted in this thesis, one can take as a model system a polymer film with a thickness of few nanometer and an AFM tip

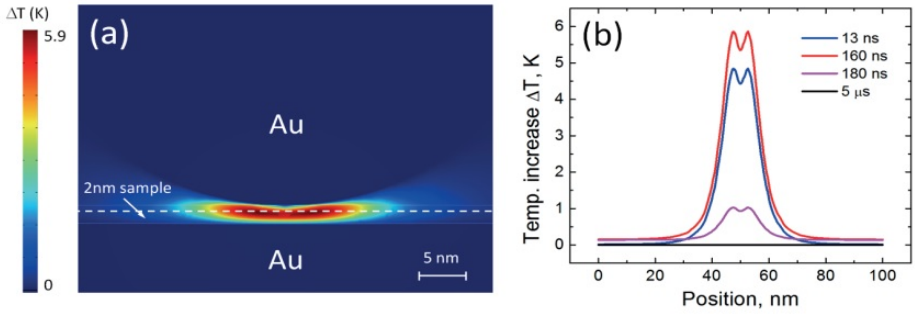

Figure 4.12. a)Simulation of temperature increase in a monolayer at the end of a single 160 ns pulse. b) Temperature variation along the white dash line in a) during a single 160 ns pulse(13 ns, 160 ns) and after (180 ns, 5 µs) the pulse. The sample is cooled to the room temperature before the next pulse arrives (assuming the repetition frequency of laser pulses is 200 kHz). [107].

with a curvature radius of ≈ 25 nm. For an applied force of the tip acting in contact mode of 10 nN, the indentation depth δ results to be of the order of 0.5 nm while the $\Delta\delta$ (considering a ΔT below 6 K) is of few pm, from which a value of F_{t-s} of the order of 0.1 nN is obtained [107].
Due to the minute nature of photoexpansion in nanometer thick sample, the AFM-IR experiment are commonly conducted in mechanical resonant mode by matching the repetition frequency of laser pulses with the resonant frequency of the bending mode of the cantilever in contact with the sample, producing resonance enhanced signal amplification and leading to a significant increase in photothermal expansion sensitivity (Fig.4.11). This technical development leads to the overcoming of the use of high-energy optic pulses with the consequent excessive increase in temperature of the sample, in order to have a detectable photoexspansion signal [200].
The small oscillation amplitude $z(t)$ of the AFM cantilever in contact mode and in resonant excitation can be derived representing its motion by a damped harmonic oscillator equation

$$\frac{d^2z}{dt^2} + 2\zeta\omega_0\frac{dz}{dt} + \omega_0^2 z = \frac{f(t)}{m} \tag{4.7}$$

where $\zeta = \frac{1}{2Q}$ is the damping coefficient with Q being the quality factor of the mode, $\omega_0 = 2\pi f_0$ is the resonant angular frequency of the bending mode of the AFM cantilever in contact with sample, $m = \frac{k}{\omega_0^2}$ with k being the force constant of the cantilever and $f(t)$ is the applied external force. Since the sample heats up and cools down on a much shorter time scale (Fig.4.12 b) than the cantilever response time (typically 2–20 μm corresponding to the period of the modes [201]), the sample is cooled to the room temperature before the next pulse arrives and the force on the cantilever may be represented as a train of delta functions

$$f(t) = I_0 \sum_{n=0}^{+\infty} \delta(t - nT) \tag{4.8}$$

where the impulse from the absorption-induced mechanical force on the tip $I_0 = \int F_{t-s}dt$ can be estimated as $I_0 = F_{t-s}\tau$, with τ the duration of a laser pulse, while

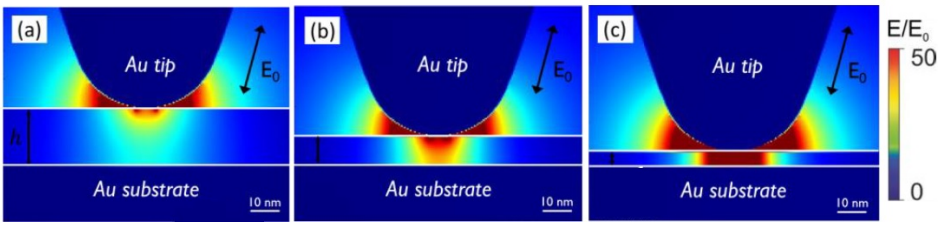

Figure 4.13. Simulated maps of electric field modulus E normalized by the electric field modulus of the incident beam E_0, for different sample thicknesses (20 nm, 10 nm, 5 nm).

$T = \frac{2\pi}{\omega_0}$ is the laser pulse repetition rate. Therefore, the solution of eq. 4.7 results to be

$$z(t) = \frac{1}{T}\frac{2QI_0}{k} sin(\omega_0 t) \tag{4.9}$$

Hence, the cantilever deflection amplitude results to be proportional to the absorption-induced mechanical force acting on the AFM tip F_{t-s}, which in turn is proportional to the sample thermal expansion $\Delta\delta$ induced by IR absorption (see eq.4.5). Finally, the IR absorption spectrum can thus be obtained tuning the emission wavelength λ of the QCL and recording the variation in the cantilever deflection $\Delta z(\lambda)$ through the four-quadrant photodiode during the thermal expansion, that is expected to follow the molecular absorption $\alpha_{abs}(\lambda)$ after normalization to the incident laser intensity $I(\lambda)$

$$\frac{\Delta z(\lambda)}{I(\lambda)} \propto \alpha_{abs}(\lambda) \tag{4.10}$$

In resonant enhanced mode the cantilever deflection signal from the photodetector is fed into a lock-in amplifier referenced by the QCL trigger signal (Fig.4.10a).
The spatial resolution of AFM-IR measurement is principally determined by thermal diffusion length in sample during laser pulse l_d, which can be estimated as

$$l_d \approx \sqrt{\frac{w\tau}{\rho C}} \tag{4.11}$$

where w is the thermal conductance,ρ the volume density, C the heat capacity of the sample and τ, again, the duration of the laser pulse. Since the illumination spot of the IR laser is much larger ($30\mu m$x$100\mu m$ in our experimental configuration) than the size of the tip ($\approx 25\ nm$), the thermal diffusion from the sample regions surrounding the area under the tip can limit the lateral resolution to hundreds of nanometres, that is a typical value of l_d for a polymeric sample [200]. It has been demonstrated that for nanometer-thick sample, a plasmonic nanogap configuration can improve the spatial resolution of AFM-IR experiments, as well as their sensitivity. This is achieved by employing a metallic-coated AFM tip and a metallic sample support, in order to get an electromagnetic enhancement of the optical field intensity in the sample region between the two metallic surfaces (Fig.4.13). The AFM tip effectively acts as resonant plasmonic antenna in the mid-IR and the metallic surface further enhanced the field localization as in a nanoparticle-on-mirror configuration. Hence, the local field intensity enhancement effectively increases the mid-IR absorption cross-section of molecules under the AFM tip and also improves the spatial resolution,

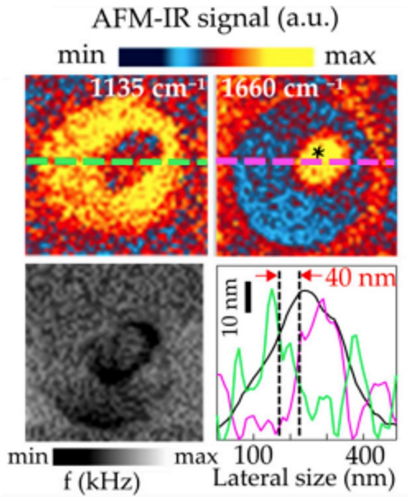

Figure 4.14. Top: AFM-IR maps acquired at 1135 cm^{-1} (left) and at 1660 cm^{-1} (right) on a single microvesicle. Bottom left: map of the mechanical resonance frequency *f*. Bottom right: line-scan profiles taken along the microvesicle in the topography map (black curve) and along the AFM-IR map acquired at 1135 cm^{-1} (green curve) and at 1660 cm^{-1} (violet curve) [126].

which results to be determined only by the dimensions of the hotspot under the AFM tip [107] where the temperature increase is much higher than the rest of the illuminated sample area (Fig.4.12 a).

As an example of the spatial resolution achievable in AFM-IR measurements, I report here illustrative results that we obtained in a study conducted on extracellular microvesicles [126]. The latter are lipid membrane-delimited structures that are involved in inter-cellular communication, transporting diverse biological material. When placed on solid metallic surface for AFM-IR analysis, individual microvesicles exhibit a maximum height of tens of nanometer. In Fig.4.14, AFM-IR maps obtained on a single microsvesicle produced by glial cells are shown. In this specific case, the microvesicle contains a protein cargo distinguishable both mechanically, evidenced by a lower cantilever resonance frequency (left bottom panel), and spectroscopically, as indicated by a strong absorption signal at 1660 cm^{-1} (right top panel) respect to the outer ring that instead is dominated by the acid nucleic signal at 1135 cm^{-1}(left top panel). The line-scan profiles depicted in the right bottom panel (green curve for the map at 1135 cm^{-1} and violet curve for the one at 1660 cm^{-1}) emphasize the achievement of a lateral resolution of 40 nm in our experiment for using IR photoexpansion spectroscopy.

The AFM-IR setup employed in the experiments of this thesis is the NanoIR2 platform by *Anasys Instruments* (today *Bruker*) equipped with the MIRcat-QT mid-IR EC-QCL produced by *Daylight Solutions*. It emits p-polarized light in the spectral range of 900–1800 cm^{-1} with 4 different chips. The emitted power of the laser can be adjusted using transmission metal-mesh filters in front of the QCL output and in the experiments it never exceeded the value of 100 mW. The repetition frequency of the emission and the pulse duration is chosen based on the mechanical properties of the AFM tip used. The laser beam is focused by a parabolic mirror

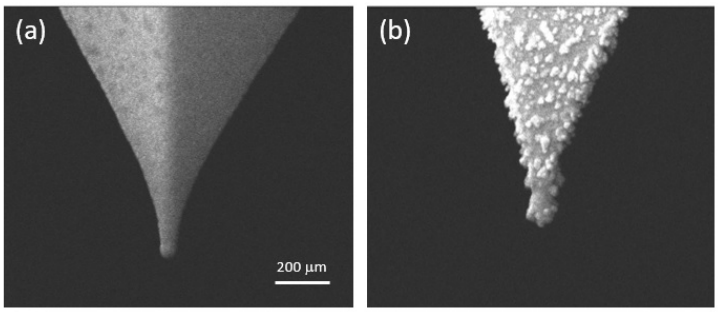

Figure 4.15. SEM images of the two different model of tip employed in AFM-IR experiments.

with a focal length of 75 mm and it impinges on the sample plane with an angle of incidence of about 70° relative to the surface normal, which gives a spot size of about 30 μm x 100 μm.
The commercial AFM tips used are of two different types:

- Contact mode NIR2 probes, model PR-EX-nIR2-10 by *Anasys-Bruker*: silicon bulk pyramidal probes with gold layer added by evaporation (Fig.4.15a). The curvature radius of the tip apex is about 30 *nm*, the cantilever free bending resonance frequency around 13 *kHz* and the spring constant in the range of 0.07-0.4 $\frac{N}{m}$
- Contact mode NT-IR-P-75 probes by *Next Tip*: silicon bulk with gold-ion nanocluster coating (Fig.4.15b). The curvature radius is < 8 *nm* and the cantilever resonance frequency of the free bending mode is 75 *kHz*.

4.3 Development of a new setup: integration of DC electric field control on AFM-IR

During my PhD thesis, a crucial step toward accomplishing the primary objective of the project involved customizing the NanoIR2 platform. The modification to the setup entailed the incorporation of a straightforward electrical circuit and electrical contacts for the metal-coated AFM tips and the metal sample support, already employed in our experiments for their significance in IR field enhancement on nanometer-thick samples. In analogy with a c-AFM setup, the circuit (Fig.4.16) is equipped with a low-noise current amplifier (*Femto* DHPCA-100) and a DC power source (*Keithley's Standard Series* 2400 SMU). To prevent abrupt high-frequency electrostatic discharges through the conductive tip, a low-pass filter is inserted and a bypass switch is used during the tip-to-sample approach. A 20 $M\Omega$ resistor serves to limit the current entering the amplifier in case of dielectric sample damage or inadvertent contact between the tip and the metallic substrate.
It is essential to reiterate that the primary aim of this thesis is to apply voltage to single cell membranes embedding photosensitive proteins to investigate the voltage-dependence of their functional conformational changes, simulating transmembrane

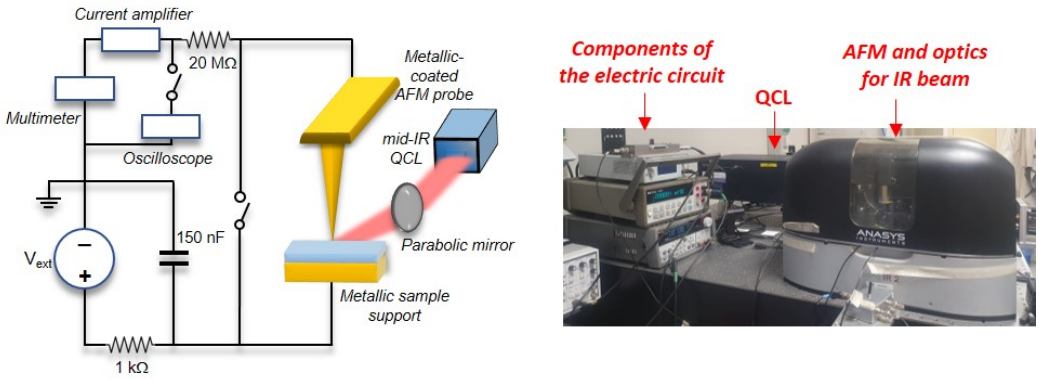

Figure 4.16. Schematic depiction and picture of the DC circuit integrated in the AFM-IR setup.

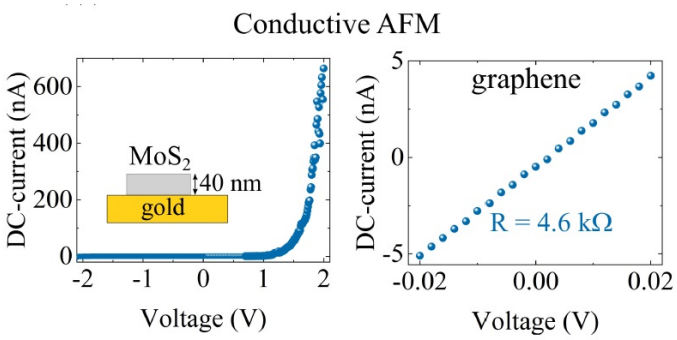

Figure 4.17. c-AFM I-V curves of a MoS_2 flake placed on a gold substrate (left panel) and of a graphene monolayer (right panel) obtained with our electrical circuit integrated in the AFM-IR setup [202].

voltage through a scanning probe approach. The results presented here for the experimental technique validation on template systems are based on polymeric samples with dielectric breakdown in the range of 5-10 $\frac{MV}{cm}$. Thus, conductive measurements are not the primary focus of this work. Nevertheless, the integrated circuit enables preliminary measurements of I-V curves to verify the circuit functionality and tip conductivity, as well as to monitor potential leakage currents during experiments. To show the effective functionality of the c-AFM component in our setup, I present in Figure 4.17 two example of I-V curves obtained using a solid-platinum probe from *Rocky Mountain Nanotechnology*. The first curve is acquired on a 40 nm-thick flake of semiconducting MoS_2 material, exfoliated onto a gold substrate serving as the counter electrode. Notably, a diode-like I-V dependence is observed, aligning with results in c-AFM literature [203]. The second I-V curve is measured on a single-layer graphene stripe deposited on a SiO_2/Si substrate, exhibiting ohmic behavior (R=4.6 kΩ) with a series resistance comprising intrinsic graphene, metal contact, scanning probe, and tip/graphene junction resistances.
Furthermore, the adaptability of the c-AFM circuit within the AFM-IR setup extends to various experimental investigations that merge mid-IR sample responses with electrical characterization. For instance, such applications involve investigating

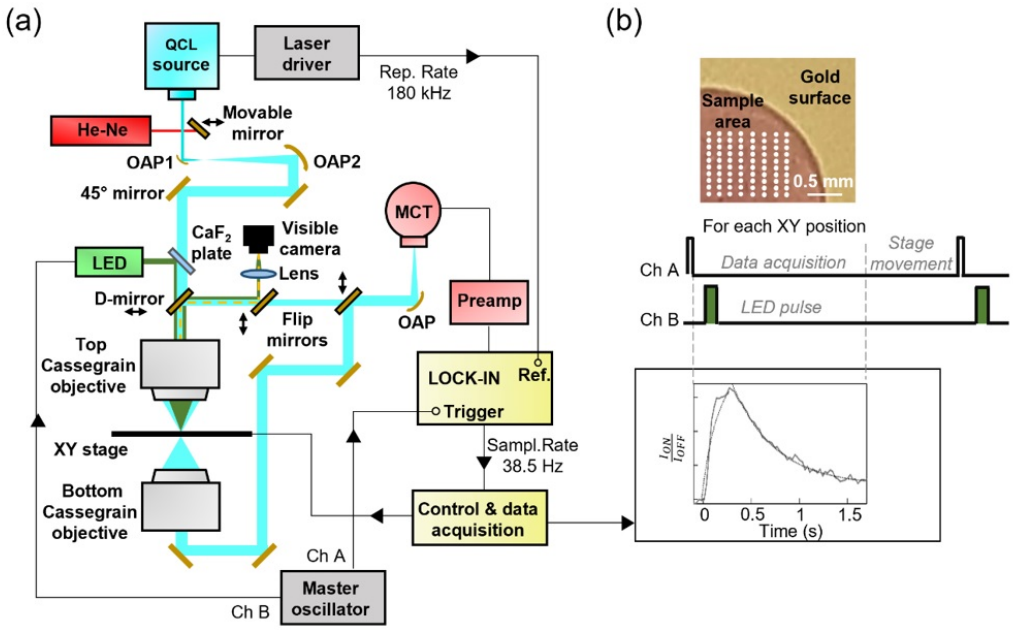

Figure 4.18. a) Schematic illustration of the QCL-microscope highlighting the principal optical elements and the hardware components for instrument control and data acquisition. b) Example of an experimental routine for the time-trace acquisition on a BR film with sample replacement at each photocycle. The XY mapping step chosen for dark-adapted sample replacement is 250 µm, and the number of steps is 80, corresponding to different locations on the sample drop [188].

photocurrents in the mid-IR range, as demonstrated in our work of ref.[202].

4.4 Home-built QCL-microscope

Up to this point, AFM-IR measurements have been limited to difference spectroscopy experiments in steady-state mode. This implies acquiring spectra under continuous external perturbation, e.g visible light or an electric field. However, it is both possible and interesting to conduct time-resolved experiments using the AFM-IR setup. This would allow for an in-depth exploration of protein kinetics on the millisecond timescale, a temporal range particularly relevant to applications of photosensitive proteins in the field of neuroscience [204]. Importantly, this timescale aligns with the bottleneck imposed by the mechanical detection capabilities of AFM-IR. In line with this perspective, as a side part of my PhD project, I have contributed to the development of a confocal laser microscope designed for mid-infrared operations with a tunable QCL source. The use of the QCL source indeed permits to reach the millisecond time scale resolution, serving as a potential benchmark for forthcoming time-resolved AFM-IR studies. Moreover, the microscope incorporates a co-aligned IR and visible illumination path, allowing the selective excitation with visible light from LEDs and probing of proteins specifically within the IR focus. This design ensures that the remaining portion of the protein sample remains in dark-adapted conditions until it is probed by the microscope beams. This distinctive feature

permits the acquisition of single time-traces at each sample position, enabling movement of the sample stage to adjacent areas without the need to wait for the time required for the recovery of the protein dark-state.
Figure 4.18 presents the schematic of the microscope that can operate both in reflection mode, with a single Cassegrain condenser/objective, and in transmission mode employing a second Cassegrain objective (a common type of reflection objective used in the IR and already introduced in sec.4.1.1). The QCL is an external cavity-tunable QCL (*Daylight Solutions*, model no. 41060), with tuning range 5.80-6.35 μm and peak output power < 300 mW. The IR radiation reflected or transmitted by the sample is detected pixel-by-pixel with a cryogen-free thermoelectric-cooled MCT detector (*Infrared Associates inc.*, model no. MCT-9-TE-1.00). The wavelength sensitivity of the detector is 11 to 5 μm, the response time is below 1 μm and the preamplifier bandwidth is 1 MHz. The use of a fast detector makes it possible to work with the repetition rate of the QCL ($\sim$100 kHz) as the reference of a lock-in amplifier (*Stanford Research corp*, model no. SR830), allowing the use of very short laser pulses, for which an external cooling of the mid-IR source is not necessary and sample heating is reduced to minimum. A master oscillator (*Quantum Composer inc.* model no. 9420) triggers the data acquisition from the lock-in amplifier with a computer and drives the LED pulses thanks to a specific driver (Thorlabs, model no. DC2200). The data acquisition software written in Python moves the piezo-driven XY stage (*Physik Instrumente*, model no. PI M-687.UO) by pre-defined X and Y steps (200 μm in the example of Fig.4.18b) after each time trace acquisition from the lock-in amplifier. An exemplificative scheme of the routine for the data acquisition in different regions of the sample (white dots in the visible image) is reported in Fig.4.18b.
Figure 4.19 shows images of the microscope taken from the three viewing angles indicated in the schematic drawing of Fig.4.19a, with the different optical paths highlighted in different colors. The mid-IR path (light blue color) starts from the QCL output port with a 3 mm diameter parallel beam (M^2 factor provided by the manufacturer is 1.2 and <5 $mrad$ of beam divergence) (Fig. 4.19b). A Gaussian beam expander made by two 90° off-axis parabolic mirrors (OAP1 and OAP2), with focal lengths of 25 and 100 mm respectively, expands the QCL beam diameter to 12 mm, a value that matches the entrance aperture diameter of the infinity corrected Cassegrain microscope objectives with NA=0.4 (*Beck Optronic Solutions*, model no. 5002), visible in Fig.4.19c. A He-Ne laser (*Melles Griot*, model no. 05-LHP-911) emitting in the red with beam diameter of 3 mm is co-aligned with the QCL beam through an input turret (see red color beam in Fig.4.19d). It is used for alignment of the beam expander, of the objectives and of the sample focal plane, also exploiting a visible CMOS camera installed in the reflection path (*Thorlabs*, model no. DCU224C, yellow color beam in Fig. 4.19b). Fig.4.19c displays the sample stage with the two objectives mounted along a vertical optical axis, defined through a large 45° plane mirror (50 mm diameter) with easy-to-access alignment knobs. The MCT detector is installed on the optical table and reached with a second 45° mirror followed by a last adjustable parabolic mirror (not visible in the pictures of Fig.4.19). For operation in reflection mode, a D-shaped half mirror is positioned by a manual stage after the 45° mirror and above the illumination objective. The output mid-IR beam reflected by the D-mirror is sent down to the optical table to the same detector (see Fig.4.19b) by

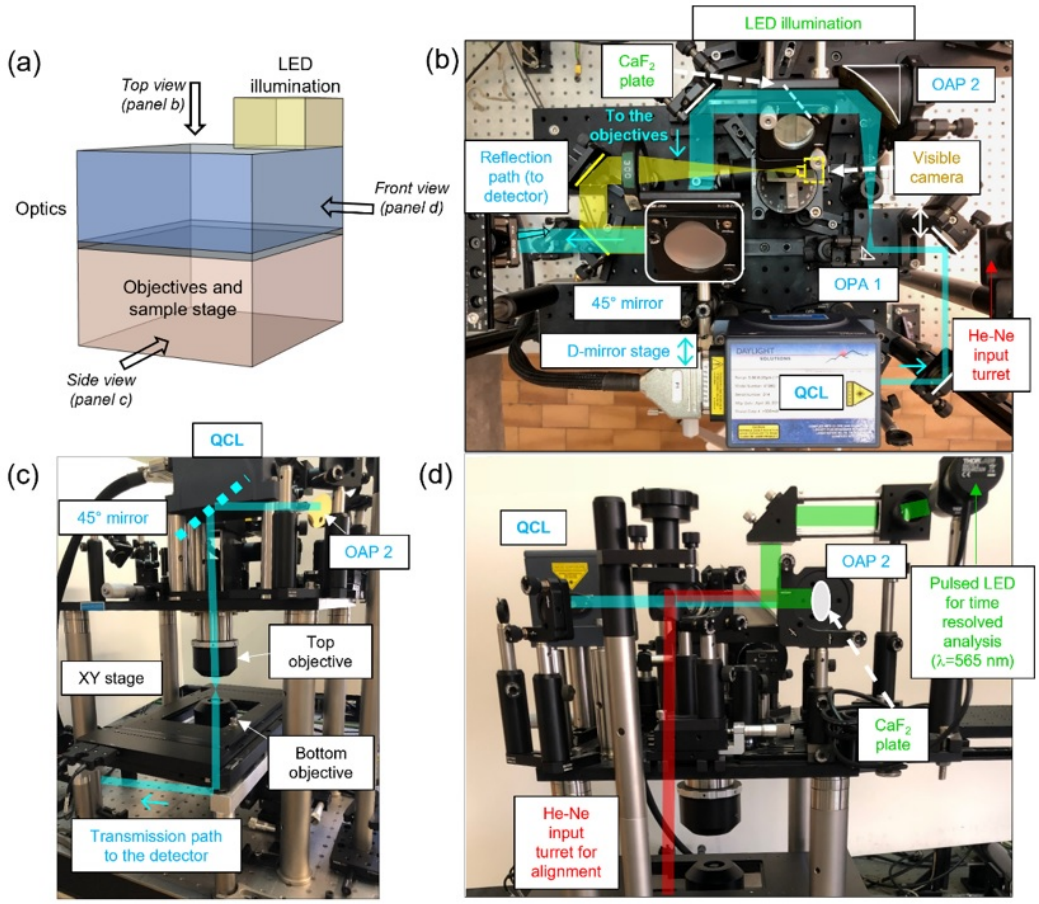

Figure 4.19. a) Schematic representation of the three main sections of the microscope and pictures of b) the top view, c) the side view, and d) the front view. The different optical paths are represented with different colors: QCL beam in light blue, visible CMOS camera path in yellow, alignment He–Ne beam in red, and exciting LED beam in green [188].

displacing the flip-mirror previously used for alignment with the CMOS camera. For operation in transmission mode, a second identical Cassegrain objective positioned below the XY piezo stage is precisely co-aligned to ensure confocality using the He-Ne beam and a second CMOS camera. The objectives feature a large working distance of 20 mm useful for complicated sample mounts (microfluidics, cryogenic, etc.). The total free space between the objectives in transmission mode is 40 mm. The visible LED illumination channel use the same top Cassegraing objective (green color beam in Fig.4.19d) and the collimation of the LED lens telescope is adjusted to make the LED and mid-IR foci to perfectly overlap on the sample surface. The aluminum-coated reflective objectives provide a fully achromatic focusing behavior in the mid-IR and visible ranges, allowing one to choose the illumination wavelength in the entire LED availability range from violet to near-IR (Thorlabs MxxxLx series, output power around 250 mW), according to the specific protein under study. Multi-color illumination can also be implemented with dichroic filters mounted in a filter

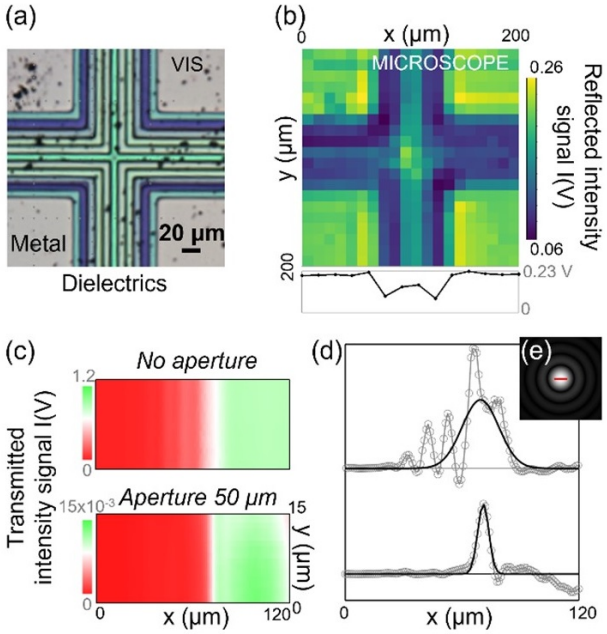

Figure 4.20. a) Visible image of a lithographic target employed for the spatial resolution test and b) mid-IR image in reflection mode with a D-mirror at $\lambda = 6.08\ \mu m$ of the same target. The pixel size is $10{\times}10\ \mu m^2$. The different resolution in the x and y directions is due to the use of a D-mirror. c) Experimental maps of a gold/silicon lithographic edge acquired in transmission mode without an aperture (top) and with a 50 μm aperture at the detector position (bottom). The step size is 1 μm. d) Numerical differentiation of the data in c) averaged along the y-direction (dotted grey curves) and Gaussian fitting curve (black curve). e) Image of the Airy disk in which the dimension of the FWHM used for the lateral resolution estimation is highlighted (red line)[188].

box. The LED illumination is passed into a lens telescope equipped with an iris pupil that produces an approximately collimated beam of 10 mm diameter, and sent to a 1-mm thick CaF_2 plate that works as dichroic beam combiner for mid-IR and LED beams (see Fig.4.19b and d). The CaF_2 plate transmits 96% of the mid-IR power and reflects 4% of the visible illumination power, i.e. around 10 mW. Note that in reflection mode the LED illumination power is halved by the presence of the D-mirror just like the IR probe power, but the LED current can be adjusted to provide double illumination power.
For the median QCL wavelength $\lambda = 6.08\mu m$ and almost ideal QCL M^2 factor of 1.2, we can expect the mid-IR spot size in transmission mode to be an Airy disk with diameter

$$D = 1.22\frac{\lambda}{NA} = 18.5\mu m \tag{4.12}$$

given by diffraction theory. The theoretical lateral resolution limit obtained with the Abbe's formula is

$$\Delta x = 0.5\frac{\lambda}{NA} = 7.5\mu m \tag{4.13}$$

To quantitatively evaluate the laser spot size in the focal plane and demonstrate the confocality of our microscope, IR transmission maps were taken across the edge

of a fully gold-coated patch defined by electron-beam lithography (edge sharpness <100 nm) on a silicon wafer. They are reported in Fig.4.20c, acquired, respectively, without any aperture and with an aperture of 50 μm in the focal plane of the MCT detector. The sensitive element of the detector is 1×1 mm^2 so it cannot enforce confocality without a pinhole aperture. The maps have a 120×15 μm^2 dimension and a step-size of 1 μm. To compare the lateral resolution of the microscope in the two configurations, we averaged the signal acquired along the x-direction over the 15 rows to increase the signal-to-noise ratio. We then calculated the first derivative of the x-scan signal (dotted grey curves in Fig.4.20 d), and we did a Gaussian fit (black curve in Fig.4.20d). The lateral resolution was thus estimated as the FWHM of the Gaussian fit, obtaining a value of 22 μm in the absence of any aperture and an improved value of 6.6 μm ($\sim$1.1λ) by adding the 50 μm aperture at the detector position. Fig. 4.20 e represents the theoretical intensity pattern due to diffraction from a circular aperture (Airy disk and rings), where we approximately indicate with a red arrow the definition of lateral resolution, i.e., the FWHM of the central disk estimated from a Gaussian fit. The experimental value of 6.6 μm compares well with the Abbe formula calculation (7.6 μm), with the small discrepancy probably due to the exclusion of the negative feature at x = 75 μm in Fig. 4.20 d from the fitting range. In Fig.4.20 a-b, we report also the imaging in reflection mode of a cross-shaped lithographic pattern on a silicon substrate filled with evaporated gold and dielectric materials. The chosen pixel size of 10×10 μm^2, comparable to the employed wavelength of 6.08 μm, evidences the good imaging and material contrast capabilities of our microscope: different materials provide different reflectance values, although the feature size is sometimes smaller than the wavelength. One can note that the spatial resolution along the y-direction is lower than that along the x-direction. This asymmetric behavior is due to the elongated spot size of the IR beam caused by the presence of the D mirror in the reflectance measurements.

Chapter 5

Conformational changes of Channelrhodopsin at the nanoscale

As outlined in Chapter 2 sec.2.5, in 2019 my research group demonstrated the applicability of the AFM-IR technique for studying conformational changes of photosensitive proteins. The experiments focused on the prototype BR protein and achieved the sensitivity limit of difference spectroscopy measurements in a double cell membrane configuration, as detailed in ref.[20]. Building upon this experimental progress, the initial phase of my PhD project involved conducting similar experiments on ChR2 samples. ChR2 is a crucial photosensitive protein widely recognized as a valuable optogenetic tool, and therefore understanding the specific mechanisms governing its functionality is of paramount importance for its practical applications. In addition to the objective of minimizing the number of probed proteins to emulate a more physiological configuration in the IR measurements involving a single lipid membrane embedding the protein, it is important to recognize that optogenetic setups inherently necessitate a close proximity between the cell membrane and miniaturized probes and electrodes. In various in vivo optogenetic techniques, metal electrodes or metal-coated optical fibers are indeed frequently brought into direct contact with the cell membrane. This raises a biophysical question regarding the potential impact of metal surfaces on the functions of photosensitive proteins. Investigating whether such metal-protein interactions influence the functionality of photosensitive proteins adds an additional layer of complexity to the understanding of optogenetic mechanisms but it is crucial for optimizing and advancing the field. Our experimental AFM-IR setup, utilizing the metal-coated AFM tip and metal surfaces sandwiching the cell membranes, stands as a valuable tool to address several pertinent aspects and questions related to the close interaction between proteins and metal components in optogenetic setups.

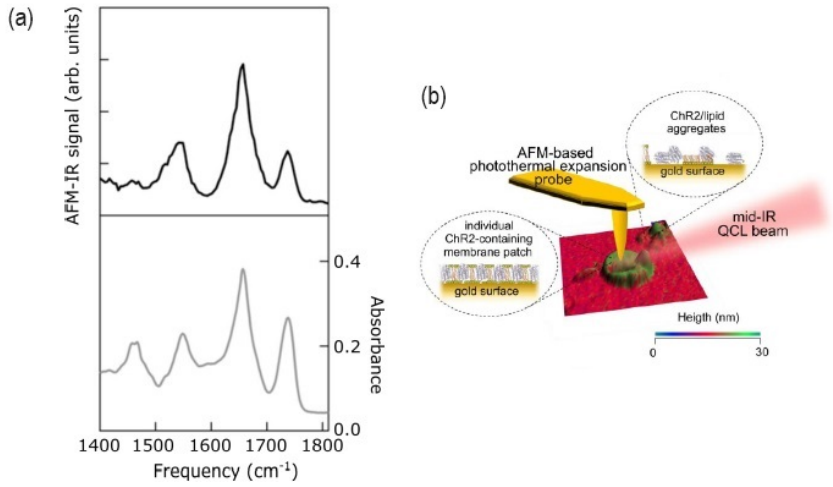

Figure 5.1. a)AFM-IR (black curve) and micro-FTIR (grey) absorption spectra of ChR2 C128S sample deposited on a ultraflat gold surface. They are obtained on 150 nm-thick and more than 1 μm-thick sample area, respectively (adapted from [21]). b) Sketch of the AFM-IR setup suitable for the identification of homogeneous individual lipid membranes.

5.1 Nanospectroscopy and nanoimaging of single cell membrane patches

The sample employed in the experiment consists of artificial reconstructed lipid membranes containing the slow mutant C128S of ChR2. The rhodopsin proteins have been expressed in COS cells and the mutations were generated by site-directed mutagenesis [205]. After the mutations, the rhodopsins were purified and incubated in a buffer solution (20 mM BTP, 130 mM NaCl, 1 mM MgCl2) containing L-α-Phosphatidylcholine (*Avanti Polar Lipids, Inc., Alabaster, AL*) with a molar concentration of 3 $\frac{mg}{ml}$. The molar ratio of lipid:protein is around 100:1 [206]. The sample stored in a buffer solution with pH=7.8 is dropcast onto 1 cm $\times$ 1 cm template-stripped gold chips (*Platypus Technologies*, 0.3 nm rms roughness) and let dry in air. After 10 minutes, the samples is rinsed with milli-Q water and subsequently dried for 1 h in an atmosphere with humidity below 10%. This procedure promotes the deposition of isolated lipid membrane patches and ensures the elimination of crystallized salts that may form on the solid surface during the drying process.

As a first result I show a representative AFM-IR spectrum (black curve in Fig.5.1a) acquired on a 150 nm-thick area of the ChR2 C128S sample, corresponding to a stack of overlapped lipid membranes. For all the measurements of this experiment a silicon bulk AFM tip with a gold coating (NIR2 by *Anasys-Bruker*) is employed and the QCL source provides 260 nm long light pulses at a repetition rate chosen as to be in resonance with the second mechanical bending mode frequency of the cantilever ($\sim$ 200 kHz). The resolution of the spectra is of 4 cm^{-1}, with $\sim$0.3 s per step subdivided in integration time and tuning time. The comparison with a micro-FTIR spectrum (grey curve in Fig.5.1a), acquired on an area of the same

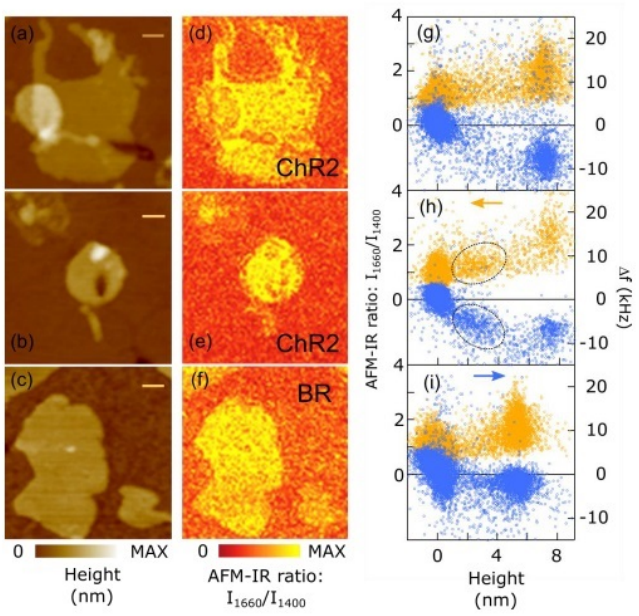

Figure 5.2. a-c) Representative AFM topography maps of lipid membranes containing either ChR2 or BR proteins. The scale bar is 100 nm. d-f) Corresponding AFM-IR ratio maps $\frac{I_{1660}}{I_{1400}}$ obtained by dividing the map acquired at 1660 cm^{-1} by the map acquired at 1400 cm^{-1}. g-i) Scatter plot of $\frac{I_{1660}}{I_{1400}}$ (yellow dots) and $\Delta f = f - f_{Au}$ (blue dots) as a function of topographic height, calculated from the corresponding topography and AFM-IR maps in panels a-f. The height range has been restricted to the (-2 nm, +9 nm) range to better highlight the differences between individual membrane patches containing either ChR2 or BR [21].

sample, displays a good agreement between the results obtained with the two techniques. The micro-FTIR experiments are performed at the synchrotron radiation source BESSY II of Helmoltz-Zentrum Berlin, employing an internal IR source of a gas-purged Nicolet Continuum Infrared Microscope with a MCT detector, a 32× Cassegrain reflective objective with spherical aberration compensation and a knife-edge aperture of $100\mu m \times 200\mu m$. Both the micro-FTIR and the AFM-IR spectra show bands attributed to main vibrational modes of protein peptide bond, that are the C=O stretching at 1660 cm^{-1} (amide I) and the in-plane NH bending at 1550 cm^{-1} (amide II) [82]. The bands at 1450 cm^{-1} and 1740 cm^{-1} are associated with the lipid environment, respectively due to the CH_2 bending of hydrocarbon chains and C=O stretching of ester carbonyl groups [207]. In the micro-FTIR spectrum an absorption band at 1590 cm^{-1} is also present and it appears in the majority of the micro-FTIR spectra acquired on different areas of the sample. It can be attributed to a vibrational mode of nanocrystals, visible in the optical microscope, formed during evaporation of the buffer solution. The locality of the AFM-IR technique (see the sketch in Fig.5.1b) enables to acquire the spectrum far from the nanocrystals so as to avoid this unwanted contribution in the AFM-IR spectra and to identify the isolated patches, as in the case of Fig.5.2a where a membrane patch of around 7 nm of thickness is shown, while on the left-hand side there is an overlap of two and even three patches (thickness around 14 nm and 21 nm, respectively). Artificial

cell membranes incorporating ChR2 often display aggregates of lipid matrix or unfolded proteins with a random orientation, as depicted in the top-left corner of Fig. 5.2b. This is notably in contrast to the situation observed in the BR sample, where purple membrane patches exhibit greater stability. Consequently, it is easier to identify individual and well-ordered structures, as illustrated in the topography of Fig. 5.2c. The utilization of AFM nanoimaging and, moreover, the acquisition of AFM-IR maps plays an important contribution in delving into the uniformity of mechanical and spectroscopic properties within lipid membranes. Specifically, AFM-IR maps are obtained at 1660 cm^{-1}, corresponding to the peak of the amide I band. These maps are then normalized by the AFM-IR maps acquired in the same area but at a different frequency (in this case, 1400 cm^{-1}), which does not align with any IR absorption of the sample. This normalization step effectively eliminates background interference arising from the thermal expansion of the gold tip and substrate. In Fig.5.2d-f, the AFM-IR nanoimaging maps obtained as the intensity ratio $\frac{I_{1660}}{I_{1400}}$ are reported displaying the homogeneity of the membrane patches in terms of protein embedding. Furthermore, during AFM-IR nanoimaging, mechanical properties such as local stiffness for each pixel can be extracted by assessing the frequency f of the mechanical resonance of the AFM cantilever in contact-mode with the sample [208]. For a more expeditious interpretation, scatter plots in Fig.5.2g-i illustrate the normalized AFM-IR signal $\frac{I_{1660}}{I_{1400}}$ (depicted by yellow dots) and the frequency variation $\Delta f = f - f_{Au}$ (depicted by blue dots), where f_{Au} represents the frequency of the contact resonance on the bare ultraflat gold surface. These scatter plots are presented as a function of topographic height from the mean gold surface height, revealing a pixel distribution divided into two distinct clusters discernible in both the $\frac{I_{1660}}{I_{1400}}$ and Δf plots. In each plot, one cluster is centered at a height value of 0 nm, representing the bare ultraflat gold surface, while a second cluster is centered at a height value of 7 nm for the ChR2 samples (Fig.5.2g-h) and 5 nm for the BR sample (Fig.5.2i), indicative of the single membrane patch. Comparing the Δf clusters in the scatter plots for ChR2 with those of BR reveals that the mean Δf is approximately 7 kHz for ChR2 membranes and around 2 kHz for BR membranes. Given the consistent use of the same AFM probe and gold support across all measurements, the disparity in the mean value of Δf suggests that ChR2 patches exhibit significantly lower stiffness compared to BR patches. This could be ascribed to the lower protein-to-lipid ratio as compared to BR samples, due to the higher Young modulus of proteins than lipids. Indeed the quantity f can be used to evaluate the photothermal expansion force F_{t-s} from the AFM-IR signal amplitude, using the formulas reported in eq.4.5 and 4.7, and then the Young modulus E*. Notably, in Fig.5.2h, there is a third cluster (within the dashed ellipse region), corresponding to the top-left corner of Fig.5.2b. The lower values in both IR signal and Δf in this cluster suggest the concurrent presence on the gold surface of membranes and non-membrane aggregates comprising unoriented proteins and/or lipids. This careful investigation and selection of homogeneous region of the sample ensures that subsequent investigations into the light-induced activity of ChR are conducted in regions free from ambiguities, thereby preventing any confounding factors in the analysis of the experimental IR data.

In Fig.5.3a some AFM-IR spectra acquired on different thicknesses of the C128S sample (see topography in Fig.5.3b) are shown and compared with the spectrum

acquired on a single BR lipid membrane (see topography in Fig.5.3c). The spectra have been normalized using the AFM-IR spectrum obtained on the bare ultraflat gold surface, known to generate a non-zero background signal due to the expansion of the gold-coated AFM tip and the gold surface. When normalized to the amide I peak, a reduction in the intensity of the amide II is observed at the positions corresponding to the three (blue), double (violet), and single membrane (red) compared to the 150 nm-thick area (black). To interpret this observation, electromagnetic simulations conducted with the finite-difference time-domain method (FDTD) at the frequency of the amide II band are also reported. The comparison of the electric field modulus (E_{tot}) and the electric field component in the vertical direction (E_z) (Fig.5.3d-e) reveals a predominantly vertical (z-oriented) electric field orientation in films with a thickness up to 21 nm. This outcome aligns with expectations, considering that the QCL beam is p-polarized and impinges on the tip plane from the side at an angle of 70° relative to the surface normal. In this context, an almost complete vertical orientation of ChR2 molecules in the single membrane patches and ordered stacks can be considered, as the N-H bending mode is nearly perpendicular to the protein axis. Consequently, it is less efficiently excited in this configuration, as illustrated in the schematic on the right panel of Fig.5.3. The electromagnetic simulations also enable an estimation of the number of proteins contributing to the AFM-IR signal. In the presence of strong field enhancement in the tip-surface nanogap, as illustrated in the case of a single membrane in Fig. 5.3d, the sample volume contributing to the AFM-IR signal corresponds to the region beneath the tip apex. This region forms a cylinder with a radius equal to the AFM tip radius (here, 25 nm as confirmed by scanning electron microscopy characterization) and a thickness of 7 nm. For a protein:lipid ratio of 1:100 and an approximate surface extension (in the plane of the membrane) of an individual ChR monomer and lipid of 6 nm^2 and 0.5 nm^2, respectively, one can estimate that in the probed area of $\pi(25nm)^2 \sim 2000nm^2$ there are approximately 64 ChR proteins and 6400 lipids.

5.2 Difference spectroscopy results

For the implementation of AFM-IR difference nanospectroscopy experiments, a visible illumination system has been built to control the protein photocycle. In the case of ChR2 C128S, two LEDs are employed: a blue LED (Thorlabs M470L3, 470 nm) for the photoactivation of the protein photocycle, and a green LED (M505L3, 505 nm) for restoring the dark state. The output beams of the LEDs are made collinear through the use of lenses and a dichroic filter (Thorlabs - MD498) before being focused onto the sample (Fig. 5.4a). The power density of both LEDs is approximately $\sim 10\ \frac{mW}{cm^2}$. The alternating wavelengths effectively enable an on-off switching of the photocycle, a feature previously demonstrated by photocurrent measurements discussed in Chapter 1, sec. 1.8. The procedure for acquiring difference spectra involves measuring a spectrum under blue illumination, denoted as $A_{blue}(\nu)$, followed by a consecutive measurement under green illumination, denoted as $A_{green}(\nu)$. Each spectrum is acquired over a duration of approximately 30 seconds. The difference spectrum, $\Delta A(\nu) = A_{blue}(\nu) - A_{green}(\nu)$, is then directly

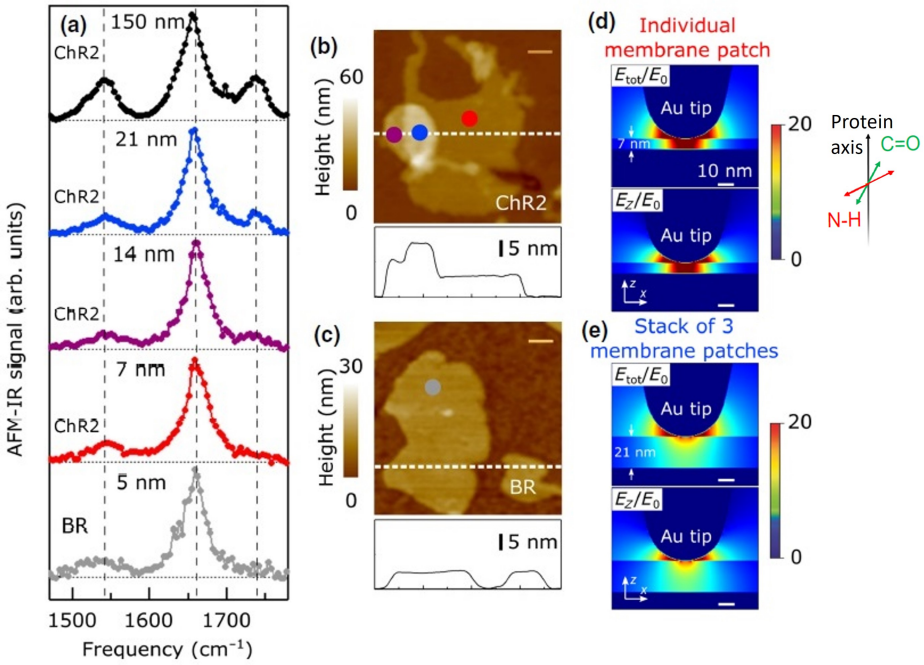

Figure 5.3. a)AFM-IR spectra obtained at different locations of the ChR2 sample and one comparative AFM-IR spectra acquired on a single BR lipid membrane. b-c) AFM topography maps and line profiles of isolated lipid membrane containing either ChR2 or BR. The colored dots indicate the positions at which the AFM-IR spectra have been acquired. The scale bar is 100 nm. d-e) Simulated maps of electric field modulus E_{tot} (top panels) and electric field z component normal to the gold surface E_z (bottom panels) normalized by the electric field modulus of the incident beam E_0, for an individual ChR2 membrane patch and a stack of three lipid membrane patches, respectively. Adapted from [21].

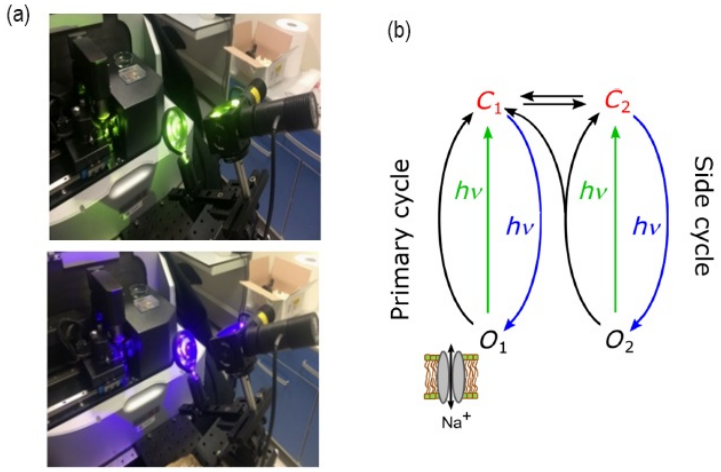

Figure 5.4. a) Visible illumination system comprising the two LEDs at 505 nm (top panel) and 470 nm (bottom panel), the dichroic filter and the lenses. b)Four-state photocycle model which consists of a primary cycle (dark closed state C_1 and open conductive state O_1 for Na+ ions) and a side cycle (dark closed state C_2 and open conductive state O_2) [21].

calculated and averaged over 15 repeated measurements. Micro-FTIR spectra have also been acquired on areas with an estimated thick of $\sim 1\mu m$ as a benchmark for AFM-IR data. In this case, the micro-FTIR difference-spectra are calculated as $\Delta A = A_{blue} - A_{green} = log(\frac{R_{green}}{R_{blue}})$ and averaged over 15 repetitions. R_{blue} and R_{green} are the reflection spectra obtained under the visible light illumination provided by the same system as used for the AFM-IR experiments. The spectrum acquisition under steady-state visible illumination lasts around 22 seconds and the spectral resolution is of 4 cm^{-1}.

Concerning steady-state measurements, it is essential to note that the unbranched photocycle, as illustrated in Fig. 1.9 and suitable for describing a single-turnover transition starting from the dark-adapted protein, is inadequate for continuous illumination of ChR2 [205, 209]. Under continuous illumination, a branching reaction occurs, leading to either a 13-*cis*, C=N-*anti* or a 13-*cis*,C=N-*syn* retinal conformation. In the case of 13-*cis*, C=N-*anti*, the photocycle involves sequential H^+ and Na^+ conductance in a late M-like state and an N-like open-channel state, representing the primary cycle. On the other hand, the 13-*cis*,C=N-*syn* isomer corresponds to a second closed-channel state identical to the long-lived P480 state. The P480 state has previously been assigned to a late intermediate in a single-photocycle model. Light excitation of P_{480} induces a parallel (side) *syn*-photocycle characterized by an open-channel state with small conductance and high proton selectivity. Hence, in Fig. 5.4b, a simplified representation of the proposed parallel two-cycle model is presented. This model includes two closed states (C_1 and C_2) and two open states (O_1 and O_2), which exhibit distinct population characteristics in the dark state and under repetitive or continuous illumination. This distinction is crucial for the subsequent interpretation of the AFM-IR results reported below.

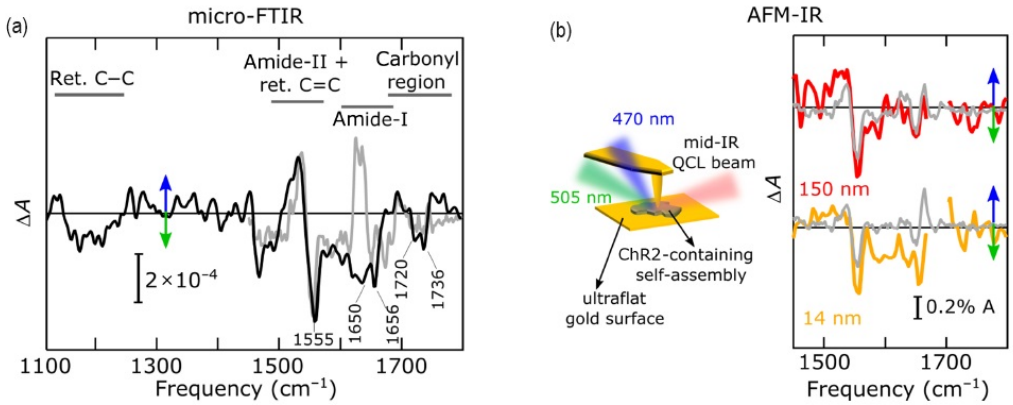

Figure 5.5. a) Micro-FTIR ΔA (black curve) obtained on a micrometer-thick area of a ChR2 sample deposited on an ultraflat gold surface and the corresponding fitting curve (grey curve). b) AFM-IR ΔA obtained on 150-nm-thick (red curve) and 14-nm-thick (yellow curve) areas of ChR2 deposited on the same gold surface, and the corresponding best fit curves. Adapted from [21].

Figure 5.5 presents the AFM-IR difference spectra acquired from a ChR2 sample with thicknesses of 150 nm and 14 nm (Fig.5.5b). These spectra are compared with the micro-FTIR difference spectrum (depicted by the black curve in Fig.5.5a) obtained from a distinct region of the same gold support. In this region, the protein assembly thickness exceeds 1 μm, and therefore not less than 10^7 proteins are probed. It is worth noting that the AFM-IR measurements are conducted on two-membrane patches (with a thickness of 14 nm) instead of monolayers. This choice is motivated by the observed physical degradation of the sample after prolonged contact-mode AFM measurements on 7 nm-thick single membrane patches. Note that the missing data in AFM-IR curves (Fig.5.5b) in the frequency region between 1670 and 1700 cm^{-1} are due to the chip transition and low emitting power of the QCL source. The ability to investigate light-induced conformational changes in ChR2 using AFM-IR is substantiated by the strong agreement observed between the micro-FTIR and AFM-IR results. Notably, the key spectral features are largely consistent, as the distinctive C=C retinal stretching vibration peak (around 1555 cm^{-1}) and the two negative peaks in the carbonyl region at approximately 1720 cm^{-1} and 1736 cm^{-1}. In accordance with the model illustrated in Fig.5.5b, the positive bands in our experimental difference spectra ΔA predominantly represent vibrational signatures arising from a combination of the open states O_1 and O_2, which are achieved under blue illumination. Conversely, the negative bands can be attributed to vibrations associated with a combination of the closed states C_1 and C_2, obtained under green illumination. The micro-FTIR ΔA spectrum shows spectral features that can be associated with both the primary and the side cycle, if compared to the FTIR results of ref.[209].

To assess whether any effects or alterations occur in the photocycle process when the proteins are investigated in the AFM-IR configuration, a comparative analysis is conducted on the micro-FTIR and AFM-IR ΔA spectra obtained from assemblies of varying thicknesses: micrometer-thick, 150-nm-thick, and 14-nm-thick. To facilitate this comparison, conventional FTIR serves as the reference for ΔA spectra. Specif-

ically, these reference spectra are time-dependent sets obtained from absorbance spectra recorded on the same sample in a liquid cuvette. The time resolution is set at 200 ms during alternating illumination with two different wavelengths for 5 seconds each. The difference spectra are then calculated by subtracting a reference spectrum that represents the state before the start of the illumination protocol. However, the corresponding kinetics exhibit a complex behavior due to the strong overlap of several parallel processes. To discern independent components contributing to the time-dependent spectral dataset, a combination of singular value decomposition and a rotation procedure is employed [210]. This approach enables the isolation of spectral contributions and the extraction of the pure kinetics of three independent processes, as illustrated in Fig. 5.6. In the first component (Fig.5.6a) distinct bands in the amide I and amide II region appear mainly reflecting adjustment of residues along the protein backbone, i.e., the helices. Bands indicative of changes in the retinal geometry are broadened and present double peaks (1247 and 1237 cm^{-1}, 1202 and 1186 cm^{-1}), similarly to those seen in the photostationary state [205]. This difference absorbance component, labeled as ΔA_{helix}, appears within seconds and remains unchanged under alternation of visible illuminations (Fig.5.6b). The small increase is due to a weak variation in time of the absorption baseline. The second component (Fig.5.6c) shows a band around 1800 cm^{-1} in the region sensitive to retinal alterations and at a frequency associated to the side cycle of the protein [205]. Indeed, its kinetic (Fig.5.6d) suggests that it is formed in parallel with the first one, since it also appears within seconds, but then it immediately starts to decay with a decay time of 65 s. This decay time is in agreement with the kinetic of the formation of a side cycle, and we therefore use $\Delta A_{sidecyc}$ to refer to this difference spectral component. In the third component (Fig.5.6e), the dominating feature is in the region around 1550 cm^{-1} caused by the Schiff base. In the fingerprint region characteristic for retinal C-C stretching vibrations, a distinct pattern of bands also appears showing close similarities with the bands that indicate all-*trans*/13-*cis* isomerization in the spectra of Schiff base protonated. Most importantly, the kinetic of this component is the only one that showed a time-dependent behavior strictly following the alternating blue and green illuminations (Fig.5.6f). It can therefore be identified with the transition between the blue-absorbing conducting state and the green-absorbing non conducting state, corresponding to the cyclic process of the opening and closing of the internal transmembrane gate [211]. This difference spectrum is then identified as ΔA_{gate}.

To discern the varying contributions of the identified spectral components in the data obtained with both micro-FTIR and AFM-IR, we proceeded to fit the following expression of the difference absorbance ΔA to the acquired datasets::

$$\Delta A = c_{helix}\Delta A_{helix} + c_{sidecyc}\Delta A_{sidecyc} + c_{gate}\Delta A_{gate} \tag{5.1}$$

where c_{helix}, $c_{sidecyc}$ and c_{gate} are the best-fit linear combination coefficients. The obtained fitting curves are reported in grey and superimposed to the data in Fig.5.5. Firstly, a good agreement is evident between the experimental and fitting curves. The main difference being the positive band at around 1640 cm^{-1} presents only in the fitting curves may be ascribed to the different hydration levels in the time-resolved FTIR experiments in a liquid cell respect to the micro-FTIR and AFM-IR experiments with the sample drop-cast on a metal surface and dried in air. The

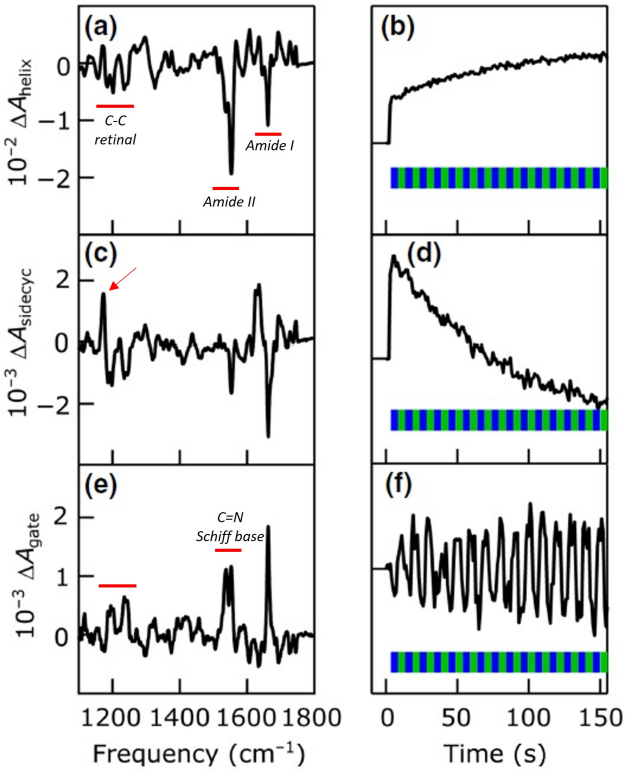

Figure 5.6. a,c) and e) Base spectral components and b),d) and f) the relative kinetics of the three independent ΔA spectral contributions characterizing the time-resolved FTIR data of C128S during alternating blue and green illuminations. Adapted from [21].

Data and sample thickness	c_{helix}	$c_{sidecyc}$	c_{gate}
micro-FTIR d>1 μm	0.017	0.15	0.33
AFM-IR d=150 nm	0.022	0.07	0.30
AFM-IR d=14 nm	0.022	0.03	0.28

Table 5.1. Values of the best-fit linear combination coefficients c_{helix}, $c_{sidecyc}$ and c_{gate} obtained for the micro-FTIR and AFM-IR data on sample areas with different thickness d.

coefficients c for the different curves and thicknesses d of the sample are detailed in table 5.1. The obtained values reveal a consistent weight for ΔA_{helix} and ΔA_{gate} across the three curves. This suggests that the AFM-IR investigation does not induce alterations in the opening/closing process of the gate and the conformational changes in the protein backbone, confirming the proper light-induced functional activation of ChR2. Conversely, a significant reduction in $c_{sidecyc}$ is observed as the sample thickness d decreases. Given that micro-FTIR and AFM-IR samples are in the same form, including protein hydration, the primary effect of decreasing sample thickness is an increase in the number of probed proteins in contact with the gold substrate and the AFM tip. This leads to the hypothesis of a reduction in the probability of entering the parasitic side cycle for proteins in close proximity to gold surfaces. The reason for this phenomenon, however, is unclear. From the plasmonic point of view, the main impact in the mid-IR range is the enhancement of the field intensity. Plasmonic effects leading to heat generation, arising from gold absorption, can be safely neglected since the temperature increase is expected to be very low, as also supported by thermal simulations previously conducted on BR samples [20]. Additionally, plasmonic-assisted charge transfer can be ruled out at IR frequencies, given the low photon energy involved. The hypothesis of a strong interaction, known to induce a redistribution of spectral weight in the molecular vibrational spectrum [212], can also be excluded due to the significant losses in the plasmonic cavity [106]. This places the system outside the conditions of strong light-matter coupling, although marginally. In conclusion, a potential mechanism contributing to the decrease in the side cycle probability with decreasing thickness of the self-assemblies could be an alteration of the membrane surface potential. Contact with metal surfaces may induce charge redistribution between the two sides of the membrane patches, subsequently leading to a variation in the branching ratio [209]. The AFM-IR results therefore offer intriguing implications for potential applications and perspectives. On one hand, they suggest a promising avenue for enhancing the efficiency of optogenetic gates by bringing them into proximity with metal surfaces. For instance, utilizing metal nanoparticles could be explored, given their ability to securely bind to neurons, even in in vivo experiments. On the other hand, these results underscore the importance of additional experimental investigations to delve deeper into understanding the influence of the membrane potential on the functionality of transmembrane proteins. Exploring how these proteins respond to variations in the membrane potential they are exposed to could unveil critical insights into the intricate interplay between the molecular mechanism and the electrochemical environment. This avenue of research holds promise for unraveling the variations of

transmembrane protein behavior in different physiological contexts.

Chapter 6

Measuring the vibrational spectra under external electric fields on nanometric layers

In this chapter, I report the experiments conducted using the customized voltage-controlled AFM-IR setup aiming to delve into the impact of the electric fields on the IR response. The focus of these investigations is based on the use of films of the homogeneous poly-methyl methacrylate (PMMA) polymer with varying thicknesses as a calibration sample. The results derived from these experiments not only provide a means to validate the efficacy of this innovative nanoscale technique but also furnish valuable insights into the electromagnetic design. Diverse AFM probes with distinct shapes and dimensions have been employed. The motivation behind this approach is to discern the diverse responses in terms of the spatial homogeneity of the applied static field, the enhancement of the IR field, and the spatial resolution of the probed volume. As an illustrative example, observations related to the electric field effects within different regions of the multiphase ferroelectric polymer Polyvinylidene Fluoride (PVDF) are summarized. Furthermore, this chapter delves into the first results of IR difference spectroscopy obtained by subjecting a purple membrane system, which embed BR proteins, to an externally applied electric field. The presentation of these findings not only pave the way to the comprehension of the interaction between electric fields and biological systems but also showcases the versatility of the AFM-IR setup in exploring a range of materials and their responses to external electric fields.

6.1 Generation and observation of Vibrational Stark Effect in PMMA films

To validate the capabilities of the new setup, I started from the investigation of the polymer poly-methyl methacrylate (PMMA). The structure of the MMA unit is reported in Fig.6.1a. In this study, the IR investigation as a function of the external applied electric field is focused on the absorption peak of the C=O stretching vibration around 1730 cm^{-1} (see Fig.6.1c). Electric-field-dependent FTIR

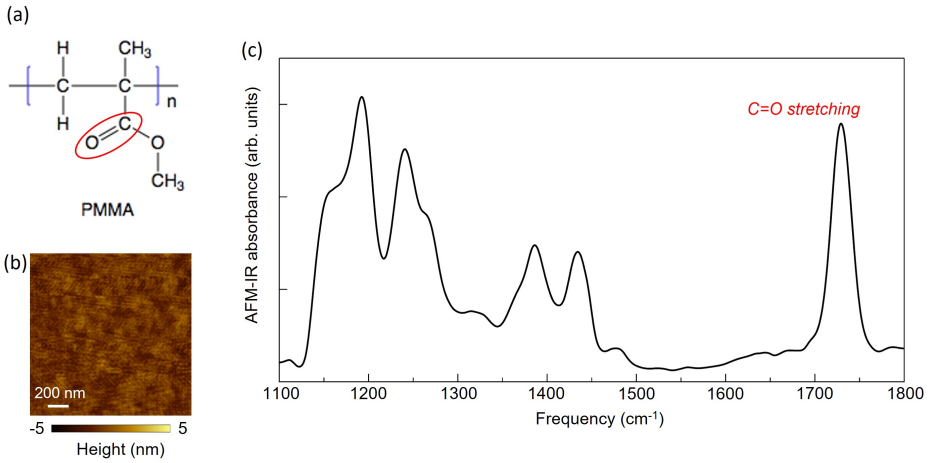

Figure 6.1. a)Structure of the MMA unit. b) Representative AFM topography obtained on a film of PMMA with thickness of 23 nm. c) Representative AFM-IR spectrum of PMMA.

experiments on 500 nm thick PMMA samples have been already realized [151], observing that in this kind of sample, the main IR spectral differences caused by the presence of static electric fields are due to the vibrational Stark effect (VSE), even at room temperature because of the poor orientational degree of freedom in the molecular chain.

For the AFM-IR experiments three thin films with different thickness d have been realized at CNR-IFN (Rome). The sample substrates have to be conductive to be exploited as one of the electrode. They are made of heavily doped (100) silicon (boron doped, resistivity: 0.001-0.005 $\frac{\Omega}{cm}$), covered with a thin adhesion layer of evaporated titanium (100 Å) followed by an evaporated gold layer (800 Å). A 6% diluted PMMA (All Resist AR-P 669.06) was diluted in ethil-lactate to obtain a 1% diluted solution which was spin-coated on the conductive substrate at different rotation speed resulting in different values of the film thickness d. Solvent evaporation was then promoted using a hot plate heating step at T=170°C for 5 minutes. Three samples with different thickness of PMMA have been realized: d=23nm (spin-coating rotational speed: 3000 rpm), d=30nm (2000 rpm) and d=55nm (obtained after 2 subsequent coating processes at 2000 rpm). As expected, the spin-coated samples do not show inhomogenities at the micron scale (see representative AFM topography in Fig.6.1b) and their thickness was measured with AFM mapping in a purposely scratched area of the films.

The requirement of a conductive tip with IR field enhancement translates into the choice of standard silicon AFM probes with pyramidal tip for AFM-IR measurements, which are coated with a gold layer added by evaporation (the specifics are reported in Chapter 4, at the end of sec.4.2.3). For the experimental purposes, they have been modified to obtain a flat-top shape by melting the small portion of gold coating forming the tip apex, which is done by passing a DC current through the probe while in contact-mode (see a representative electron microscopy image in Fig.6.2a). The area of the flat tip apex is around 80×80 nm^2 and this permits to safely reproduce a parallel-plate capacitor where the two electrodes are separated by the thin PMMA

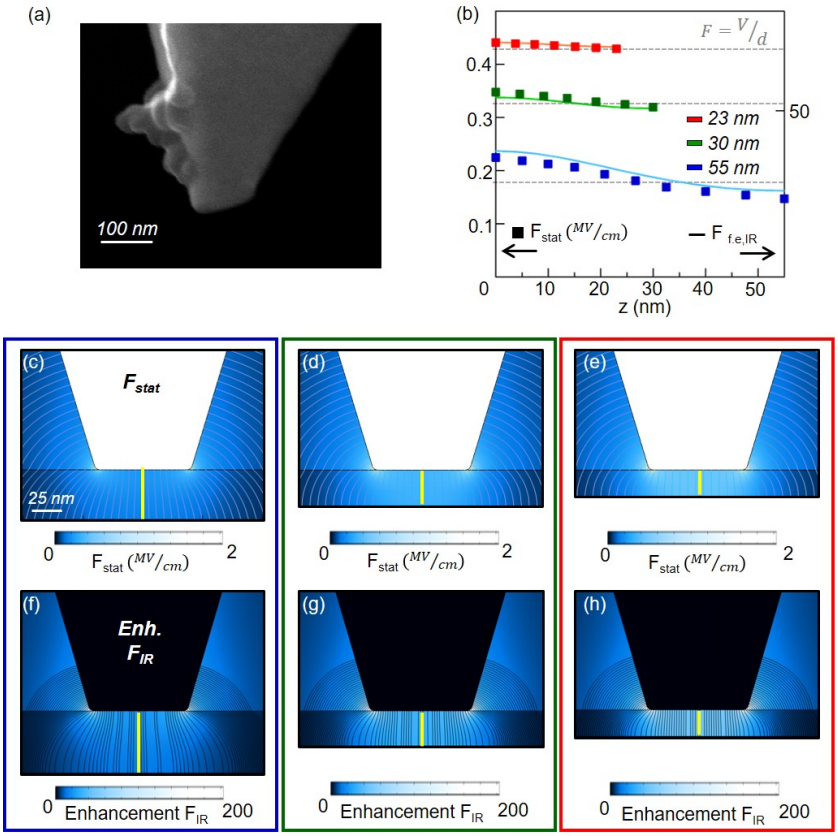

Figure 6.2. a) SEM image of the flat AFM tip. b) Profiles of the static electric field (squares, left axis scale) and of IR field enhancement (continuous lines, right axis scale) extracted from the simulations in (c-e) and (i-h) along the yellow line direction for the three thicknesses of the sample. The grey dotted lines represent the nominal value of the static electric field $F_{stat} = \frac{V}{d}$ for the parallel-plate capacitor model (left axis scale). (c-e) Numerical simulations of the static electric field F_{stat} applied with the flat tip on the PMMA sample with thickness of 55 nm (blue), 30 nm (green) and 23 nm (red) for a voltage V= 1.0 V. (f-h) Electromagnetic simulations of the IR field F_{IR} enhancement at $\lambda = 5.8\mu m$ in the same experimental conditions of (c-e).

film obtaining a constant value of the static electric field $F_{stat} = \frac{V}{d}$ along the sample thickness. This is confirmed by numerical electrostatic simulations in Fig.6.2c-e for the three thicknesses of the sample, which show a nearly constant value of the static field F_{stat} for V=1.0 V along the z direction below the tip apex. Moreover, the volume occupied by the static field lines overlaps with the one of the enhanced IR field F_{IR} in the electromagnetic simulations of Fig.6.2f-h for the same sample thicknesses. Along the z distance from the tip apex (yellow line in Fig.6.2c-h), the static field lines and the IR enhancement lines have the same decay of the intensity as reported in the plot of Fig.6.2b. In other words, the intensity enhancement of F_{IR} in the plasmonic-gap configuration is such that the AFM-IR photoexpansion signal can be considered as entirely produced by the sample volume located in the nanogap between tip and substrate, which almost perfectly overlaps with the material volume

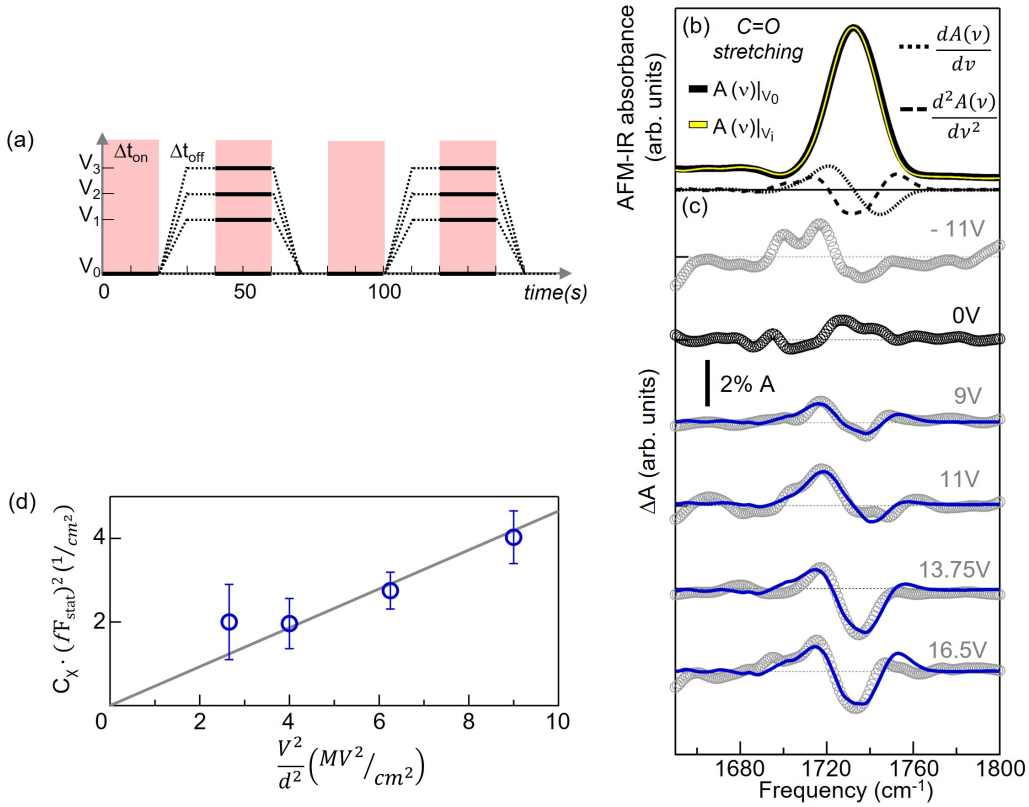

Figure 6.3. a)Time scheme of the procedure followed for the acquisition of the difference-spectroscopy data $\delta A = A(\Delta t_{on})|_V - A(\Delta t_{off})|_{V_0}$. The case of 2 repetitions of the procedure is represented. b) Representative AFM-IR spectra recorded on the 55 nm-thick PMMA film with the flat-tip in absence (black) and in presence (yellow) of an applied external voltage V. The dotted and dashed black curves represent the first and second derivative of the absorption spectrum, respectively. c) Difference-spectra calculated for different values of the applied voltage (grey circular points) and the best VSE fitting curves (using eq.6.1) reported in blue for the 55 nm-thick sample. d) Plot of the second derivative coefficients $C_\chi \cdot (fF_{stat})^2$ (empty circles) obtained from the fitting curves in panel c), highlighting the linear dependence on $(\frac{V}{d})^2$.

under the static electric field.
To monitor the effect of an external bias on the AFM-IR spectrum of PMMA, spectra at constant bias values were recorded and consequently the difference spectra $\delta A(\nu)_i = A(\nu)|_{V_i} - A(\nu)|_{V_0}$ were calculated, where $A(\nu)|_{V_i}$ and $A(\nu)|_{V_0}$ represent the spectra acquired at constant bias V_i and at zero bias V_0, respectively. The experimental spectral acquisition sequence is schematically reported in Fig.6.3b. Δt_{on} represents the time interval for the AFM-IR spectra acquisition and it is $\sim 20s$ for the wavenumber range between 1650-1800 cm^{-1} with spectral resolution equal to 1 cm^{-1}. Δt_{off} represents the time of the voltage ramp plus a settle time for static charge removal ($\Delta t_{off} \sim \Delta t_{on}$). For each bias value V_i, the acquisition has been repeated 10 times, averaging the resulting difference-absorption curves $\delta A(\nu)_i$ to obtain the final difference spectra $\Delta A(\nu)_i$. In Fig.6.3b-c the results obtained for PMMA film of thickness d=55 nm are reported. In Fig.6.3b, typical AFM-IR spectra measured with the flat tip in the C=O stretching region of PMMA are shown. If then one looks at the $\Delta A(\nu)_i$ curves reported in Fig.6.3c (depicted with grey circular points) for different values of the applied voltage, one can clearly see that there is an evident feature whose amplitude increases with increasing bias, and that all the curves differ from the reference black $\Delta A(\nu)_0$. The measured difference spectra $\Delta A(\nu)_i$ are clearly reminiscent of the second order derivative of the absorption spectrum, which is compatible with the hypothesis of VSE for an isotropic sample without orientational degrees of freedom, as detailed in Chapter 2 sec.3.1.2. Indeed, in the case of isotropic molecule distribution with respect to the static electric field, as for thick PMMA films, neither red or blue Stark shift is observed, but rather a line broadening proportional to the square of the static electric field [157], as in the case of sample cells used in refs. [148, 213, 214]. Therefore, the theoretical framework of ref.[157] can be used, as already did also for FTIR data on PMMA in ref.[151]. Hence, the difference spectra in Fig.6.3c are fitted to the VSE equation valid for an isotropic and immobilized sample:

$$\Delta A(\nu) = (f\vec{F}_{stat})^2\{A_\chi A(\nu) + B_\chi \nu \frac{d}{d\nu}(\frac{A(\nu)}{\nu}) + C_\chi \nu \frac{d^2}{d\nu^2}(\frac{A(\nu)}{\nu})\} \qquad (6.1)$$

where f is the local field correction factor, typically approximated by a scalar number with a value estimated between 1.0 and 2.0, and A_χ, B_χ and C_χ are molecule-dependent parameters that depend on the χ angle between the direction of the IR electric field and the static electric field [156, 161]. According to the theory by Boxer [157], in isotropic conditions the first order derivative term B_χ is mainly related to the polarizability difference, while the second order derivative term C_χ is instead the one proportional to the square of the dipole moment change $\Delta\mu^2$ and the dominant contributor to the Stark effect. The best fitting curves obtained using eq.6.1 are superimposed as blue curves to the experimental difference spectra in Fig.6.3c and show a good agreement with the experimental data. If we now plot the second-derivative fitting coefficient $C_\chi \cdot (fF_{stat})^2$ vs $(\frac{V}{d})^2$ (Fig.6.3d), we can observe that a linear dependence is obtained. According to the VSE theory, the linear dependence is expected since $C_\chi \propto \Delta\mu^2$ and, due to the perturbation theory, $\Delta\vec{\mu}$ does not depend on the field intensity.
It is worth to highlight that, starting from the fitted values of C_χ and assuming f=1.0, the absolute value of $\Delta\vec{\mu}$ for the C=O bond results compatible with the

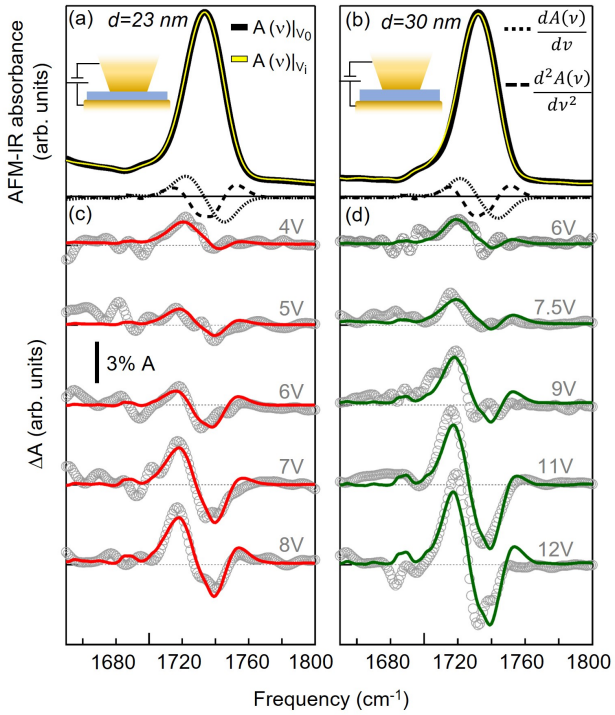

Figure 6.4. a-b) Representative AFM-IR spectra recorded on the 23 nm and 30 nm-thick PMMA film, respectively with the flat-tip in absence (black) and in presence (yellow) of an applied external voltage V. The dotted and dashed black curves represent the first and second derivative of the absorption spectrum, respectively. c-d) Difference-spectra calculated for different values of the applied voltage (grey circular points) and the best VSE fitting curves reported in red and green for the 23 nm and 30 nm-thick sample.

values reported in ref. [151, 161]. Indeed, since $C_\chi \propto |\Delta\vec{\mu}|^2$, an estimation of $\Delta\vec{\mu}$ can be retrieved. In particular,

$$C_\chi = \frac{1}{30h^2c^2}|\Delta\vec{\mu}|^2[5 + 2(3cos^2\chi - 1)] \tag{6.2}$$

where χ is the already mentioned angle between the direction of the IR electric field F_{IR} and the static electric field F_{stat}, h is the Planck constant and c the speed of light [149]. Considering $\chi = 0$, one obtains $C_\chi = \frac{9|\Delta\vec{\mu}|^2}{30h^2c^2}$. In the experimental condition the angle χ is equal to 0 because the IR electric field and the static electric field have the same direction in the probed volume under the tip, as also confirmed by the electromagnetic simulations reported in Fig.6.2. Hence, from the experimental data, an average value of $C_\chi = 0.36 \pm 0.06\frac{1}{MV^2}$ is obtained and so $\Delta\vec{\mu} = 6.5 \pm 0.6 \cdot 10^{-2} D$ (Debye, electric dipole moment unit equal to $3.34 \cdot 10^{-30} C \cdot m$). This a further evidence that the static electric field applied with the flat tip can be safely determined as $F_{stat} = \frac{V}{d}$ and that the sample volume probed by AFM-IR corresponds to the one where the static field is applied and is nearly constant. The same experiment of electric-field-dependent difference spectroscopy is then repeated on the PMMA films with d=23 nm and 30 nm . The data reported in Fig.6.4 (depicted with grey circular points) are interpreted in the same way and fitted to the

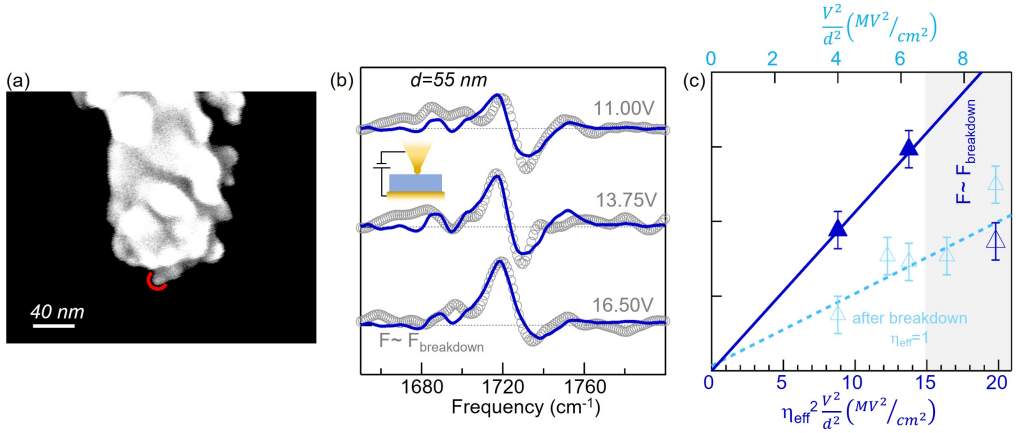

Figure 6.5. a) SEM image of the sharp tip with the gold-ion cluster coating. The tip apex is highlighted by the red semicircle. b) Difference-spectra calculated for different values of the voltage applied on the 55 nm-thick sample with the sharp tip (grey dotted curves) and the best VSE fitting curves reported in blue for the 55 nm-thick. c) Plot of the second derivative coefficients $C_\chi \cdot (\frac{V}{d})^2$ (triangles) obtained from the fitting curves in (b) fir the 55 nm-thick sample, respectively. The continuous lines are those obtained for the flat-tip as a function of $\frac{V^2}{d^2}$ (here reported by the dashed lines) multiplied by the gain factor $\eta_{eff,exp}$ to fit the linear trend of the filled triangles. The grey areas highlight the static electric field values for which the polymer breakdown is reached and the hollow triangles are the $C_\chi \cdot (\frac{V}{d})^2$ coefficients obtained from the data collected after the breakdown. In particular, the light-blue triangles resembling the linear trend of the flat-tip, are a set of data obtained in the 55 nm-thick sample with a sharp-tip after it experienced the polymer breakdown.

eq.6.1 (red and green curves). However, in this case, an higher contribution of the first-derivative-term occurs, as also evident from the shape of the difference spectra. While the isotropic assumption should hold in the case of randomly folded PMMA chains independently on the film thickness, the immobilization hypothesis seems to fail for the d=23 nm and 30 nm samples and the PMMA molecules probably acquire an orientational degree of freedom that largely defines the IR spectral changes. This can be ascribed to molecule reorientation in the external electric field so that the resulting IR spectral changes overlap with the VSE contribution, and even dominate it. The higher orientational freedom of the 23 nm and 30 nm thick PMMA sample is probably due to the film thickness becoming comparable to the typical end-to-end distance of the polymer chain, which in the case of the present experiment for a molecular weight of the PMMA of 600 kDa can be estimated to be around 22 nm [215].

6.2 Results employing a sharp AFM tip

Using different probe tip geometry with much sharper apex, equivalent results on VSE observation are collected on the 55 nm thick PMMA, but with the advantage of restricting the probed volume to a hemispherical volume located below the AFM tip apex. In particular, in Fig.6.5 we show the results obtained using a sharp tip

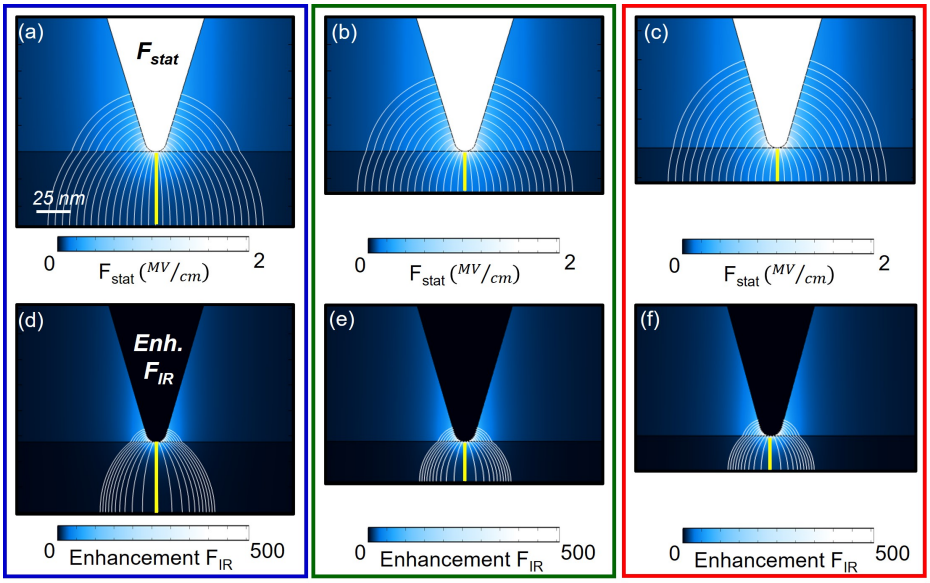

Figure 6.6. (a-c) Numerical simulations of the static electric field F_{stat} applied with the flat tip on the PMMA sample with thickness of 55 nm (blue), 30 nm (green) and 23 nm (red) for a voltage V= 1.0 V. (d-f) Electromagnetic simulations of the IR field F_{IR} enhancement at $\lambda = 5.8\mu m$ in the same experimental conditions of (a-c).

with a gold-ion nanocluster coating (SEM images in Fig.6.5a and specifics reported in Chapter 4, at the end of sec.4.2.3) featuring a few-nanometers tip apex, estimated to be around 8 nm. Difference-spectra obtained for the sample of thickness d=55 nm are shown in Fig.6.5b and are very similar to those obtained with the flat-tip of Fig.6.3c. However, the second derivative coefficient $C_\chi \cdot (\frac{V}{d})^2$ values vs $(\frac{V}{d})^2$ (two filled triangles in Fig. 6.5c) obtained from the fitting procedure considering $F_{stat} = F_{flat} = \frac{V}{d}$, are above the calibration line get from the data collected with the flat tip (dashed lines in Fig. 6.5c) on the same sample. The steeper trend indicates that a field intensity gain should exist when using the sharp tip respect to the flat one. More precisely an effective field intensity gain factor $\eta_{eff,exp}$ can be defined to retrieve the value of the static electric field when the sharp tip is employed and a voltage V is applied, as:

$$F^*_{sharp} = \eta_{eff,exp} \cdot F_{flat} = \eta_{eff,exp} \cdot (\frac{V}{d}) \tag{6.3}$$

F^*_{sharp} indicates the effective static field in the probed volume since, as shown by electromagnetic simulations for the three thicknesses of PMMA in Fig.6.6a-c, $F_{sharp}(z)$ is not constant but rather has a decaying dependence on the z-distance from the tip apex. From the experimental data a gain factor $\eta_{eff,exp} = 1.50 \pm 0.05$ is obtained for the 55 nm thickness, as represented by the continuous line in Fig.6.5c fitting the experimental slope of the two filled triangle markers. It is very important to note that the intensity gain that occurs for the static field and the decay along the z-distance from the tip apex also apply for the IR field enhancement, as shown by simulations in Fig.6.6d-f and the plot in the inset of Fig.6.7 (continuous lines). Therefore the region of higher static field also produces most of the radiation heating

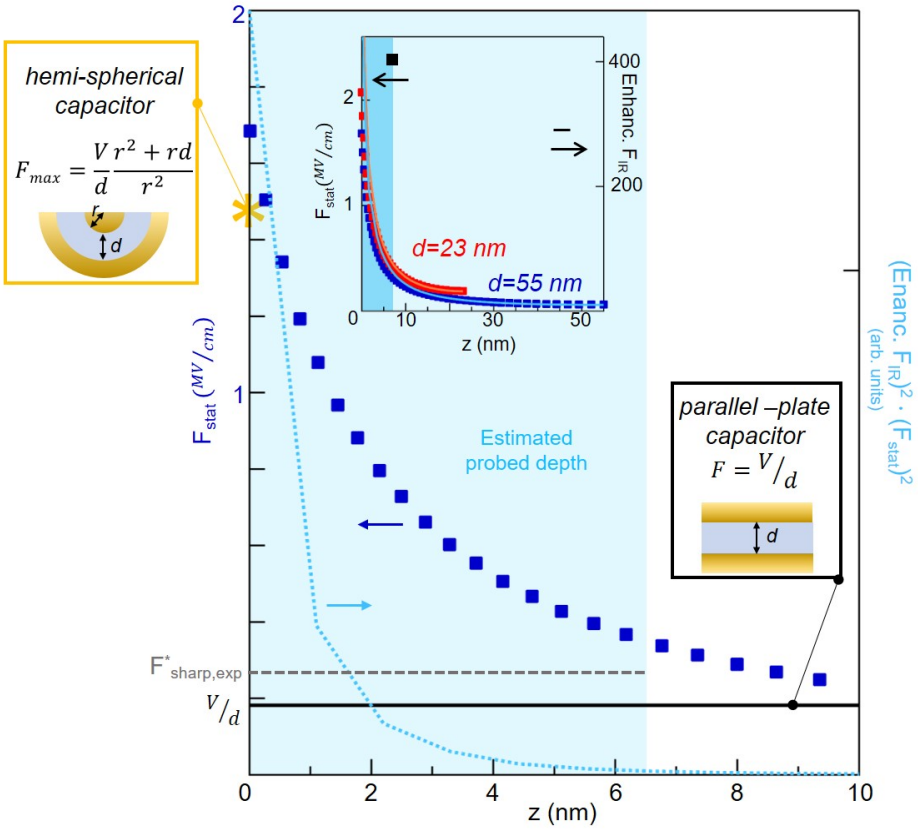

Figure 6.7. Profile of the static electric field extracted from the simulations in Fig.6.6a along the yellow line in the first 10 nm below the tip of the 55 nm-thick sample (blue squares, left axis scale). The light-blue dashed line is calculated as $F_{IR}^2 \cdot F_{stat}^2$ to estimate the thickness of the sample from which the ΔA signal is originated (light-blue area). The black line represents the static electric field for a parallel-plate capacitor model with V=1.0V and d=55nm, while the yellow asterisk is the value of the static electric field at the tip apex estimated with the same V and d for a hemi-spherical capacitor that models the experimental condition of the sharp tip. The grey dashed line is the experimentally estimated value of the the effective static field in the probed volume. In the inset, the profiles of the static electric field for V=1.0V (squares, left axis scale) and of IR field enhancement at $\lambda = 5.8\mu m$ (continuous lines, right axis scale) along the z direction under the tip are plotted for the 23 nm-thick (red) and 55 nm-thick (blue) samples.

which originates the photo-thermal expansion phenomena behind the AFM-IR detection mechanism. This clarifies that the probed sample area remains in the close proximity of the tip surface, where both IR and static fields are strongly enhanced by the sharp tip, independently on the sample thickness. The difference-absorption signal ΔA_{AFM-IR} can be expressed as being proportional to $F_{IR}^2 \cdot F_{stat}^2$, formulated as

$$\Delta A_{AFM-IR} \propto \int dxdydz \Delta\epsilon(x,y,z) F_{IR}^2(x,y,z) \propto \int dxdydz C_\chi F_{stat}^2 F_{IR}^2(x,y,z) \tag{6.4}$$

where $\Delta\epsilon$ is the difference in the imaginary part of the dielectric function of the sample due to the application of the static field, directly proportional to F_{static}^2 according to eq.6.1. This approximation holds true when the F_{IR} and F_{static} maps are nearly identical, apart from a normalization factor. Referring to this quantity (illustrated by the dashed light-blue line in Fig.6.7 for the 55 nm thick sample), an estimation of the probed sample depth equal to 6.5 nm can be derived. A classical electromagnetic model can be also employed to formulate an estimation for the maximum value of the static field achievable at the sharp tip apex for a given voltage V. Beginning with the capacitance C of the capacitors formed by the metal tip and the substrate, filled by the sample material as the dielectric medium, an estimation of the total charge $Q = C \cdot V$ accumulating on the tip and substrate surfaces is derived. From this, the surface charge density σ and the field at the tip surface $\frac{\sigma}{\epsilon}$ as a function of z can be determined. Finally, the relationship between F_{flat} and F_{sharp} is established for the field intensity gain η_{eff} at the tip surface when using a sharp tip. For the flat tip, a parallel-plate capacitor model is employed with a surface area $A = 80x80nm^2$ and d equal to the sample thickness. Meanwhile, for the sharp tip, a hemispherical capacitor model is used, with an internal radius r equivalent to the measured curvature radius of the tip apex (8 nm, see Fig.6.5a) and an external radius $R = d + r$. Hence, one obtains the following equation:

$$\eta_{eff} = \frac{F_{sharp}}{F_{flat}} = \frac{r^2 + rd}{r^2} \tag{6.5}$$

which gives 7.8 for d= 55 nm and r=8nm. The field profile inside the sample can be also estimated with this classical model as $F(z) \propto \frac{1}{(z+r)^2}$.
With a reasonable estimation of the static electric field applied by the sharp tip at hand, one can see what happens if an electric field higher than the breakdown field of PMMA estimated around 4.0 to 6.0 $\frac{MV}{cm}$ is applied [216, 217]. A DC current starts to flow in the dielectric layer with minor effects on the layer itself, however the ion cluster network that constitutes the gold coating of the sharp tip is severely affected. A voltage $V_{breakdown}$ = 16.5 V on the 55 nm sample corresponds to F_{sharp} around 4.5 $\frac{MV}{cm}$, considering the $\eta_{eff,exp}$ experimentally obtained. Similar effects are observed applying 6.0 V to the 23 nm sample corresponding to F_{sharp} around 4.0 $\frac{MV}{cm}$. This is consistent with a picture of electrons injected into the first nanometers of the PMMA layer that travel through the entire layer (where the field is probably lower than the breakdown field) and produce a leakage current that damages the sharp tips. Indeed, in this leakage condition a lower ΔA is measured, as it is possible to see from the bottom curve of Fig.6.5b and from the hollow triangle marker in

the grey region of the $C_\chi \cdot (\frac{V}{d})^2$ plot in Fig.6.5c. Also, by repeating the experiment after this "leakage-annealing" event, a slope of $C_\chi \cdot (\frac{V}{d})^2$ vs. $F^2 = (\frac{V}{d})^2$ perfectly matching the flat tip slope is obtained (light-blue hollow triangles in Fig. 6.5c), indicating that the curvature radius of the tip apex has been compromised and, hence, the gain in electric field has been cancelled.

6.3 Electric-field-dependent effects on the multiphase PVDF polymer

The experiments conducted on PMMA demonstrate that employing a sharp tip (curvature radius <10 nm) the effective probed volume of the electric-field-dependent effects with our platform is located close to the tip apex and comparable or smaller than the usual AFM-IR lateral resolution (typically of 30 to 100 nm from the tip apex in the presence of plasmonic field enhancement, and much larger in the absence of it). Importantly, this small volume coincides with the volume to which the electric field is applied, due to the almost perfect correspondence of DC and IR field enhancements. This fact can be exploited to measure different electric-field-induced signals in subwavelength-sized polymer droplets belonging to an inhomogeneous mixture. In particular, we have chosen the ferroelectric polymer PVDF, which is expected to show a strong electric-field-dependence of the IR spectra from FTIR experiments in the literature performed on large areas (of the order of 1 mm^2) [218]. PVDF features different crystal phases with clearly different IR spectra and different response to DC electric fields, since it often appears in multi-phase drop-cast films under the form of micrometric "droplets" formed upon solvent drying, spin-coating and baking processes. In particular, the two phases observed in our experiments are the α-phase and the β-phase. They differ for the chain conformation in the crystallized state that results to be non-polar in the α-phase because of the anti-parallel packing of the dipoles (see the chain structure in the top panel of Fig.6.8a) and polar in the β-phase which is the phase showing ferroelectric and piezoelectric properties (bottom panel of Fig.6.8a). Moreover, the α-phase has a non-hysteretic behavior, where the polarization direction of the electric domains returns to a disordered configuration after the removal of an external *poling* field. The β-phase, instead, is hysteretic and retains domain orientation after the removal of the *poling* field.
The PVDF solution was prepared at a concentration of 2 wt% dissolving PVDF pellets in dimethylformamide (DMF) and acetone with a 1:1 ratio of the two solvents. The process lasted 3 hours on a hot plate at a fixed temperature of 70° C under mechanical stirring. The obtained solution was then cast on the conductive substrate and the spin coating process was realized at a speed of 500 rpm for 10 s and of 1000 rpm for 30 s. Solvent evaporation was then promoted using a oven heating step at T=110° C for 3 minutes. The estimated thickness of the obtained film is around 100 nm. In Fig.6.8b the topography of a micrometric region of the polymer film is reported, from which the inhomogeneity in the morphology is already evident. The AFM-IR maps acquired at 1210 cm^{-1} and 1275 cm^{-1} in Fig.6.8c-d are almost complementary in the intensity signal, thus confirming the different PVDF phase-composition. The 1210 cm^{-1} and 1275 cm^{-1} frequencies indeed are assigned to the characteristic absorption peaks of the α-phase and β-phase [219, 220], respectively,

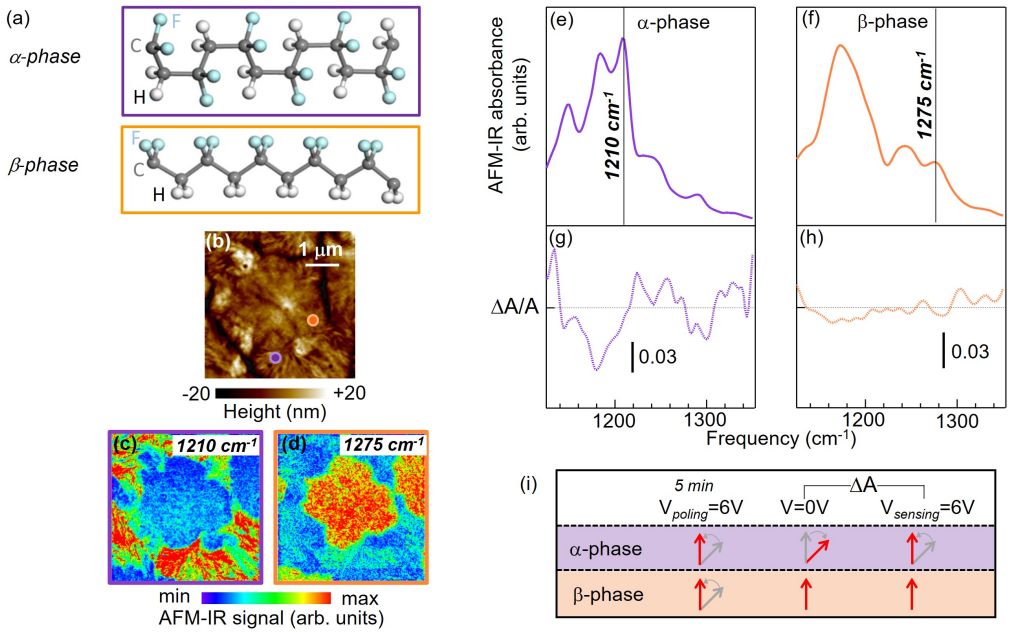

Figure 6.8. a) Chain structure of the α-phase and β-phase of the PVDF polymer. b) AFM topography of an heterogeneous area of the PVDF film. c)AFM-IR map acquired at a frequency corresponding to a characteristic absorption peak of the *alpha*-phase (1210 cm^{-1}). d) AFM-IR map acquired at a frequency corresponding to a characteristic absorption peak of the *beta*-phase (1275 cm^{-1}). e) AFM-IR spectrum acquired in a region of the PVDF film featuring an *alpha*-phase structure (purple dot in panel b). f) AFM-IR spectrum acquired in a region of the PVDF film featuring a *beta*-phase structure (orange dot in panel b). g) Difference spectrum for the *alpha*-phase normalized by the absorption spectrum measured under the applied external electric field F=0.6$\frac{MV}{cm}$. h) Difference spectrum for the *beta*-phase normalized by the absorption spectrum measured under the applied external electric field F=0.6$\frac{MV}{cm}$. i) Time-scheme of the procedure for the acquisition of the difference spectra: 5 minutes of poling, acquisition of the spectrum with no voltage applied (lasting ∼30 seconds) and acquisition of the spectrum with 6V applied (lasting ∼30 seconds). The arrows represent the orientation of the bond dipole moment in presence and absence of the external electric field.

as appears also in the AFM-IR spectra of Fig.6.8 e-f.
In our experiment, a poling field of 6 V is applied for 5 minutes with the scanning probe itself to the specific sample location that is subsequently probed by AFM-IR. This corresponds to an electric field of $\sim F = 0.9\frac{MV}{cm}$ considering the thickness of the film $d \sim 100$ nm and the gain factor for the sharp tip $\eta_{eff,exp} = 1.5$. Then, the voltage bias is slowly switched back to zero. Finally, an AFM-IR difference spectra is acquired with/without a sensing field, obtained with a sensing voltage of 6 V identical in amplitude to the poling voltage but applied for 30 seconds only (i.e. the duration of the AFM-IR measurement). One can expect a weak ΔA for the permanent ferroelectric β-phase, as the presence or absence of the sensing field will not change the bond dipole orientations considerably, and a strong ΔA for the quasi-paraelectric α-phase, whose dipole directions are still sensitive to the presence of the sensing field. More clearly, the $\frac{\Delta A}{A}$ of the α-phase in Fig.6.8g shows distinct

positive (negative) spectral features corresponding to the increase (decrease) of the scalar product of the IR field with the specific dipole moments of the bond vibrations. The direction of bond dipoles will inevitably change during the domain re-orientation that takes place with the application of the sensing field to the non-hysteretic α-phase that has no memory of the previously applied poling field. On the other hand, $\frac{\Delta A}{A}$ in Fig.6.8h has no spectral features for the β-phase, indicating that the sensing field is still increasing the absolute dipole moments of the ferroelectric domains, but it is not changing the bond dipole orientations significantly, because they have been already fixed by the previously applied poling field. Notably, the electric-field-induced changes in Fig. 6.8g-h are not attributable to the VSE because, at odds with PMMA, PVDF molecules have an orientational degree of freedom in all phases of the condensed polymer form, which provides very strong ΔA signals that make any VSE-related spectral change not measurable. After the observation of spectral characteristics attributable to orientational movement in thinner PMMA films (23 nm and 30 nm), PVDF provides another case of this electric-field-effect observable with IR spectroscopy, where it is also possible to distinguish the different response of the system based on the structure of the polymer chain at the micrometric scale.

6.4 Conformational changes of the BR protein subjected to an external electric field

The electric-field-dependent results obtained on polymeric systems with the AFM-IR setup effectively demonstrate the feasibility of realizing the objective of my PhD thesis through this innovative platform. Specifically, this involves delving into the study of the photosensitive protein activity in relation to the experienced transmembrane potential. However, reaching the ultimate goal poses challenges and requires some intermediate steps. In initiating experiments on protein samples, I started from the investigation of the BR protein, recognized as the prototype of photosensitive proteins due to its elevated structural stability and an high filling factor within the natural cell membrane. Notably, the experiments presented herein are conducted in the absence of any photoactivation of the protein functionality. The primary objective at this stage is to prove the capability of the AFM-IR setup to discern the IR response of proteins when subjected to an external electric field and try to understand the induced effects.
The sample was prepared following the same procedure for the sample preparation already presented for the ChR in Chapter 4. The buffer solutions (20mM Bis-Tris propane, 100 mM NaCl, 1 mM $MgCl_2$) containing patches of cell membranes filled with the slow mutant BR D96N were cast in droplets of 2 μl onto 1 cm $\times$ 1 cm template-stripped gold chips (*Platypus Technologies* 0.3 nm rms roughness) and let dry in air. After 10 minutes, the samples was rinsed with milli-Q water to promote the adhesion of individual cell membrane patches on the surface and subsequently it is dried for 1 h in an atmosphere with humidity below 10%. For the interpretation of the measurements, it is important to recall that, in the BR molecule, the seven anti-parallel helix structures run from the extra-cellular (EC) side to the cytoplasmic (CP) side of the cell membrane as sketched in Fig.6.9a. Along the polypeptide chain, the distribution of the peptide C=O bonds is anisotropic since they are almost aligned

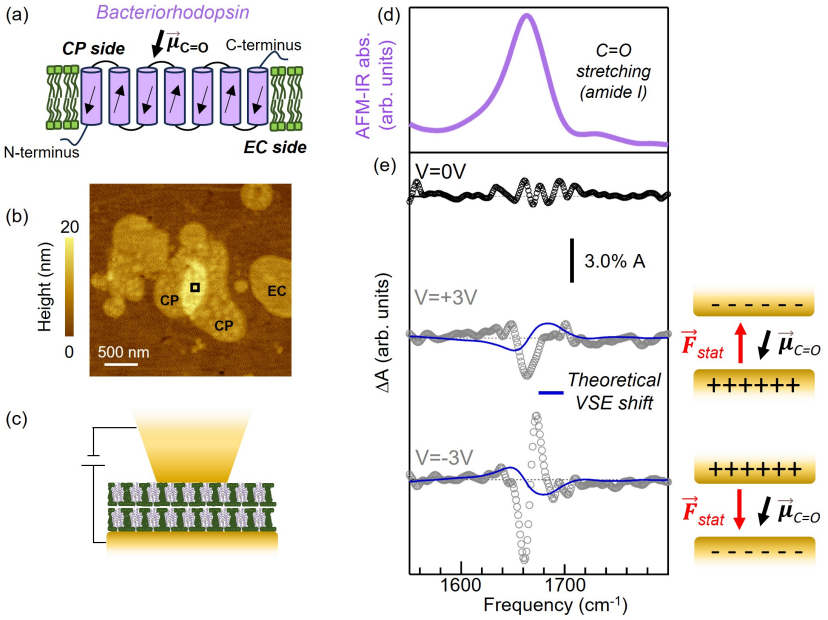

Figure 6.9. a) Schematic of the seven α-helix BR structure inserted in the lipid cell membrane highlighting the orientation of the resultant C=O dipole moment $\vec{\mu}_{C=O}$. b) AFM topography of the two overlapping cell membrane exposing the CP side on which the AFM-IR measurement have been conducted. Cell membrane patches showing the less rough EC side can be also identified. c) Sketch of the AFM-IR experimental configuration to probe the 10 nm-thick stack made of the two cell membrane using a flat AFM tip. d) Amide I band of a representative AFM-IR spectrum acquired on the area pointed by the black square in panel b). e) $\Delta A(\nu)_0$ (black curve) and $\Delta A(\nu)_{\pm 3V}$ (grey curves) obtained in the area pointed by the black square in panel b) applying a voltage V of 0V, +3V and -3V, respectively. The calculated spectral contribution related to the VSE (continuous blue lines) are also represented. On the right, a schematic of the $\vec{\mu}_{C=O}$ orientation with respect to the applied static field $\vec{F}_{static}$ is presented when a voltage V of +3V and -3V is applied.

parallel to the helix axis, so that the total dipole moment of the C=O vibration will be dominated by the four odd helices only partly cancelled by the three even helices. A stack of two overlapping cell membrane patches deposited on a gold surface with a total thickness of 10 nm is selected to conduct the difference spectroscopy experiments, due to the higher mechanical stability observed respect to the case of a single membrane with a typical phospholipid bilayer thickness of 5 nm. The AFM topography map is reported in Fig.6.9b. Given the high degree of homogeneity in the sample composition and the desire for a nearly constant value of the applied F_{stat} across the protein system, opting for a flat tip configuration is favored over a sharp tip configuration (see Fig. 6.9c). Both purple membrane flakes forming the 10 nm-thick stack can be assumed to be oriented with the EC side towards the metal surface support, as suggested by the rough surface peculiar of the CP side obtained by AFM topography (Fig.6.9b) [221]. We focus the attention on the 1610-1690 cm^{-1} spectral region of the amide I band, which arises from coupled protein backbone C=O stretching vibrations (Fig.6.9d) and it is the IR band most sensitive to protein

conformation. Electric-field-induced IR absorption changes ΔA of few percent of the maximum absorption peak at 1660 cm^{-1} (grey curves in Fig. 6.9e) are obtained at bias $V = \pm 3V$ averaging over 20 acquisitions $\delta A(\nu)_{\pm 3V}$. These relative changes are comparable to those observed in the IR difference spectra of thicker PMMA samples at slightly higher V. The SNR of our technique hampers to obtain relative absorption variations that significantly differ from reference curve (black curve, $\Delta A = A(\Delta t_{on})|_0 - A(\Delta t_{off})|_0$) for bias values lower than $\pm 3V$. By looking at the $\Delta A(\nu)_{\pm 3V}$ reported in Fig.6.9e, one can clearly observe that different features are obtained for the two polarities, with a very clear first-derivative lineshape in the case of $V = -3V$. The VSE is expected in the amide I band with similar coefficients as in PMMA due to the C=O stretching origin of the absorption peak [222]. The anisotropy of the C=O dipole orientations in the BR helices imposes a VSE lineshape similar to the vibrational Stark shift [164], reproduced by our calculations as blue line in Fig.6.9e. The resulting Stark shift $\Delta\nu = -\Delta\vec{\mu} \cdot \vec{F}_{stat}$ is indeed expected to be equal to $\Delta\nu = \pm 3cm^{-1}$ for $\pm 3V$, respectively, assuming a Stark tuning rate of the carbonyl mode $\Delta\vec{\mu}_{C=O} \sim 1cm^{-1}/\frac{MV}{cm}$ [164, 138, 223], $\Delta\vec{\mu}_{C=O}$ almost parallel/anti-parallel to $\vec{F}_{stat}$ [224] (as schematically represented in the sketches in the right panels of Fig.6.9e), and a static electric field $F_{stat} = \frac{V}{d} = 3\frac{MV}{cm}$. It is apparent that the VSE theory cannot reproduce the combined $V = \pm 3V$ data. To explain the observed amide-I features, one then has to resort to changes of the protein backbone orientation in external electric fields [225, 147], which is reasonable to assume given the large freedom of movement of BR helices. Helix length change, helix axis tilt, and helix partial unfolding would all produce IR difference signals at the amide-I maximum around 1660 cm^{-1} [226, 227, 228], and molecular dynamics calculations are required in order to identify the specific electric field-induced changes of the BR backbone. Note that ΔA related to such conformational changes can have different intensity and shape for the two different signs of V_i due to steric hindrance given that the directional symmetry is broken in the CP-up orientation of both membrane patches.

One has also to consider that the external electric field can affect the lipid bilayer constituting the membrane. A strong external electric field can destabilize membranes and induce the formation of pores, which increase the conductivity of the membrane and its permeability [229]. This phenomenon is known as membrane electroporation or dielectric breakdown and involves rearrangement of the phospholipid bilayer, presumably leading to the formation of aqueous pores. The voltage threshold for electric breakdown in a lipid membrane depends on the specific lipid composition of the bilayer and the conditions in which the lipid membrane is found, ranging from around 0.5-1 $\frac{MV}{cm}$ [230, 231, 232] up to 5-10 $\frac{MV}{cm}$[233]. In the purple membrane sample, the high filling factor of the bacteriorhodopsin protein (lipid:protein molar ratio of 25:75) should contribute to stabilizing the membrane due to its strong interaction with nearby lipids, resulting in an increase in the voltage breakdown for membranes. Therefore, in the present experiments, the estimated transmembrane electric field value of 3 $\frac{MV}{cm}$(3 V on a stack of two overlapped membranes with a total sample thickness of 10 nm) falls within the range of voltage threshold values found in the literature. Indeed, there is no experimental evidence that electroporation occurred during the experiments upon the application of the external electric field.

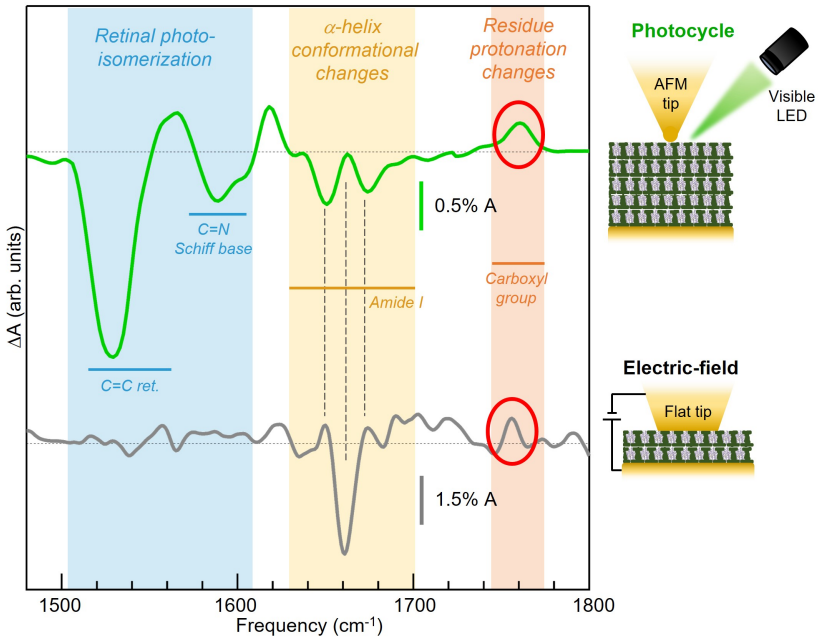

Figure 6.10. AFM-IR difference spectrum acquired on a stack of BR cell membranes under visible light illumination (green curve) compared to the one obtained with applied bias of -3V on a double membrane system (grey curve).

This is confirmed by the absence of pore formation in the membrane flakes as observed via AFM topography after the application of the bias. Additionally, there were no significant modifications in the AFM-IR signal amplitude (i.e., variations in the sample-tip interaction) recorded between the spectra acquired with and without the applied voltage.

One could then use this experimental approach also to simultaneously monitor structural reorientations of BR proteins and protonation of amino acid residues under static electric field by keeping the membranes in high hydration conditions to accumulate sufficient water molecule density within the molecules [234]. Indeed, IR difference spectra can show an absorption peak related to the protonation change of carboxyl group around ∼1750-1760 cm^{-1}. Upon photoactivation, this is a spectroscopic marker of proton transport across BR [235] that occurs through different steps along the protein and includes the protonation of Asp-85 in the M intermediate (see *Appendix I*). The positive peak at 1760 cm^{-1} could be previously observed in BR sample using the same AFM-IR setup under visible light illumination without any static field applied [20]. An AFM-IR light-induced difference spectrum is here reported (green curve in Fig.6.10) as a benchmark to electric-field-induced effects. The light-induced spectrum displays the protonation marker of Asp-85 (orange shade), the protein conformational change features (yellow shade) and the retinal photo-isomerization and Schiff base protonation feature (blue shade) [46]. To make a comparison, a $\Delta A(\nu)_{-3V}$ spectrum (grey curve in Fig.6.10) is obtained in dark conditions on another double stack of purple membranes (respect to the results presented previously) with the same CP-up orientation and high hydration. With

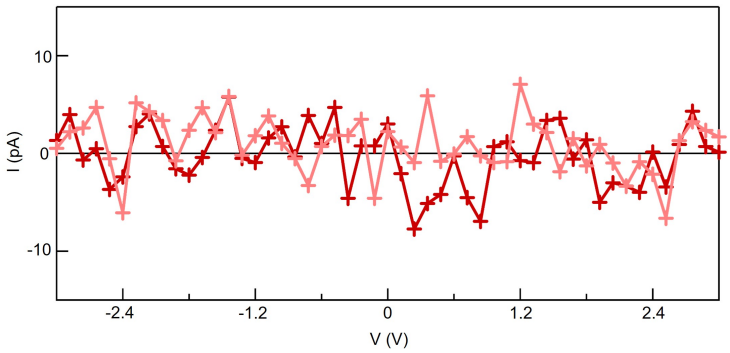

Figure 6.11. Two I-V measurements on double stacks of membrane patches.

$V = -3V$, one could hypothesize that protons are transferred within the protein by the electric force, as suggested by the presence of the protonation change marker in the difference-spectrum (grey curve, orange shade), for which the assignment to a specific amino acid requires further experimental evidence. Obviously, the retinal photo-isomerization and Schiff-base features are not seen in dark conditions (grey curve, blue shade), where the external electric field must therefore be entirely responsible for the proton transfer without the mediation of the Schiff base. Interestingly, the protein conformational change features (yellow shade) are quite different in the two cases. Note the different sign of the helix-tilt features (yellow shade): the green curve mostly represents the difference between the conformation of the conducting M intermediate of the BR photocycle and the dark BR state, while the grey curve represents the difference between conformation with and without an electric field, always in the dark BR state. This indicates that the conformational changes are different: actually, the helix tilt seems to be opposite. This interpretation may require further investigation also based on molecular dynamics calculations. Note that DC electric current on similar system of double stack of membrane patches with applied voltage $V = (-3V, +3V)$ could not be measured with a transimpedance amplifier connected to the tip, even if a solid platinum AFM probe is employed (Fig.6.11), since its magnitude is below the detection limit of the measuring system [236]. This suggests that the sensitivity of the IR-probe for charge transport, following the activation of photosensitive proteins with light or application of electric fields on voltage-gated transmembrane proteins, may be even higher than electric probes at the individual-membrane level.

Beyond the scope of this preliminary experiment, the objective of future investigations envisions a comprehensive integration of light-activation of the proteins and precise control of external electric fields. In this future framework, the measurements here reported would be relevant and useful to discriminate light-induced effects from those induced by the electric field. Indeed, this strategic approach aims to elucidate intriguing phenomena, such as the dependency of the light-capture efficiency of BR-based applications on applied external bias [237], which plays a pivotal role in mediating proton and electron transport [12, 238]. Moreover, the pursuit of experiments at physiologically relevant voltages for membrane proteins becomes paramount. Upcoming experiments may clarify the complex interplay between

light-induced conformational changes and the activity of the photosensitive proteins as a function of the experienced transmembrane potential, especially in the case of proteins like ChR [52, 239]. The significance of unraveling these complexities extends beyond fundamental scientific curiosity, finding practical applications in the neurobiological field and further enhancing the understanding of these proteins behavior in physiological contexts.

Chapter 7

Development of a new QCL-microscope for time-resolved light-activation studies

In this chapter, I report the time-resolved results obtained on BR sample employing the home-built QCL-microscope already described in Chapter 4 sec.4.4.
The investigation of small mid-IR relative absorption differences of the order of 10^{-3} to 10^{-4} during the light-activation of the rhodopsin photocycle typically necessitates a high SNR. Consequently, time-resolved experiments are generally conducted by averaging over numerous repeated photocycles [41, 91]. Furthermore, there is a need for a delay between two consecutive visible light pulses that exceeds the time required for the proteins to return to the dark-adapted state, here on referred to as BR*. This recovery time can vary from a few tens of milliseconds, as observed in the wild-type BR in a liquid environment [41], to several minutes, particularly in certain mutants of ChR [53, 240], depending on the specific protein and environmental conditions [37]. In cases where proteins exhibit a slow photocycle, spanning seconds or minutes, this results in extended total experimental durations, sometimes lasting several hours or even days.
Using the QCL-microscope, the strategic movement across a sample area not previously exposed to visible light allows for the recording of measurements from a dark-adapted region. This approach minimizes both the overall experimental time and the photodegradation of the sample. Specifically, experiments are conducted on both the BR wild type and the BR slow mutant D96N to compare the responses of these two samples with distinct characteristic intermediate times. This comparison underscores the significance of sample replacement, particularly when dealing with extended recovery times of the dark state, reaching up to seconds. Assuming a simplified photocycle model with only two dominant states, the dark-adapted state BR* and the intermediate M, it becomes feasible also to estimate the excitation and relaxation times of the conductive intermediate M under dry conditions. Furthermore, by selectively activating visible light only in the molecules present within the IR focal spot spanning a few tens of microns, sample consumption is reduced.

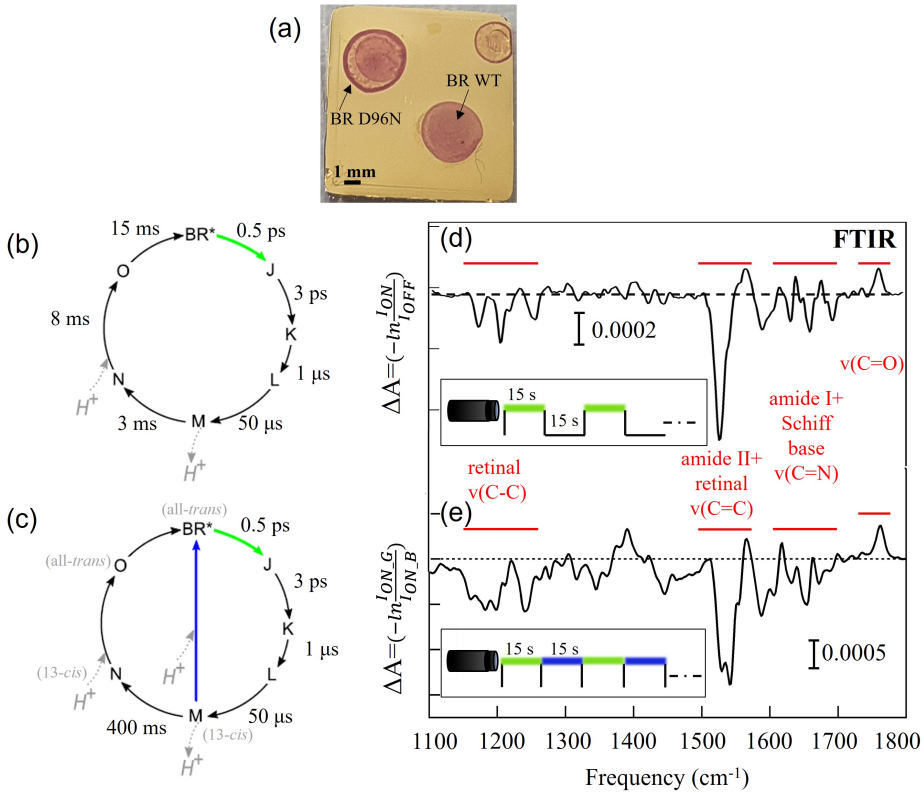

Figure 7.1. a) Picture of the films obtained by drop casting on the gold solid substrate both the BR WT and the D96N slow mutant. b,c) Sketch of the photocycle of the two BR protein variants. The approximative lifetime of each step in liquid environment is indicated [37, 48]. d,e) FTIR difference spectra resulting from the average of 80 repeated photocycles together with the indication of the main vibrational bands (in red) and the employed time/visible light structure of the LED illumination (square waves vs. time). Adapted from [241].

This is a common challenge in biomolecular studies. Small droplets on the order of a few microliters, resulting in a millimeter-sized sample area, offer 10^2–10^3 distinct dark-adapted locations for signal co-adding, thereby permitting the enhancement of the SNR.
Looking ahead, the data acquired through the QCL-microscopy approach constitute a first step towards future AFM-IR time-resolved difference spectroscopy of rhodopsins operating on the millisecond time scale.

7.1 Steady-state characterization of the intermediate M in BR WT and D96N slow mutant

To conduct experiments in reflection mode, buffer solutions (20mM Bis-Tris propane, 100 mM NaCl, 1 mM $MgCl_2$) containing patches of cell membranes densely filled with either wild-type BR or its mutant BR D96N were deposited in droplets of 10 μl onto 1 cm × 1 cm template-stripped gold chips (*Platypus Technologies*). Subsequently, the

samples were allowed to dry under controlled low-humidity conditions (see Fig.7.1a). In Figure 7.1b,c, the photocycles of BR WT and BR D96N are depicted, respectively, emphasizing the relative illumination wavelengths and characteristic lifetimes of the intermediates for both variants in a liquid environment. As explained in Chapter 1, sec.1.2.1, the intermediate M is referred to as the conductive state of the photocycle, as, during its lifetime, a proton is released towards the extracellular surface of the protein. In the case of D96N, the substitution of the proton donor results in a prolonged lifetime of the intermediate M. Furthermore, it is established that the lifetime of intermediate M is further extended when the sample is deposited on a rigid support and allowed to dry, owing to the reduced abundance of protons [242], a condition consistent with the sample in the current experiments.
The difference absorbance spectra (ΔA) presented in Fig,7.1 are obtained through conventional FTIR measurements in steady-state conditions, involving continuous illumination with a green LED (565 nm) throughout the spectra acquisition, which lasts for 15 seconds. In the case of BR D96N, an additional LED in the blue range (420 nm), absorbed by the M intermediate state, is employed to expedite the slow recovery of the photocycle to the dark-adapted state. Without this operation, the recovery typically occurs through the N and O intermediates. The visible illumination system used is the same as in the ChR experiments, utilizing the M565L3 and M420L3 LEDs by *Thorlabs*. The ΔA spectra are presented here to illustrate the spectral features characterizing the M intermediate. This information is crucial for interpreting the sign of the time-traces reported below and acquired at specific wavelengths in the mid-IR range. The most prominent band is situated around 1525 cm^{-1} and is assigned to the C=C bond of the retinal, while the bands corresponding to the C-C bonds fall within the range of 1150 to 1280 cm^{-1}. Regarding the conformational changes of the protein backbone, they are discernible between 1500 and 1600 cm^{-1} (amide II) and between 1600 and 1700 cm^{-1} (amide I). The peak around 1760 cm^{-1} is attributed to the C=O stretching vibration of protonated carboxylic acids, serving as an indicator for proton transport reactions across the BR protein.
It is worth noting that in FTIR difference spectroscopy, it is feasible to collect hundreds of difference spectra within a reasonable time frame. However, in the context of slow mutants, certain alterations or branching of the photocycle may occur. For instance, the proton capture dynamics in proteins that absorbed blue light can differ significantly from those that underwent the N and O intermediates. In Fig.7.1e, a double-dip structure is indeed observed in the difference spectrum of the slow mutant around 1530 cm^{-1}, indicating the simultaneous population of two distinct final states (BR* and X*)[20]. Therefore, for the slow mutant BR D96N, a protocol involving dark-adapted sample replacement eliminates the need for a second visible wavelength. This approach allows for probing the lifetime of the intermediate state M without spurious effects and within a reasonable time frame.

7.2 Time-resolved kinetic studies of the intermediate M in BR WT and D96N slow mutant

The time-resolved experiments using the QCL-microscope are conducted on BR samples deposited on the gold support (see Fig. 7.1), with the 565 nm LED integrated

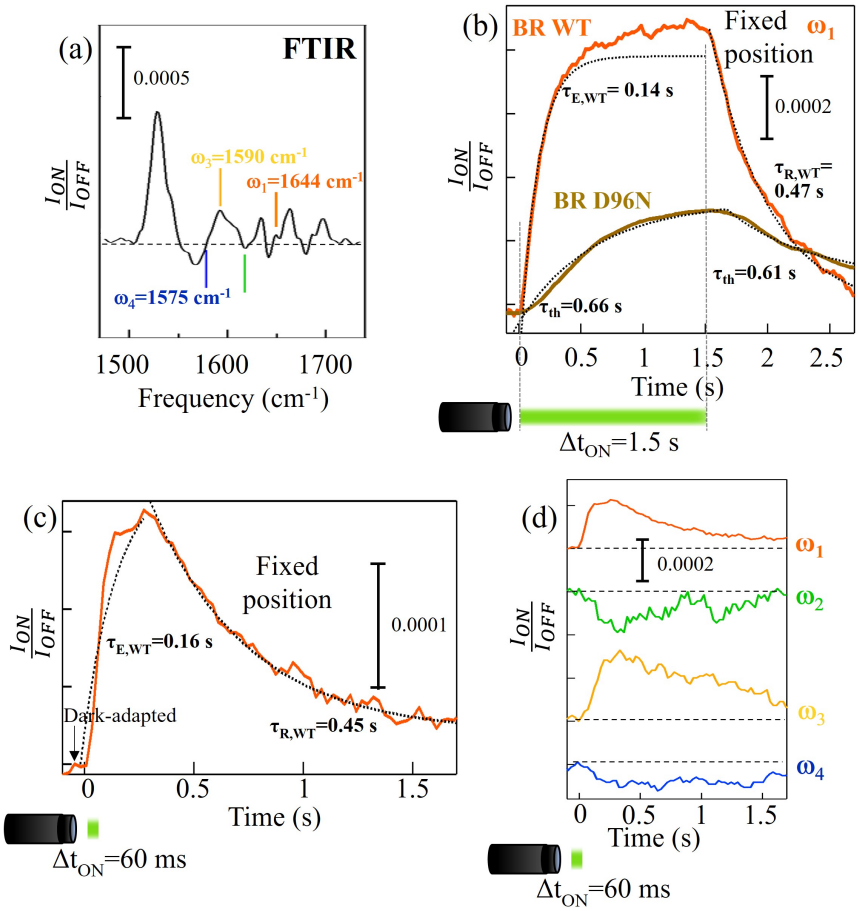

Figure 7.2. a) FTIR reference difference spectrum replotted from Fig.7.1d, highlighting the wavenumbers at which time traces are acquired. b) Time traces at ω_1 averaged over 80 repeated measurements on the same x-y position for BR WT (orange curve) and for the slow mutant BR D96N (gold curve) acquired with a visible illumination time Δt_{ON} of 1.5 s and a time resolution of 30 ms. c) The same of b) for BR WT with Δt_{ON}=60 ms. d) Time traces acquired at different wavenumbers (same color code of panel a) on BR WT with Δt_{ON}=60 ms. Adapted from [241].

into the visible optical channel, as illustrated in Fig.4.19. In the initial experiment, reflected-intensity time traces, denoted as $I_{ON}(t)$, are obtained for both BR WT and D96N. The green illumination pulse duration, Δt_{ON}, is set to 1.5 s, with a wait time of 1.8 s before the next pulse. The curve in Fig.7.2a represents the same FTIR data as in Fig.7.1d, but in this case, the quantity $\frac{I_{ON}}{I_{OFF}}$ is depicted, where I_{ON} and I_{OFF} represent the values of the reflected intensity under visible illumination and just before turning the LED on, respectively. The mid-IR frequencies selected for the time-resolved experiments are highlighted. Specifically, the orange one corresponds to $\lambda_1 = 6.08\ \mu m$ ($\omega_1 = 1644\ \text{cm}^{-1}$), which is close to the center of the amide I band where the α-helix absorption is maximized, and atmospheric attenuation is minimal. The time traces at ω_1, averaged over 80 photocycles excited at the same fixed position of the x-y stage, are presented in Fig.7.2b for both BR WT (orange

curve) and D96N (gold curve). The rapid BR WT photocycle is not significantly influenced by the repetition of subsequent illumination cycles with a total period of a few seconds. Consequently, meaningful time traces can be acquired without replacing the sample in the focus of the microscope. Specifically, the curve exhibits an exponential increase with a characteristic excitation time, τ_E, of 0.14 s, determined through fitting. This exponential increase is succeeded by a non-perfect asymptotic behavior and then by a slower exponential decay to the dark-adapted intensity value, with a characteristic relaxation time, τ_R, of 0.47 s, higher than τ_E. In Fig.7.2c, a time trace acquired on the WT at a fixed position, with the illumination time reduced to Δt_{ON}=60 ms, is also presented. This demonstrates that the excitation and relaxation times obtained from exponential fitting are consistent with those of the Δt_{ON}=1.5 s curve. Additionally, time traces of the BR WT protein have been acquired at different laser wavelengths and are depicted in Fig.7.2d. It is noteworthy that the sign of the spectral differences aligns with that of Fig.7.2a.
In contrast to the observations on BR WT, the BR D96N trace exhibits a slight increase with a characteristic photothermal time constant, τ_{th}, of 0.66 s. When the illumination is turned off, it decreases approximately with the same relaxation time constant τ_{th}. This suggests that, in the case of the slow mutant, without replacing the sample in the microscope focus, the conformational changes have a straightforward photothermal origin, specifically a local temperature increase due to the absorption of visible light from the LED illumination. The amide I signal increases and decreases with visible illumination turning on and off, respectively, without revealing any intrinsic photocycle dynamics. This can be elucidated by considering that after the first LED pulse, which excites the proteins in their dark-adapted BR* state, the subsequent 79 LED pulses hit the same proteins in a non-dark-adapted state, most likely a high vibrational level of the M state. This scenario does not initiate any photocycle but only induces photothermal effects. Consequently, this observation underscores the importance of the correct procedure, suggesting that measuring the photocycle of the slow mutant BR D96N is best achieved by mapping the sample to probe the proteins, always starting from the dark-adapted state.
In this context, the experiment on BR D96N is reiterated by acquiring single time traces at 80 distinct positions, marked by the grid of white spots in Fig.7.3a. The data obtained with a visible single pulse illumination of Δt_{ON}=1.5 s are subsequently averaged to derive the final time trace. To avoid potential effects of diffuse light within the droplet, the replacement step is set at 250 μm. Time traces are acquired at two different mid-IR wavelengths: $\lambda_1 = 6.08\ \mu m$ (ω_1 =1644 cm^{-1}) and $\lambda_4 = 6.35\ \mu m$ (ω_4 = 1575 cm^{-1}), highlighted in the FTIR difference spectrum of Fig.7.3b. The resulting curve at ω_1 (amide I) is depicted in Fig.7.3c (dark red curve). In these conditions, the photothermal contribution to the amide I difference signal cannot be neglected, as done in Fig.7.2b for the BR WT. Hence, it becomes important to eliminate the signal contribution from proteins that undergo no conformational changes associated with the photocycle, as their signal is only due to temperature increase. Subsequently, an exponential profile with τ_{th}=0.66 s is subtracted from the raw data (dashed gold curve), both in the increasing and decreasing ranges of the signal, as observed from the curve acquired on the BR D96N in a fixed position. The resulting red curve in Fig.7.3c reveals two distinct characteristic times that can be fitted with simple exponential relations: a short $\tau_{E,D96N}$=0.88 s for the excitation

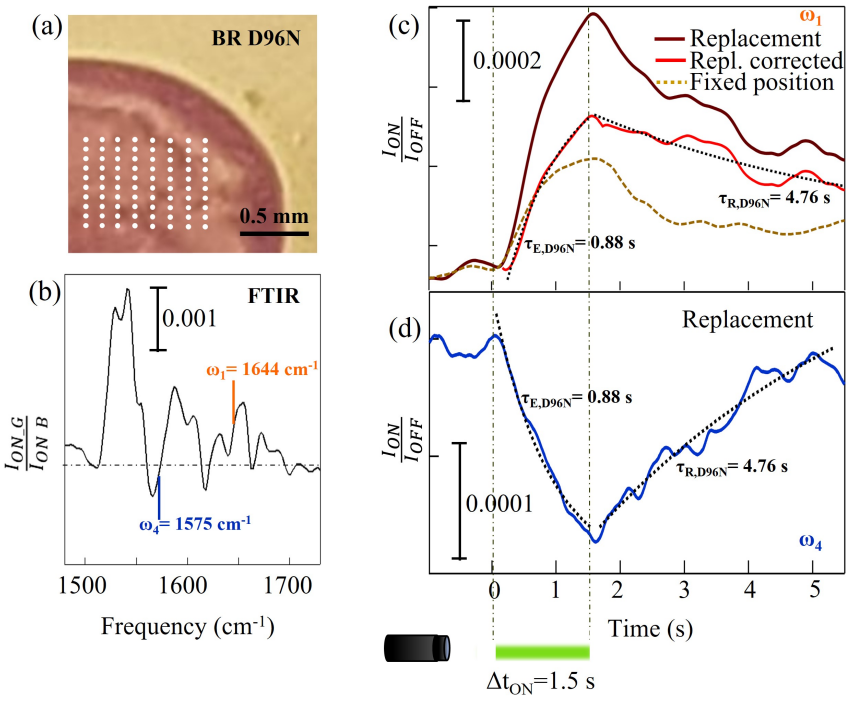

Figure 7.3. a) Picture of part of the BR D96N dried drop with indication of the array of probed areas (white spots) by mapping with the QCL-microscope. b) FTIR reference difference spectrum replotted from Fig.7.1e. c) Time traces at ω_1 with and without sample replacement for the slow mutant D96N (dark red and dashed gold curves, respectively). The red curve is the subtraction between the other two curves. d) Time trace at ω_2 showing the opposite sign of the spectral difference as expected from panel b). Adapted from [241].

of the M intermediate under green light illumination, and a long $\tau_{R,D96N}$=4.8 s for relaxation back to the dark-adapted state BR* after the light pulse is turned off. This gradual relaxation from the intermediate M to the dark-adapted state BR* stands as the primary characteristic of the slow mutant BR D96N, linked to the substitution of the hydrogen-binding amino acid aspartic acid in position 96 with asparagine. This substitution inhibits the hydrogen-transfer capability to the retinal, slowing down the M to BR* transition. Fig.7.3d illustrates the time trace acquired on the same sample at ω_4=1575 cm^{-1}, which is associated with conformational changes of the retinal. In the case of BR, only when the protein undergoes its conformational change from the M to the N and finally to the O state the retinal reverts its photoisomerization. Consequently, there exists a notable correlation between the relaxation time of the amide I and retinal signals, as verified by the fitting curves in Fig.7.3d (dotted black curves). These curves are obtained by imposing the same τ_E and τ_R values derived from the fitting of the red curve in Fig.7.3c. Remarkably, there is no need to subtract the photothermal signal at this wavenumber, corresponding to the edge of the strongest retinal absorption change, as the signal is nearly insensitive to temperature.
It is then possible to establish a connection between the experimentally observed τ_E

and τ_R and the photochemical reaction rates of the BR* to M transition in both BR WT and the D96N mutant. Specifically, the reactions can be expressed as follows:

$$BR^* \underset{k_1}{\overset{k_2}{\leftrightarrows}} M \tag{7.1}$$

during the visible light illumination, and

$$M \overset{k_2}{\rightarrow} BR^* \tag{7.2}$$

after the light excitation.
As previously mentioned, the experiment conducted allows for the assumption of a simplified photocycle with only two dominant states: the dark-adapted state BR* and the longest lifetime intermediate M. This occurrence is distinctive of BR proteins in dry conditions, as also demonstrated by FTIR spectroscopy (Fig.7.1). The scarcity of protons in the dry environment slows down the M to N transition, and the green light is partly absorbed by the N and O intermediates, depopulating them. However, the M intermediate does not significantly absorb the green light, as its optical absorbance peaks sharply in the blue light. The rate law of the chemical kinetics can be applied to the reversible reaction BR* $\leftrightarrows$ M. During the excitation light pulse, not only does BR* transition to M (forward reaction rate k_1), but also the fast non-radiative relaxation from M to BR* occurs (backward reaction rate $k_2 < k_1$) [243]. When the LED is turned off, the intermediate state M is depleted with a rate k_2 and without any counter reaction. The values of k_1 and k_2 can then be derived from the experimentally determined τ_E and τ_R as follows:

$$k_1 + k_2 = \frac{1}{\tau_E} \tag{7.3}$$

$$k_2 = \frac{1}{\tau_R} \tag{7.4}$$

For BR WT, the derived reaction rates are $k_{1,WT}$=4.0 s^{-1} and $k_{2,WT}$=2.2 s^{-1}. It is worth to note that the population of the M state reached at the end of the LED pulse, when chemical equilibrium is established, is lower than the initial BR* population by an efficiency factor of $\frac{k_1}{(k_1+k_2)}$=0.64. However, the WT BR time trace in Fig.7.2b (orange curve) does not reach an asymptote at $t > 5\tau_E$=0.7 s due to unavoidable photothermal effects. In both BR WT and BR D96N, temperature increases caused by visible light absorption result in small secondary structure changes, continuing to occur in the time interval 0.7–1.5 s. Regarding the slow mutant BR D96N, the reaction rates are $k_{1,D96N}$=0.93 s^{-1} and $k_{2,D96N}$=0.21 s^{-1}. The efficiency factor is 0.82, higher than that of BR WT, due to the much slower backward reaction rate, $k_{2,D96N} << k_{2,WT}$, correlated to the longer lifetime of the intermediate M state. As mentioned earlier, the backward reaction rate of the slow mutant BR D96N is obtained from the fitting of the time trace acquired by averaging over 80 photocycles with sample replacement. This measurement approach would not be feasible while resting at a fixed position with alternating green and blue light illumination periods, as done in the FTIR experiment of Fig.7.1e. This is because the absorption of blue light shortcuts the photocycle, preventing its completion.

Conclusions

My PhD project has focused on the application to membrane proteins of a state-of-the-art nanoscale IR spectroscopy technique, known as AFM-IR, with the implementation of the capability to control static electric fields applied through the metal-coated AFM tip. The primary motivation of this project is to investigate the conformational changes of proteins as a function of an external electric field, a phenomenon not easily accessible with existing biophysical methods and particularly important for transmembrane proteins, which are naturally exposed to the membrane potential. In the last decades, the AFM-IR technique has been widely applied to biological matter. Indeed, by operating in contact mode, the AFM tip detects the photo-induced thermal expansion of the sample, which is particularly advantageous for biological samples characterized by low thermal conduction and high thermal expansion coefficients. The new aspect introduced here, i.e. the ability to control static electric fields exploiting AFM tips as nanoelectrodes, brings an innovative dimension to AFM-IR studies in biology.

Let me now summarize my results. Firstly, I have demonstrated the capability of the nanospectroscopy platform AFM-IR to monitor the conformational changes of about 10^2 protein molecules of the Channelrhodopsin photosensitive protein on a double cell membrane stack with a total thickness of 14 nm [21]. The achievement holds importance for neuroscience research due to ChR role as a key optogenetic tool. The obtained results not only deepen the understanding of the protein function at the molecular level but also paves the way for optimizing its performance in optogenetic applications, ultimately advancing the ability to modulate neuronal activity with precision. In addition, the comparison between IR spectroscopy results obtained through conventional far-field IR spectroscopy and those from AFM-IR reveals some variations in the conformational changes of the proteins. These differences can be attributed to the distinct response of ChR when in contact with metallic surfaces, possibly arising from the different electrostatic environment.

Secondly, after the successful integration and optimization of an electric circuit in the AFM-IR setup, I began the validation and calibration process of the electric-field dependent AFM-IR technique on homogeneous PMMA films. When the polymer thickness is higher (55 nm) than the typical end-to-end chain length ($\sim$ 22 nm), the main observed effect on the IR spectral signature has been attributed to the Vibrational Stark Effect, owing to the limited orientational degree of freedom of the chemical bonds. In reverse, thin film with thickness $\leq$ 30 nm showed orientational freedom. In this phase of the study, I also tested and employed various AFM probes with different shapes and dimensions of the tip apex to examine and compare with numerical simulations the spatial electromagnetic configuration of both the IR

field-enhancement and the static electric field.
Moving to the ferroelectric polymer PVDF, characterized by multi-phase regions at the nanoscale, distinct responses could be discerned within the paraelectric α-phase and the ferroelectric β-phase upon application of an electric field, predominantly attributable to non-permanent and permanent reorientational motions.
Finally, proceeding towards membrane proteins, I performed the first experiments on a Bacteriorhodopsin double-stack made of individual cell membranes. In the absence of photoexcitation, which is the charge transport energy source in the natural protein function, our results revealed changes in the protein secondary structure and protonation state of amino acid residues when a voltage of $\pm 3V$ was applied. The results shed light on the protein dynamic behavior in response to external electric stimuli, arising as a starting point for the realization and interpretation of future experiments. Looking ahead, the objective is to integrate the photoexcitation in our setup with external potential control mimicking the membrane potential and aligning with physiological conditions. However, achieving this goal may require improvements in the signal-to-noise ratio of the current AFM-IR setup, as discernible spectral signatures of protein variations were not evident when we tried to reduce the intensity of the applied electric field.
Additionally, the perspective of investigating the kinetics of protein activity through time-resolved measurements on the millisecond time scale with AFM-IR is both fascinating and promising. In view of this innovation, I also worked in the development of an IR microscope featuring a quantum cascade laser source to probe the protein kinetics and a parallel visible illumination channel for the photoexcitation. This setup enabled to conduct IR time-resolved measurements on Bacteriorhodopsin samples (wild-type and D96N "slow mutant") by leveraging the mapping mode, which allows for sample replacement after each visible photoexcitation [188, 241]. This instrument can therefore serve as an initial reference and a benchmark for potential future addition of time-resolution to AFM-IR experiments.
In summary, this PhD work represents a significant contribution to both the field of nanoscale IR spectroscopy and the field of membrane protein biophysics. On one side, it introduces the capability to probe electric-field-dependent effects on diverse samples at the nanoscale, thereby expanding the potential of IR nanospectroscopy. On the other side, it provides a suitable experimental configuration to correlate the functional activity of membrane proteins with the value of the transmembrane potential experienced by the proteins themselves.

Appendix I: Bacteriorhodopsin photocycle

To show the complexity of the processes involved in the BR photocycle, I report here the main steps that allow the passage of the proton through the amino acid residues:

- BR_{568}: the amino acid residues Asp-212, Asp-85, Arg-82 and the protonated Schiff base interact to form an electrostatically active site. A network of residues connected by hydrogen bonds (water, Asp-212, Tyr-185 and Thr-89) allows a partial protonation of Asp-212 through negative charge delocalization, in correspondence with the partial deprotonation observed in Tyr-185.

- K_{590}: the retinal isomerization from all-*trans* to 13-*cis* destroys the network of hydrogen bonds corresponding to the protonation increase of Tyr-185.

- L_{550}: in the transition between the L and M intermediates, the Schiff base deprotonates in favor of the Asp-85 residue, while a proton is released into the extracellular environment by a network of hydrogen bonds comprising molecules of water and the amino acid residues Arg-82, Glu-204 and Glu-194.

- M_{412}: as soon as the intermediate M is formed, a network of hydrogen bonds is established involving several water molecules in addition to the residues Asp-96, Thr-46, Thr-89, Thr-185 and Asp-212. This network has the effect of acting as a proton chain increasing the protonation status of Asp-212. In the transition between the intermediates M and N a rigid movement of the seventh α-helix is observed to allow the Schiff base to orient from the proton release site to the purchase site, thereby determining the directionality of the proton pump.

- N_{530}: in the transition between the M and N intermediates the Schiff base reprotonation takes place. This occurs through a network of residues linked by hydrogen bonds comprising also Asp-212. The latter, being the closest amino acid residue to the Schiff base, is also the last proton donor. The whole process thus includes the transfer of a proton from Asp-212 to Schiff base and the simultaneous entry of a proton from Asp-96 into the hydrogen bond network.

- O_{640}: the transition between N and O intermediates involves the reprotonation of Asp-96 from the cytoplasmic environment and the simultaneous reisomerization of the retinal from 13-*cis* to all-*trans*.

Appendix II: Operating principles of FTIR

In a FTIR interferometer the light beam emitted by the source and collimated by a parabolic mirror is divided in two light beams through a beamsplitter, which reflects part of the light and transmits the rest. The two light beams then travel different paths with different distances: one is reflected by a fixed mirror and the other by a moving mirror. After that, they are recombined into one beam to interact with the sample and be revealed at the detector position. Considering the fixed mirror at a distance D with respect to the beamsplitter, the position of the moving mirror is equal to $D+x$, which results in a optical path difference of $\delta = 2x$ that is the difference in distance travelled by the two light beams. When the two distances are identical, then $\delta = 0$ and the condition is called zero path difference, or ZPD. The recombination of the two beams causes an interference, which means that the two wave amplitudes add together to form a single wave. We can assume, for simplicity, to have a monochromatic beam of wavelength λ. If $\delta = 0$, the two beams are perfectly in phase when they recombine on the beamsplitter and the interference is said to be constructive, i.e. the intensity of the beam reaching the detector is equal to the sum of the intensity of the two beams (Fig.7.4a). This condition is always satisfied when the optical path difference between the two beams is a multiple of their wavelength $\delta = n\lambda$, with n integer. When the moving mirror shifts with respect to the position of the ZPD, the way the two beams interfere changes. If $\delta = \frac{1}{2}\lambda$, the two beams are out of phase and give rise to a destructive interference, i.e. the intensity of the beam reaching the detector is equal to the difference of the intensity of the two beams (Fig.7.4b). This happens every time the condition $\delta = (n + \frac{1}{2})\lambda$ is satisfied. If the mobile mirror moves with a constant velocity, the light intensity detected as a function of the optical path difference, i.e. the interferogram, has a sinusoidal shape and the maximum of the signal is registered every time that $\delta = n\lambda$. So that the intensity of the light $I(\delta)$ can be written as

$$I(\delta) = \frac{1}{2} I(\nu_0)(1 + cos(2\pi\nu_0\delta)) \tag{7.5}$$

Where I(ν_0) represents the total intensity of the radiation emitted at frequency ν_0 and the additive constant term can be neglected since it is not important in spectrometric measurements. Thus one obtains

$$I(\delta) = \frac{1}{2} I(\nu_0) cos(2\pi\nu_0\delta) \tag{7.6}$$

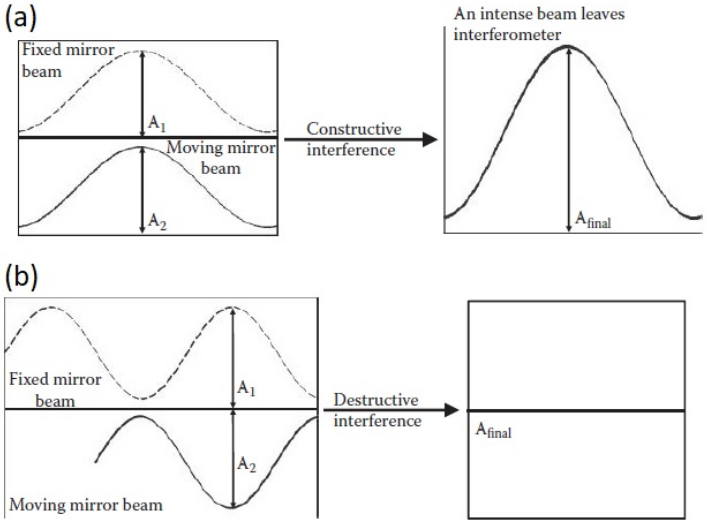

Figure 7.4. (a) Constructive interference of the two in phase beams reflected, respectively, by the fixed and by the moving mirror in the interferometer. (b) Destructive interference of the two beams out-of-phase [186].

Some side effects, such as beamsplitter efficiency, detector response and amplifier characteristics which can affect the maximum intensity of the signal amplitude, must be taken into consideration. Combining all these effects in a single frequency-dependent correction factor, the term $B(\nu_0)$ gives the intensity of the source at a wavenumber as modified by the instrumental characteristics and the trend of the interferogram results to be equal to

$$I'(\delta) = B(\nu_0)cos(2\pi\nu_0\delta) \tag{7.7}$$

where, matematically, $I'(\delta)$ is the cosine Fourier transform of $B(\nu_0)$. The spectrum is indeed calculated from the interferogram by computing the cosine Fourier transform of $I'(\delta)$. Considering a broadband source, the measured interferogram is the result of all the interferograms at the different wavelengths λ, which can be written as an integral over all the frequencies

$$I'(\delta) = \int_{-\infty}^{+\infty} B(\nu)cos(2\pi\nu\delta)d\nu \tag{7.8}$$

whose Fourier transform is

$$B(\nu) = \int_{-\infty}^{+\infty} I'(\delta)cos(2\pi\nu\delta)d\delta \tag{7.9}$$

since $I(\delta)$ is an even function

$$B(\nu) = 2\int_{0}^{+\infty} I'(\delta)cos(2\pi\nu\delta)d\delta \tag{7.10}$$

The equation shows the case in which the spectrum is recorded in frequency from 0 to $+\infty$. This is practically not possible as a movement of the mirror for an infinite

distance would be necessary. The consequence of integration over a finite optical path is a finite resolution of the spectrum. Thus, if the maximum retardation of an interferometer is Δ, the best resolution that could be obtained using this interferometer $\Delta\nu$ is given by $\Delta\nu = (\Delta)^{-1}$. This mathematically corresponds to multiply the complete interferogram (between $\delta = -\infty$ and $\delta = +\infty$) by a truncation function, $D(\delta)$

$$D(\delta) = \begin{cases} 1 & \text{if } -\Delta < \delta < +\Delta \\ 0 & \text{if } \delta > |\Delta| \end{cases} \tag{7.11}$$

it is often called a boxcar truncation function. The spectrum thus results to be

$$B(\nu) = \int_{-\infty}^{+\infty} I'(\delta) D(\delta) cos(2\pi\nu\delta) d\delta \tag{7.12}$$

The Fourier transform of the product of two functions is the convolution of the Fourier transform of each function, so that

$$G(\nu) = B(\nu) * f(\nu) = \int_{-\infty}^{+\infty} B(\nu') f(\nu - \nu') d\nu' \tag{7.13}$$

where B(ν) is the Fourier transform of the real spectrum $I'(\delta)$ and $f(\nu)$ is the Fourier transform of $D(\delta)$, defined as

$$f(\nu) = 2\Delta \frac{sin 2\pi\nu\Delta}{2\pi\nu\Delta} = 2\Delta sinc(2\pi\nu\Delta) \tag{7.14}$$

The spectrum thus results to be convoluted with the sinc function *f*. When the sinc function is convoluted with a single spectral line of wavenumber ν_1 the resulting curve is

$$B(\nu) = 2\Delta B(\nu_1) sinc[2\pi(\nu_1 - \nu)\Delta] \tag{7.15}$$

Since the function intersects the frequency axis at $(2\Delta)^{-1} cm^{-1}$ on either side of ν_1, it can be seen that two lines separated by twice this amount, would be completely resolved, hence the spectral resolution is better than this value [244].

List of publications

I report here the list of articles published in international peer-reviewed journals related to the topic of my PhD work:

- Venanzi, T., Giliberti, V., **Temperini, M. E.**, Sotgiu, S., Polito, R., Mattioli, F., Pitanti, A., Mišeikis, V., Coletti, C., Roddaro, S., Baldassarre L. and Ortolani, M. Mid-infrared photocurrent nano-spectroscopy exploiting the thermoelectric effect in graphene. *Applied Physics Letters*, 123(15), 2023.

- Intze, A., **Temperini, M. E.**, Baldassarre, L., Giliberti, V., Ortolani, M. and Polito, R. Time-resolved investigation of nanometric cell membrane patches with a mid-infrared laser microscope. *Frontiers in Photonics*, 4, 1175033, 2023.

- **Temperini, M. E.**, Polito, R., Intze, A., Gillibert, R., Berkmann, F., Baldassarre, L., Giliberti, V. and Ortolani, M. A mid-infrared laser microscope for the time-resolved study of light-induced protein conformational changes. *Review of Scientific Instruments*, 94(6), 2023.

- **Temperini, M. E.**, Di Giacinto, F., Romanò, S., Di Santo, R., Augello, A., Polito, R., Baldassarre, L., Giliberti, V., Papi, M., Basile, U., Niccolini, B., Krasnowska, E .K., Serafino, A., De Spirito, M., Di Gaspare, A., Ortolani, M. and Ciasca, G. Antenna-enhanced mid-infrared detection of extracellular vesicles derived from human cancer cell cultures. *Journal of Nanobiotechnology*, 20(1), 1-20, 2022.

- Polito, R., **Temperini, M. E.**, Ritter, E., Puskar, L., Schade, U., Broser, M., Hegemann, P., Baldassarre, L., Ortolani, M. and Giliberti, V. Conformational changes of a membrane protein determined by infrared difference spectroscopy beyond the diffraction limit. *Physical Review Applied*, 16(1), 014048, 2021.

- Polito, R., Musto, M., **Temperini, M. E.**, Ballerini, L., Ortolani, M., Baldassarre, L., Casalis, L. and Giliberti, V. Infrared nanospectroscopy of individual extracellular microvesicles. *Molecules*, 26(4), 887, 2021.

Submitted manuscript:

- **Temperini M. E.**, Polito, R., Venanzi, T., Baldassarre, L., Hu, H., Ciracì, C., Pea, M., Notargiacomo, A., Mattioli, F., Ortolani, M. and Giliberti, V. An Infrared Nanospectroscopy Technique for the Study of Electric-field Induced Molecular Dynamics and Charge Transport.
  Under review on *Nano Letters*, 2024.

Bibliography

[1] Nikolai Vsevolodov. *Biomolecular electronics: an introduction via photosensitive proteins*. Springer Science & Business Media, 2012.

[2] Karl Svennersten, Karin C Larsson, Magnus Berggren, and Agneta Richter-Dahlfors. Organic bioelectronics in nanomedicine. *Biochimica et Biophysica Acta (BBA)-General Subjects*, 1810(3):276–285, 2011.

[3] Elena G Govorunova, Oleg A Sineshchekov, Hai Li, and John L Spudich. Microbial rhodopsins: diversity, mechanisms, and optogenetic applications. *Annual review of biochemistry*, 86:845–872, 2017.

[4] Zhouting Jiang, Le You, Wenhui Dou, Tingting Sun, and Peng Xu. Effects of an electric field on the conformational transition of the protein: A molecular dynamics simulation study. *Polymers*, 11(2):282, 2019.

[5] Taeyoung Yoon, Wooboum Park, Yoonjung Kim, and Sungsoo Na. Electric field-mediated regulation of enzyme orientation for efficient electron transfer at the bioelectrode surface: A molecular dynamics study. *Applied Surface Science*, 608:155124, 2023.

[6] Mathias Grote, Martin Engelhard, and Peter Hegemann. Of ion pumps, sensors and channels—perspectives on microbial rhodopsins between science and history. *Biochimica et Biophysica Acta (BBA)-Bioenergetics*, 1837(5):533–545, 2014.

[7] Aleksei Mikhailovich Bonch-Bruevich and Khodovoĭ. Current methods for the study of the stark effect in atoms.

[8] Tao Jiang, Biao-Feng Zeng, Bintian Zhang, and Longhua Tang. Single-molecular protein-based bioelectronics via electronic transport: fundamentals, devices and applications. *Chemical Society Reviews*, 2023.

[9] Andrea Alessandrini, Marco Salerno, Stefano Frabboni, and Paolo Facci. Single-metalloprotein wet biotransistor. *Applied Physics Letters*, 86(13), 2005.

[10] Jerry A Fereiro, Xi Yu, Israel Pecht, Mordechai Sheves, Juan Carlos Cuevas, and David Cahen. Tunneling explains efficient electron transport via protein junctions. *Proceedings of the National Academy of Sciences*, 115(20):E4577–E4583, 2018.

[11] Joseph M Brisendine, Sivan Refaely-Abramson, Zhen-Fei Liu, Jing Cui, Fay Ng, Jeffrey B Neaton, Ronald L Koder, and Latha Venkataraman. Probing charge transport through peptide bonds. *The journal of physical chemistry letters*, 9(4):763–767, 2018.

[12] Yongdong Jin, Noga Friedman, Mordechai Sheves, Tao He, and David Cahen. Bacteriorhodopsin (br) as an electronic conduction medium: Current transport through br-containing monolayers. *Proceedings of the National Academy of Sciences*, 103(23):8601–8606, 2006.

[13] Izhar Ron, Lior Sepunaru, Stella Itzhakov, Tatyana Belenkova, Noga Friedman, Israel Pecht, Mordechai Sheves, and David Cahen. Proteins as electronic materials: Electron transport through solid-state protein monolayer junctions. *Journal of the American Chemical Society*, 132(12):4131–4140, 2010.

[14] John T Pelton and Larry R McLean. Spectroscopic methods for analysis of protein secondary structure. *Analytical biochemistry*, 277(2):167–176, 2000.

[15] Li Cui, Bo Liu, David Vonlanthen, Marcel Mayor, Yongchun Fu, Jian-Feng Li, and Thomas Wandlowski. In situ gap-mode raman spectroscopy on single-crystal au (100) electrodes: tuning the torsion angle of 4, 4-biphenyldithiols by an electrochemical gate field. *Journal of the American Chemical Society*, 133(19):7332–7335, 2011.

[16] Zheng Liu, Song-Yuan Ding, Zhao-Bin Chen, Xiang Wang, Jing-Hua Tian, Jason R Anema, Xiao-Shun Zhou, De-Yin Wu, Bing-Wei Mao, Xin Xu, et al. Revealing the molecular structure of single-molecule junctions in different conductance states by fishing-mode tip-enhanced raman spectroscopy. *Nature communications*, 2(1):305, 2011.

[17] Stefan Kradolfer, Ewelina Lipiec, Chiara Baldacchini, Anna Rita Bizzarri, Salvatore Cannistraro, and Renato Zenobi. Vibrational changes induced by electron transfer in surface bound azurin metalloprotein studied by tip-enhanced raman spectroscopy and scanning tunneling microscopy. *ACS nano*, 11(12):12824–12831, 2017.

[18] Dean Kos, Giuliana Di Martino, Alexandra Boehmke, Bart de Nijs, Dénes Berta, Tamás Földes, Sara Sangtarash, Edina Rosta, Hatef Sadeghi, and Jeremy J Baumberg. Optical probes of molecules as nano-mechanical switches. *Nature Communications*, 11(1):5905, 2020.

[19] A Dazzi, R Prazeres, F Glotin, and JM Ortega. Local infrared microspectroscopy with subwavelength spatial resolution with an atomic force microscope tip used as a photothermal sensor. *Optics letters*, 30(18):2388–2390, 2005.

[20] Valeria Giliberti, Raffaella Polito, Eglof Ritter, Matthias Broser, Peter Hegemann, Ljiljana Puskar, Ulrich Schade, Laura Zanetti-Polzi, Isabella Daidone, Stefano Corni, et al. Tip-enhanced infrared difference-nanospectroscopy of the proton pump activity of bacteriorhodopsin in single purple membrane patches. *Nano Letters*, 19(5):3104–3114, 2019.

[21] Raffaella Polito, Maria Eleonora Temperini, Eglof Ritter, Ljiljana Puskar, Ulrich Schade, Matthias Broser, Peter Hegemann, Leonetta Baldassarre, Michele Ortolani, and Valeria Giliberti. Conformational changes of a membrane protein determined by infrared difference spectroscopy beyond the diffraction limit. *Physical Review Applied*, 16(1):014048, 2021.

[22] Wilfred D Stein and Thomas Litman. *Channels, carriers, and pumps: an introduction to membrane transport*. Elsevier, 2014.

[23] Zoe Cournia, Toby W Allen, Ioan Andricioaei, Bruno Antonny, Daniel Baum, Grace Brannigan, Nicolae-Viorel Buchete, Jason T Deckman, Lucie Delemotte, Coral Del Val, et al. Membrane protein structure, function, and dynamics: a perspective from experiments and theory. *The Journal of membrane biology*, 248:611–640, 2015.

[24] A Rachael Curran and Donald M Engelman. Sequence motifs, polar interactions and conformational changes in helical membrane proteins. *Current opinion in structural biology*, 13(4):412–417, 2003.

[25] Laura Orellana. Large-scale conformational changes and protein function: breaking the in silico barrier. *Frontiers in molecular biosciences*, 6:117, 2019.

[26] Martin Karplus and J Andrew McCammon. Molecular dynamics simulations of biomolecules. *Nature structural biology*, 9(9):646–652, 2002.

[27] Stephen H Wright. Generation of resting membrane potential. *Advances in physiology education*, 28(4):139–142, 2004.

[28] Biologie 2e. `https://openstax.org/books/biology-2e/pages/preface`.

[29] Mark W Barnett and Philip M Larkman. The action potential. *Practical neurology*, 7(3):192–197, 2007.

[30] Bruce P Bean. The action potential in mammalian central neurons. *Nature Reviews Neuroscience*, 8(6):451–465, 2007.

[31] Kenhub. `https://www.kenhub.com/en/library/anatomy/action-potential`.

[32] Jeremy Nathans. Rhodopsin: structure, function, and genetics. *Biochemistry*, 31(21):4923–4931, 1992.

[33] Santosh T Menon, May Han, and Thomas P Sakmar. Rhodopsin: structural basis of molecular physiology. *Physiological reviews*, 81(4):1659–1688, 2001.

[34] Xiuwen Zhou, Dage Sundholm, Tomasz A Wesołowski, and Ville RI Kaila. Spectral tuning of rhodopsin and visual cone pigments. *Journal of the American Chemical Society*, 136(7):2723–2726, 2014.

[35] Eriko Nango, Antoine Royant, Minoru Kubo, Takanori Nakane, Cecilia Wickstrand, Tetsunari Kimura, Tomoyuki Tanaka, Kensuke Tono, Changyong Song, Rie Tanaka, et al. A three-dimensional movie of structural changes in bacteriorhodopsin. *Science*, 354(6319):1552–1557, 2016.

[36] Sławomir Filipek, Ronald E Stenkamp, David C Teller, and Krzysztof Palczewski. G protein-coupled receptor rhodopsin: a prospectus. *Annual review of physiology*, 65(1):851–879, 2003.

[37] Oliver P Ernst, David T Lodowski, Marcus Elstner, Peter Hegemann, Leonid S Brown, and Hideki Kandori. Microbial and animal rhodopsins: structures, functions, and molecular mechanisms. *Chemical reviews*, 114(1):126–163, 2014.

[38] J Dobler, Wolfgang Zinth, Wolfgang Kaiser, and Dieter Oesterhelt. Excited-state reaction dynamics of bacteriorhodopsin studied by femtosecond spectroscopy. *Chemical physics letters*, 144(2):215–220, 1988.

[39] KC Hasson, Feng Gai, and Philip A Anfinrud. The photoisomerization of retinal in bacteriorhodopsin: experimental evidence for a three-state model. *Proceedings of the National Academy of Sciences*, 93(26):15124–15129, 1996.

[40] Janos K Lanyi. Bacteriorhodopsin. *Annu. Rev. Physiol.*, 66:665–688, 2004.

[41] Joachim Heberle, Jörg Fitter, Hans Jürgen Sass, and Georg Büldt. Bacteriorhodopsin: the functional details of a molecular machine are being resolved. *Biophysical chemistry*, 85(2-3):229–248, 2000.

[42] Pooja Singh, Shelly Singh, Neena Jaggi, Ki-Hyun Kim, and Pooja Devi. Recent advances in bacteriorhodopsin-based energy harvesters and sensing devices. *Nano Energy*, 79:105482, 2021.

[43] Norbert Hampp and Dieter Oesterhelt. Bacteriorhodopsin and its potential in technical applications. *Nanobiotechnology: concepts, applications and perspectives*, pages 146–167, 2004.

[44] Yu-Tao Li, Ye Tian, He Tian, Tao Tu, Guang-Yang Gou, Qian Wang, Yan-Cong Qiao, Yi Yang, and Tian-Ling Ren. A review on bacteriorhodopsin-based bioelectronic devices. *Sensors*, 18(5):1368, 2018.

[45] Mark S Braiman, Tatsushi Mogi, Thomas Marti, Lawrence J Stern, H Gobind Khorana, and Kenneth J Rothschild. Vibrational spectroscopy of bacteriorhodopsin mutants: light-driven proton transport involves protonation changes of aspartic acid residues 85, 96, and 212. *Biochemistry*, 27(23):8516–8520, 1988.

[46] Christian Zscherp and Joachim Heberle. Infrared difference spectra of the intermediates l, m, n, and o of the bacteriorhodopsin photoreaction obtained by time-resolved attenuated total reflection spectroscopy. *The Journal of Physical Chemistry B*, 101(49):10542–10547, 1997.

[47] Jin-An He, Lynne Samuelson, Lian Li, Jayant Kumar, and Sukant K Tripathy. Bacteriorhodopsin thin-film assemblies—immobilization, properties, and applications. *Advanced Materials*, 11(6):435–446, 1999.

[48] Martin Holz, Lel A Drachev, Tatsushi Mogi, Harald Otto, Andrey D Kaulen, Maarten P Heyn, Vladimir P Skulachev, and H Gobind Khorana. Replacement

of aspartic acid-96 by asparagine in bacteriorhodopsin slows both the decay of the m intermediate and the associated proton movement. *Proceedings of the National Academy of Sciences*, 86(7):2167–2171, 1989.

[49] Karl Deisseroth and Peter Hegemann. The form and function of channelrhodopsin. *Science*, 357(6356):eaan5544, 2017.

[50] Karl Deisseroth. Optogenetics. *Nature methods*, 8(1):26–29, 2011.

[51] Oleksandr Volkov, Kirill Kovalev, Vitaly Polovinkin, Valentin Borshchevskiy, Christian Bamann, Roman Astashkin, Egor Marin, Alexander Popov, Taras Balandin, Dieter Willbold, et al. Structural insights into ion conduction by channelrhodopsin 2. *Science*, 358(6366):eaan8862, 2017.

[52] Víctor A Lórenz-Fonfría, Tom Resler, Nils Krause, Melanie Nack, Michael Gossing, Gabriele Fischer von Mollard, Christian Bamann, Ernst Bamberg, Ramona Schlesinger, and Joachim Heberle. Transient protonation changes in channelrhodopsin-2 and their relevance to channel gating. *Proceedings of the National Academy of Sciences*, 110(14):E1273–E1281, 2013.

[53] André Berndt, Ofer Yizhar, Lisa A Gunaydin, Peter Hegemann, and Karl Deisseroth. Bi-stable neural state switches. *Nature neuroscience*, 12(2):229–234, 2009.

[54] Ali A Kermani. A guide to membrane protein x-ray crystallography. *The FEBS journal*, 288(20):5788–5804, 2021.

[55] Yunfei Hu, Kai Cheng, Lichun He, Xu Zhang, Bin Jiang, Ling Jiang, Conggang Li, Guan Wang, Yunhuang Yang, and Maili Liu. Nmr-based methods for protein analysis. *Analytical chemistry*, 93(4):1866–1879, 2021.

[56] Radostin Danev, Haruaki Yanagisawa, and Masahide Kikkawa. Cryo-electron microscopy methodology: current aspects and future directions. *Trends in biochemical sciences*, 44(10):837–848, 2019.

[57] Antoine Royant, Peter Nollert, Karl Edman, Richard Neutze, Ehud M Landau, Eva Pebay-Peyroula, and Javier Navarro. X-ray structure of sensory rhodopsin ii at 2.1-å resolution. *Proceedings of the National Academy of Sciences*, 98(18):10131–10136, 2001.

[58] Arisu Shigeta, Shota Ito, Keiichi Inoue, Takashi Okitsu, Akimori Wada, Hideki Kandori, and Izuru Kawamura. Solid-state nuclear magnetic resonance structural study of the retinal-binding pocket in sodium ion pump rhodopsin. *Biochemistry*, 56(4):543–550, 2017.

[59] Kyle Tucker, Savitha Sridharan, Hillel Adesnik, and Stephen G Brohawn. Cryo-em structures of the channelrhodopsin chrmine in lipid nanodiscs. *Nature communications*, 13(1):4842, 2022.

[60] Jean-Jacques Lacapere, Eva Pebay-Peyroula, Jean-Michel Neumann, and Catherine Etchebest. Determining membrane protein structures: still a challenge! *Trends in biochemical sciences*, 32(6):259–270, 2007.

[61] Majed Chergui and Eric Collet. Photoinduced structural dynamics of molecular systems mapped by time-resolved x-ray methods. *Chemical reviews*, 117(16):11025–11065, 2017.

[62] Harshwardhan Poddar, Derren J Heyes, Giorgio Schirò, Martin Weik, David Leys, and Nigel S Scrutton. A guide to time-resolved structural analysis of light-activated proteins. *The FEBS Journal*, 289(3):576–595, 2022.

[63] Toshio Ando, Takayuki Uchihashi, and Noriyuki Kodera. High-speed afm and applications to biomolecular systems. *Annual review of biophysics*, 42:393–414, 2013.

[64] Alma P Perrino, Atsushi Miyagi, and Simon Scheuring. Single molecule kinetics of bacteriorhodopsin by hs-afm. *Nature Communications*, 12(1):7225, 2021.

[65] Christopher P Toseland. Fluorescent labeling and modification of proteins. *Journal of chemical biology*, 6:85–95, 2013.

[66] Hisham Mazal and Gilad Haran. Single-molecule fret methods to study the dynamics of proteins at work. *Current opinion in biomedical engineering*, 12:8–17, 2019.

[67] Reinhard Schweitzer-Stenner. Advances in vibrational spectroscopy as a sensitive probe of peptide and protein structure: A critical review. *Vibrational Spectroscopy*, 42(1):98–117, 2006.

[68] Yusaku Hontani, Keiichi Inoue, Miroslav Kloz, Yoshitaka Kato, Hideki Kandori, and John TM Kennis. The photochemistry of sodium ion pump rhodopsin observed by watermarked femto-to submillisecond stimulated raman spectroscopy. *Physical Chemistry Chemical Physics*, 18(35):24729–24736, 2016.

[69] David Buhrke and Peter Hildebrandt. Probing structure and reaction dynamics of proteins using time-resolved resonance raman spectroscopy. *Chemical reviews*, 120(7):3577–3630, 2019.

[70] Eglof Ritter, Katja Stehfest, Andre Berndt, Peter Hegemann, and Franz J Bartl. Monitoring light-induced structural changes of channelrhodopsin-2 by uv-visible and fourier transform infrared spectroscopy. *Journal of Biological Chemistry*, 283(50):35033–35041, 2008.

[71] Christof Grewer, Armanda Gameiro, Thomas Mager, and Klaus Fendler. Electrophysiological characterization of membrane transport proteins. *Annual review of biophysics*, 42:95–120, 2013.

[72] Areles Molleman. *Patch clamping: an introductory guide to patch clamp electrophysiology*. John Wiley & Sons, 2003.

[73] LA Drachev, AA Jasaitis, AD Kaulen, AA Kondrashin, EA Liberman, IB Nemecek, SA Ostroumov, A Yu Semenov, and V Poo Skulachev. Direct measurement of electric current generation by cytochrome oxidase, h+-atpase and bacteriorhodopsin. *Nature*, 249(5455):321–324, 1974.

[74] Patrick Schulz, Juan J Garcia-Celma, and Klaus Fendler. Ssm-based electrophysiology. *Methods*, 46(2):97–103, 2008.

[75] Greg S Harms, Galya Orr, Mauricio Montal, Brian D Thrall, Steve D Colson, and H Peter Lu. Probing conformational changes of gramicidin ion channels by single-molecule patch-clamp fluorescence microscopy. *Biophysical journal*, 85(3):1826–1838, 2003.

[76] H Peter Lu. Combined single-molecule electrical recording and single-molecule spectroscopy studies of ion channel conformational dynamics. *Methods in cell biology*, 90:435–451, 2008.

[77] Dibyendu Kumar Sasmal and H Peter Lu. Single-molecule patch-clamp fret microscopy studies of nmda receptor ion channel dynamics in living cells: revealing the multiple conformational states associated with a channel at its electrical off state. *Journal of the American Chemical Society*, 136(37):12998–13005, 2014.

[78] Jana Katharina Staffa. Electric fields at biomimetic interfaces, spectroelectrochemical studies on the vibrational stark effect of artificial membranes, 2019.

[79] Wikipedia. `https://en.wikipedia.org/wiki/Morse_potential`.

[80] Wikipedia. `https://en.wikipedia.org/wiki/Peptide_bond`.

[81] Pin-Yen Lin, Pei-Yu Huang, Yao-Chang Lee, and Chen Siang Ng. Analysis and comparison of protein secondary structures in the rachis of avian flight feathers. *PeerJ*, 10:e12919, 2022.

[82] Andreas Barth. Infrared spectroscopy of proteins. *Biochimica et Biophysica Acta (BBA)-Bioenergetics*, 1767(9):1073–1101, 2007.

[83] Maria Eleonora Temperini, Valeria Giliberti, Raffaella Polito, Leonetta Baldassarre, and Michele Ortolani. Infrared nanospectroscopy and nanoimaging of individual cell membranes and microvesicles exposed to air. *OSA Continuum*, 3(9):2564–2572, 2020.

[84] Eglof Ritter, Ljiljana Puskar, Franz J Bartl, Emad F Aziz, Peter Hegemann, and Ulrich Schade. Time-resolved infrared spectroscopic techniques as applied to channelrhodopsin. *Frontiers in Molecular Biosciences*, 2:38, 2015.

[85] Hari Prasad Lamichhane and Gary Hastings. Calculated vibrational properties of pigments in protein binding sites. *Proceedings of the National Academy of Sciences*, 108(26):10526–10531, 2011.

[86] Victor A Lórenz-Fonfría and Hideki Kandori. Bayesian maximum entropy (two-dimensional) lifetime distribution reconstruction from time-resolved spectroscopic data. *Applied spectroscopy*, 61(4):428–443, 2007.

[87] Bernd-Joachim Schultz, Hendrik Mohrmann, Victor A Lorenz-Fonfria, and Joachim Heberle. Protein dynamics observed by tunable mid-ir quantum cascade lasers across the time range from 10 ns to 1 s. *Spectrochimica Acta Part A: Molecular and Biomolecular Spectroscopy*, 188:666–674, 2018.

[88] Víctor A Lórenz-Fonfría, Bernd-Joachim Schultz, Tom Resler, Ramona Schlesinger, Christian Bamann, Ernst Bamberg, and Joachim Heberle. Pregating conformational changes in the cheta variant of channelrhodopsin-2 monitored by nanosecond ir spectroscopy. *Journal of the American Chemical Society*, 137(5):1850–1861, 2015.

[89] Agnieszka A Gil, Allison Haigney, Sergey P Laptenok, Richard Brust, Andras Lukacs, James N Iuliano, Jessica Jeng, Eduard H Melief, Rui-Kun Zhao, EunBin Yoon, et al. Mechanism of the appabluf photocycle probed by site-specific incorporation of fluorotyrosine residues: Effect of the y21 p k a on the forward and reverse ground-state reactions. *Journal of the American Chemical Society*, 138(3):926–935, 2016.

[90] Jessica L Klocke, Markus Mangold, Pitt Allmendinger, Andreas Hugi, Markus Geiser, Pierre Jouy, Jérôme Faist, and Tilman Kottke. Single-shot sub-microsecond mid-infrared spectroscopy on protein reactions with quantum cascade laser frequency combs. *Analytical chemistry*, 90(17):10494–10500, 2018.

[91] Victor A Lorenz-Fonfria. Infrared difference spectroscopy of proteins: from bands to bonds. *Chemical reviews*, 120(7):3466–3576, 2020.

[92] Mirta R Alcaráz, Andreas Schwaighofer, Christian Kristament, Georg Ramer, Markus Brandstetter, Héctor Goicoechea, and Bernhard Lendl. External-cavity quantum cascade laser spectroscopy for mid-ir transmission measurements of proteins in aqueous solution. *Analytical chemistry*, 87(13):6980–6987, 2015.

[93] Erik Goormaghtigh, Vincent Raussens, and Jean-Marie Ruysschaert. Attenuated total reflection infrared spectroscopy of proteins and lipids in biological membranes. *Biochimica et Biophysica Acta (BBA)-Reviews on Biomembranes*, 1422(2):105–185, 1999.

[94] Anatoly V Zayats and Igor I Smolyaninov. Near-field photonics: surface plasmon polaritons and localized surface plasmons. *Journal of Optics A: Pure and Applied Optics*, 5(4):S16, 2003.

[95] Paolo Biagioni, Jer-Shing Huang, and Bert Hecht. Nanoantennas for visible and infrared radiation. *Reports on Progress in Physics*, 75(2):024402, 2012.

[96] Rohit Chikkaraddy, VA Turek, Nuttawut Kongsuwan, Felix Benz, Cloudy Carnegie, Tim Van De Goor, Bart De Nijs, Angela Demetriadou, Ortwin Hess, Ulrich F Keyser, et al. Mapping nanoscale hotspots with single-molecule emitters assembled into plasmonic nanocavities using dna origami. *Nano letters*, 18(1):405–411, 2018.

[97] Xiang Wang, Sheng-Chao Huang, Shu Hu, Sen Yan, and Bin Ren. Fundamental understanding and applications of plasmon-enhanced raman spectroscopy. *Nature Reviews Physics*, 2(5):253–271, 2020.

[98] Daniel Rodrigo, Andreas Tittl, Nadine Ait-Bouziad, Aurelian John-Herpin, Odeta Limaj, Christopher Kelly, Daehan Yoo, Nathan J Wittenberg, Sang-Hyun Oh, Hilal A Lashuel, et al. Resolving molecule-specific information in dynamic lipid membrane processes with multi-resonant infrared metasurfaces. *Nature communications*, 9(1):2160, 2018.

[99] Maria Eleonora Temperini, Flavio Di Giacinto, Sabrina Romanò, Riccardo Di Santo, Alberto Augello, Raffaella Polito, Leonetta Baldassarre, Valeria Giliberti, Massimiliano Papi, Umberto Basile, et al. Antenna-enhanced mid-infrared detection of extracellular vesicles derived from human cancer cell cultures. *Journal of Nanobiotechnology*, 20(1):1–20, 2022.

[100] Masatoshi Osawa, Ken-Ichi Ataka, Katsumasa Yoshii, and Yuji Nishikawa. Surface-enhanced infrared spectroscopy: the origin of the absorption enhancement and band selection rule in the infrared spectra of molecules adsorbed on fine metal particles. *Applied spectroscopy*, 47(9):1497–1502, 1993.

[101] Kenichi Ataka, Tilman Kottke, and Joachim Heberle. Thinner, smaller, faster: Ir techniques to probe the functionality of biological and biomimetic systems. *Angewandte Chemie International Edition*, 49(32):5416–5424, 2010.

[102] Frank Neubrech, Annemarie Pucci, Thomas Walter Cornelius, Shafqat Karim, Aitzol García-Etxarri, and Javier Aizpurua. Resonant plasmonic and vibrational coupling in a tailored nanoantenna for infrared detection. *Physical review letters*, 101(15):157403, 2008.

[103] Ronen Adato, Ahmet A Yanik, Jason J Amsden, David L Kaplan, Fiorenzo G Omenetto, Mi K Hong, Shyamsunder Erramilli, and Hatice Altug. Ultra-sensitive vibrational spectroscopy of protein monolayers with plasmonic nanoantenna arrays. *Proceedings of the National Academy of Sciences*, 106(46):19227–19232, 2009.

[104] Ronen Adato and Hatice Altug. In-situ ultra-sensitive infrared absorption spectroscopy of biomolecule interactions in real time with plasmonic nanoantennas. *Nature communications*, 4(1):2154, 2013.

[105] Leonetta Baldassarre, Emilie Sakat, Jacopo Frigerio, Antonio Samarelli, Kevin Gallacher, Eugenio Calandrini, Giovanni Isella, Douglas J Paul, Michele Ortolani, and Paolo Biagioni. Midinfrared plasmon-enhanced spectroscopy with germanium antennas on silicon substrates. *Nano letters*, 15(11):7225–7231, 2015.

[106] Florian Huth, Andrey Chuvilin, Martin Schnell, Iban Amenabar, Roman Krutokhvostov, Sergei Lopatin, and Rainer Hillenbrand. Resonant antenna probes for tip-enhanced infrared near-field microscopy. *Nano letters*, 13(3):1065–1072, 2013.

[107] Feng Lu, Mingzhou Jin, and Mikhail A Belkin. Tip-enhanced infrared nanospectroscopy via molecular expansion force detection. *Nature photonics*, 8(4):307–312, 2014.

[108] B Knoll and F Keilmann. Near-field probing of vibrational absorption for chemical microscopy. *Nature*, 399(6732):134–137, 1999.

[109] Francesco Simone Ruggeri, Benedetta Mannini, Roman Schmid, Michele Vendruscolo, and Tuomas PJ Knowles. Single molecule secondary structure determination of proteins through infrared absorption nanospectroscopy. *Nature Communications*, 11(1):2945, 2020.

[110] Andrea Centrone. Infrared imaging and spectroscopy beyond the diffraction limit. *Annual review of analytical chemistry*, 8:101–126, 2015.

[111] Samuel Berweger, Duc M Nguyen, Eric A Muller, Hans A Bechtel, Thomas T Perkins, and Markus B Raschke. Nano-chemical infrared imaging of membrane proteins in lipid bilayers. *Journal of the American Chemical Society*, 135(49):18292–18295, 2013.

[112] Andreas J Huber, Fritz Keilmann, J Wittborn, Javier Aizpurua, and Rainer Hillenbrand. Terahertz near-field nanoscopy of mobile carriers in single semiconductor nanodevices. *Nano letters*, 8(11):3766–3770, 2008.

[113] Rainer Jacob, Stephan Winnerl, Markus Fehrenbacher, Jayeeta Bhattacharyya, Harald Schneider, Marc Tobias Wenzel, Hans-Georg von Ribbeck, Lukas M Eng, Paola Atkinson, Oliver G Schmidt, et al. Intersublevel spectroscopy on single inas-quantum dots by terahertz near-field microscopy. *Nano letters*, 12(8):4336–4340, 2012.

[114] Th Taubner, R Hillenbrand, and F Keilmann. Nanoscale polymer recognition by spectral signature in scattering infrared near-field microscopy. *Applied Physics Letters*, 85(21):5064–5066, 2004.

[115] Zhe Fei, AS Rodin, Gregory O Andreev, Wenzhong Bao, AS McLeod, M Wagner, LM Zhang, Zeng Zhao, M Thiemens, Gerardo Dominguez, et al. Gate-tuning of graphene plasmons revealed by infrared nano-imaging. *Nature*, 487(7405):82–85, 2012.

[116] Siyuan Dai, Wenjing Fang, Nicholas Rivera, Yijing Stehle, Bor-Yuan Jiang, Jialiang Shen, Roland Yingjie Tay, Christopher J Ciccarino, Qiong Ma, Daniel Rodan-Legrain, et al. Phonon polaritons in monolayers of hexagonal boron nitride. *Advanced materials*, 31(37):1806603, 2019.

[117] Markus Brehm, Thomas Taubner, Rainer Hillenbrand, and Fritz Keilmann. Infrared spectroscopic mapping of single nanoparticles and viruses at nanoscale resolution. *Nano Letters*, 6(7):1307–1310, 2006.

[118] Iban Amenabar, Simon Poly, Wiwat Nuansing, Elmar H Hubrich, Alexander A Govyadinov, Florian Huth, Roman Krutokhvostov, Lianbing Zhang, Mato Knez, Joachim Heberle, et al. Structural analysis and mapping of individual

protein complexes by infrared nanospectroscopy. *Nature communications*, 4(1):2890, 2013.

[119] Emanuel Pfitzner and Joachim Heberle. Infrared scattering-type scanning near-field optical microscopy of biomembranes in water. *The Journal of Physical Chemistry Letters*, 11(19):8183–8188, 2020.

[120] Georg Ramer, Vladimir A Aksyuk, and Andrea Centrone. Quantitative chemical analysis at the nanoscale using the photothermal induced resonance technique. *Analytical chemistry*, 89(24):13524–13531, 2017.

[121] Jeffrey J Schwartz, Devon S Jakob, and Andrea Centrone. A guide to nanoscale ir spectroscopy: resonance enhanced transduction in contact and tapping mode afm-ir. *Chemical Society Reviews*, 51(13):5248–5267, 2022.

[122] Alexandre Dazzi, R Prazeres, F Glotin, JM Ortega, M d Al-Sawaftah, and M De Frutos. Chemical mapping of the distribution of viruses into infected bacteria with a photothermal method. *Ultramicroscopy*, 108(7):635–641, 2008.

[123] Eamonn Kennedy, Rasoul Al-Majmaie, Mohamed Al-Rubeai, Dominic Zerulla, and James H Rice. Quantifying nanoscale biochemical heterogeneity in human epithelial cancer cells using combined afm and ptir absorption nanoimaging. *Journal of biophotonics*, 8(1-2):133–141, 2015.

[124] Valeria Giliberti, Michela Badioli, Alessandro Nucara, Paolo Calvani, Eglof Ritter, Ljiljana Puskar, Emad Flear Aziz, Peter Hegemann, Ulrich Schade, Michele Ortolani, et al. Heterogeneity of the transmembrane protein conformation in purple membranes identified by infrared nanospectroscopy. *Small*, 13(44):1701181, 2017.

[125] Francesco Simone Ruggeri, Tomas Šneideris, Michele Vendruscolo, and Tuomas PJ Knowles. Atomic force microscopy for single molecule characterisation of protein aggregation. *Archives of biochemistry and biophysics*, 664:134–148, 2019.

[126] Raffaella Polito, Mattia Musto, Maria Eleonora Temperini, Laura Ballerini, Michele Ortolani, Leonetta Baldassarre, Loredana Casalis, and Valeria Giliberti. Infrared nanospectroscopy of individual extracellular microvesicles. *Molecules*, 26(4):887, 2021.

[127] Jonathan R Felts, Kevin Kjoller, Michael Lo, Craig B Prater, and William P King. Nanometer-scale infrared spectroscopy of heterogeneous polymer nanostructures fabricated by tip-based nanofabrication. *ACS nano*, 6(9):8015–8021, 2012.

[128] S Sauvage, A Driss, F Réveret, P Boucaud, A Dazzi, R Prazeres, F Glotin, J-M Ortéga, A Miard, Y Halioua, et al. Homogeneous broadening of the s to p transition in ingaas/gaas quantum dots measured by infrared absorption imaging with nanoscale resolution. *Physical Review B*, 83(3):035302, 2011.

[129] Aaron M Katzenmeyer, Jungseok Chae, Richard Kasica, Glenn Holland, Basudev Lahiri, and Andrea Centrone. Nanoscale imaging and spectroscopy of plasmonic modes with the ptir technique. *Advanced Optical Materials*, 2(8):718–722, 2014.

[130] Hong Khoa Ly, Murat Sezer, Nattawadee Wisitruangsakul, Jiu-Ju Feng, Anja Kranich, Diego Millo, Inez M Weidinger, Ingo Zebger, Daniel H Murgida, and Peter Hildebrandt. Surface-enhanced vibrational spectroscopy for probing transient interactions of proteins with biomimetic interfaces: electric field effects on structure, dynamics and function of cytochrome c. *The FEBS journal*, 278(9):1382–1390, 2011.

[131] Innocent Bekard and Dave E Dunstan. Electric field induced changes in protein conformation. *Soft Matter*, 10(3):431–437, 2014.

[132] Ayelet Vilan, Dinesh Aswal, and David Cahen. Large-area, ensemble molecular electronics: motivation and challenges. *Chemical Reviews*, 117(5):4248–4286, 2017.

[133] Vimala Dhayal, SZ Hashmi, Upendra Kumar, BL Choudhary, AE Kuznetsov, Saurabh Dalela, Shalendra Kumar, Savas Kaya, SN Dolia, and PA Alvi. Spectroscopic studies, molecular structure optimization and investigation of structural and electrical properties of novel and biodegradable chitosan-go polymer nanocomposites. *Journal of Materials Science*, 55:14829–14847, 2020.

[134] Daeyeong Kim, Sang A Han, Jung Ho Kim, Ju-Hyuck Lee, Sang-Woo Kim, and Seung-Wuk Lee. Biomolecular piezoelectric materials: from amino acids to living tissues. *Advanced Materials*, 32(14):1906989, 2020.

[135] Benjamin S Hoener, Hui Zhang, Thomas S Heiderscheit, Silke R Kirchner, Agampodi S De Silva Indrasekara, Rashad Baiyasi, Yiyu Cai, Peter Nordlander, Stephan Link, Christy F Landes, et al. Spectral response of plasmonic gold nanoparticles to capacitive charging: morphology effects. *The journal of physical chemistry letters*, 8(12):2681–2688, 2017.

[136] Sunghwan Shin, Youngwook Park, Hani Kang, and Heon Kang. Electric field effect on condensed-phase molecular systems. iv. conformational change of 1, 2-dichloroethane in a frozen molecular solid. *The Journal of Physical Chemistry C*, 121(45):25342–25346, 2017.

[137] Eun Sun Park, Steven S Andrews, Robert B Hu, and Steven G Boxer. Vibrational stark spectroscopy in proteins: A probe and calibration for electrostatic fields. *The Journal of Physical Chemistry B*, 103(45):9813–9817, 1999.

[138] Eun Sun Park and Steven G Boxer. Origins of the sensitivity of molecular vibrations to electric fields: Carbonyl and nitrosyl stretches in model compounds and proteins. *The Journal of Physical Chemistry B*, 106(22):5800–5806, 2002.

[139] Francisco Bezanilla. How membrane proteins sense voltage. *Nature reviews Molecular cell biology*, 9(4):323–332, 2008.

[140] Jan Antosiewicz and Dietmar Porschke. The nature of protein dipole moments: Experimental and calculated permanent dipole of. alpha.-chymotrypsin. *Biochemistry*, 28(26):10072–10078, 1989.

[141] Xianwei Wang, Yongxiu Li, Xiao He, Shude Chen, and John ZH Zhang. Effect of strong electric field on the conformational integrity of insulin. *The Journal of Physical Chemistry A*, 118(39):8942–8952, 2014.

[142] Yusuke Shuto, Erik Walinda, Daichi Morimoto, and Kenji Sugase. Conformational fluctuations and induced orientation of a protein, its solvation shell, and bulk water in weak non-unfolding external electric fields. *The Journal of Physical Chemistry B*, 127(34):7417–7430, 2023.

[143] Hirofumi Sakai, CP Safvan, Jakob Juul Larsen, Karen Marie Hilligso/e, Kasper Hald, and Henrik Stapelfeldt. Controlling the alignment of neutral molecules by a strong laser field. *The Journal of Chemical Physics*, 110(21):10235–10238, 1999.

[144] Lotte Holmegaard, Jonas L Hansen, Line Kalhøj, Sofie Louise Kragh, Henrik Stapelfeldt, Frank Filsinger, Jochen Küpper, Gerard Meijer, Darko Dimitrovski, Mahmoud Abu-Samha, et al. Photoelectron angular distributions from strong-field ionization of oriented molecules. *Nature Physics*, 6(6):428–432, 2010.

[145] Hans GL Coster and Terry C Chilcott. Electric field effects in proteins in membranes. *Bioelectrochemistry*, 56(1-2):141–146, 2002.

[146] Innocent Bekard and Dave E Dunstan. Electric field induced changes in protein conformation. *Soft Matter*, 10(3):431–437, 2014.

[147] Isabella Daidone, Massimiliano Aschi, Laura Zanetti-Polzi, Alfredo Di Nola, and Andrea Amadei. On the origin of ir spectral changes upon protein folding. *Chemical Physics Letters*, 488(4-6):213–218, 2010.

[148] Arun Chattopadhyay and Steven G Boxer. Vibrational stark effect spectroscopy. *Journal of the American Chemical Society*, 117(4):1449–1450, 1995.

[149] Gerold U Bublitz and Steven G Boxer. Stark spectroscopy: applications in chemistry, biology, and materials science. *Annual review of physical chemistry*, 48(1):213–242, 1997.

[150] Lisa N Silverman, Michael E Pitzer, Peter O Ankomah, Steven G Boxer, and Edward E Fenlon. Vibrational stark effect probes for nucleic acids. *The Journal of Physical Chemistry B*, 111(40):11611–11613, 2007.

[151] Kenji Takashima and Yukio Furukawa. Vibrational stark effect (vse) on the infrared spectrum of a poly (methyl methacrylate) thin film. *Vibrational Spectroscopy*, 78:54–59, 2015.

[152] Jana K Staffa, Lisa Lorenz, Michael Stolarski, Daniel H Murgida, Ingo Zebger, Tillmann Utesch, Jacek Kozuch, and Peter Hildebrandt. Determination of the local electric field at au/sam interfaces using the vibrational stark effect. *The Journal of Physical Chemistry C*, 121(40):22274–22285, 2017.

[153] Aimin Ge, Pablo E Videla, Gwendolynne L Lee, Benjamin Rudshteyn, Jia Song, Clifford P Kubiak, Victor S Batista, and Tianquan Lian. Interfacial structure and electric field probed by in situ electrochemical vibrational stark effect spectroscopy and computational modeling. *The Journal of Physical Chemistry C*, 121(34):18674–18682, 2017.

[154] Jong Hyeon Lim, Daeheum Cho, Heon Kang, and Jin Yong Lee. Electronic and nuclear contributions to vibrational stark shifts of hydroxyl stretching frequencies of water clusters. *The Journal of Physical Chemistry C*, 122(24):12970–12974, 2018.

[155] Hani Kang, Josée Maurais, Youngwook Park, Patrick Ayotte, and Heon Kang. Electric field effect on condensed-phase molecular systems. viii. vibrational stark effect and dipolar inversion in a carbon monoxide crystal. *The Journal of Physical Chemistry C*, 123(51):31262–31271, 2019.

[156] Stephen D Fried and Steven G Boxer. Measuring electric fields and noncovalent interactions using the vibrational stark effect. *Accounts of chemical research*, 48(4):998–1006, 2015.

[157] Steven G Boxer. Stark realities. *The Journal of Physical Chemistry B*, 113(10):2972–2983, 2009.

[158] Hartwig Lehle, Jan M Kriegl, Karin Nienhaus, Pengchi Deng, Stephanus Fengler, and G Ulrich Nienhaus. Probing electric fields in protein cavities by using the vibrational stark effect of carbon monoxide. *Biophysical journal*, 88(3):1978–1990, 2005.

[159] David J Lockhart and Peter S Kim. Internal stark effect measurement of the electric field at the amino terminus of an α helix. *Science*, 257(5072):947–951, 1992.

[160] Joshua D Slocum and Lauren J Webb. Measuring electric fields in biological matter using the vibrational stark effect of nitrile probes. *Annual Review of Physical Chemistry*, 69:253–271, 2018.

[161] Steven S Andrews and Steven G Boxer. Vibrational stark effects of nitriles i. methods and experimental results. *The Journal of Physical Chemistry A*, 104(51):11853–11863, 2000.

[162] Wenhui Hu and Lauren J Webb. Direct measurement of the membrane dipole field in bicelles using vibrational stark effect spectroscopy. *The Journal of Physical Chemistry Letters*, 2(15):1925–1930, 2011.

[163] Hendrik Mohrmann, Ines Kube, Victor A Lorenz-Fonfria, Martin Engelhard, and Joachim Heberle. Transient conformational changes of sensory rhodopsin ii investigated by vibrational stark effect probes. *The Journal of Physical Chemistry B*, 120(19):4383–4387, 2016.

[164] Benjamin Pollard, Eric A Muller, Karsten Hinrichs, and Markus B Raschke. Vibrational nano-spectroscopic imaging correlating structure with intermolecular coupling and dynamics. *Nature Communications*, 5(1):3587, 2014.

[165] I Zawisza, A Lachenwitzer, V Zamlynny, SL Horswell, JD Goddard, and J Lipkowski. Electrochemical and photon polarization modulation infrared reflection absorption spectroscopy study of the electric field driven transformations of a phospholipid bilayer supported at a gold electrode surface. *Biophysical journal*, 85(6):4055–4075, 2003.

[166] Hayato Isoda and Yukio Furukawa. Electric-field-induced dynamics of polymer chains in a ferroelectric melt-quenched cold-drawn film of nylon-11 using infrared spectroscopy. *The Journal of Physical Chemistry B*, 119(44):14309–14314, 2015.

[167] Shogo Toda and Shinsuke Shigeto. Hydrogen bonded structures of confined water molecules and electric field induced shift of their equilibrium revealed by ir electroabsorption spectroscopy. *The Journal of Physical Chemistry B*, 121(22):5573–5581, 2017.

[168] X Jiang, E Zaitseva, M Schmidt, F Siebert, M Engelhard, R Schlesinger, K Ataka, R Vogel, and J Heberle. Resolving voltage-dependent structural changes of a membrane photoreceptor by surface-enhanced ir difference spectroscopy. *Proceedings of the National Academy of Sciences*, 105(34):12113–12117, 2008.

[169] Xi Yu, Robert Lovrincic, Lior Sepunaru, Wenjie Li, Ayelet Vilan, Israel Pecht, Mordechai Sheves, and David Cahen. Insights into solid-state electron transport through proteins from inelastic tunneling spectroscopy: The case of azurin. *ACS nano*, 9(10):9955–9963, 2015.

[170] Ke Bian, Christoph Gerber, Andreas J Heinrich, Daniel J Müller, Simon Scheuring, and Ying Jiang. Scanning probe microscopy. *Nature Reviews Methods Primers*, 1(1):36, 2021.

[171] Amanda M Moore and Paul S Weiss. Functional and spectroscopic measurements with scanning tunneling microscopy. *Annu. Rev. Anal. Chem.*, 1:857–882, 2008.

[172] M Morgenstern, Chr Wittneven, R Dombrowski, and R Wiesendanger. Spatial fluctuations of the density of states in magnetic fields observed with scanning tunneling spectroscopy. *Physical Review Letters*, 84(24):5588, 2000.

[173] Y Niimi, T Matsui, H Kambara, K Tagami, M Tsukada, and Hiroshi Fukuyama. Scanning tunneling microscopy and spectroscopy of the electronic local density of states of graphite surfaces near monoatomic step edges. *Physical Review B*, 73(8):085421, 2006.

[174] Matteo Passoni, Fabio Donati, A Li Bassi, CARLO SPARTACO Casari, and CARLO ENRICO Bottani. Recovery of local density of states using scanning tunneling spectroscopy. *Physical Review B*, 79(4):045404, 2009.

[175] L Limot, T Maroutian, P Johansson, and R Berndt. Surface-state stark shift in a scanning tunneling microscope. *Physical review letters*, 91(19):196801, 2003.

[176] Masa Ishigami, Jay Deep Sau, Shaul Aloni, Marvin L Cohen, and A Zettl. Observation of the giant stark effect in boron-nitride nanotubes. *Physical review letters*, 94(5):056804, 2005.

[177] José Ignacio Pascual, Jennifer J Jackiw, Zhen Song, Paul S Weiss, Horst Conrad, and H-P Rust. Adsorbate-substrate vibrational modes of benzene on ag (110) resolved with scanning tunneling spectroscopy. *Physical review letters*, 86(6):1050, 2001.

[178] Norio Okabayashi, Youhei Konda, and Tadahiro Komeda. Inelastic electron tunneling spectroscopy of an alkanethiol self-assembled monolayer using scanning tunneling microscopy. *Physical review letters*, 100(21):217801, 2008.

[179] Jeffrey M Mativetsky, Emanuele Treossi, Emanuele Orgiu, Manuela Melucci, Giulio Paolo Veronese, Paolo Samorí, and Vincenzo Palermo. Local current mapping and patterning of reduced graphene oxide. *Journal of the American Chemical Society*, 132(40):14130–14136, 2010.

[180] Degao Xu, Gerald D Watt, John N Harb, and Robert C Davis. Electrical conductivity of ferritin proteins by conductive afm. *Nano letters*, 5(4):571–577, 2005.

[181] JA Christman, H Maiwa, S-H Kim, AI Kingon, and RJ Nemanich. Piezoelectric measurements with atomic force microscopy. *MRS Online Proceedings Library (OPL)*, 541:617, 1998.

[182] Hyungoo Lee, Rodrigo Cooper, Ke Wang, and Hong Liang. Nano-scale characterization of a piezoelectric polymer (polyvinylidene difluoride, pvdf). *Sensors*, 8(11):7359–7368, 2008.

[183] Lars JC Jeuken. Afm study on the electric-field effects on supported bilayer lipid membranes. *Biophysical journal*, 94(12):4711–4717, 2008.

[184] Tao Wang and Christian A Nijhuis. Molecular electronic plasmonics. *Applied Materials Today*, 3:73–86, 2016.

[185] Maoning Wang, Tao Wang, Oluwafemi S Ojambati, Thorin Jake Duffin, Keehoon Kang, Takhee Lee, Elke Scheer, Dong Xiang, and Christian A Nijhuis. Plasmonic phenomena in molecular junctions: Principles and applications. *Nature Reviews Chemistry*, 6(10):681–704, 2022.

[186] Brian C Smith. *Fundamentals of Fourier transform infrared spectroscopy*. CRC press, 2011.

[187] Paul Bassan, Miles J Weida, Jeremy Rowlette, and Peter Gardner. Large scale infrared imaging of tissue micro arrays (tmas) using a tunable quantum cascade laser (qcl) based microscope. *Analyst*, 139(16):3856–3859, 2014.

[188] Maria Eleonora Temperini, Raffaella Polito, Antonia Intze, Raymond Gillibert, Fritz Berkmann, Leonetta Baldassarre, Valeria Giliberti, and Michele Ortolani. A mid-infrared laser microscope for the time-resolved study of light-induced protein conformational changes. *Review of Scientific Instruments*, 94(6), 2023.

[189] Bo Huang, Mark Bates, and Xiaowei Zhuang. Super-resolution fluorescence microscopy. *Annual review of biochemistry*, 78:993–1016, 2009.

[190] Gergely Huszka and Martin AM Gijs. Super-resolution optical imaging: A comparison. *Micro and Nano Engineering*, 2:7–28, 2019.

[191] Mark Bates, Bo Huang, Graham T Dempsey, and Xiaowei Zhuang. Multicolor super-resolution imaging with photo-switchable fluorescent probes. *Science*, 317(5845):1749–1753, 2007.

[192] Lukas Novotny and Bert Hecht. *Principles of nano-optics*. Cambridge university press, 2012.

[193] Anatoly V Zayats and David Richards. *Nano-optics and near-field optical microscopy*. Artech House, 2009.

[194] Itay Rousso and Akshay Deshpande. Applications of atomic force microscopy in hiv-1 research. *Viruses*, 14(3):648, 2022.

[195] Alma P Perrino, Atsushi Miyagi, and Simon Scheuring. Single molecule kinetics of bacteriorhodopsin by hs-afm. *Nature Communications*, 12(1):7225, 2021.

[196] J. Faist. *Quantum cascade lasers*. Oxford, 2014.

[197] Andreas Schwaighofer, Markus Brandstetter, and Bernhard Lendl. Quantum cascade lasers (qcls) in biomedical spectroscopy. *Chemical Society Reviews*, 46(19):5903–5924, 2017.

[198] Christopher K Akhgar, Georg Ramer, Mateusz Zbik, Artur Trajnerowicz, Jarosław Pawluczyk, Andreas Schwaighofer, and Bernhard Lendl. The next generation of ir spectroscopy: Ec-qcl-based mid-ir transmission spectroscopy of proteins with balanced detection. *Analytical Chemistry*, 92(14):9901–9907, 2020.

[199] Tom Resler, Bernd-Joachim Schultz, Víctor A Lórenz-Fonfría, Ramona Schlesinger, and Joachim Heberle. Kinetic and vibrational isotope effects of proton transfer reactions in channelrhodopsin-2. *Biophysical Journal*, 109(2):287–297, 2015.

[200] Feng Lu and Mikhail A Belkin. Infrared absorption nano-spectroscopy using sample photoexpansion induced by tunable quantum cascade lasers. *Optics express*, 19(21):19942–19947, 2011.

[201] Jeremie Mathurin, Ariane Deniset-Besseau, Dominique Bazin, Emmanuel Dartois, Martin Wagner, and Alexandre Dazzi. Photothermal afm-ir spectroscopy and imaging: Status, challenges, and trends. *Journal of Applied Physics*, 131(1), 2022.

[202] T Venanzi, V Giliberti, ME Temperini, S Sotgiu, R Polito, F Mattioli, A Pitanti, V Mišeikis, C Coletti, S Roddaro, et al. Mid-infrared photocurrent nanospectroscopy exploiting the thermoelectric effect in graphene. *Applied Physics Letters*, 123(15), 2023.

[203] F Giannazzo, G Fisichella, A Piazza, S Agnello, and F Roccaforte. Nanoscale inhomogeneity of the schottky barrier and resistivity in mos 2 multilayers. *Physical Review B*, 92(8):081307, 2015.

[204] Edward S Boyden, Feng Zhang, Ernst Bamberg, Georg Nagel, and Karl Deisseroth. Millisecond-timescale, genetically targeted optical control of neural activity. *Nature neuroscience*, 8(9):1263–1268, 2005.

[205] Eglof Ritter, Patrick Piwowarski, Peter Hegemann, and Franz J Bartl. Light-dark adaptation of channelrhodopsin c128t mutant. *Journal of Biological Chemistry*, 288(15):10451–10458, 2013.

[206] Matthias Elgeti, Roman Kazmin, Martin Heck, Takefumi Morizumi, Eglof Ritter, Patrick Scheerer, Oliver P Ernst, Friedrich Siebert, Klaus Peter Hofmann, and Franz J Bartl. Conserved tyr2235. 58 plays different roles in the activation and g-protein interaction of rhodopsin. *Journal of the American Chemical Society*, 133(18):7159–7165, 2011.

[207] Lukas K Tamm and Suren A Tatulian. Infrared spectroscopy of proteins and peptides in lipid bilayers. *Quarterly reviews of biophysics*, 30(4):365–429, 1997.

[208] Alexandre Dazzi and Craig B Prater. Afm-ir: Technology and applications in nanoscale infrared spectroscopy and chemical imaging. *Chemical reviews*, 117(7):5146–5173, 2017.

[209] Jens Kuhne, Johannes Vierock, Stefan Alexander Tennigkeit, Max-Aylmer Dreier, Jonas Wietek, Dennis Petersen, Konstantin Gavriljuk, Samir F El-Mashtoly, Peter Hegemann, and Klaus Gerwert. Unifying photocycle model for light adaptation and temporal evolution of cation conductance in channelrhodopsin-2. *Proceedings of the National Academy of Sciences*, 116(19):9380–9389, 2019.

[210] Matthias Elgeti, Eglof Ritter, and Franz J Bartl. New insights into light-induced deactivation of active rhodopsin by svd and global analysis of time-resolved uv/vis-and ftir-data. *Zeitschrift für Physikalische Chemie*, 222(8-9):1117–1129, 2008.

[211] Melanie Nack, Ionela Radu, Michael Gossing, Christian Bamann, Ernst Bamberg, Gabriele Fischer von Mollard, and Joachim Heberle. The dc gate in channelrhodopsin-2: crucial hydrogen bonding interaction between c128 and d156. *Photochemical & Photobiological Sciences*, 9:194–198, 2010.

[212] Rohit Chikkaraddy, Bart De Nijs, Felix Benz, Steven J Barrow, Oren A Scherman, Edina Rosta, Angela Demetriadou, Peter Fox, Ortwin Hess, and Jeremy J Baumberg. Single-molecule strong coupling at room temperature in plasmonic nanocavities. *Nature*, 535(7610):127–130, 2016.

[213] Nicholas M Levinson, Stephen D Fried, and Steven G Boxer. Solvent-induced infrared frequency shifts in aromatic nitriles are quantitatively described by the vibrational stark effect. *The journal of physical chemistry B*, 116(35):10470–10476, 2012.

[214] Samuel H Schneider and Steven G Boxer. Vibrational stark effects of carbonyl probes applied to reinterpret ir and raman data for enzyme inhibitors in terms of electric fields at the active site. *The Journal of Physical Chemistry B*, 120(36):9672–9684, 2016.

[215] Hiroyuki Aoki, Kazuki Mori, Toshiaki Takahashi, and Shinzaburo Ito. Quantitative analysis of end-to-end distance of single polymer chain in ultra-thin film by super-resolution fluorescence imaging. *Chemical Physics*, 419:54–58, 2013.

[216] HQ Zhang, Y Jin, and Y Qiu. The optical and electrical characteristics of pmma film prepared by spin coating method. In *IOP Conference Series: Materials Science and Engineering*, volume 87, page 012032. IOP Publishing, 2015.

[217] Saumil P Samant, Christopher A Grabowski, Kim Kisslinger, Kevin G Yager, Guangcui Yuan, Sushil K Satija, Michael F Durstock, Dharmaraj Raghavan, and Alamgir Karim. Directed self-assembly of block copolymers for high breakdown strength polymer film capacitors. *ACS applied materials & interfaces*, 8(12):7966–7976, 2016.

[218] Kenji Takashima and Yukio Furukawa. Voltage-induced infrared absorption from a spin-cast thin film of ferroelectric poly (vinylidene fluoride-co-trifluoroethylene)(p (vdf-trfe)). *Analytical Sciences*, 33(1):59–64, 2017.

[219] Subramaniyan Ramasundaram, Sun Yoon, Kap Jin Kim, and Jong Soon Lee. Direct preparation of nanoscale thin films of poly (vinylidene fluoride) containing β-crystalline phase by heat-controlled spin coating. *Macromolecular Chemistry and Physics*, 209(24):2516–2526, 2008.

[220] Xiaomei Cai, Tingping Lei, Daoheng Sun, and Liwei Lin. A critical analysis of the α, β and γ phases in poly (vinylidene fluoride) using ftir. *RSC advances*, 7(25):15382–15389, 2017.

[221] Helmut F Knapp, Patrick Mesquida, and Andreas Stemmer. Imaging the surface potential of active purple membrane. *Surface and Interface Analysis: An International Journal devoted to the development and application of techniques for the analysis of surfaces, interfaces and thin films*, 33(2):108–112, 2002.

[222] Ian T Suydam and Steven G Boxer. Vibrational stark effects calibrate the sensitivity of vibrational probes for electric fields in proteins. *Biochemistry*, 42(41):12050–12055, 2003.

[223] Ryan D Pensack, Kyle M Banyas, and John B Asbury. Vibrational solvatochromism in organic photovoltaic materials: method to distinguish molecules at donor/acceptor interfaces. *Physical Chemistry Chemical Physics*, 12(42):14144–14152, 2010.

[224] Derek Marsh and Tibor Pali. Infrared dichroism from the x-ray structure of bacteriorhodopsin. *Biophysical journal*, 80(1):305–312, 2001.

[225] Elena Della Valle, Paolo Marracino, Olga Pakhomova, Micaela Liberti, and Francesca Apollonio. Nanosecond pulsed electric signals can affect electrostatic environment of proteins below the threshold of conformational effects: The case study of sod1 with a molecular simulation study. *PLoS One*, 14(8):e0221685, 2019.

[226] Andreas Barth and Christian Zscherp. What vibrations tell about proteins. *Quarterly reviews of biophysics*, 35(4):369–430, 2002.

[227] Jonas Schartner, Konstantin Gavriljuk, Andreas Nabers, Philipp Weide, Martin Muhler, Klaus Gerwert, and Carsten Kötting. Immobilization of proteins in their physiological active state at functionalized thiol monolayers on atr-germanium crystals. *ChemBioChem*, 15(17):2529–2534, 2014.

[228] Víctor A Lórenz-Fonfría and Joachim Heberle. Channelrhodopsin unchained: structure and mechanism of a light-gated cation channel. *Biochimica et Biophysica Acta (BBA)-Bioenergetics*, 1837(5):626–642, 2014.

[229] Tadej Kotnik, Lea Rems, Mounir Tarek, and Damijan Miklavčič. Membrane electroporation and electropermeabilization: mechanisms and models. *Annual review of biophysics*, 48:63–91, 2019.

[230] Johannes Akinlaja and Frederick Sachs. The breakdown of cell membranes by electrical and mechanical stress. *Biophysical journal*, 75(1):247–254, 1998.

[231] C Chen, SW Smye, MPea Robinson, and JA Evans. Membrane electroporation theories: a review. *Medical and Biological Engineering and Computing*, 44:5–14, 2006.

[232] RP Joshi, V Sridhara, and KH Schoenbach. Microscopic calculations of local lipid membrane permittivities and diffusion coefficients for application to electroporation analyses. *Biochemical and Biophysical Research Communications*, 348(2):643–648, 2006.

[233] Mounir Tarek. Membrane electroporation: a molecular dynamics simulation. *Biophysical journal*, 88(6):4045–4053, 2005.

[234] Norbert A Dencher, Hans Jürgen Sass, and Georg Büldt. Water and bacteriorhodopsin: structure, dynamics, and function. *Biochimica et Biophysica Acta (BBA)-Bioenergetics*, 1460(1):192–203, 2000.

[235] Tzvetana Lazarova, Carolina Sanz, Enric Querol, and Esteve Padrós. Fourier transform infrared evidence for early deprotonation of asp85 at alkaline ph in the photocycle of bacteriorhodopsin mutants containing e194q. *Biophysical Journal*, 78(4):2022–2030, 2000.

[236] Yongdong Jin, Tal Honig, Izhar Ron, Noga Friedman, Mordechai Sheves, and David Cahen. Bacteriorhodopsin as an electronic conduction medium for biomolecular electronics. *Chemical Society Reviews*, 37(11):2422–2432, 2008.

[237] Yujia Lv, Dawei Liang, Shanfu Lu, Doron Aurbach, and Yan Xiang. Unidirectional electron injection and accelerated proton transport in bacteriorhodopsin based bio-pn junctions. *Biosensors and Bioelectronics*, 173:112811, 2021.

[238] Sudipta Bera, Jerry A Fereiro, Shailendra K Saxena, Domenikos Chryssikos, Koushik Majhi, Tatyana Bendikov, Lior Sepunaru, David Ehre, Marc Tornow, Israel Pecht, et al. Near-temperature-independent electron transport well beyond expected quantum tunneling range via bacteriorhodopsin multilayers. *Journal of the American Chemical Society*, 145(45):24820–24835, 2023.

[239] Katrin Feldbauer, Dirk Zimmermann, Verena Pintschovius, Julia Spitz, Christian Bamann, and Ernst Bamberg. Channelrhodopsin-2 is a leaky proton pump. *Proceedings of the National Academy of Sciences*, 106(30):12317–12322, 2009.

[240] Franziska Schneider, Christiane Grimm, and Peter Hegemann. Biophysics of channelrhodopsin. *Annual review of biophysics*, 44:167–186, 2015.

[241] Antonia Intze, Maria Eleonora Temperini, Leonetta Baldassarre, Valeria Giliberti, Michele Ortolani, and Raffaella Polito. Time-resolved investigation of nanometric cell membrane patches with a mid-infrared laser microscope. *Frontiers in Photonics*, 4:1175033, 2023.

[242] Constanta Ganea, Csilla Gergely, Krisztina Ludmann, and Gyorgy Váró. The role of water in the extracellular half channel of bacteriorhodopsin. *Biophysical journal*, 73(5):2718–2725, 1997.

[243] He Tian, Thomas P Sakmar, and Thomas Huber. Measurement of slow spontaneous release of 11-cis-retinal from rhodopsin. *Biophysical Journal*, 112(1):153–161, 2017.

[244] Peter R Griffiths. Fourier transform infrared spectrometry. *Science*, 222(4621):297–302, 1983.